Quantification of MT & CEST MRI for *in vivo* applications

by

Andrew John Carradus, MSci

Thesis submitted to The University of Nottingham
for the degree of Doctor of Philosophy

January 2021

Abstract

Z-spectroscopy is a form of magnetic resonance imaging (MRI) in which the free water signal is modulated by exchange with other sources of protons resonating at different frequencies. However, interpretation of these signals is not trivial, and care must be taken when attempting to quantify the physical parameters which give rise to these effects. This thesis describes the development of methods to assess and quantify z-spectrum effects, along with *in vivo* application of these methods with the aim of moving towards clinical use.

Initially z-spectrum data from the brain were analysed using a look-up table fitting approach described previously. The MT pool size was used as a marker of myelination across subjects. This was then compared to subject age showing a quadratic trend with age, suggesting that cerebral myelination peaks at 43 years of age in grey matter and 42 years of age in white matter. This was repeated for T_1 measurements, which indicated peak myelination slightly later in life, most likely due to the combined effects of myelination and cerebral iron content. The concept of measuring myelination using NOE as a marker was explored, and it was found that NOE measurements also followed a parabolic trend with age, albeit weaker than the trend shown by the MT signal. Nevertheless this may be a useful finding for understanding the nature and origin of the NOE signal.

However, the look-up table used here could only fit for pool size. The main physical parameters of interest in z-spectroscopy are the pool size and the exchange rate, which are difficult to mathematically uncouple. This thesis introduces a particle swarm

optimisation (PSO) algorithm as a tool to iteratively solve this problem, by effectively taking many initial guesses at the solutions simultaneously, and then mimicking the collective intelligence of a swarm to move towards the best solution. This was proven to be robust in simulations and phantoms, and was used to quantify the z-spectra from *in vivo* brain tissue and *ex vivo* blood, both of which are of great clinical importance. When quantifying cerebral grey and white matter *in vivo* it was found that there is a statistically significantly increased pool size fractions of both MT and the NOE peak located at -1.7ppm in white matter compared to grey matter, while exchange rates remained consistent between the two types of brain tissue. The NOE signals from *ex vivo* human blood were found to have exchange rates of 10Hz for the pool located at -3.5ppm and 13Hz for the pool located at -1.7ppm. CEST fitting with glycosaminoglycans and glucose pools was attempted on this spectrum, however the fitting results suggest that underlying CEST pools may not have been accounted for.

Finally the potential for performing z-spectroscopy in the abdomen was investigated, first at clinical field strengths to assess the potential to accurately quantify the MT effect for use as a marker for fibrosis. The challenges of abdominal z-spectroscopy at ultra-high fields were then explored before development of a protocol capable of measuring the evolution of liver glycogen *in vivo*.

This thesis is written in Computer Modern Unicode Sans-Serif typeface, which has been shown to improve reading performance among dyslexic readers compared to other common fonts (L. Rello and R. Baeza-Yates. Good fonts for dyslexia. *Proceedings of the 15th international ACM SIGACCESS conference on computers and accessibility* 1-8, 2013).

Contents

Acknowledgements

Firstly, I would like to thank my supervisors Professor Penny Gowland and Dr. Olivier Mougin for their endless support, patience and encouragement throughout my PhD. I couldn't have hoped for a better source of inspiration and guidance during my journey at Nottingham, and I feel immensly lucky to have worked with you both.

There are so many people who have made the SPMIC feel like home over the past few years. There are far too many names to list here, but please know you are all valued immensely and your friendship will never be forgotten. A few special mentions have to go to Daisie and Ben, for always being dependable companions throughout the PhD journey; Emma, the coffee and gossip sessions were always just what I needed; and George, both your pub quiz knowledge and unlicensed post pub quiz therapy was and always will be hugely appreciated.

A special thank you to Jodi for keeping me sane (within reason) during the writing of this thesis, and for generally being the most interesting person on the planet. I couldn't have wished for a better person to spend a global pandemic with.

Finally, a huge thank you to my parents John and Wanda, who have provided me with nothing short of relentless love and support ever since I popped into the world, for which I am immeasurably grateful for. This thesis would not exist without you or Michael being there every step of the way.

Introduction

Since its introduction in the early 1970s, magnetic resonance imaging (MRI) has been responsible for saving millions of lives around the world. In terms of clinical imaging techniques it is relatively new: roughly eighty years younger than planar X-ray imaging, twenty-five years younger than clinical ultrasound, and six years younger than x-ray computed tomography (CT). Its only major drawbacks compared to these other modalities are its higher running costs and longer acquisition times, but in exchange it offers significant clinical advantages. MRI is performed without the use of ionising radiation, which is a limiting factor for CT, and is capable of producing images of sub-millimetre resolution. Standard MRI acquires signal from the water protons in the human body, and by probing the local properties of these protons is capable of producing images with high contrast based on a range of endogenous mechanisms.

In addition to directly measuring the concentration or NMR relaxation times of water protons, a range of methods of generating other contrasts have been created. Arterial spin labelling (ASL), for example, selectively saturates the water protons in arterial blood before entering an organ in order to measure perfusion. Magnetic resonance elastography (MRE) is a method of measuring the stiffness of tissue by imaging the vibrations from an external plate, used mainly to assess kidney fibrosis. And as a final example, functional magnetic resonance imaging (fMRI) measures the local decrease in the volume fraction of paramagnetic deoxygenated blood volume in the brain which arises when a particular region is activated.

This thesis, however, is concerned with contrast generated from z-spectroscopy. Sim-

ilar in certain aspects to ^1H magnetic resonance spectroscopy (MRS), z-spectroscopy is sensitive to the presence of molecular species containing hydrogen atoms. However unlike ^1H MRS, z-spectroscopy is based on the water signal which is modulated by exchange with other molecules rather than on the protons in those molecules themselves. The process of exchange effectively amplifies the signal from the molecules of interest and allows them to be detected with a signal to noise ratio of the order of the water signal. This means that the z-spectrum can be encoded in a standard MRI scan, allowing the acquisition of data at high spatial resolution.

This exchange can occur through several mechanisms, which can produce a variety of z-spectrum signals. These are magnetisation transfer (MT), which describes exchange of magnetisation between macromolecular species and water protons, chemical exchange saturation transfer (CEST), which describes direct exchange between labile proton groups (-NH, -OH and -SH), and finally magnetisation can be exchanged through the nuclear Overhauser enhancement (NOE) effect. While the quantity of certain molecules present has obvious clinical relevance, the rate at which protons exchange their magnetisation is also of great interest, as this is sensitive to local pH and temperature. Accurate quantification of exchange rates therefore has huge clinical potential, as it is currently extremely challenging to non-invasively measure pH *in vivo*. However, measurement of exchange rates is not trivial, and a large portion of this thesis is dedicated to outline a new, robust method of accurately quantifying exchange rates.

The first chapter of this thesis provides a theoretical overview of nuclear magnetic resonance and its exploitation as an imaging technique. Methods of signal acquisition are introduced and the basic methods of contrast generation are discussed. Common imaging sequences are described, some of which will be utilised in the remainder of this thesis.

The second chapter presents the theory behind the processes involved around z-spectroscopy. The Bloch-McConnell equations are introduced, which describe the evolution of magnetisation when exchanging pools are present. These equations are

core to the work performed in this thesis. The methods of acquiring the z-spectrum are described, and finally an analysis of current methods of analysing z-spectrum effects is performed, starting with more simplistic metrics and moving towards more complex and powerful methods.

Chapter 3 describes work which used the quantitative MT pool size as a marker for myelination in the human brain. A number of subjects were analysed with ages between 19 and 62 years, and the global variation of the MT signal with age was analysed, along with local variation in each of the four lobes, largely showing a quadratic variation in myelin over the adult lifespan, with peak myelination levels around age 42. This was compared with the variation in T_1 values and NOE pool size measures with age. Finally the thickness of each subject's cortex was assessed, and while the cortex was found to decline with age as previously reported, it was found that the thickness of the cortex did not correlate with the presence of myelin, suggesting that cortical thinning in later life is not directly due to demyelination.

Chapter 4 introduces the Particle Swarm Optimisation algorithm (PSO) as a new method of quantifying z-spectrum effects. Built around the Bloch-McConnell equations, this algorithm mimics the behaviour of swarms found in nature. Initial guesses at the solutions are made, and these guesses act as individual members of the swarm, communicating with each other to move towards the optimal global solution, i.e. the underlying physical parameters which best model the acquired z-spectrum data. This was tested in simulations and a phantom, before going on to quantify z-spectra acquired from *in vivo* human cerebral grey and white matter.

Chapter 5 describes the use of the PSO algorithm to analyse the signals from *ex vivo* human blood samples. A statistical analysis was performed in order to identify possible sources of signal giving rise to the shape of the human blood z-spectrum. This was followed by an investigation into whether measuring blood-glucose levels is possible using this method within a physiologically applicable range, and finally an experiment was performed in which the pH levels of *ex vivo* human blood samples was measured through the quantification of the exchange rates of Iopamidol, an exogenous CEST

agent, which is already known to be suitable for clinical use in CT imaging.

Chapter 6 describes the application of z-spectroscopy in abdominal imaging. Difficulties in measuring abdominal MT are explored, and a 'prompted-breathing' method of z-spectrum acquisition is presented, which was found to yield robust, reliable z-spectra. This was performed *in vivo* in human liver, kidney, and back muscle, at a clinical (3T) field strength. The advantages and issues of moving abdominal z-spectroscopy to ultra-high field (7T) were then explored, before an experiment to measure the evolution of the CEST signal arising from liver glycogen was described. This experiment was performed but suffered from systematic errors. Therefore an optimised protocol for this experiment is also presented which should yield robust quantifiable results.

Chapter 1

MR Theory

This chapter will describe the fundamentals of Nuclear Magnetic Resonance (NMR) and how these principles are utilised to form an image in Magnetic Resonance Imaging (MRI).

1.1 Nuclear Magnetic Resonance

First introduced by Rabi in 1937 [1], and demonstrated by Bloch [2] and Purcell [3] in 1946, nuclear magnetic resonance describes the phenomenon which occurs when a nuclear spin interacts with an externally applied magnetic field. With a simple system involving a single spin, it is appropriate to describe this phenomenon with quantum mechanics, however realistically in magnetic resonance imaging (MRI) the number of spins in a system is very large, and so it becomes viable to implement a simplified classical description of the system.

1.1.1 Quantum theory of NMR

Intrinsic angular momentum, commonly referred to as spin, is a fundamental property of protons, neutrons, and electrons. The magnitude of this angular momentum, **J**, can be defined by

$$|\mathbf{J}| = \hbar\sqrt{\mathbf{I}(\mathbf{I}+1)} \tag{1.1.1}$$

where I is the spin quantum number and can take integer and half integer values only, and $\hbar = \frac{h}{2\pi}$, the reduced Planck's constant. There are 2I+1 possible spin states for a nucleus with spin I, defined by the quantum number m_i, where $m_i = I, (I-1), (I-2), ..., +\frac{1}{2}, -\frac{1}{2}, ..., I$ for half integer spins.

Nuclei with an odd number of protons and/or neutrons have a non-zero net spin; in the case of a hydrogen atom the nucleus consists of a single proton with spin quantum number $\mathbf{I} = +\frac{1}{2}$. The rotating nucleus gives rise to an effective current loop, as it is positively charged, and in turn generates a magnetic moment dependent on the intrinsic angular momentum of the nucleus, defined by

$$\boldsymbol{\mu} = \gamma\mathbf{J} \tag{1.1.2}$$

where γ is the gyromagnetic ratio of said nucleus. This gyromagnetic ratio takes different values dependent on the mass and the charge of the nucleus in question. The most commonly probed nucleus in MRI experiments is the hydrogen nucleus ^1H, as it has the highest gyromagnetic ratio and abundance in living tissue. Table 1.1 presents the gyromagnetic ratios of various nuclei commonly probed by *in vivo* NMR experiments.

Nucleus	Spin	Gyromagnetic ratio (MHz/T)
^{1}H	1/2	42.57
^{13}C	1/2	10.71
^{19}F	1/2	40.05
^{23}Na	3/2	11.26
^{31}P	1/2	17.24

Table 1.1.1: Gyromagnetic ratios, γ, of various NMR sensitive nuclei.

1.1.2 Application of external B_0 field

^1H nuclei have spin $\frac{1}{2}$, and therefore have two possible spin states: $m_i = +\frac{1}{2}$ and $m_i = -\frac{1}{2}$. In the absence of an external magnetic field, the spins in a given sample will point in random directions, and will also transfer energy randomly with each other, producing a net magnetisation of zero. However, in the presence of an external magnetic field (B_0), the spins will align either parallel or anti-parallel to the field, as displayed in Figure 1.1.1.

In MRI experiments the external magnetic field is conventionally aligned along the z-axis, $\mathbf{B_0} = B_0\hat{\mathbf{z}}$. We can therefore describe the z-component of the magnetic moment of a ^1H nucleus as

$$\mu_z = \gamma\hbar m_z = \pm\frac{1}{2}\gamma\hbar. \tag{1.1.3}$$

There are two possible energy states for the ^1H nucleus in an external magnetic field, described by $E = -\boldsymbol{\mu}\mathbf{B} = \pm\frac{1}{2}\gamma\hbar B_0$. The energy difference between lower energy and the higher energy state is therefore

$$\Delta E = \gamma\hbar B_0. \tag{1.1.4}$$

The energy levels in a spin $\frac{1}{2}$ system are displayed in Figure 1.1.2.

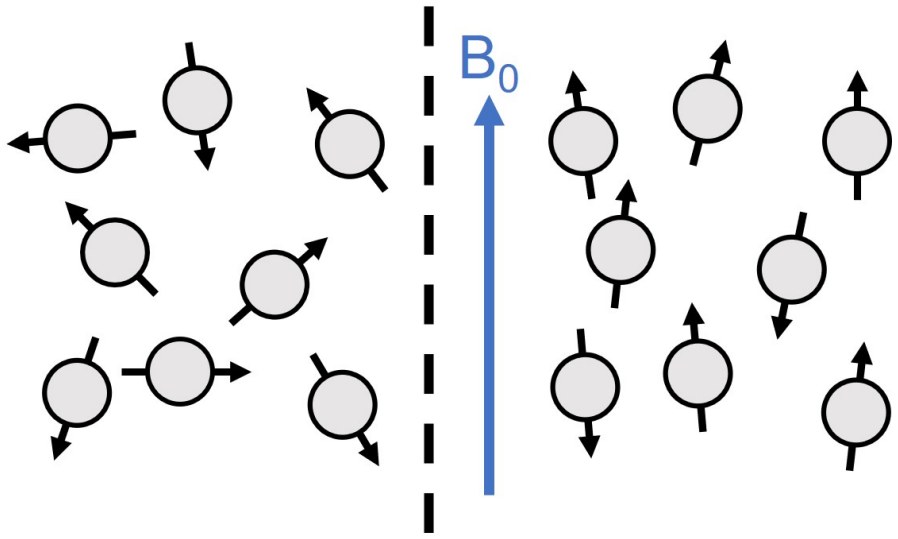

Figure 1.1.1: The effects of an external field, B_0, on the alignment of nuclear spins (exaggerated for this diagram).

Spins in an ensemble naturally prefer to occupy the lower energy state aligned parallel to the B_0 field, however the difference in spin populations in a typical system is relatively small. When a spin system is at equilibrium, the ratio of the number of parallel spins ($N\uparrow$) to the number of antiparallel spins ($N\downarrow$) can be described by the Boltzmann distribution:

$$\frac{N\uparrow}{N\downarrow} = e^{\frac{\Delta E}{k_B T}} \tag{1.1.5}$$

where k_B is the Boltzmann constant, 1.38×10^{-23} m^2 kg s^{-2} K^{-1}, and T is the temperature of the system in Kelvin. From here we can derive the population difference between the ($N\uparrow$) and ($N\downarrow$) state. We know that the energy difference is small, $\Delta E \ll k_B T$, and so can perform a Taylor expansion to yield

$$\frac{N\uparrow}{N\downarrow} = 1 + \frac{\Delta E}{k_B T}. \tag{1.1.6}$$

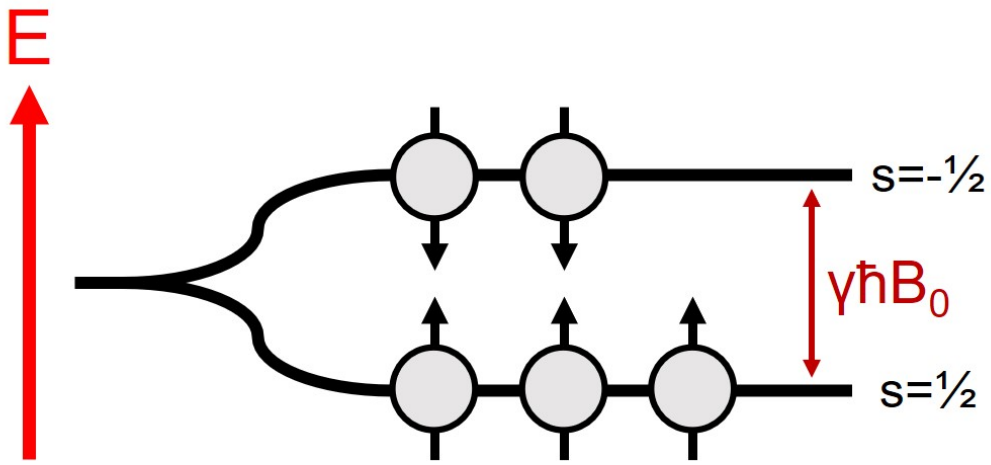

Figure 1.1.2: Possible energy states for a spin $\frac{1}{2}$ system.

This can be rearranged to give the population difference between states:

$$N\uparrow - N\downarrow = N\frac{\gamma\hbar B_0}{2k_BT} \tag{1.1.7}$$

where N is the total number of spins in the system.

The bulk (or net) magnetisation of the sample is determined by the sum of each of the spins in the system. As the x- and y- components of each spin are random, these cancel leaving only the z- components of the magnetisation. We can therefore define the bulk magnetisation of a sample, M_0, as

$$\mathbf{M_0} = \frac{\gamma^2\hbar^2 B_0 N}{4k_BT}\hat{\mathbf{z}}. \tag{1.1.8}$$

1.1.3 Application of B_1 field

In reality, spins in a linear magnetic field do not align exactly with the z- direction, but instead precess about the z- axis with an angular frequency ω_0. This frequency is

known as the Larmor frequency [4], and is defined as

$$\omega_0 = \gamma B_0. \tag{1.1.9}$$

In NMR physics, it is often more appropriate to use the classical model to describe the macroscopic observations of a spin system; while this cannot provide a complete description of the system it is capable of providing a clearer description of the phenomena observed.

In the classical model, when we place a magnetic moment $\mathbf{M}$ into an external magnetic field $\mathbf{B}$, the magnetic moment experiences a torque $\mathbf{L}$ proportional to the change in angular momentum, described by

$$\mathbf{L} = \mathbf{M} \times \mathbf{B} = \frac{d\mathbf{J}}{dt} \tag{1.1.10}$$

From here we can substitute in equation 1.1.2 to give the Bloch equation [2] in its standard form:

$$\frac{d\mathbf{M}}{dt} = \gamma \mathbf{M} \times \mathbf{B} \tag{1.1.11}$$

which can be extended to describe the x-, y- and z- components of the evolution of magnetisation:

$$\frac{d\mathbf{M}}{dt} = \gamma(\mathbf{M} \times \mathbf{B}) - \frac{M_z - M_0}{T_1}\hat{\mathbf{z}} - \frac{M_x\hat{\mathbf{x}} + M_y\hat{\mathbf{y}}}{T_2} \tag{1.1.12}$$

This describes the time evolution on the bulk magnetisation and introduces the variables T_1 and T_2, which govern the longitudinal recovery and transverse decay times of the magnetisation of the system respectively. This can be solved in the x-, y- and

z- directions to give

$$M_x(t) = M_x(0)\cos(\gamma B_z t) + M_y(0)\sin(\gamma B_z t) \tag{1.1.13}$$

$$M_y(t) = -M_x(0)\sin(\gamma B_z t) + M_y(0)\cos(\gamma B_z t) \tag{1.1.14}$$

$$M_z(t) = 0 \tag{1.1.15}$$

The basis for magnetic resonance imaging comes from applying a second magnetic field in the xy- plane, conventionally known as the B_1 field, in order to perturb the spins aligned with the B_0 field. The B_1 field is produced by a radio frequency pulse, and is usually on the order of micro-Tesla, compared to Tesla for the B_0 field. The B_1 field is time dependent, and so can generally be described by

$$\mathbf{B_1}(t) = 2B_1\cos(\omega t)\hat{\mathbf{x}} \tag{1.1.16}$$

This can be resolved into two components rotating about the x- axis, anti-clockwise and clockwise respectively.

$$\mathbf{B_a}(t) = B_1(t)[\cos(\omega t)\hat{\mathbf{x}} + \sin(\omega t)\hat{\mathbf{y}}] \tag{1.1.17}$$

$$\mathbf{B_c}(t) = B_1(t)[\cos(\omega t)\hat{\mathbf{x}} - \sin(\omega t)\hat{\mathbf{y}}] \tag{1.1.18}$$

The B_1 field is chosen to be on-resonance with the precession of the ^1H spins at the given B_0 field strength ($\omega = \omega_0$), as described by equation 1.1.9. The contribution from $\mathbf{B_a}(t)$ under this condition is negligible, as it rotates at $-2\omega_0$, far off-resonance. $\mathbf{B_c}(t)$, however, rotates at ω_0, on-resonance. This creates an additional torque on the magnetic moment, such that its motion can be described by

$$\frac{d\boldsymbol{\mu}}{dt} = \gamma\boldsymbol{\mu} \times [\mathbf{B} + \mathbf{B_c}(t)] \tag{1.1.19}$$

As a result of this torque, application of the B_1 field causes the net magnetisation of the sample to spiral clockwise towards the xy- plane. However in NMR experiments it is simpler to visualise things in a frame of reference rotating at the Larmor frequency, known as the rotating frame [5], in which the B_1 field appears stationary, as shown in Figure 1.1.3.

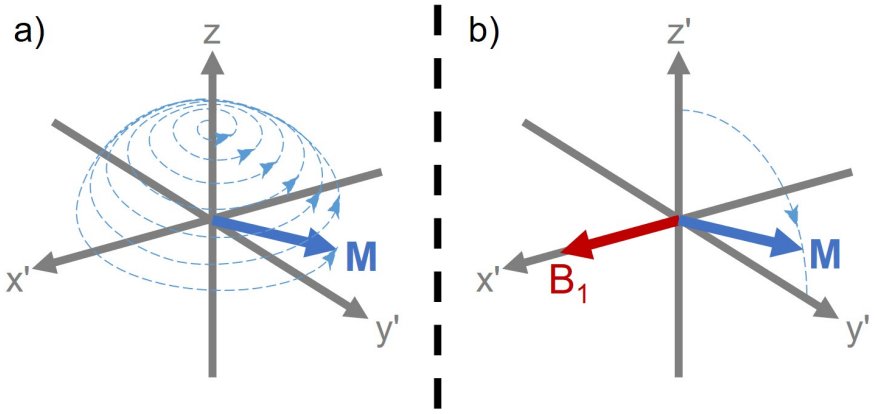

Figure 1.1.3: The evolution of the net magnetisation, **M**, after the application of the B_1 field, shown in a) the laboratory frame, and b) the rotating frame of reference.

We can take the x-, y- and z- components of the B_1 field from equation 1.1.18, and transform into the rotating frame using a rotation matrix.

$$\begin{bmatrix} B_{1,x'}(t) \\ B_{1,y'}(t) \\ B_{1,z'}(t) \end{bmatrix} = \begin{bmatrix} \cos(\omega_0 t) & \sin(\omega_0 t) & 0 \\ -\sin(\omega_0 t) & \cos(\omega_0 t) & 0 \\ 0 & 0 & 1 \end{bmatrix} \begin{bmatrix} B_{1,x}(t)\cos(\omega t) \\ B_{1,y}(t)\sin(\omega t) \\ 0 \end{bmatrix} \tag{1.1.20}$$

which reduces to

$$\begin{bmatrix} B_{1,x'}(t) \\ B_{1,y'}(t) \\ B_{1,z'}(t) \end{bmatrix} = \begin{bmatrix} B_1(t)\cos^2(\omega_0 t) + B_1(t)\sin^2(\omega_0 t) \\ B_1(t)\sin(\omega_0 t)\cos(\omega_0 t) - B_1(t)\cos(\omega_0 t)\sin(\omega_0 t) \\ 0 \end{bmatrix} \tag{1.1.21}$$

and so

$$\begin{bmatrix} B_{1,x'}(t) \\ B_{1,y'}(t) \\ B_{1,z'}(t) \end{bmatrix} = \begin{bmatrix} B_1(t) \\ 0 \\ 0 \end{bmatrix} \tag{1.1.22}$$

In the rotating frame, the net magnetisation is tipped towards the xy- plane. The angle by which the magnetisation is tipped around the x'- axis, α, is dependent on both the magnitude and duration of the applied B_1 field, and is described by

$$\alpha = \int_0^\tau \gamma B_1(t) dt \tag{1.1.23}$$

where τ is the pulse duration. Common choices of flip angle include a 90° saturation pulse to tip the magnetisation into the xy- plane, and allow the spins to dephase, resulting in a net magnetisation of zero, or a 180° inversion pulse, which is used in T_1 weighted imaging and will be detailed later.

1.2 Relaxation

When a radiofrequency $B_1(t)$ pulse is applied to a sample, it is taken out of thermal equilibrium, and the conditions $M_z = M_0$, and $M_x = M_y = 0$ no longer hold true. The spins are tipped toward the xy- plane, but after the RF pulse is switched off the spins will relax back towards thermal equilibrium. This occurs via two processes: longitudinal (T_1) relaxation and transverse (T_2 and T_2^*) relaxation, which are two key sources of image contrast in MRI.

1.2.1 Longitudinal relaxation, T_1

Once a spin system has been excited, the net longitudinal magnetisation will return to the equilibrium Boltzmann distribution through exchange of energy from the spin system to the surrounding thermal reservoir (historically defined as the lattice). This process is not instantaneous, and is defined by a time constant T_1, the longitudinal relaxation time. Longitudinal recovery of the magnetisation can be defined by

$$\frac{dM_z(t)}{dt} = \frac{M_0 - M_z(t)}{T_1}. \tag{1.2.1}$$

The T_1 relaxation time varies depending on the efficiency of energy transfer between the spin system and the lattice, which occurs via collisions and rotations of molecules through dipole-dipole interactions. The mechanisms through which energy exchange occurs means that the T_1 is shorter in samples in which molecules are tightly packed or bound than in samples in which molecules are freer. For example, pure water has a relatively long relaxation time, as water molecules are not strongly bound to each other and have a high motional frequency. In the cortex, grey matter has a much shorter T_1 than water, and white matter has a shorter T_1 still, due to the presence of myelin in white matter which restricts the motion of water molecules (although this

is also influenced by iron).

T_1 is typically measured with an inversion recovery experiment [6]. Here, a 180° RF pulse is applied to the sample, which inverts the net magnetisation, so that $M_z(0) = -M_0$. Following an inversion pulse, we can solve equation 1.2.1 by integrating from time $t = 0$ to $t = TI$ to give

$$M_z(t) = M_0(1 - 2e^{\frac{-TI}{T_1}}) \tag{1.2.2}$$

By using variable time intervals, TI, we can plot the recovery of the magnetisation, as shown in Figure 1.2.1, and fit an exponential to determine the T_1 of the sample.

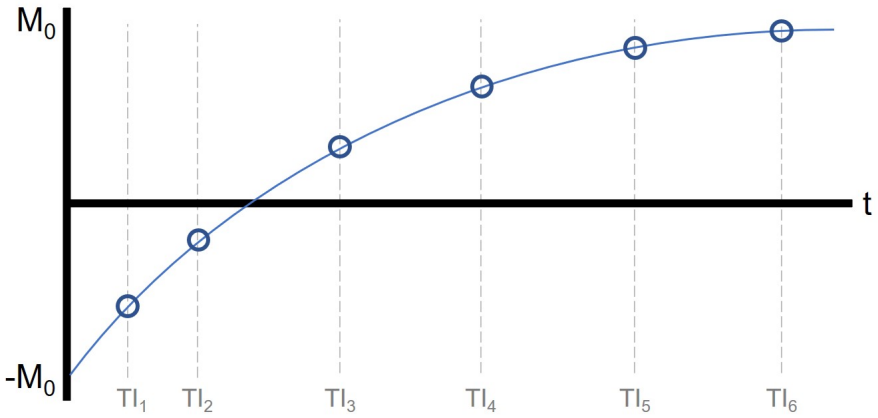

Figure 1.2.1: Recovery of magnetisation after an inversion pulse with a fitted exponential to measure T_1.

However, this experiment can be time consuming, as the time between the 180° pulse and the readout (TR, repetition time), will approach 5 times T_1 at its longest values, to allow for complete recovery of M_0 each time. A method of speeding up T_1 measurement is by using the Look-Locker readout scheme [7], which allows a single inversion recovery pulse to be used, followed by multiple low flip angle readouts, as shown in Figure 1.2.2.

The Look-Locker readouts are equally spaced by time TI_2, which partially saturate

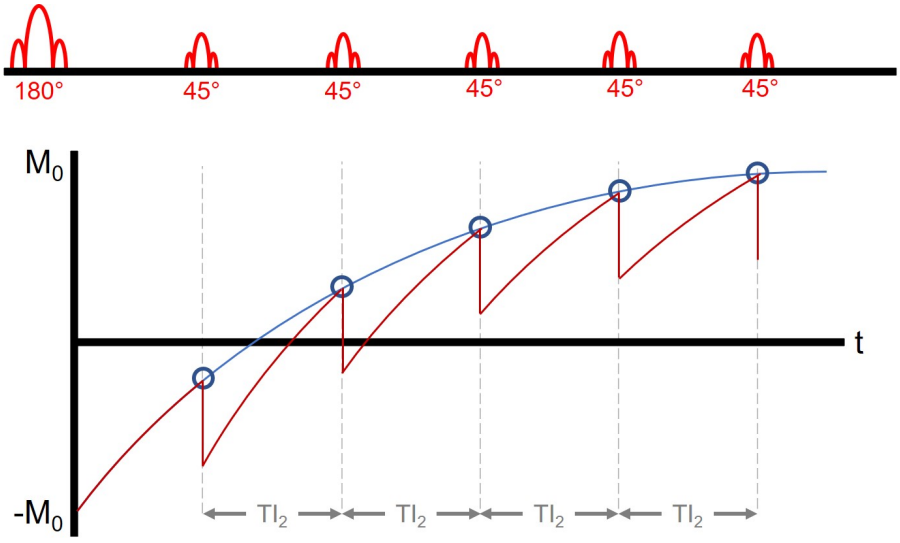

Figure 1.2.2: Look-Locker readout scheme and recovery curve with a flip angle of 45°.

the magnetisation. As a result of this, an apparent T_1 is measured, denoted here by $T_{1,LL}$. The true T_1 can be calculated from this value using the equation

$$\frac{1}{T_1} = \frac{1}{T_{1,LL}} + \frac{\ln(\cos(\alpha))}{TI_2} \tag{1.2.3}$$

where α is the flip angle of the readout pulses.

1.2.2 Transverse relaxation, T_2

As well as longitudinal magnetisation recovering over time, phase coherence of an excited spin system decreases at a rate dependent on the transverse relaxation time, T_2. If we consider immediately after a 90° RF pulse is applied to a system, $M_z = 0$ as all spins are tipped into the M_{xy} plane and precessing around the z- axis. Random dipole-dipole interactions between neighbouring spins in a system create microscopic magnetic fields, which disturb the precessional frequency of local spins. As a result of

this, certain spins precess about the z- axis slightly faster or slower than the Larmor frequency. Over time this leads to complete phase decoherence, as all of the excited spins are oriented randomly in the xy- plane. Transverse relaxation of a system can be defined by

$$\frac{dM_{xy}(t)}{dt} = \frac{M_{xy}(t)}{T_2}. \tag{1.2.4}$$

In order to measure T_2, the effects of T_2' need to be considered, which will be discussed in the following section. T_2 is typically measured using a spin-echo sequence, detailed in section 1.3.2.

1.2.3 Observed transverse relaxation, T_2^*

In practice, phase coherence of a system is lost faster than described by equation 1.2.4, due to external B_0 inhomogeneities arising from either hardware issues or magnetic susceptibility differences in the sample. This leads to frequency shifts in the rotation of nearby spins, and therefore further coherence loss. This additional effect is termed T_2', and so the apparent transverse relaxation time needs to consider the true T_2 of the system along with these additional effects. This apparent transverse relaxation time is termed T_2^*, and is described by

$$\frac{1}{T_2^*} = \frac{1}{T_2} + \frac{1}{T_2'}. \tag{1.2.5}$$

T_2' effects are more significant at higher B_0 field strengths, as susceptibility induced field inhomogeneities scale linearly with B_0, leading to shorter T_2^*, which presents as signal loss or image distortions.

Equations 1.2.1 and 1.2.4 can be combined to give the Bloch equation [2]

$$\frac{d\mathbf{M}}{dt} = -\frac{\mathbf{M_x}}{T_2}\hat{\mathbf{x}} - \frac{\mathbf{M_y}}{T_2}\hat{\mathbf{y}} + \frac{\mathbf{M_0} - \mathbf{M_z}}{T_1}\hat{\mathbf{z}} + \gamma\mathbf{M} \times (\mathbf{B_1} + \Delta\mathbf{B_0}) \tag{1.2.6}$$

where $\Delta\mathbf{B_0}$ is the difference between the given field strength of the magnet (B_0), and the local magnetic field experienced by the spin system. The Bloch equations underpin the evolution of magnetisation for a given imaging sequence, and can be modified to describe various systems, a particular variant of which (termed the Bloch-McConnell equations) will be explored later in this thesis.

1.3 Signal acquisition

Samples in an NMR experiment are excited in order to create a recordable, measurable signal. This signal is dependent on the NMR properties of the sample, and as well as being measurable can be manipulated through by RF pulses and changes in the applied magnetic fields to encode its NMR properties.

1.3.1 Free induction decay

The simplest NMR experiment is the creation and acquisition of a Free Induction Decay (FID) signal [8, 9]. A sample in a uniform B_0 field is allowed to reach thermal equilibrium before being excited by an external B_1 field and tipped into the xy- plane as described in section 1.1. We can then use a receive coil to detect a voltage produced by Faraday induction. The resulting signal is an exponential decay which oscillates at the resonant frequency. The rate of this decay is dependent on the rate constant T_2^*. It is often difficult to measure the earliest part of the FID, due to having to gate the receive coil off while the B_1 field is transmitted. To overcome this, echoes of the signal are created via either spin-echo or gradient-echo sequences. Echoes are used in MRI to refocus static field inhomogeneities, and to provide a symmetric signal which

has a solely real Fourier transform.

1.3.2 Spin and gradient echoes

The spin-echo sequence [10] was briefly mentioned in section 1.2.2 as the primary experiment used to measure T_2. In this experiment, a 90° RF pulse is applied to the system, tipping the magnetisation into the xy- plane. The spins begin to lose phase coherence as described previously. After a time τ, a 180° RF pulse is applied, inverting the spins and therefore reversing the direction of the phase shifts. Therefore after time 2τ, the phase shifts of the spins are all zero, meaning that the signal is fully refocused, forming an echo (Figure 1.3.1). Dephasing due to any T_2 effects is not reversed by the inversion pulse, meaning that the echo is dependent only on T_2'.

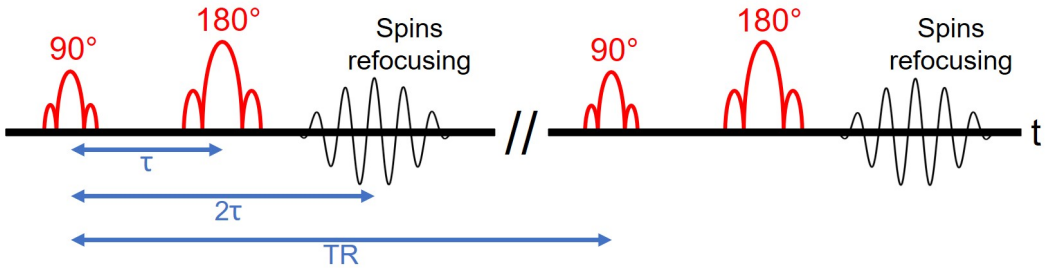

Figure 1.3.1: Spin-echo pulse sequence.

As the name suggests, a gradient echo is formed by applying a linear magnetic field gradient across a sample [11]. A gradient echo is not reliant on RF pulses of any particular angle, instead forming an echo based on the positions of spins in the magnetic field gradient. An RF pulse of angle α is applied, followed by a negative field gradient. This causes the spins to precess and therefore dephase dependent on both their position, and on the length of time (τ) the field gradient is applied for. We can then apply a positive field gradient of the same magnitude for the same amount of time, which reverses the direction of phase accumulation. This means that spins which were acquiring phase more quickly are now acquiring phase more slowly, and

vice versa, and so after τ the spins rephase and create an echo, as illustrated in Figure 1.3.2. A gradient echo cannot refocus local field inhomogeneities, and so is dependent on T_2^* rather than solely on T_2.

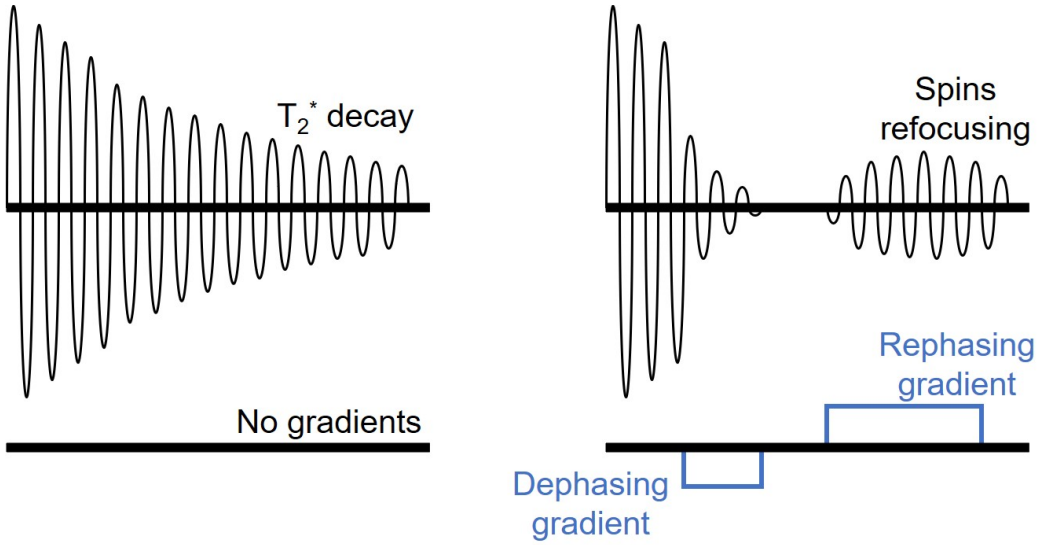

Figure 1.3.2: Gradient-echo sequence.

1.3.3 Chemical shift

T_2 and T_2^* processes are not the only mechanisms which affect the precessional frequency of the spins. Spins in a sample can also be affected by their surrounding chemical environment [12]. Electronic shielding due to other molecules can lead to spins experiencing varying degrees of the B_0 field, due to induced fields generated by the free electrons of nearby molecules. We define chemical shift as the term δ, measured in parts per million (ppm), where

$$\delta = \frac{\omega - \omega_{ref}}{\omega_{ref}} \times 10^6 \tag{1.3.1}$$

Here, ω_{ref} is the reference frequency, which in magnetic resonance spectroscopy

(MRS) experiments is the Larmor frequency of protons present in tetramethylsilane (4.7ppm upfield from water protons), and in CEST experiments ω_{ref} is the Larmor frequency of protons present in water. Using MRS experiments, we can gain chemical information about the sample by acquiring a FID and analysing its frequency spectrum post Fourier transform. In conventional MRI, chemical shifts such as between water and fat can cause artefacts, but they can also be utilised in NMR spectroscopy, magnetisation transfer (MT) and chemical exchange saturation transfer (CEST) experiments, which will be detailed heavily in chapter 2.

1.4 Principles of imaging

In order to form an image, it is necessary to be able to spatially localise any signals which we acquire. This is done through the application of linear field gradients to vary the resonant frequencies of the spins based on their position. Through this method we can describe the Larmor frequency of any given spin as a function of the applied gradients at a given time:

$$\omega(x, y, z) = \gamma(B_0 + xG_x(t) + yG_y(t) + zG_z(t)) \tag{1.4.1}$$

Gradients are applied orthogonally to create linear frequency variation along their respective axes. The following chapter will outline methods for localising the NMR signal, before providing examples of how this is performed in practice.

1.4.1 Slice selection

A common method of acquiring three dimensional information in MRI is by acquiring a series of two dimensional images along a third dimension. These individual images are known as slices. In order to acquire a slice, we must perform slice selection, also

known as selective excitation. Here, a slab of spins is excited through the use of an applied RF pulse and an applied field gradient. An RF pulse of a particular bandwidth will excite all spins within that frequency range, regardless of their position. Through application of a magnetic field gradient, for example along the z- axis, the Larmor frequency of spins becomes dependent on their position along that axis. As shown in Figure 1.4.1, application of an RF pulse with a given bandwidth will excite a slice in the presence of a field gradient, the thickness of which is dependent on both the bandwidth of the RF pulse and the strength of the magnetic field gradient [13].

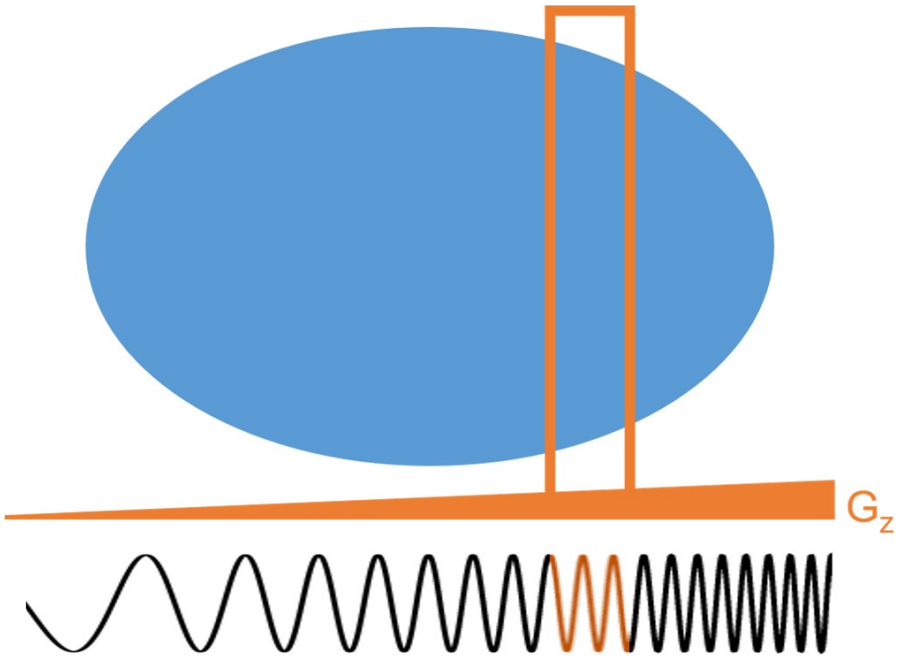

Figure 1.4.1: The magnetic field gradient G_z alters the resonance frequencies of the sample dependent on their position. A slice of the sample can be excited by applying an RF pulse with frequency components matching the range of frequencies in the target slice.

In order to create an RF pulse of a given bandwidth, its Fourier transform must be considered. In an ideal world, the reverse Fourier transform of a 'top hat' function would be used, as this excites a narrow band of frequencies equally, and nothing more. However, the solution to this is a sinc shaped pulse, which is infinitely long. As

we unfortunately do not have infinite time, modified versions of this shape must be considered, such as a truncated sinc pulse or a Gaussian pulse, the profiles and Fourier transforms of which are displayed in Figure 1.4.2.

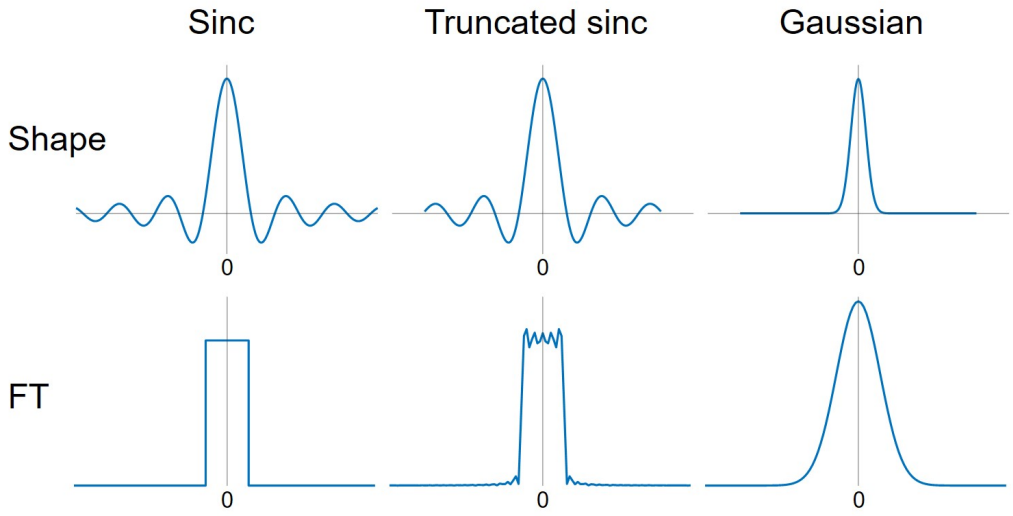

Figure 1.4.2: Shapes and Fourier transforms of a sinc profile, a truncated sinc, and a Gaussian

Because the slice profiles generated by these RF pulses are not completely rectangular, interference between slices can arise where the slice profiles overlap [14]. This can lead to reduced contrast on an image. There are two widely used solutions to this problem, the simplest of which is to leave a gap between slices, usually around 10% of the slice thickness. However, if it is important that no gaps are left, odd and even numbered slices can be acquired using two separate acquisitions.

If more time is available to perform the RF pulse, adiabatic pulses are often used [15]. Here a B_1 field is applied for a certain length of time, but the frequency of the field is swept slowly from below resonance to above resonance. When the B_1 is applied below resonance, the net magnetisation precesses around a vector B_{eff}, at an acute angle to the B_0 field. As the frequency is increased, the net magnetisation will follow B_{eff}. When the RF frequency is matched to the resonance frequency, B_{eff} is aligned with the xy- plane, and as the RF frequency moves above resonance the net magnetisation

continues to follow B_{eff} until it has been completely inverted. This technique can be useful as the flip angle is no longer dependent on the magnitude of the B_1 field as described in equation 1.1.23, and the magnetisation should theoretically become insensitive to B_1 inhomogeneities.

1.4.2 Frequency encoding

Once a slice has been selected, spatial encoding in the x- and y- direction is required in order to produce an image. In order to do this we can first perform frequency encoding, here applied along the x- direction [16]. A field gradient is applied along the x- direction during the readout, and making the precessional frequency of the spins excited through slice selection dependent on their position along the x- axis such that

$$\omega(x,t) = \gamma(B_0 + xG_x(t)) \tag{1.4.2}$$

which is a simplified version of equation 1.4.1. We can use this to gain information about the distribution of proton density of the sample. For a location **r**, the measured signal $S(\mathbf{r},t)$ at time t is proportional to the proton density ρ, such that

$$S(\mathbf{r},t) \propto \rho(\mathbf{r}) e^{i\int_0^t \omega(\mathbf{r},t')t'}. \tag{1.4.3}$$

For an entire volume of space, we can express this as

$$S(t) \propto \int_x \int_y \int_z \rho(\mathbf{r}) e^{i\int_0^t \omega(\mathbf{r},t')dt'} dxdydz \tag{1.4.4}$$

We can then demodulate this signal to remove the ω_0 component, by applying a low-pass filter, eliminating the higher frequencies in the MHz range arising from the B_0 field, and leaving only the gradient induced frequencies in the kHz range. The signal

is then defined as

$$S(t) \propto \int_x \int_y \int_z \rho(\mathbf{r}) e^{i \int_0^t \mathbf{r}.G_r(t')dt'} dxdydz \tag{1.4.5}$$

We can here introduce the reciprocal gradient space vector, known as k-space. This is the space represented by phase evolution, and will be detailed further in section 1.4.4. We define this vector as

$$\mathbf{k}(t) = \gamma \int_0^t \mathbf{G}(t')dt \tag{1.4.6}$$

and combining equation 1.4.5 with 1.4.6, we can describe the signal in the form of a 3D Fourier Transform:

$$S(t) \propto \int_x \int_y \int_z \rho(\mathbf{r}) e^{i\mathbf{r}.\mathbf{k}(t)} dxdydz. \tag{1.4.7}$$

We can therefore obtain information about the proton density of an image by performing an inverse Fourier Transform of the received signal.

1.4.3 Phase encoding

It is impossible to fully localise spins solely using frequency encoding. In order to form an image, another method of spin localisation must be applied orthogonally to the frequency encoding field gradient [16]. Phase encoding field gradients create phase variation along the applied direction, which here is chosen as the y- direction. Phase encoding gradients work in the same way as frequency encoding gradients in that they alter the precessional frequency of spins along the applied direction, such that

$$\omega(y,t) = \gamma(B_0 + yG_y(t)) \tag{1.4.8}$$

Unlike frequency encoding gradients however, this field gradient is switched off before the readout. After applying a phase encoding gradient between time $t = 0$ to $t = T$, spins will have accumulated phase due to their temporarily altered precessional frequencies, described as

$$\phi_y(y) = \gamma y \int_0^T G_y(t)dt \tag{1.4.9}$$

The signal acquired from spins can then be described by

$$S(t) \propto \int_x \int_y \int_z \rho(\mathbf{r}) e^{-i\phi_y - i\gamma x G_x t} dxdydz \tag{1.4.10}$$

Frequency and phase encoding gradients are not always chosen along the x- and y-directions. Poor choice of the phase encoding direction can lead to major image artefacts. Aliasing of the image can occur when part of the object protrudes out of the field of view in the phase encoding direction [17]. This can lead to the image appearing as if parts of the object outside of the defined field of view have been folded over into the main part of the image. For this reason the phase encoding direction is typically chosen along the shortest object dimension, which also speeds up the acquisition. Motion artefacts are also propagated along the phase encoding direction, and so the choice can sometimes be altered so that these effects do not spill over into the region of interest. For example, when acquiring an axial image of the head, phase encoding is usually performed from left to right to avoid spillover from motion artefacts from the eyes into the brain.

1.4.4 k-space

As described in equation 1.4.10, we acquire image data in time encoded in a way which corresponds directly to the form of a 3D Fourier transform of the object. By varying the strength, duration, and/or direction of frequency and phase encoding gradients, we are sampling different parts of the spatial frequency domain, known as k-space [18]. Higher spatial frequencies appear at the edges [19], and so in order to acquire an image of sufficient detail, a k-space grid is chosen with suitable coverage of k-space, both in the centre where information about coarse structures is, and moving away from the centre where information about the finer details of the image are held. An example of k-space data along with the illustration of a k-space grid is shown in Figure 1.4.3.

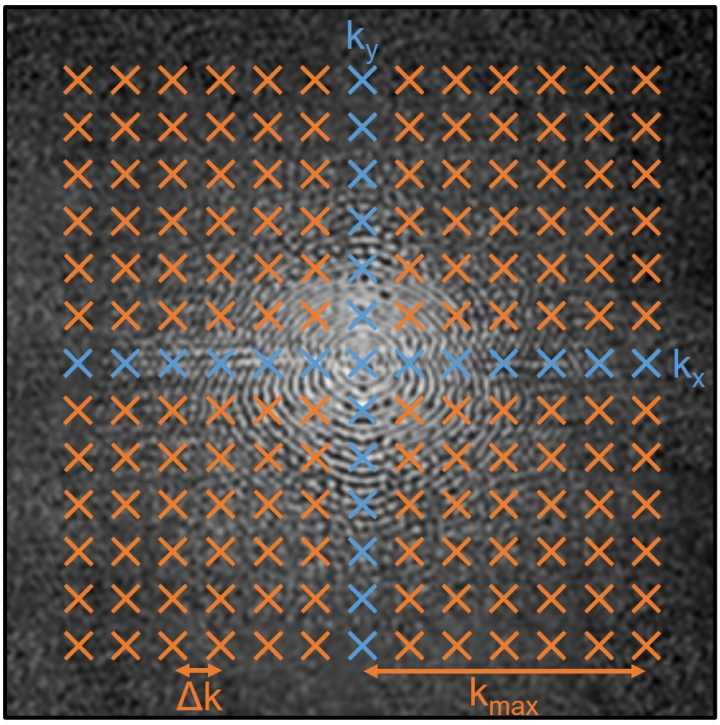

Figure 1.4.3: Illustration of a k-space grid superimposed on typical data in k space. The field of view is dependent on Δk and the pixel size in the image is dependent on k_{max}.

It is important to note that each point in the k-space grid does not correspond directly to a single pixel on the image. Instead, each point in the k-space grid contains information about every pixel in the image, with points on the k_x and k_y axes containing information about the spatial frequencies along the pure x- and y- directions of the image.

We begin the image acquisition process at the sampling position, $k_x = k_y = 0$, immediately after slice selection. By performing frequency encoding as described in section 1.4.2, the signal acquired is along a line of k-space along the k_x direction. We can move in the k_y direction by performing phase encoding, and the following readout will be along a line in the k_x direction with a different value of k_y.

We can alter both the field of view and the pixel size of an image by changing our sampling of k-space. The total range of k-space frequencies, $k_{x,y,max}$ is inversely proportional to the pixel size in the image, as higher spatial frequencies are located at the outside of k-space, and therefore with a lower sampled range, less information can be acquired about the finer details of the image. Similarly, the spacing between data points in the k-space grid is inversely proportional to the field of view, as fewer points in the frequency domain are sampled, leading to fewer total pixels in the real image.

1.4.5 Real and imaginary signals

Each data point in the k-space grid is a complex number. We obtain the MR signal in complex form by acquiring it from two orthogonal phase sensitive detectors (or two orthogonal receiver coils) in order to determine the magnitude and phase (or real and imaginary) components of the signal. While the signal received by one coil is deemed as the real signal and the signal received by the other is deemed imaginary, both signals are equally real, the only salient difference is that they receive the signal in orthogonal directions to each other. However, by describing the signal this way, it allows us to denote the signal in the form $S = Re + iIm$. From this we can obtain magnitude and

phase data about the image, where $Mag = \sqrt{Re^2 + Im^2}$, and $\phi = \tan^{-1}(Im/Re)$. Ignoring the effects of relaxation, the magnitude image represents the proton density, and is the most commonly used in clinical MRI, whereas the phase image is sometimes used, for instance to observe field inhomogeneities or the effects of flow.

Theoretically the signal received from two orthogonal coils will be identical to each other, save for a 90° phase shift. However, the signal received by both channels will contain noise. Therefore by detecting the signal in quadrature, we can also increase the signal to noise ratio (SNR) by a factor of $\sqrt{2}$.

We can speed up imaging sequences through partial Fourier techniques, which only sample a part of k-space [20]. These take advantage of the fact that k-space possesses conjugate symmetry, where if a data point located at (+kx,+ky) has a value $a + bi$, the corresponding data point located at (-kx,-ky) will be the complex conjugate of the original, $a - bi$. However, while this means that theoretically only half of k-space need ever be acquired, phase variations in acquisition mean that this can often lead to image artefacts. These variations can arise from a range of sources, such as B_0 and B_1 inhomogeneity, susceptibility variations, flow, or subject motion.

1.4.6 Pulse sequences for image acquisition

Spin Warp imaging combines slice selection, frequency encoding,and phase encoding in the simplest manner, in order to create an image [21]. The pulse sequence for this technique is displayed in Figure 1.4.4. Here, a line of k-space is acquired per excitation, and repeated until k-space has been adequately sampled. After excitation, a negative gradient is applied along the frequency encoding direction to dephase the spins, while phase encoding is also performed. After a time T, the gradient in the frequency encoding direction is reversed, and applied for a time $2T$, reversing the phase accumulation performed by the initial negative gradient. The result of this is that spins keep the phase added from the phase encoding gradient, but during the readout the positive frequency encoding gradient causes spins which had rapidly dephased to come

back into phase with slower dephasing spins, which forms an echo. This process is then repeated multiple times, but using a different strength phase encoding gradient to acquire a different line of k-space. Image acquisition using Spin Warp imaging can therefore take a long time, due to the fact that the magnetisation needs to recover after each line of k-space is acquired.

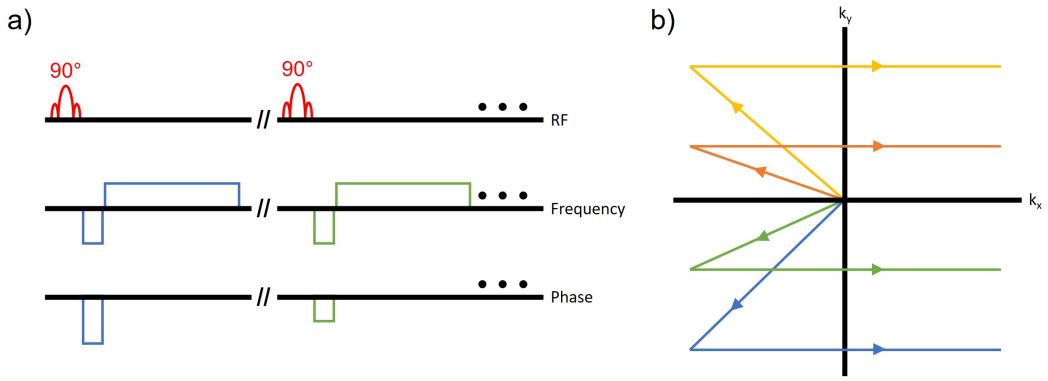

Figure 1.4.4: Spin Warp a) pulse sequence, and b) traversal of k-space. Pulse sequence shown for the first two lines of k-space acquired. The 90° RF pulse is applied at the same time as the slice select gradient (not displayed here). Following excitation, phase encoding is applied along with a negative frequency encoding gradient. The frequency encoding gradient is then applied in a positive direction, sampling one line of k-space. The change in colour represents the start of a new TR.

There are various techniques that can speed up image acquisition. Turbo field echo imaging is one such technique. This is also a gradient echo sequence, similar to Spin Warp imaging, however here the RF pulse used for excitation is much smaller, usually around $10°$. As a result of this a large component of the magnetisation is left in the longitudinal plane, while just tipping enough of the magnetisation into the transverse plane to record a signal. Immediately after excitation a spoiler gradient is applied, which destroys any transverse magnetisation and results in any acquired images being dependent solely on T_1. After a sufficient number of excitation pulses, evenly spaced by a time TR, the longitudinal magnetisation will reach a steady state, dependent on the T_1 of the sample, the TR of the sample and the chosen flip angle of the excitation pulses. The resulting signal from this sequence can be described as

$$S_{TFE} = M_0 \frac{\sin(\alpha)(1 - e^{-\frac{TR}{T_1}})}{1 - \cos(\alpha)e^{-\frac{TR}{T_1}}} e^{-\frac{TE}{T_2^*}} \tag{1.4.11}$$

assuming that all of the transverse magnetisation is destroyed by the gradient spoiler. From this, we can differentiate with respect to α to find the excitation angle which would give the maximum signal. This is called the Ernst angle [22], and is given by

$$\alpha_E = \cos^{-1}(e^{-\frac{TR}{T_1}}). \tag{1.4.12}$$

From equation 1.4.11, we can see that if we modify our imaging parameters, we can instead produce an image that is strongly weighted by T_2^* rather than T_1. This is done by making the TE relatively long, the TR relatively long compared to T_1, and a relatively low flip angle, which reduces the effects of T_1. Between excitations, the transverse magnetisation is destroyed by a spoiler gradient, so that each separate acquisition is independent of the last. However in practice, the sequence will be excessively long if $TR > T_1$. The spoiler gradient used is enough to reduce the T_1 signal, and the steady state is reached early when a low flip angle is used.

Image acquisition can be improved further by using a sequence termed Rapid Acquisition with Refocused Echoes, or RARE. Originally described in 1986 [23], this is a modification of the typical spin-echo sequence described in section 1.3.2. Instead of creating one echo per excitation, the RARE sequence uses a series of refocusing pulses to create multiple echoes per excitation. As shown in Figure 1.4.5, multiple gradients are applied to create multiple echoes, so that during the readout of each echo, a line of k-space is acquired. The number of echoes acquired per excitation is called the echo train length, and is typically around 8 for conventional imaging. This speeds up image acquisition by a factor of 8, meaning that there may be time for a longer TR to allow for greater recovery of the longitudinal magnetisation, or for more lines of k-space to be acquired. With a larger echo train length, the imaging sequence becomes faster, but effects due to T_2 also become greater. Effects due to magnetisation transfer may

also become visible, due to repeated saturation of the bound pool [24], which will be covered in detail in chapter 2. Multiple excitation pulses may also lead to increased tissue heating, which must be closely monitored when using a large echo train length.

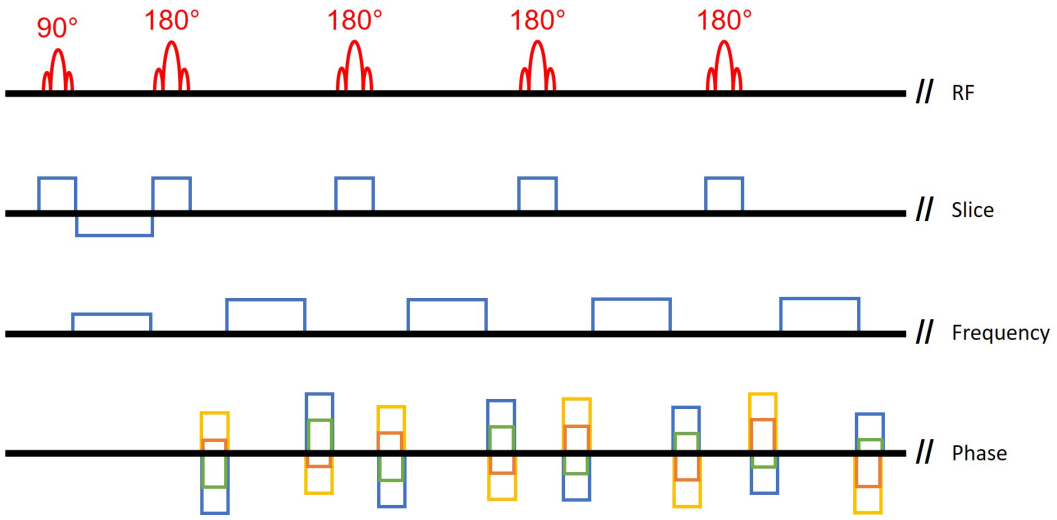

Figure 1.4.5: RARE pulse sequence, displayed here with an echo train length of 4, which creates 4 echoes and acquires 4 lines of k-space per TR. Each TR is represented in a different colour on the phase encoding line, and in this example 16 lines of k-space are acquired in total over 4 TRs.

While recent developments have seen the TR of RARE based sequences reduced to 0.6s [25], EPI is capable of acquiring entire slices in just 50-100ms [26]. First introduced by Mansfield in 1977 [16], EPI pushes temporal resolution high enough that it makes techniques such as fMRI [27] possible. This is because the whole of k-space is acquired within a singular RF pulse. Following excitation, the frequency encoding gradient sweeps k-space in alternating directions, while the phase encoding gradient is applied in short bursts of smaller magnitude as the frequency encoding gradient changes direction. This leads to a rapid repeated refocusing and defocusing of gradient echoes as k-space is traversed in a 'snakes and ladders' type direction, as shown in Figure 1.4.6.

Of course, imaging at this rate comes with drawbacks. B_0 or B_1 field inhomogeneities can lead to severe phase accumulation as the image is acquired, resulting in noticeable

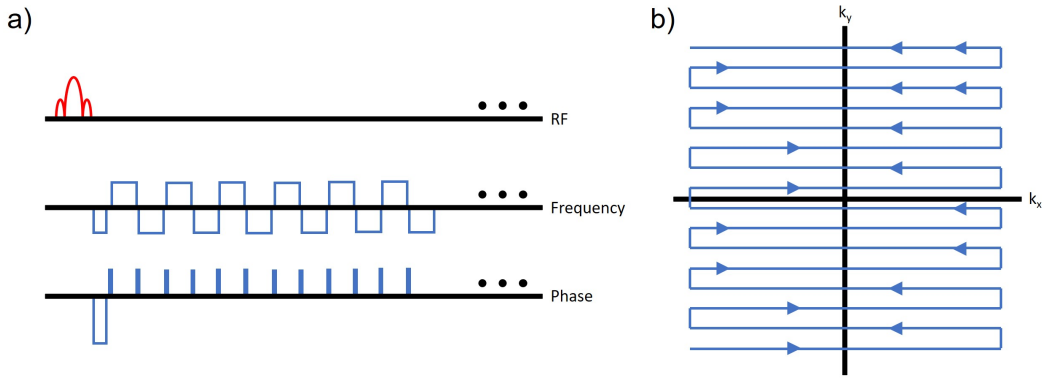

Figure 1.4.6: Echo planar imaging a) pulse sequence, and b) traversal of k-space. EPI requires only one 90° pulse to traverse the whole of k-space by utilising alternating positive and negative frequency encoding gradients, with blipped phase encoding gradients between them, resulting in vastly reduced acquisition times compared to previously discussed techniques. Slice select gradient not shown here.

image distortions. Fat signals can also be severely affected, as the phase variation from chemical shift effects also accumulates during k-space acquisition. Finally, the alternating direction of the frequency encoding gradient can lead to an artefact called a Nyquist ghost [28], due to imperfections in gradient coils or timing errors. This artefact appears as a duplicate overlaid image, shifted in the phase encoding direction by half the image length and wrapped around, as illustrated in Figure 1.4.7.

This type of EPI is termed 'single-shot', due to the fact that only a single RF pulse is applied. We can also implement 'multi-shot' EPI, which can reduce some of the effects of phase accumulation [29]. Here the whole of k-space is sampled in one RF excitation, but with slightly larger magnitude phase encoding gradients, which samples k-space more quickly but at a lower resolution. A second RF pulse is then applied and this process is repeated, but slightly shifted in the phase encoding direction. This is repeated multiple times until k-space is fully sampled, as illustrated in Figure 1.4.8.

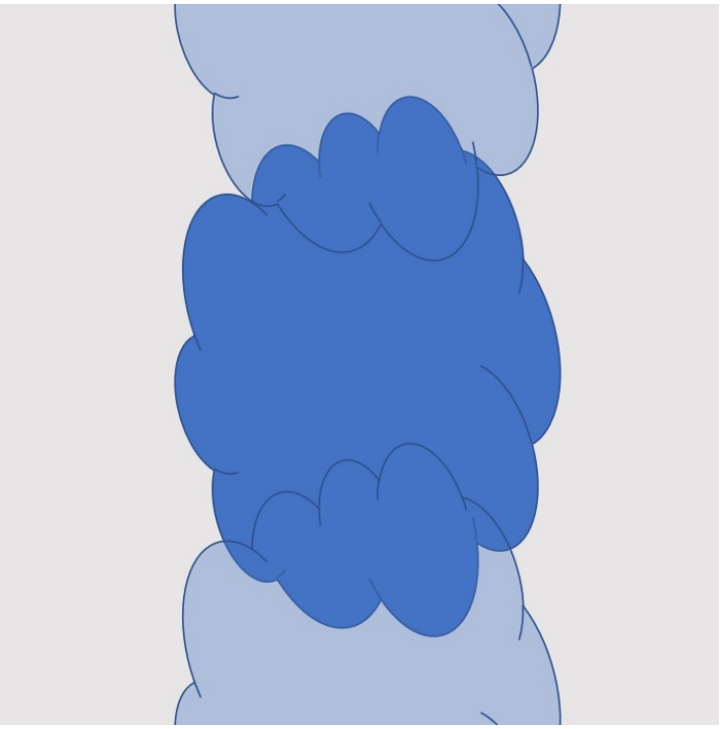

Figure 1.4.7: Illustration of the Nyquist ghost artefact. The 'real' sample is displayed as the dark blue shape in the middle, and the lighter blue shapes are representative of how the artefact may appear.

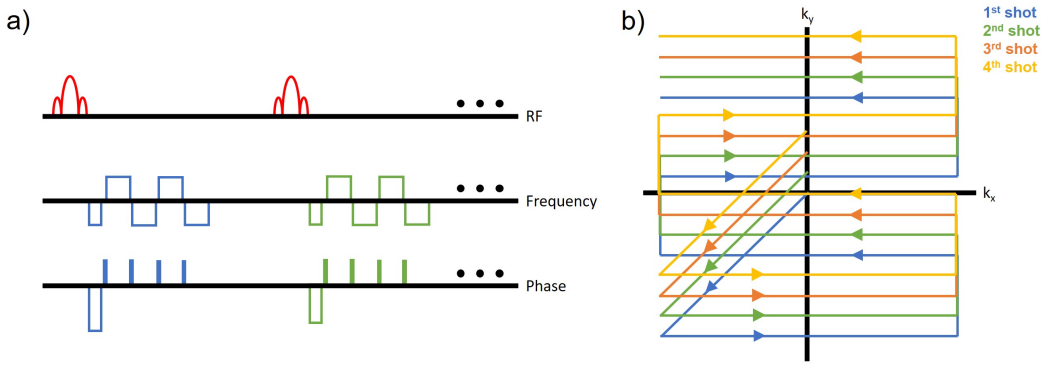

Figure 1.4.8: Multi-shot echo planar imaging a) pulse sequence, and b) traversal of k-space. This technique utilises the principles of EPI but acquires k-space more sparsely than standard EPI, over several TRs, which helps to reduce image distortions from phase accumulation. Slice select gradient not shown here.

1.4.7 B_0 and B_1 mapping

It is often important to acquire field maps for quantitative MRI, to identify regions of inhomogeneity which lead to artefacts. In the context of this thesis, quantitative MRI is defined as the case where meaningful physical metrics are obtained through calculations performed on the pixel values in acquired images. As explained throughout Chapter 2, this thesis focuses on estimation of physical and chemical properties such as the size, exchange rate, and apparent T_2 of exchanging proton pools, and therefore all subsequent mentions of MRI can be classified as quantitative.

We can produce a map of the B_0 field using a dual gradient echo sequence [30]. By measuring the phase difference $\Delta\phi(x, y, z)$ between two gradient echoes, shown in Figure 1.4.9, we can find the local frequency shifts in the B_0 field, as the local spatial B_0 field variation ΔB_z causes phase shifts dependent on the TE of the sequence and the frequency variation in the field. Therefore the spatial phase variation can be used to produce a map of B_0 variation, as shown in equation 1.4.13.

$$\Delta B_z(x, y, z) = \frac{\Delta\phi(x, y, z)}{\gamma \Delta TE}. \tag{1.4.13}$$

One way to produce a true map of the B_1 field is to acquire multiple images with varied flip angles, and fit to a function $M_0 \sin(c\alpha)$ for each separate voxel in the image, where c is a constant that describes the field variation. However, this requires a long TR between each image to allow for full recovery of the magnetisation, and as such is too long to be feasible in clinical scans. The most common method of overcoming this is using a technique called Actual Flip angle Imaging (AFI) [31]. This is a sequence consisting of two identical RF pulses, each with an identical flip angle, α, each followed by a delay of times TR_1 and TR_2 respectively. The signals from these, S_1 and S_2, are acquired via a gradient echo, as shown in Figure 1.4.10.

Instead of waiting for the longitudinal magnetisation to recover, the condition $TR_1 < TR_2 < T_1$ is met, and therefore the longitudinal magnetisation of the system is in

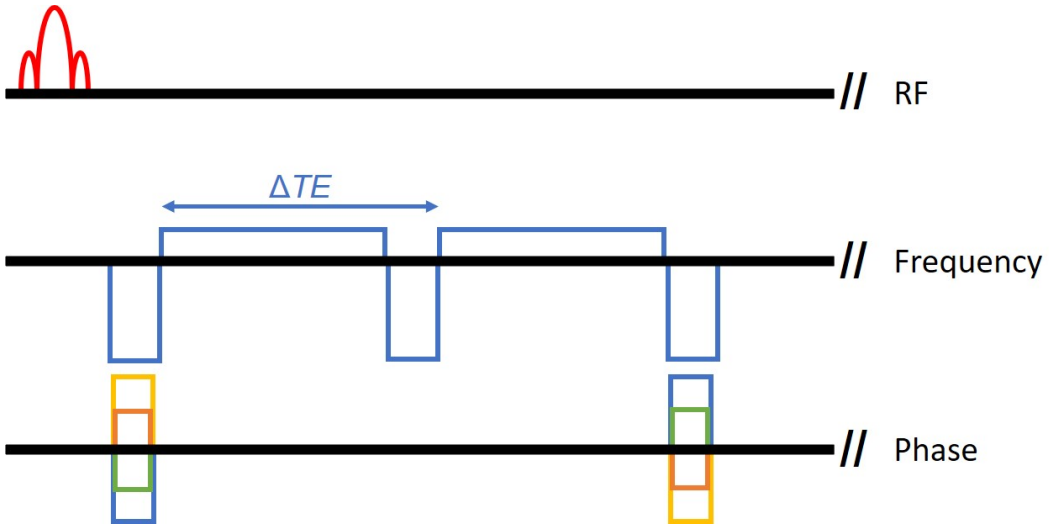

Figure 1.4.9: Dual GE pulse sequence with flyback to produce a B_0 map. Two theoretically identical gradient echoes are acquired, and the phase difference between the two is directly related to the inhomogeneities in the B_0 field.

a pulsed steady state. Assuming transverse magnetisation is completely destroyed by spoiler gradients after each TR, we can describe the magnetisation of the system via a consecutive solution to the Bloch equations:

$$M_{z,1} = M_0 \frac{1 - E_2 + (1 - E_1)E_2 \cos(\alpha)}{1 - E_1 E_2 \cos^2(\alpha)} \tag{1.4.14}$$

$$M_{z,2} = M_0 \frac{1 - E_1 + (1 - E_2)E_1 \cos(\alpha)}{1 - E_1 E_2 \cos^2(\alpha)} \tag{1.4.15}$$

where $E_{1.2} = e^{-TR_{1,2}/T_1}$. The signals we acquire are dependent on the chosen TE, and can be expressed as

$$S_{1,2} = M_{z1,2} e^{-TE/T_2^*} \sin(\alpha) \tag{1.4.16}$$

The ratio of these can therefore be expressed as

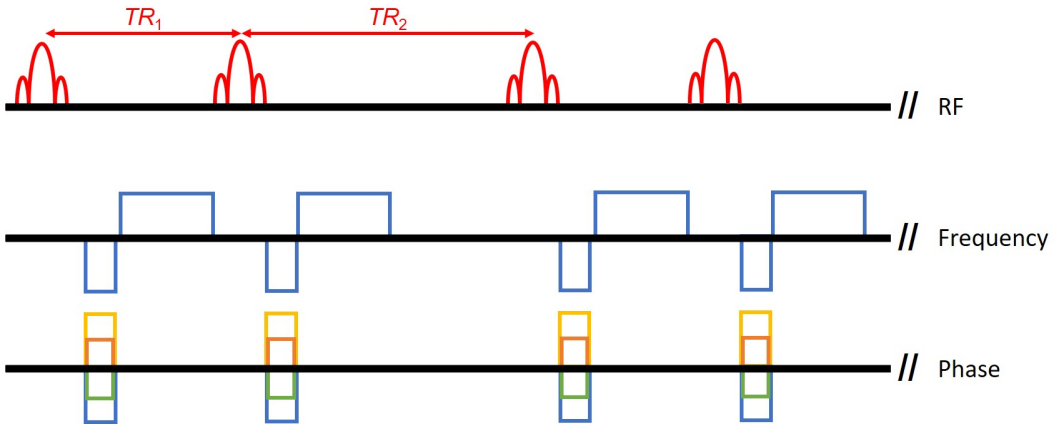

Figure 1.4.10: AFI pulse sequence to produce a B_1 map.

$$r = S_2/S_1 = \frac{1 - E_1 + (1 - E_2)E_1 \cos(\alpha)}{1 - E_2 + (1 - E_1)E_2 \cos(\alpha)} \tag{1.4.17}$$

Because TR_1 and TR_2 are sufficiently short, we can apply a first-order approximation to the exponential terms, to give

$$r \approx \frac{1 + (TR_2/TR_1)\cos(\alpha)}{(TR_2/TR_1) + \cos(\alpha)} \tag{1.4.18}$$

and therefore the signal ratio can be used to measure the actual flip angle independently of T_1.

$$\alpha \approx \cos^{-1}\left(\frac{r(TR_2/TR_1) - 1}{TR_2/TR_1 - r}\right) \tag{1.4.19}$$

This approximation holds for most practical applications, save for some cases with high flip-angle and short T_1, where the relationship described in equation 1.4.19 begins to deviate. B_1 maps are typically displayed as a relative flip angle (the measured flip angle divided by the input flip angle).

1.5 Summary

This chapter has described the fundamental principles underpinning NMR and MRI, which are necessary to understand experiments involving magnetisation transfer (MT) and chemical exchange saturation transfer (CEST) experiments. The theory behind these particular processes will be detailed in the following chapter, which are then explored further throughout this thesis.

References

[1] I. I. Rabi. Space quantization in a gyrating magnetic field. *Physical Review*, 1937. ISSN 0031899X. doi: 10.1103/PhysRev.51.652.

[2] F. Bloch, W. W. Hansen, and M. Packard. The nuclear induction experiment. *Physical Review*, 1946. ISSN 0031899X. doi: 10.1103/PhysRev.70.474.

[3] E. M. Purcell, H. C. Torrey, and R. V. Pound. Resonance absorption by nuclear magnetic moments in a solid [7], 1946. ISSN 0031899X.

[4] J. Larmor. LXIII. On the theory of the magnetic influence on spectra; and on the radiation from moving ions . *The London, Edinburgh, and Dublin Philosophical Magazine and Journal of Science*, 1897. ISSN 1941-5982. doi: 10.1080/14786449708621095.

[5] I. I. Rabi, N. F. Ramsey, and J. Schwinger. Use of rotating coordinates in magnetic resonance problems. *Reviews of Modern Physics*, 1954. ISSN 00346861. doi: 10.1103/RevModPhys.26.167.

[6] G. M. Bydder and I. R. Young. Mr imaging: Clinical use of the inversion recovery sequence. *Journal of Computer Assisted Tomography*, 1985. ISSN 15323145. doi: 10.1097/00004728-198507010-00002.

[7] D. C. Look and D. R. Locker. Time saving in measurement of NMR and EPR relaxation times. *Review of Scientific Instruments*, 1970. ISSN 00346748. doi: 10.1063/1.1684482.

[8] N. Bloembergen, E. M. Purcell, and R. V. Pound. Relaxation effects in nuclear magnetic resonance absorption. *Physical Review*, 1948. ISSN 0031899X. doi: 10.1103/PhysRev.73.679.

[9] E. L. Hahn. Nuclear induction due to free larmor precession [18], 1950. ISSN 0031899X.

[10] E. L. Hahn. Free Nuclear Induction. *Physics Today*, 1953. ISSN 19450699. doi: 10.1063/1.3061075.

[11] M. L. Winkler, D. A. Ortendahl, T. C. Mills, L. E. Crooks, P. E. Sheldon, L. Kaufman, and D. M. Kramer. Characteristics of partial flip angle and gradient reversal MR imaging, 1988. ISSN 00338419.

[12] W. G. Proctor and F. C. Yu. The dependence of a nuclear magnetic resonance frequency upon chemical compound [6], 1950. ISSN 0031899X.

[13] John Pauly, Dwight Nishimura, Albert Macovski, and Patrick Le Roux. Parameter Relations for the Shinnar-Le Roux Selective Excitation Pulse Design Algorithm. *IEEE Transactions on Medical Imaging*, 1991. ISSN 1558254X. doi: 10.1109/42.75611.

[14] J. B. Kneeland, A. Shimakawa, and F. W. Wehrli. Effect of intersection spacing on MR image contrast and study time. *Radiology*, 1986. ISSN 00338419. doi: 10.1148/radiology.158.3.3945757.

[15] Robin A. De Graaf and Klaas Nicolay. Adiabatic rf pulses: Applications to in vivo NMR. *Concepts in Magnetic Resonance*, 1997. ISSN 10437347. doi: 10.1002/(sici)1099-0534(1997)9:4<247::aid-cmr4>3.3.co;2-a.

[16] P. Mansfield and A. A. Maudsley. Medical imaging by NMR. *British Journal of Radiology*, 1977. ISSN 00071285. doi: 10.1259/0007-1285-50-591-188.

[17] Alfred Stadler, Wolfgang Schima, Ahmed Ba-Ssalamah, Joachim Kettenbach, and Edith Eisenhuber. Artifacts in body MR imaging: Their appearance and how to eliminate them, 2007. ISSN 09387994.

[18] Stig Ljunggren. A simple graphical representation of fourier-based imaging methods. *Journal of Magnetic Resonance (1969)*, 1983. ISSN 00222364. doi: 10.1016/0022-2364(83)90060-4.

[19] Reuben Mezrich. A perspective on K-space, 1995. ISSN 00338419.

[20] D. A. Feinberg, J. D. Hale, J. C. Watts, L. Kaufman, and A. Mark. Halving MR imaging time by conjugation: Demonstration at 3.5 kG. *Radiology*, 1986. ISSN 00338419. doi: 10.1148/radiology.161.2.3763926.

[21] W. A. Edelstein, J. M.S. Hutchison, G. Johnson, and T. Redpath. Spin warp NMR imaging and applications to human whole-body imaging. *Physics in Medicine and Biology*, 1980. ISSN 00319155. doi: 10.1088/0031-9155/25/4/017.

[22] R. R. Ernst and W. A. Anderson. Application of fourier transform spectroscopy to magnetic resonance. *Review of Scientific Instruments*, 1966. ISSN 00346748. doi: 10.1063/1.1719961.

[23] J. Hennig, A. Nauerth, and H. Friedburg. RARE imaging: A fast imaging method for clinical MR. *Magnetic Resonance in Medicine*, 1986. ISSN 15222594. doi: 10.1002/mrm.1910030602.

[24] David L. Thomas, Enrico De Vita, Steven Roberts, Robert Turner, Tarek A. Yousry, and Roger J. Ordidge. High-resolution fast spin echo imaging of the human brain at 4.7 T: Implementation and sequence characteristics. *Magnetic Resonance in Medicine*, 2004. ISSN 07403194. doi: 10.1002/mrm.20106.

[25] Andreas M. Loening, Manojkumar Saranathan, Nichanan Ruangwattanapaisarn, Daniel V. Litwiller, Ann Shimakawa, and Shreyas S. Vasanawala. Increased speed and image quality in single-shot fast spin echo imaging via variable refocusing flip angles. *Journal of Magnetic Resonance Imaging*, 2015. ISSN 15222586. doi: 10.1002/jmri.24941.

[26] Michael K. Stehling, Robert Turner, and Peter Mansfield. Echo-planar imaging: Magnetic resonance imaging in a fraction of a second, 1991. ISSN 00368075.

[27] J. W. Belliveau, D. N. Kennedy, R. C. McKinstry, B. R. Buchbinder, R. M. Weisskoff, M. S. Cohen, J. M. Vevea, T. J. Brady, and B. R. Rosen. Functional mapping of the human visual cortex by magnetic resonance imaging. *Science*, 1991. ISSN 00368075. doi: 10.1126/science.1948051.

[28] Qing X. Yang, Stefan Posse, Denis L.E. Bihan, and Michael B. Smith. Double-sampled echo-planar imaging at 3 tesla. *Journal of Magnetic Resonance - Series B*, 1996. ISSN 10641866. doi: 10.1006/jmrb.1996.0167.

[29] David Atkinson, David A. Porter, Derek L.G. Hill, Fernando Calamante, and Alan Connelly. Sampling and reconstruction effects due to motion in diffusion-weighted interleaved echo planar imaging. *Magnetic Resonance in Medicine*, 2000. ISSN 07403194. doi: 10.1002/1522-2594(200007)44:1<101::AID-MRM15>3.0.CO;2-S.

[30] Peter Jezzard and Robert S. Balaban. Correction for geometric distortion in echo planar images from B0 field variations. *Magnetic Resonance in Medicine*, 1995. ISSN 15222594. doi: 10.1002/mrm.1910340111.

[31] Vasily L. Yarnykh. Actual flip-angle imaging in the pulsed steady state: A method for rapid three-dimensional mapping of the transmitted radiofrequency field. *Magnetic Resonance in Medicine*, 2007. ISSN 07403194. doi: 10.1002/mrm.21120.

Chapter 2

MT, CEST, and NOE theory

First described by Grad and Byrant in 1990 [1], z-spectroscopy refers to the method of probing the presence of molecules or compounds containing ^1H groups through selective saturation of frequencies off-resonance from water, and observing the resulting change in intensity of the water signal due to proton, molecular or magnetisation exchange. This chapter will describe the three processes visible in z-spectroscopy, namely magnetisation transfer (MT), chemical exchange saturation transfer (CEST), and the nuclear Overhauser enhancement (NOE) effect, and will explore the possible proposed ways of measuring these effects.

2.1 Physical basis of z-spectroscopy

The field of z-spectroscopy originates from NMR investigations into chemical exchange in the 1950s and 1960s by McConnell [2] and Forsén and Hoffman [3] in which the effects of exchange were modelled (explored here in section 2.2) and experimentally visualised. These early experiments showed the separation of two proton pools, and how these signals undergo increasing coalescence as the rate of exchange between the

two proton pools increases relative to their chemical shift separation.

There are three main categories which describe the way the exchange of proton magnetisation exchange occurs *in vivo*. The first of these to be discovered was magnetisation transfer by Wolff and Balaban in 1989 [4], which accounts for exchange between large soluble macromolecules and water. This was followed by the observation of chemical exchange saturation transfer by Ward and Balaban in 2000 [5], which describes exchange between smaller molecules containing labile protons. The third source of signal, nuclear Overhauser enhancement, is a little more complex. In z-spectroscopy, this was first observed by Ling in 2008 [6], and arises from cross-relaxation of nearby protons. It is thought that the NOE effect may be indicative of the presence of aliphatic protons, which will be explored further in section 2.1.3.

2.1.1 Magnetisation Transfer

While conventional clinical MRI observes the properties of relatively unrestricted ('free') water protons, it is not the only source of the ^1H MR signal. Macromolecules such as large intracellular proteins or collagen have ^1H components, and so contribute to the NMR signal in some way. However, the protons in these macromolecules cannot be imaged directly as they have highly restricted motion, and therefore very short T_2 relaxation times ($\ll$1ms), meaning that the signal dephases before it can be acquired using MRI methods [7].

In addition to this, a few layers of water molecules close to the surface of a macromolecule undergo some degree of hydrogen bonding with the macromolecular surface. This causes their motion to be restricted, and therefore these particular water molecules also share a very short T_2. We refer to these hydration layers as 'bound water', and due to their similarities with macromolecules, bound water and macromolecules are collectively known as the 'bound pool'. As shown in Figure 2.1.1, bound water interfaces with free water, which is where the transfer of magnetisation can occur.

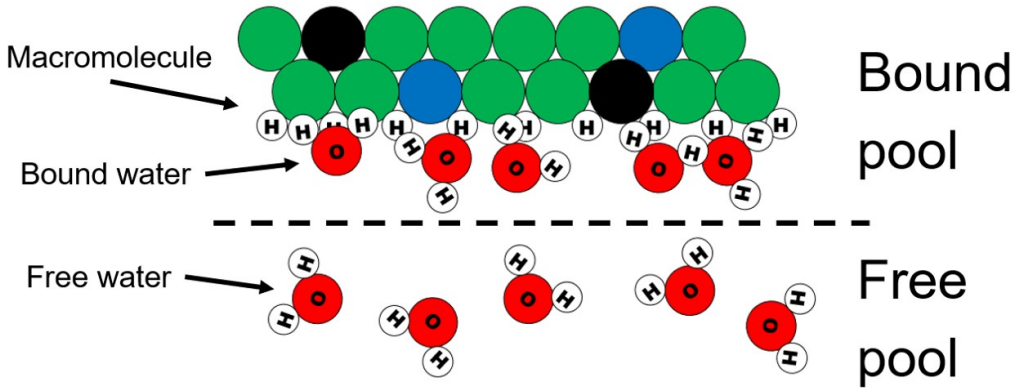

Figure 2.1.1: Illustration of the 'bound pool' of protons, consisting of macromolecular protons and bound water, and the 'free pool' consisting of free, mobile water.

While free water has a narrow resonance frequency with a maximum range of 100Hz at 7T, the bound pool lies across a very broad frequency range. If we take Figure 2.1.1 as a simplified example tissue, Figure 2.1.2 shows an illustration of how the acquired ^1H MRS signal might look from this tissue with respect to frequency if all spins were NMR visible. For simplicity, magnetisation transfer experiments define the resonance frequency of free water as being at zero, and due to convention we display frequency diagrams with positive frequencies on the left and negative frequencies on the right. We use parts per million (ppm) as the measure of frequency offset here, as it gives us independence from the B_0 field strength used. This can be calculated in the same way as chemical shift in equation 1.3.1, except here we take ω_{ref} to be the resonance frequency of protons in free water. In practice, this makes interchanging between Hz and ppm extremely simple, as we can divide the frequency offset in Hz by the Larmor frequency of $1H$ nuclei at the relevant B_0 in MHz, to yield the offset in ppm. For example, at a B_0 of 3T, an offset of +128Hz is equivalent to an offset of +1ppm.

While we are unable to image the bound pool directly, we can probe the presence of macromolecules through selective saturation of the bound pool at particular off-resonance frequencies, due to the magnetisation transfer (MT) effect. By saturating a chosen frequency off-resonance from free water, we would stimulate only the bound

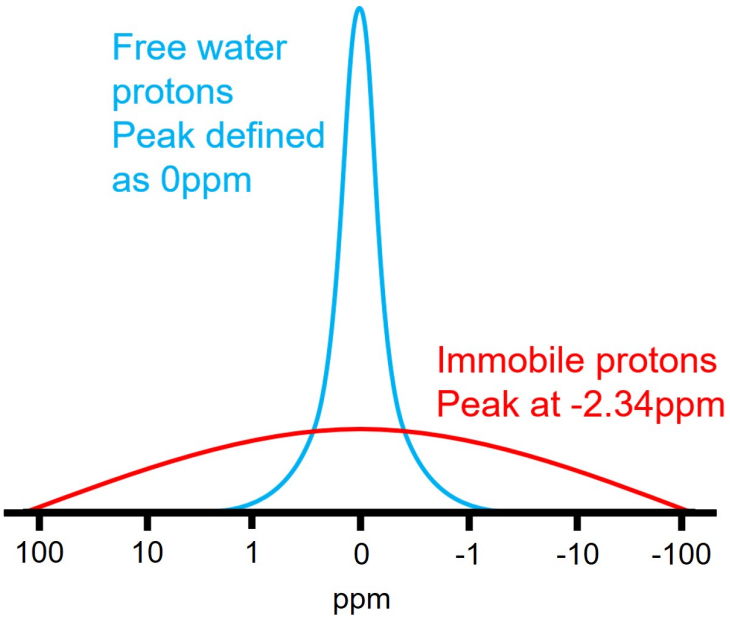

Figure 2.1.2: Illustration of the signal components arising from the bound pool and the free pool as a function of resonance frequency.

pool of protons. These protons then return to equilibrium, by transferring their magnetisation to free water, primarily through dipole-dipole interactions [8]. This in turn saturates the free pool, which reduces the water signal. We can therefore measure the water signal before and after a saturation pulse, and the ratio of the initial signal (S_0) to the final signal (S_{sat}) is dependent on the presence of macromolecules and their properties.

2.1.2 Chemical Exchange Saturation Transfer

Other molecular components of tissue can also lead to suppression of the water signal, which can give us a further level of chemical specificity. Labile protons are capable of physically exchanging their protons with free water protons, and by saturating these labile protons, we can observe a change in the water signal and determine the presence and properties of certain molecular groups. This process is called chemical exchange

saturation transfer (CEST), and molecules which contain labile protons are sometimes referred to as CEST agents, with resonating functional groups usually located downfield of water (>0ppm) [5]. CEST agents can be exogenous or endogenous, and the first endogenous CEST agent to be detected *in vivo* was the amide group [9]. CEST contrast arising solely from amides is also sometimes referred to as amide proton transfer (APT), and is the most widely used endogenous CEST agent due to its relatively large CEST signal *in vivo*, and sufficient separation from free water resonance (+3.5ppm). However, many other CEST agents have been detected *in vivo*, such as glycogen which has a resonance between +0.5ppm and +1.5ppm [10], glycosaminoglycans which have a dual resonance at +3.2 ppm and between +0.9ppm and +1.9ppm [6], creatine which has a resonance at +1.8ppm [11], and others. Each of these typically comes with an abbreviation to describe the molecular specificity of the experiment, i.e. glycoCEST, gagCEST, and CrCEST respectively.

2.1.3 Nuclear Overhauser Enhancement

There is another mechanism through which the transfer of magnetisation can occur. Only labile protons are exchangeable, and so signals we see upfield of water arise from nuclear Overhauser enhancement (NOE), which is where energy is exchanged between two spins which are relatively close (0.5nm) to each other. Exchange due to NOE can occur via dipole-dipole cross relaxation, where non-labile protons exchange their spin states with nearby free water protons, or through exchange relayed NOE (sometimes referred to as rNOE), where non-labile protons exchange their spin states with labile protons in that same molecule, which then exchange with free water via the CEST mechanism [12, 13]. This can get more complex, as non-labile protons can exchange their spin states with other nearby non-labile protons in a molecule, which continues until exchange with a different labile proton occurs, in a process known as spin diffusion. An illustration of NOE exchange mechanisms is shown in Figure 2.1.3.

The largest and therefore most commonly seen NOE signal in *in vivo* z-spectroscopy has an off-resonance frequency of -3.5ppm, and is generally attributed to the presence

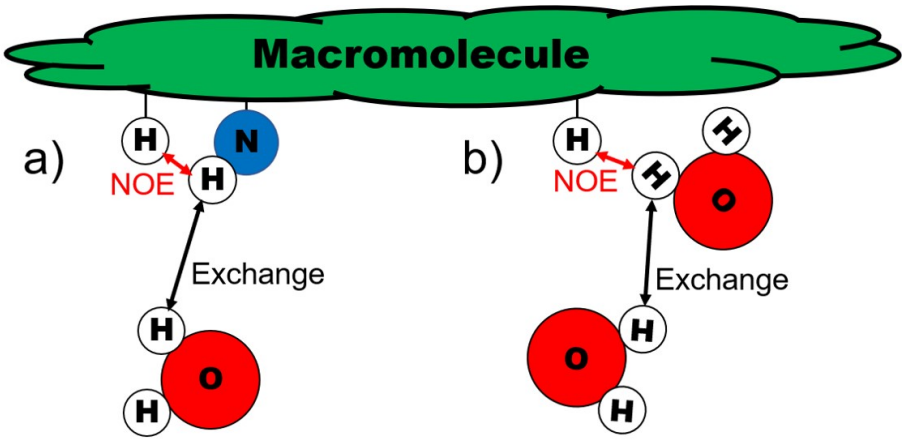

Figure 2.1.3: Illustration of two NOE processes: a) relayed NOE through labile proton groups (here the N atom could equally be an O or S atom), and b) cross-relaxation between nearby protons directly from the bound pool to the free pool.

of aliphatic protons [14]. Recently however, several studies have observed a new NOE mediated signal at -1.7ppm. One study observed this signal in ischaemic stroke tissue, and hypothesised that it may be indicative of phospholipid choline headgroups [15]. Another study speculated that this signal may arise from the α-carbons of mobile membrane proteins [14], and indeed this may be backed up by a study observing this signal in concentrated red blood cells, which then disappeared when the blood cells were lysed [16].

2.2 Modelling of exchange processes

We can model the evolution of magnetisation of a sample containing exchanging pools using the Bloch-McConnell equations, which are the Bloch equations modified for chemical exchange [2]. In the absence of exchanging pools, we can separate out the time dependent Bloch equation into its constituent x-, y-, and z- components [17] to give

$$\frac{dM_x}{dt} = \Delta\omega M_y(t) - \frac{1}{T_2}M_x(t) \tag{2.2.1}$$

$$\frac{dM_y}{dt} = -\Delta\omega M_x(t) - \frac{1}{T_2}M_y(t) + \omega_1(t)M_z(t) \tag{2.2.2}$$

$$\frac{dM_z}{dt} = -\omega_1 M_y(t) - \frac{1}{T_1}[M_z(t) - M_z^0] \tag{2.2.3}$$

where $\omega_1(t) = \gamma B_1(t)$, $\Delta\omega = \omega_0 - \omega$, the offset frequency of the applied B_1 field ω with respect to the Larmor frequency ω_0, and M_z^0 is the equilibrium magnetisation in the z- direction without application of the B_1 field.

We can convert equations 2.2.1-2.2.3 into a homogeneous linear differential equation, to give

$$\frac{d\mathbf{M}}{dt} = \mathbf{A}.\mathbf{M} \tag{2.2.4}$$

where

$$\mathbf{M} = \begin{bmatrix} M_x(t) & M_y(t) & M_z(t) & 1 \end{bmatrix}^T \tag{2.2.5}$$

in which T symbolises the matrix transpose, and

$$\mathbf{A} = \begin{bmatrix} -\frac{1}{T_2} & \Delta\omega & 0 & 0 \\ -\Delta\omega & -\frac{1}{T_2} & \omega_1(t) & 0 \\ 0 & -\omega_1(t) & -\frac{1}{T_1} & \frac{M_z^0}{T_1} \\ 0 & 0 & 0 & 0 \end{bmatrix} \tag{2.2.6}$$

We can solve equation 2.2.4 to give the general solution

$$\mathbf{M}(t) = e^{\mathbf{A}t}\mathbf{M}(0) \tag{2.2.7}$$

which in practical terms is laborious to solve, as it involves the matrix exponential term $e^{\mathbf{A}t}$, which requires calculation via a Maclaurin series ($e^{\mathbf{A}t} = \sum_{k=0}^{\infty} \frac{\mathbf{A}^k t^k}{k!}$). The most basic method of evaluating this expression is to perform repeated calculations for varying k up to a sensible cutoff point where further summations become negligible [18]. Further methods have been explored to speed up this calculation, for example Mathematica [19] and MATLAB [20] both use a scaling and squaring algorithm [21, 22] in which a matrix exponential $e^{\mathbf{A}} = e^{2^{-s}\mathbf{A}} \approx r_m(2^{-s}\mathbf{A})^{2^s}$, where s is a non-negative integer chosen for computational efficiency, and r_m is the Padé approximation of $e^{\mathbf{A}}$, as defined elsewhere [23]. This mathematical framework is key when exchanging pools are considered.

2.2.1 Example three pool model

In this section we can consider a simple model with three exchanging pools: free water as considered in the preliminary example above (denoted f), the bound pool (denoted b), and an arbitrary CEST pool (denoted with a subscript c). We can take equation 2.2.4 and redefine the terms for the presence of these exchanging pools, so that

$$\mathbf{M} = \begin{bmatrix} M_{x,f}(t) & M_{y,f}(t) & M_{z,f}(t) & M_{x,c}(t) & M_{y,c}(t) & M_{z,c}(t) & M_{z,b}(t) \end{bmatrix}^T \tag{2.2.8}$$

where we ignore the x- and y- components of the bound pool, as the T_2 of the bound pool ($T_{2,b}$) is sufficiently short that transverse coherence is lost significantly before exchange occurs [24], and

$$\mathbf{A} = \begin{bmatrix} -\frac{1}{T_{2,f}} - k_{fc} & \Delta\omega_f & 0 & +k_{cf} & 0 & 0 & 0 \\ -\Delta\omega_f & -\frac{1}{T_{2,f}} - k_{fc} & +\omega_1(t) & 0 & +k_{cf} & 0 & 0 \\ 0 & -\omega_1(t) & -\frac{1}{T_{1,f}} - k_{fb} - k_{fc} & 0 & 0 & +k_{cf} & +k_{bf} \\ +k_{fc} & 0 & 0 & -\frac{1}{T_{2,c}} - k_{cf} & -\Delta\omega_c & 0 & 0 \\ 0 & +k_{fc} & 0 & +\Delta\omega_c & -\frac{1}{T_{2,c}} - k_{cf} & +\omega_1(t) & 0 \\ 0 & 0 & +k_{fc} & 0 & -\omega_1(t) & -\frac{1}{T_{1,c}} - k_{cf} & 0 \\ 0 & 0 & +k_{fb} & 0 & 0 & 0 & -\frac{1}{T_{1,b}} - R_{rfb} - k_{bf} \end{bmatrix} \tag{2.2.9}$$

where we assume the exchange between the bound pool and the CEST pool is negligible, which is appropriate when the size of the free pool is significantly larger than the size of the other pools [25]. We define two new terms here. The first of which, k_{xy}, is the exchange rate, the rate of chemical exchange which occurs from pool x to pool y, measured in Hz (number of exchanging protons per second). The second term, R_{rfb}, is specific to the bound pool, and determines the MT lineshape with respect to saturation frequency, which will be explored in greater depth in section 2.2.2.

We redefine equation 2.2.4 to account for the longitudinal relaxation of the exchanging pools [25], so that

$$\frac{d\mathbf{M}}{dt} = \mathbf{A}.\mathbf{M} + \mathbf{C} \tag{2.2.10}$$

where

$$\mathbf{C} = \begin{bmatrix} 0 & 0 & \frac{M_{0,f}}{T_{1,f}} & 0 & 0 & \frac{M_{0,c}}{T_{1,c}} & \frac{M_{0,b}}{T_{1,b}} \end{bmatrix}^T \tag{2.2.11}$$

in which $M_{0,x}$ is the equilibrium magnetisation of pool x, commonly referred to as the pool size. As previously stated, solutions to this equation are difficult to compute, however there are certain cases where analytical solutions can be derived, which will be described later in this chapter.

2.2.2 The z-spectrum

In practical situations such as human tissue, there are far more than three exchanging pools present. As well as free water and MT, there are many possible sources of CEST signal as suggested above, and while two common NOE signals have been seen, it has been theorised that up to 5 sources of the NOE signal may be present [26], corresponding to the different types of aliphatic and olefinic protons. When we saturate off-resonance frequencies and read out the water signal in order to visualise the presence of exchanging pools, this can result in the signals from different pools overlapping and coalescing. As described in section 2.1.1, off-resonance frequencies are selectively saturated and the resulting water signal is acquired. We can plot the ratio of the signal post-saturation to the initial signal (S_{sat}/S_0) against saturation frequency to yield the z-spectrum, where the reduction in water signal at particular off-resonance frequencies is dependent in part on the presence and properties of exchanging pools. An illustration of a z-spectrum is shown in Figure 2.1.1.

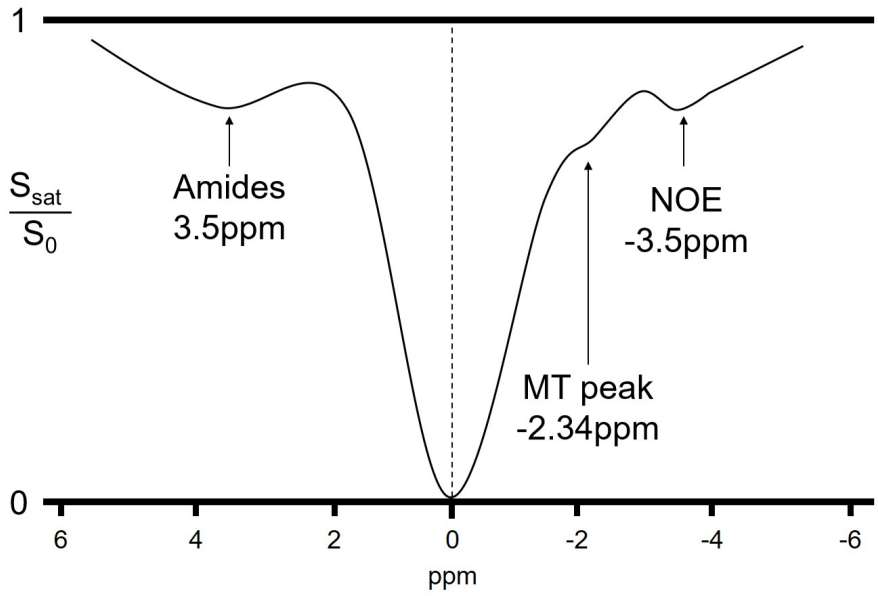

Figure 2.2.1: Illustration of the z-spectrum, showing three commonly seen peaks.

As well as being dependent on which exchanging pools are present, we can see from

equation 2.2.10 and its terms that the shape of the z-spectrum is sensitive to a number of parameters. The effects of varying some of these parameters are often difficult to distinguish (namely pool size, exchange rate, and apparent T_2 of exchanging pools), as will be illustrated below, and indeed there is no analytical method to solve the Bloch-McConnell equations for these physical parameters. Attempts have been made to approximate these, which will be detailed in section 2.5, and a novel method of quantifying these terms is presented in chapter 3.

To illustrate the effects of these parameters, a simple two pool model can be considered containing one CEST peak with an off-resonance frequency at 3.5ppm, labelled here as an amide peak. We can start by considering the effect of the CEST pool size (which tells us the amount of CEST agent present) on the shape of the z-spectrum. The relationship here is simple to understand: as the amount of CEST agent increases, the more exchangeable protons that are present, and so at a fixed exchange rate and a set saturation frequency, the CEST signal increases as the pool size increases. Figure 2.2.2 shows the relationship between pool size and the shape of the z-spectrum when all other parameters are fixed. All simulations in this section are performed with a field strength of 7T.

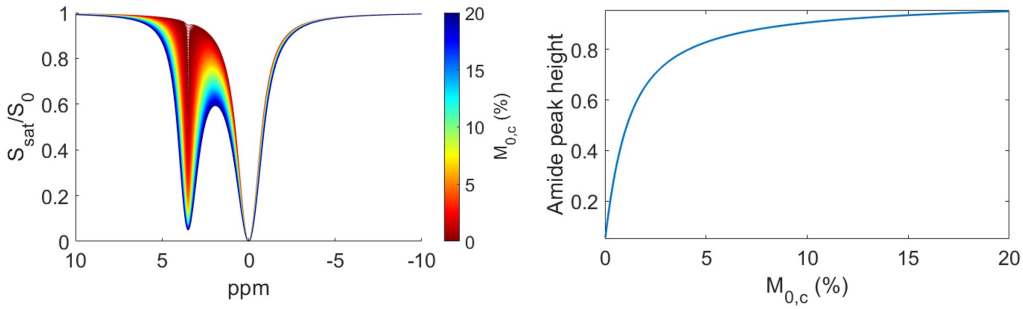

Figure 2.2.2: Effects of variation in the pool size of the measured pool of interest. Other parameters are fixed at $k_c = 50$Hz, $T_{2,c} = 50$ms, $B_{1,max} = 1\mu$T, pulse duration=3s.

The effects of varying the exchange rate of CEST pools are similar to that of varying $M_{0,c}$, but with several salient differences. It is important to note that in practice,

the term $k_{f,c}$ is typically ignored, as exchange in this direction is considered negligible due to the small CEST pool size compared to free water. Because we now only have one exchange term associated with each exchanging pool, the shorter notation k_c can be used to denote $k_{c,f}$. As expected, the initial effect of increasing k_c is that the CEST signal increases, as saturated CEST protons can exchange with the free pool at a greater rate, leading to increased overall saturation of the water signal. However, at very fast exchange rates, the CEST signal begins to coalesce with the water signal [27]. The effects of coalescence can be diminished by using an increased B_0 field strength, which causes the difference in the resonance frequencies of free water and the CEST pool in question to be farther apart. Changes in the shape of the z-spectrum due to varying exchange rate when all other parameters are fixed are illustrated in Figure 2.2.3. As well as being specific to the functional groups of the molecules in question, the exchange rate also depends on temperature and pH. The temperature dependence of the exchange rate is defined by the Arrhenius equation, $k = Ae^{\frac{-E_a}{k_B T}}$ [28], where A is the frequency of collisions when all molecules are perfectly aligned, E_a is the activation energy for the reaction, k_B is the Boltzmann constant, and T is the absolute temperature. It is also known that proton exchange is pH sensitive [29]. The direction of this depends on whether the CEST agent in question is acid-catalysed or base-catalysed. For example, amide protons are base-catalysed, meaning that exchange rate increases at higher pH as there are more exchangeable sites at higher alkalinity, however this relationship is not linear [30].

Transverse relaxation of the exchanging pools affects the shape of the z-spectrum in a different way. As $T_{2,c}$ decreases, the rate at which phase coherence is lost increases. This leads to broadening of the CEST peaks, with some reduction in the peak height at very short $T_{2,c}$s. Increases in the $T_{2,c}$ change the shape of the z-spectrum up to a point, beyond which phase coherence is maintained to a sufficient degree to not cause additional peak broadening. The effects of $T_{2,c}$ variation can be seen in Figure 2.2.4.

Changes to the RF power or the application time of the saturation pulse also changes the shape of the z-spectrum. Considering a continuous-wave pulse to remove the time dependency of $\omega_1(t)$ so that $B_{1,max} = \omega_1/\gamma$, we can choose our saturation power and

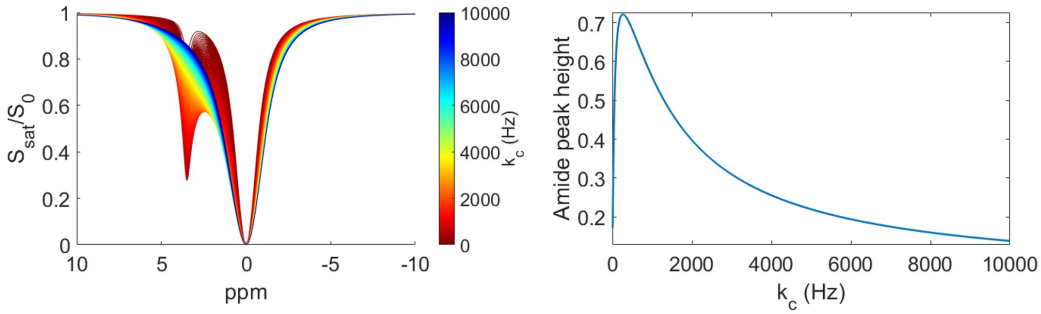

Figure 2.2.3: Effects of variation in the exchange rate of the measured pool of interest. Other parameters are fixed at $M_{0,c} = 1\%$, $T_{2,c} = 50$ms, $B_{1,max} = 1\mu$T, pulse duration=3s. Signal increases up to a point at which coalescence with water begins.

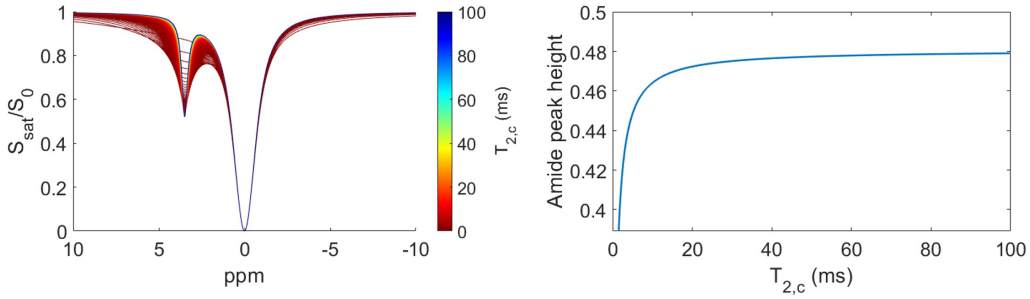

Figure 2.2.4: Effects of variation in the apparent T_2 of the measured pool of interest. Other parameters are fixed at $M_{0,c} = 1\%$, $k_c = 50$Hz, $B_{1,max} = 1\mu$T, pulse duration=3s.

duration to acquire a z-spectrum sensitive to certain desired effects. Faster exchanging pools are more prominent at higher saturation powers, and so it may be appropriate to apply a larger or smaller saturation pulse depending on the properties of the pool of interest. The effects of modifying the saturation parameters are shown in Figure 2.2.5.

Because of the drastic effects that the RF power has on the shape of the spectrum, any B_1 inhomogeneity can be a severe confounding factor if not properly accounted for. As the shape of the spectrum does not change linearly with increasing RF, unfortunately

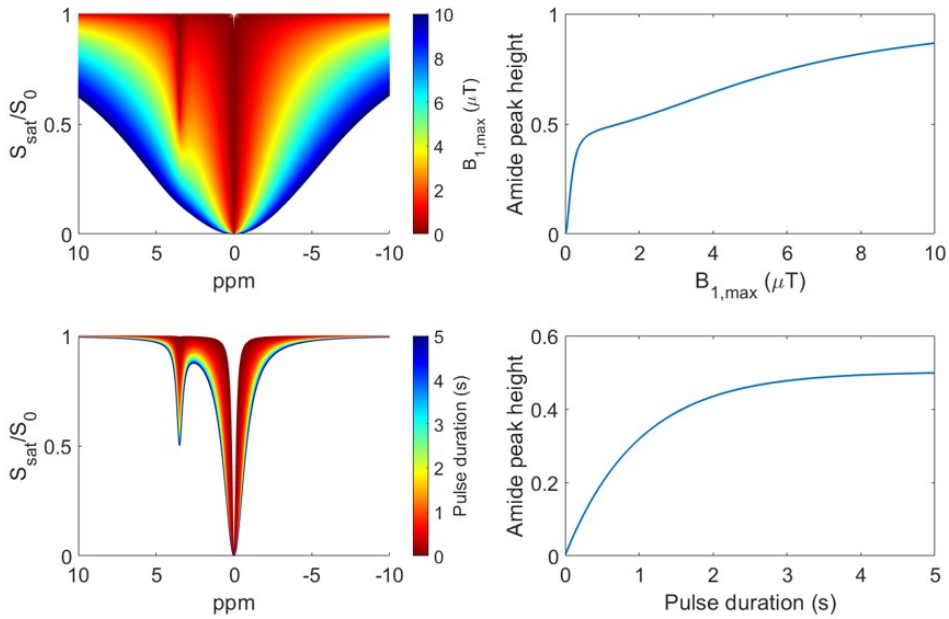

Figure 2.2.5: Effects of changing the parameters of the applied saturation pulse. Other parameters are fixed at $M_{0,c} = 1\%$, $k_c = 50$Hz, $T_{2,c} = 50$ms. Pulse duration is fixed at 3s for $B_{1,max}$ variation, $B_{1,max}$ is fixed at 1μT for pulse duration variation. As we are in the slow exchanging regime, lower B_1 amplitudes have a greater effect on the CEST signal. In the pulse duration variation, we see an increase in signal up until the steady state is reached, which will be detailed in section 2.3.1.

it is not possible to simply acquire a B_1 map and correct in post processing. In most cases, this means that RF shimming must be performed, although a method has been proposed where multiple z-spectra are acquired at varying saturation powers in addition to a B_1 map to correct the acquired data for these effects. Spline interpolation is performed between the spectra to determine the expected values at the target B_1 [31].

The z-spectrum is also affected by B_0 inhomogeneities. Deviations in the B_0 field can shift the entire spectrum on the frequency axis. This becomes increasingly problematic if multiple spectra inside a region of interest have been averaged, but local field distortions are present. There are several widely used methods of correcting z-spectra

for B_0 inhomogeneities. The first of these is to interpolate the z-spectrum around the central water frequency using a high order (e.g. twelfth-order) polynomial. Ideally this would be a low saturation power spectrum which provides a very sharp water peak. It is assumed that the lowest point in the spectrum is the resonance frequency of free water, and should be located at 0ppm. The whole z-spectrum is therefore shifted to make this the case, and this is performed on the z-spectrum from each individual pixel [32]. Another method involves acquisition of a B_0 map in the same image space as the z-spectra. The frequency offset in each of the pixels in the B_0 map can be used to shift the entire z-spectrum in each of the corresponding pixels to align pools to their correct resonance frequencies, so that the water resonance frequency is aligned with 0ppm [33]. An alternative method to these is to use "WAter Saturation Shift Referencing" (WASSR) [34]. Here an additional z-spectrum is acquired only around the water frequency with sufficiently low power for any MT or CEST exchange effects to be negligible. The frequency offset between 0ppm and the point at which the direct water saturation occurs is noted and further acquired z-spectra are shifted by this frequency offset such that water saturation occurs at exactly 0ppm. This has been shown to be accurate to 1Hz at 3T.

While it is appropriate to model CEST and NOE pools in the z-spectrum as Lorentzian lineshapes [35], the shape of the MT pool is not so straightforward. It has been shown that around the water resonance, using a Lorentzian lineshape is suitable [36], however this breaks down far off resonance, and suggestions such as a Gaussian [37] or super-Lorentzian [38] lineshape have been proposed. While the super-Lorentzian lineshape is the most commonly used in MT modelling, it has been shown that none of these lineshapes truly describe the model, and as such the most accurate way to define the MT lineshape currently is to create a flexible lineshape derived empirically from real data [38].

2.3 Z-spectrum imaging sequences

As can be seen from Figure 2.2.5, CEST effects are generally visible not from a single exchange between water protons and another species, but rather the build up of water saturation over time through repeated exchange and saturation. Saturation builds up for a certain amount of time, until the steady-state is reached, where the buildup of saturation is in equilibrium with the longitudinal relaxation of the free water pool, and as such the system is no longer time-dependent. However, due to practical limitations the steady-state cannot always be reached, and imaging must be performed in the transient-state [39]. We can modify the way saturation is applied and the way the water signal is measured, depending on the experiment we wish to perform and limitations of any hardware.

2.3.1 Saturation methods

Due to the many dependencies of the z-spectrum, the ideal way to measure any effects is through applying a long square pulse, in order to allow the system to reach the steady-state, and also to remove time dependency of the B_1 term (so that $B_1(t) = B_{1,max}$). When the RF pulse is constant (i.e. not time-dependent), we refer to the saturation method as continuous wave (CW) saturation [40]. An illustration of the pulse sequence used in the CW experiment is displayed in Figure 2.3.1. Note for the moment the image encoding section is simply denoted by a block labelled "READ", however this will be explored in the next section.

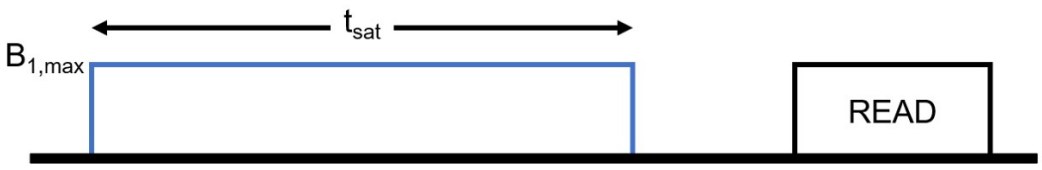

Figure 2.3.1: Pulse sequence diagram of CW saturation.

Under CW saturation and in the condition of steady-state saturation, an analytical solution for the Bloch-McConnell equations can be derived. In the z-spectrum, we normalise the z- component of the magnetisation such that $Z = M_{z,f}/M_{0,f}$. As has been shown previously [41, 42], we can solve equation 2.2.10 for a two pool model in the eigenspace of the matrix $\mathbf{A}$, to give the steady state solution

$$Z(\Delta\omega)_{ss} = \frac{\cos^2(\theta).T_{1,\rho}(\Delta\omega)}{T_{1,obs}} \tag{2.3.1}$$

where $T_{1,\rho}$ refers to the overall longitudinal relaxation time of the system in the rotating frame, and θ is the angle between the applied resonance frequency and the frequency of the pool of interest in the rotating frame ($\tan^{-1}(\omega_1/\Delta\omega)$). We can define this as a superposition of the relaxation times of each pool, so that

$$\frac{1}{T_{1,\rho}(\Delta\omega)} = R_{eff}(\Delta\omega) + R_{ex,c}(\Delta\omega) \tag{2.3.2}$$

where the term $R_{eff}(\Delta\omega)$ describes the relaxation of free water in the rotating frame, such that

$$R_{eff}(\Delta\omega) = \frac{\cos^2(\theta)}{T_{1,f}} + \frac{\sin^2(\theta)}{T_{2,f}} \tag{2.3.3}$$

in which

$$\cos^2(\theta) = \frac{\Delta\omega^2}{\omega_1^2 + \Delta\omega^2}; \sin^2(\theta) = \frac{\omega_1^2}{\omega_1^2 + \Delta\omega^2} \tag{2.3.4}$$

and for a Lorentzian lineshape, the exchange dependent relaxation can be defined by

$$R_{ex,c} = M_{0,c}k_c\frac{\omega_1^2}{\omega_1^2 + k_c(k_c + 1/T_{2,c})} \tag{2.3.5}$$

We can extend equation 2.3.2 for as many pools of interest as we like [42], for example in a four pool model containing MT, CEST, and NOE pools along with free water, the overall longitudinal relaxation time would be defined as $\frac{1}{T_{1,\rho}(\Delta\omega)} = R_{eff}(\Delta\omega) + R_{ex,b}(\Delta\omega) + R_{ex,c}(\Delta\omega) + R_{ex,n}(\Delta\omega)$. This of course assumes the bound pool also has a Lorentzian lineshape, however as previously discussed this may not be the case. An analytical solution for the case where the bound pool is defined by a super-Lorentzian lineshape has also be found; for reference this is detailed in [43], but is not implemented in this thesis for reasons which will be explained in chapter 3.

While this analytical solution has been found through consideration of the steady state only, we can extend this model to the transient state [42] to produce the expression

$$Z(\Delta\omega, t) = (\cos^2(\theta) - Z(\Delta\omega)_{ss})e^{\frac{-t_{sat}}{T_{1,\rho}}} + Z_{ss} \tag{2.3.6}$$

where Z_{ss} is the system in the steady-state condition, and t_{sat} is the time that saturation is applied for. This expression has been verified both against the full numerical solutions and in phantom work with a saturation time as short as 0.4s [43].

Although CW saturation is ideal for CEST, many clinical scanners are not capable of achieving a 100% duty cycle (percentage of time the RF amplifiers can be run). To overcome this, the constant RF pulse is replaced with a series of repetitive short pulses. This reintroduces the time dependency of the $B_1(t)$ term in the Bloch-McConnell solutions, and so the solution presented above no longer applies. An example of pulsed irradiation applied to the CEST experiment is presented in Figure 2.3.2.

Typically for pulsed irradiation, the shape of the pulses are either Gaussian [44] or truncated sinc shaped [16]. Previous work has shown that the average power transmitted by a saturation train of RF pulses produces similar effects to the RF power transmitted via CW saturation [45]. While equation 2.3.6 no longer theoretically applies, it has been shown that CEST effects between $0ppm$ to $+4ppm$ and $k_c = 0 - 500Hz$ under pulsed irradiation are on average $97 \pm 1\%$ similar to those obtained from CW saturation [46], so the CW solutions may be used as long as this uncertainty is accounted

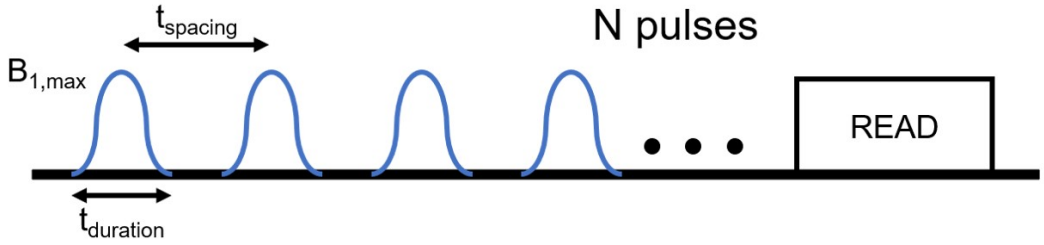

Figure 2.3.2: Pulse sequence diagram of pulsed irradiation.

for (although this may be unwise when fitting, as we have seen from the figures in section 2.2.2, a small change in the shape of the spectrum can indicate a large change in one or more of the variables).

Pulse sequences have been developed to try to overcome the limitations created by caps on maximum allowed duty cycle. Previous work [47] has shown that by using a multi-transmit RF coil, we can simulate CW saturation by alternating short square pulses on the odd and even channels of the coil. This approach is called semi-continuous wave (semi-CW) saturation, and is implemented extensively in this thesis. For an 8 channel system, we would first apply a square RF pulse on channels 1, 3, 5, and 7, followed by a square RF pulse on channels 2, 4, 6, and 8. An illustration of this pulse sequence is displayed in figure 2.3.3. As a result of this, any one channel is only on for 50% of the time, therefore satisfying the duty cycle limits, but the overall effect is a long saturation pulse with constant B_1. In practice it is important to acquire B_1 maps to make sure the saturation power of the odd and even powers is matched, as unequal saturation can lead to an unusually shaped saturation train, perturbing the magnetisation from a steady-state and adversely affecting the shape of the z-spectrum. A simulation of this effect is shown in Figure 2.3.4.

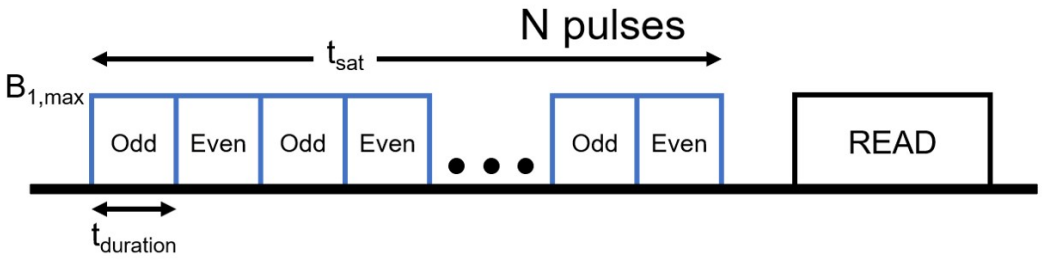

Figure 2.3.3: Pulse sequence diagram of semi-CW saturation.

2.3.2 Readout techniques

The key feature when acquiring the z-spectrum signal is that readout techniques must be relatively fast, so that the signal does not decay before being read, while being robust. There are a number of options to choose from, depending on the experiment in question. Generally speaking, EPI is the most appropriate readout method to use in MT and CEST experiments, as only one RF pulse is used and therefore the magnetisation is perturbed to a lesser degree than with other readout sequences. However, other readout techniques have also been used for improved image quality. Turbo spin echo has been used previously [48], which is fast and robust at lower fields, but is severely affected by B_1 inhomogeneities and rapid T_2 decay at higher fields. For 3D imaging, a technique called GRASE (GRadient And Spin Echo) has been proposed [49], which implements TSE in the phase direction, and EPI in the slice direction. These images are reliable and have high SNR, but are also strongly affected by B_1 inhomogeneity due to the additive effects of consecutive refocusing pulses. TFE approaches have also been used due to the increased robustness of gradient echo schemes at higher field strengths, and in particular a single-shot acquisition acquiring k-space from the centre outwards has been shown to yield high SNR in a short acquisition time at ultra-high field [50].

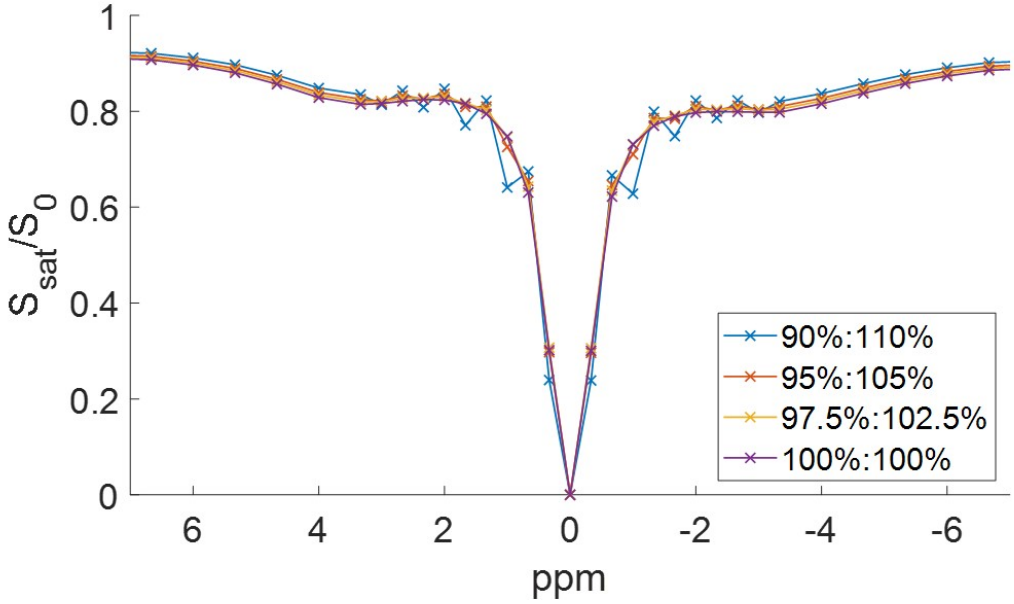

Figure 2.3.4: Simulated effects of uneven RF through odd and even channels on a sample with 10% MT, 2% amides, and 2% NOE. Ratios displayed are the ratio of the saturation power through the odd channels to the saturation power through the even channels, where 100% is equivalent to a pulse of 1μT.

2.4 Qualitative z-spectrum metrics

Due to the complexity of solving the Bloch-McConnell equations to determine the parameters contributing to z-spectrum effects, it has become commonplace to instead define metrics which indicate the presence of exchanging pools. These metrics all make certain assumptions about the nature of the system, however can still be useful depending on the nature of the experiment. These metrics range from the overly simplistic to the reasonably reliable, depending on the nature of prior assumptions made about the system.

2.4.1 Magnetisation transfer ratio

The first of these metrics to be used was the magnetisation transfer ratio (MTR), first described in the original paper where MT was introduced [4]. This technique relies on only one acquisition off-resonance, and one where no saturating pre-pulse is applied, and simply takes a normalised ratio of each of the images. We can then define the MTR in a given voxel as

$$MTR = \frac{S_0 - S_{MT}}{S_0} \tag{2.4.1}$$

where $S_{MT,0}$ is the signal in the voxel with or without the MT pre-pulse. This method is analogous to only looking at one point in the z-spectrum. Conventionally this off-resonance frequency is chosen to be +1kHz [51, 52] (roughly +16ppm at 1.5T, which is far enough off-resonance to avoid CEST effects), however this can and should be modified by the user depending on the experiment. For example, the first MTR images were acquired at -5kHz using a B_0 of 4.7T, reproduced below in Figure 2.4.1. Here we can clearly see the MT effect present in the inner medulla of the rabbit kidney.

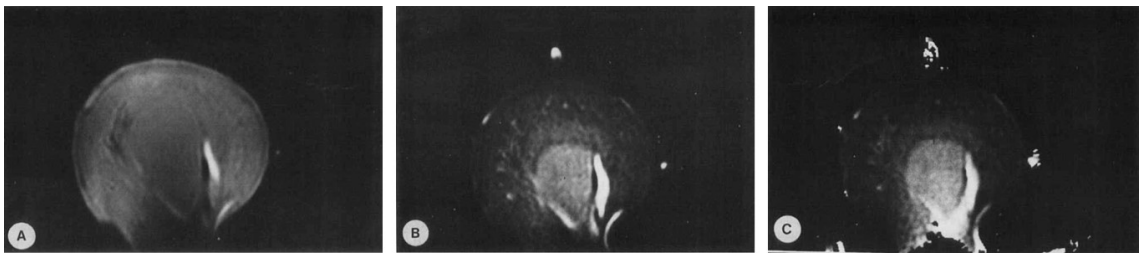

Figure 2.4.1: First MTR images, reproduced from [4], showing a) image acquired without MT pre-pulse, b) image acquired with MT pre-pulse, and c) ratio of the two images, of *ex vivo* rabbit kidney.

The main issue with acquiring an MTR image is that any MTR image collected is purely qualitative and should primarily be used for diagnostic purposes. This is because we only acquire one off-resonance image, the frequency, saturation time, saturation power, and field strength of which are all defined by the user, and altering

these will change the value of the MTR. It could be argued that MTR can be used as a quantitative measure over the course of one experiment where these parameters are all fixed, however we have recently shown that even directly consecutive repeat measurements of MTR in the abdomen can result in wildly different output images, due to the effects on B_0 and B_1 inhomogeneity arising from respiration and blood pulsatility [53].

2.4.2 MTR asymmetry

While MTR can be sufficient to produce MT-weighted images, it cannot be used to assess CEST effects. Instead, a method of quantifying CEST peaks was proposed named magnetisation transfer ratio asymmetry (MTR_{asym}) [9], where a point in the z-spectrum is compared directly to its opposing point mirrored around the water resonance. This can be expressed as

$$MTR_{asym} = \frac{S_{ref} - S_{lab}}{S_0} \tag{2.4.2}$$

where S_{lab} is the label frequency, i.e. the point in the z-spectrum at the peak of the CEST effect we want to measure, and S_{ref} is the reference frequency, i.e. the point at the opposite side of the z-spectrum about 0ppm. For example, for amides resonating at +3.5ppm, S_{lab} is the value of the z-spectrum at +3.5ppm, and S_{ref} is the value of the z-spectrum at -3.5ppm.

There are however several issues with the MTR_{asym} metric which prevent it from being a reliable measure of CEST effects, beyond the experimental factors which affect MTR. Most importantly, MTR_{asym} assumes that there are no effects in the negative side of the z-spectrum other than MT. However, we know that at higher field strengths NOE signals begin to become apparent, which alters the signal at the reference frequency. This is especially detrimental when using MTR_{asym} to measure amides, as the most prolific NOE effect is located directly opposite the resonance frequency of amide

protons. In addition to this, MTR_{asym} assumes that the only CEST effect present at the label frequency is the one being measured. Coalescing CEST peaks can affect the signal at the label frequency, causing an increase in this signal and therefore an artificial inflation in the MTR_{asym} measure. Finally, the MTR_{asym} metric assumes that the MT lineshape is symmetrical around the water resonance. However, it has been shown that the MTR lineshape is not symmetrical around 0ppm, and peaks at around -2.34ppm, which may be tissue dependent [54, 55]. Despite these obvious shortcomings, MTR_{asym} remains the most commonly used metric to measure CEST effects (as seen in such examples as [56, 57, 58]) due to its simplicity.

2.4.3 Three-offset method

To address some of the issues with using the MTR_{asym} metric to quantify CEST effects, the three offset method was developed [59]. Here, two points either side of the peak of interest are measured and averaged, and the third point is measured at the peak of interest and subtracted from the averaged point. For example, the amide signal could be measured using reference points at +3.0ppm and +4.0ppm. We could then define the resulting signal (Z_{3OM}) as

$$Z_{3OM} = (\frac{S_{3.0ppm} - S_{4.0ppm}}{2} - S_{3.5ppm})/S_0 \tag{2.4.3}$$

We can see an illustration of this in Figure 2.4.2, which shows the three-offset method applied to measurements of both the amide signal and the NOE signal.

While this metric overcomes the issues arising from both the inherent asymmetry of the MT lineshape about 0ppm and the fact that there are often effects on both sides of the z-spectrum, it does not address the fact that there may be coalescing peaks at the point of interest. It also gives rise to additional problems, such as the assumption that the underlying spectrum is linear, which it rarely is, and that there may be CEST effects at either of the new reference frequencies, adversely affecting the measurement.

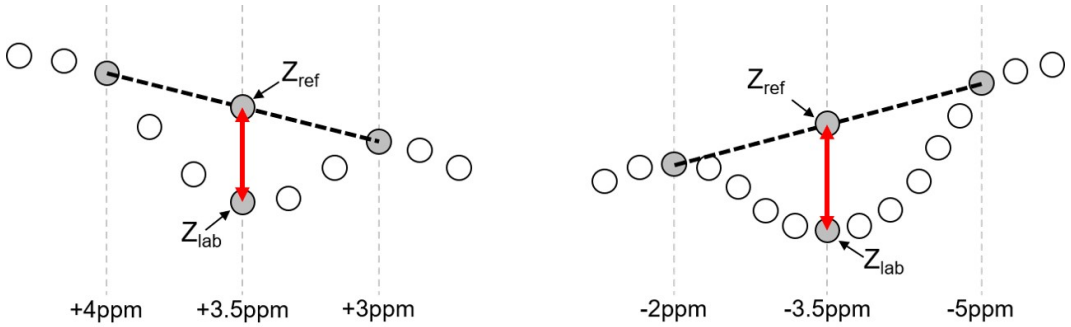

Figure 2.4.2: Three-offset method applied to the APT signal at +3.5ppm and the NOE signal at -3.5ppm.

2.4.4 Lorentzian fitting

To address some of the issues with the previously described metrics, a method of quantifying the effects in the z-spectrum using Lorentzian line-fitting was introduced [35]. First demonstrated using a three pool model, this method fits Lorentzian line-shapes with variable height and width to the spectrum, summed inversely as described in section 2.3.1. The resulting height and width of each Lorentzian is indicative of the properties of each pool. Typically the height of the Lorentzian is taken to be a measure of the effect in question. This model can be extended for as many pools of interest as desired, and has recently been seen in a six pool model used to investigate glioma [60]. An illustration of Lorentzian fitting is presented in Figure 2.4.3.

While this metric solves many of the issues associated with MTR_{asym} and the three-offset method, it includes a few key assumptions. Firstly it assumes that all peaks are known and fitted for, which may lead to artificial Lorentzian broadening if this is not the case. Also, while the MT lineshape can be modelled with a Gaussian or super-Lorentzian using this method, the assumption that any of these are correct may not be accurate.

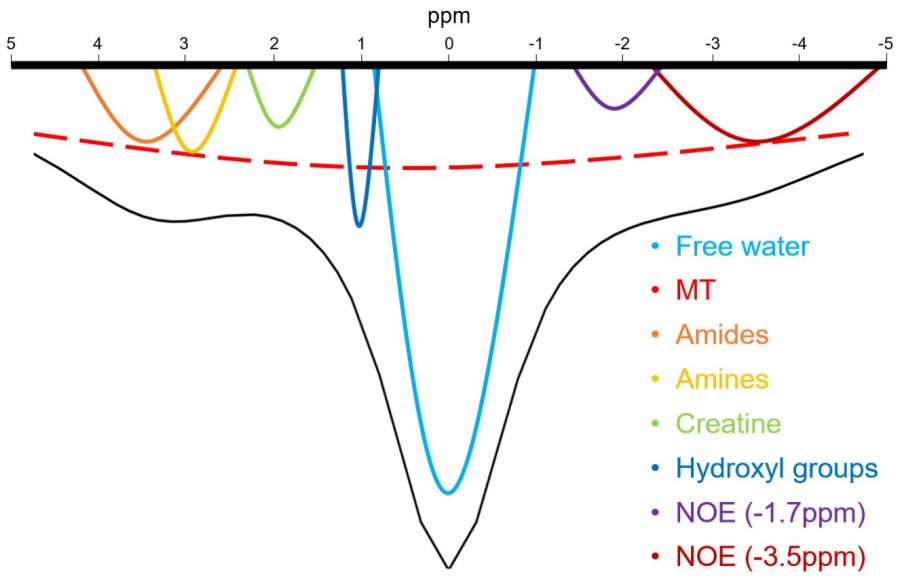

Figure 2.4.3: Illustration of underlying Lorentzian lineshapes which can be fitted to the acquired z-spectrum. 8 pools are displayed in this example for illustrative purposes.

2.4.5 Apparent exchange-dependent relaxation, AREX

As an alternative to potentially computationally heavy Lorentzian fitting, a simpler metric termed apparent exchange-dependent relaxation (AREX) has been proposed [43]. This compares the inverse of the signals at the label and reference frequency and normalises by the T_1 of free water. The AREX metric is defined as

$$AREX = (\frac{1}{Z_{lab}} - \frac{1}{Z_{ref}})/T_{1,f}. \tag{2.4.4}$$

Here the term Z_{lab} is again the point at the peak of interest, but the Z_{ref} term is less clearly defined. The first AREX studies used the same Z_{ref} value as defined by the three-offset method defined above [42], however later studies first performed Lorentzian fitting, obtaining the Z_{ref} term by recreating the spectrum through sum-

mation of the fitted Lorentzians while omitting the Lorentzian assigned to the peak of interest [43]. By taking the inverse difference, the metric is free of $T_{2,f}$ contributions, and by normalising using the T_1 of free water, also free of $T_{1,f}$ contributions. AREX is therefore free of adverse effects arising from the coalescence of the peak of interest with free water. The AREX metric breaks down around the water frequency however, as the $\frac{1}{Z_{lab}}$ and $\frac{1}{Z_{ref}}$ terms approach infinity, and so is less suitable for the measurement of CEST and NOE pools close to water, such as the CEST signal from hydroxyl groups. The assumption that all peaks are known and accounted for remains, leading to the possibility that hidden coalescing peaks may affect the AREX metric. AREX is a widely used method of quantifying CEST effects in recent years, being used to explore glioma [61], proteins [62], and the exploration of unknown peaks [63].

2.5 Exchange rate quantification

While some of the measures described in section 2.4 can be suitable for measuring effects in the z-spectrum, they are all metrics and do not truly explore full quantification of the z-spectrum. It is impossible to determine the pool size or exchange rate from these metrics alone. There have however been several suggested methods which could be capable of doing this given that certain assumptions hold true. Many of these are based on simulation of the Bloch-McConnell equations, and fitting experimental data to resulting z-spectra using a least squares methodology [64], however as discussed it is both mathematically difficult and computationally expensive to find accurate solutions based on standard model fitting alone.

2.5.1 QUESP and QUEST

First detailed in 2006 [65] and amended in 2018 [66], quantifying exchange using saturation time (QUEST) and quantifying exchange using saturation power (QUESP) are similar methods capable of quantifying the exchange rates and pool sizes of exchang-

ing pools in the z-spectrum. These methods measure several MTR_{asym} values (later amended to AREX) using varying saturation times or powers respectively. Assuming a Lorentzian lineshape for the pool of interest and that the system is in the steady-state, we can express the AREX metric as

$$AREX = M_{0,x}.k_x.\frac{\omega_1^2}{\omega_1^2 + k_x^2} \tag{2.5.1}$$

where the subscript x here denotes the exchanging pool of interest. By varying the saturation power, the ω_1 term is affected. As this term is dependent on saturation power, we can vary this and therefore determine k_x and subsequently $M_{0,x}$ using equation 2.5.1. This is the QUESP method, and holds when the system is in the steady-state and when spillover from other pools is assumed to be minimal. For this to occur, the effect of interest must be as pronounced as possible, which occurs when $B_1 = k_x/\gamma$. As k_x is initially unknown, some guesswork must be applied here, and incorrect guesses can result in completely incorrect fitted exchange rate values. It is also worth noting that because of this, different pools in a sample tissue may require separate experiments to accurately quantify, despite their effects being visible in the z-spectrum.

QUEST fitting holds further issues, as the equation used for fitting cannot separate the pool size and exchange rate. QUEST can therefore only be considered a fully quantitative method if the concentration of the pool of interest is known and can be used as an input.

2.5.2 Look-up table

An alternative proposed method of quantifying the z-spectrum is the look-up table (LUT) [67], which is capable of fitting multiple exchanging pools simultaneously. This method uses the full form of the Bloch-McConnell equations as described in equation 2.2.7 to simulate a dictionary of sample spectra based on feasible values. The study

in question fitted human brain tissue *in vivo* to a dictionary of spectra created using a four pool model including free water, MT, amides and NOE. Eight values of pool size were used for each exchanging pool, and 5 $T_{1,f}$ values were included. Six possible values for B_1 scaling were also included, to account for field inhomogeneities using acquisition. Interestingly the exchange rates and apparent T_2s of the exchanging pools had only one simulated value, presumably as including a range of these would have taken dictionary creation to an unreasonably long time (this dictionary took two weeks to fully simulate). Acquired spectra were fitted to the look-up table using a sum of least squares method, and the values from the dictionary spectrum most closely matching the data were taken.

The data from this study has been explored further in this thesis through means of interpolation of the look-up table. The aim of this was to improve the accuracy of the LUT without having to simulate a more detailed dictionary. Once the data was fitted, the dictionary spectrum and its four closest neighbours in every direction and dimension were taken. This took a smaller portion of the LUT centred around the selected dictionary spectrum, the dimensions of which were 5x5x5x5x5, each representing $M_{0,b}$, $M_{0,c}$, $_{M0,n}$, $T_{1,f}$, and B_1 scaling factor. This segment was then interpolated in all directions simultaneously using MATLAB's `interpn` function [20] to create a 65x65x65x65x65 matrix. The original data was then refit to this interpolated LUT to gain a more accurate measure of the exchanging pool sizes. A comparison of the data fitted to the pre- and post- interpolated LUT is displayed in Figure 2.5.1.

Interpolating the LUT can yield significantly more accurate results, however it does not address the fundamental issue with the LUT, namely the extraordinarily long computation time required to create the LUT. If we wanted to extend the LUT to be a truly quantitative measure, we would also have to extend the model to incorporate possible values for exchange rates and T_2s of exchanging pools, as well as considering increasing the number of fitted pools for complex tissues. The LUT is also dependent on the properties of the exchanging pools falling within the simulated values in the LUT, as it cannot fit for a property which lies outside the bounds of the dictionary.

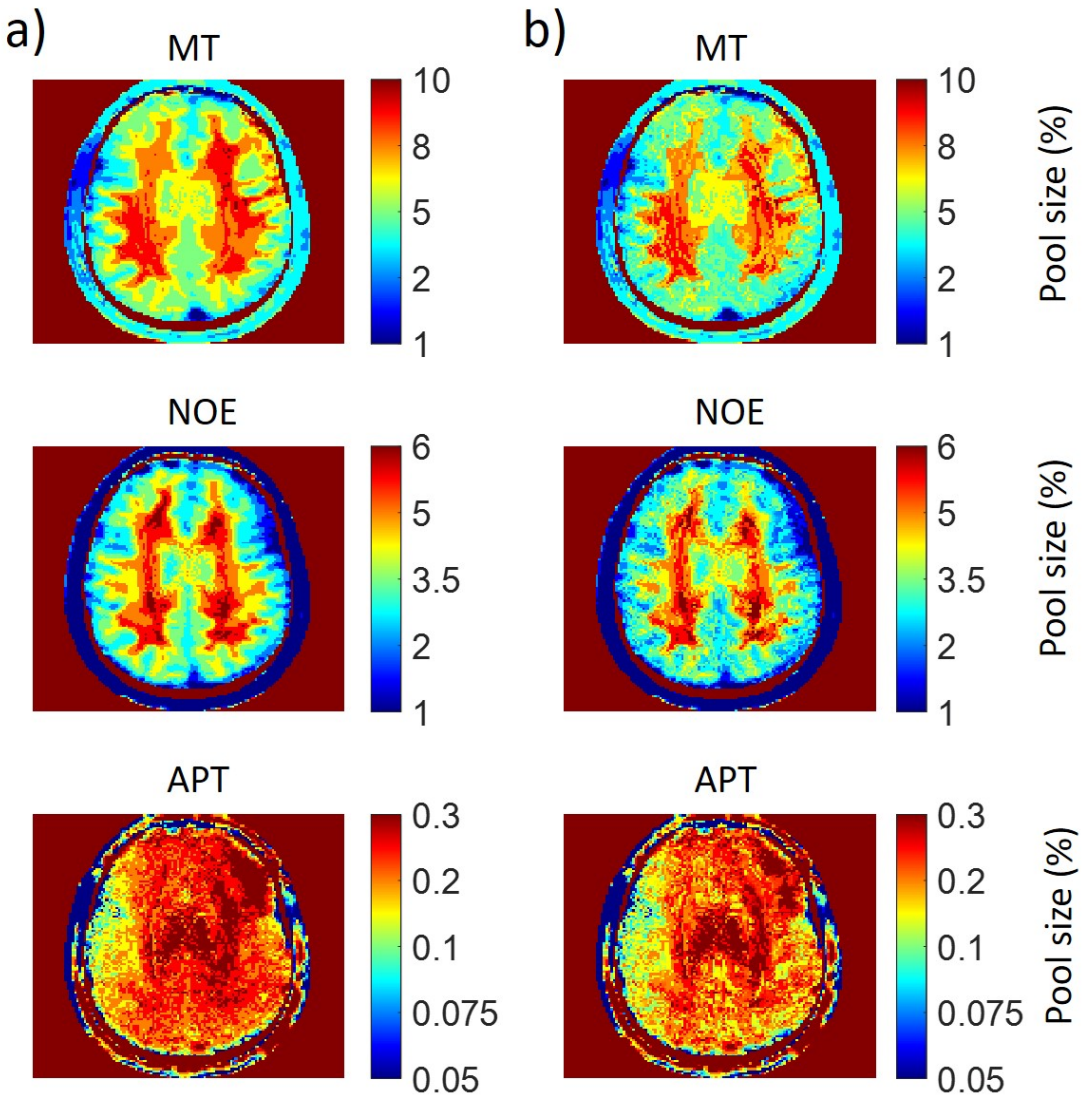

Figure 2.5.1: Maps of exchanging pool sizes, fitted with a) the LUT, and b) the interpolated LUT. Note significantly smoother contrast variation in the interpolated LUT images, indicating that interpolation has yielded meaningful results.

2.5.3 Bayesian fitting

Alternatively a Bayesian method has been suggested to quantify the parameters of exchanging pools in the z-spectrum [68]. This method begins by taking initial assumptions of all values to be fitted based on the system in question, here termed Bayesian priors, and then works towards the solution. Using the full form of the Bloch-McConnell equations as described in equation 2.2.7 as the model, the data can be described as a probability distribution which takes into account the parameters fed into the model:

$$Pr(S|\theta) = \frac{1}{\sigma\sqrt{2\pi}} e^{-\frac{[S-f(\theta)]^2}{2\sigma^2}} \tag{2.5.2}$$

where $Pr(S|\theta)$ is the probability distribution of the data given the input parameters θ, f is the model with parameters θ, S is the measured signal, $S = f(\theta) + e_1$ (here e_1 is a random noise component), and σ is the standard deviation of the white noise.

This can be inverted to give the probability of the parameters given the data, $Pr(\theta|S)$, via Bayes theorem:

$$Pr(\theta|S) \propto Pr(S|\theta).Pr(\theta) \tag{2.5.3}$$

where $Pr(\theta)$ is the previous distribution of the input parameters. By aiming to maximise this value, an iterative process can yield the parameters most likely to give rise to the data, through essentially updating our prior assumptions to take account of the given data.

While this method drastically reduces computation time compared to the LUT method (assuming the experiment in question is a new experiment and a new LUT is needed), it relies on the Bayesian priors to initialise the system. If these prior assumptions about the system are incorrect, it may bias the results towards a local minimum, and it is

possible that the correct solution may not be found. The Bayesian fitting method also once again assumes that all pools of interest are known and accounted for.

2.5.4 Deep learning

It is possible that a potential solution to some of these assumptions could be found through the use of deep learning. In theory, we could train a neural network to analyse z-spectra based on the Bloch-McConnell equations, and identify how the shape of the spectrum is affected by the parameters of exchanging pools. Once sufficiently trained, the network may be able to identify pool sizes and exchange rates of exchanging pools simply by 'looking' at the data. This could be virtually instantaneous once the network is trained.

It is possible that neural networks could go beyond this, and use z-spectra for direct diagnostic purposes. Instead of our output being the parameters of exchanging pools present in the z-spectrum, we could instead train a neural network to classify z-spectra, so that the output is tissue type. In theory this could be used for tumour grading after initial identification, as the APT signal in gliomas has been shown to increase with increased grade [69]. However, this would have to be incredibly accurate to be used clinically, as the possibility of a false diagnosis has the potential to be extremely detrimental.

2.6 Summary

We can use MRI to create image contrast dependent on the presence of certain molecules containing ^1H groups. These groups produce effects which are visible in the z-spectrum, and the nature of these effects depends on the physical properties of these groups in the sample of interest. However, characterising these properties is not trivial, and so metrics are commonly employed to characterise these effects. Methods

of quantification have been proposed, but all make assumptions about the system. The next chapter will utilise the look-up table to quantify MT and NOE data in a large sample of subjects in order to assess the effects of normal ageing on myelination levels, and chapter 4 will introduce a new method of z-spectrum quantification, which makes fewer assumptions about the system than any of the methods described above.

References

[1] Jonathan Grad and Robert G. Bryant. Nuclear magnetic cross-relaxation spectroscopy. *Journal of Magnetic Resonance (1969)*, 1990. ISSN 00222364. doi: 10.1016/0022-2364(90)90361-C.

[2] Harden M. McConnell. Reaction rates by nuclear magnetic resonance. *The Journal of Chemical Physics*, 1958. ISSN 00219606. doi: 10.1063/1.1744152.

[3] Sture Forsén and Ragnar A. Huffman. Study of moderately rapid chemical exchange reactions by means of nuclear magnetic double resonance. *The Journal of Chemical Physics*, 1963. ISSN 00219606. doi: 10.1063/1.1734121.

[4] Steven D. Wolff and Robert S. Balaban. Magnetization transfer contrast (MTC) and tissue water proton relaxation in vivo. *Magnetic Resonance in Medicine*, 1989. ISSN 15222594. doi: 10.1002/mrm.1910100113.

[5] K. M. Ward, A. H. Aletras, and R. S. Balaban. A New Class of Contrast Agents for MRI Based on Proton Chemical Exchange Dependent Saturation Transfer (CEST). *Journal of Magnetic Resonance*, 2000. ISSN 10907807. doi: 10.1006/jmre.1999.1956.

[6] Wen Ling, Ravinder R. Regatte, Gil Navon, and Alexej Jerschow. Assessment of glycosaminoglycan concentration in vivo by chemical exchange-dependent saturation transfer (gagCEST). *Proceedings of the National Academy of Sciences*

of the United States of America, 2008. ISSN 00278424. doi: 10.1073/pnas.0707666105.

[7] G. D. Fullerton, I. L. Cameron, K. Hunter, and H. J. Fullerton. Proton magnetic resonance relaxation behavior of whole muscle with fatty inclusions. *Radiology*, 1985. ISSN 00338419. doi: 10.1148/radiology.155.3.4001376.

[8] Hommo T. Edzes and Edward T. Samulski. Cross relaxation and spin diffusion in the proton NMR of hydrated collagen [9], 1977. ISSN 00280836.

[9] Jinyuan Zhou, Bachchu Lal, David A. Wilson, John Laterra, and Peter C.M. Van Zijl. Amide Proton Transfer (APT) Contrast for Imaging of Brain Tumors. *Magnetic Resonance in Medicine*, 2003. ISSN 07403194. doi: 10.1002/mrm.10651.

[10] Peter C M Van Zijl, Craig K. Jones, Jimin Ren, Craig R. Malloy, and A. Dean Sherry. MRI detection of glycogen in vivo by using chemical exchange saturation transfer imaging (glycoCEST). *Proceedings of the National Academy of Sciences of the United States of America*, 2007. ISSN 00278424. doi: 10.1073/pnas.0700281104.

[11] Feliks Kogan, Mohammad Haris, Catherine Debrosse, Anup Singh, Ravi P. Nanga, Kejia Cai, Hari Hariharan, and Ravinder Reddy. In vivo chemical exchange saturation transfer imaging of creatine (CrCEST) in skeletal muscle at 3T. *Journal of Magnetic Resonance Imaging*, 2014. ISSN 15222586. doi: 10.1002/jmri.24412.

[12] Edvards Liepinsh and Gottfried Otting. Proton exchange rates from amino acid side chains - Implications for image contrast. *Magnetic Resonance in Medicine*, 1996. ISSN 07403194. doi: 10.1002/mrm.1910350106.

[13] Peter C.M. Van Zijl, Jinyuan Zhou, Noriko Mori, Jean Francois Payen, David Wilson, and Susumu Mori. Mechanism of magnetization transfer during on-resonance water saturation. A new approach to detect mobile proteins, peptides, and lipids. *Magnetic Resonance in Medicine*, 2003. ISSN 07403194. doi: 10.1002/mrm.10398.

[14] Kimberly L. Desmond, Firas Moosvi, and Greg J. Stanisz. Mapping of amide, amine, and aliphatic peaks in the CEST spectra of murine xenografts at 7 T. *Magnetic Resonance in Medicine*, 2014. ISSN 15222594. doi: 10.1002/mrm.24822.

[15] Xiao Yong Zhang, Feng Wang, Aqeela Afzal, Junzhong Xu, John C. Gore, Daniel F. Gochberg, and Zhongliang Zu. A new NOE-mediated MT signal at around -1.6 ppm for detecting ischemic stroke in rat brain. *Magnetic Resonance Imaging*, 2016. ISSN 18735894. doi: 10.1016/j.mri.2016.05.002.

[16] Simon M. Shah, Olivier E. O.E. Olivier E. Mougin, A.J. Andrew J. Carradus, Nicolas Geades, Richard Dury, William Morley, and Penny A. P.A. Gowland. The z-spectrum from human blood at 7T. *NeuroImage*, 167, 2018. ISSN 10959572. doi: 10.1016/j.neuroimage.2017.10.053.

[17] Robert W. Brown, Yu Chung N. Cheng, E. Mark Haacke, Michael R. Thompson, and Ramesh Venkatesan. *Magnetic Resonance Imaging: Physical Principles and Sequence Design: Second Edition*. 2014. ISBN 9781118633953. doi: 10.1002/9781118633953.

[18] Kenya Murase and Nobuyoshi Tanki. Numerical solutions to the time-dependent Bloch equations revisited. *Magnetic Resonance Imaging*, 2011. ISSN 0730725X. doi: 10.1016/j.mri.2010.07.003.

[19] Wolfram Research Inc. Mathematica 12.0, 2019.

[20] Version 9.6 2019 The Mathworks, Inc. MATLAB. MATLAB - MathWorks - MATLAB, 2019.

[21] Nicholas J. Higham. The scaling and squaring method for the matrix exponential revisited. *SIAM Journal on Matrix Analysis and Applications*, 2005. ISSN 08954798. doi: 10.1137/04061101X.

[22] Awad H. Al-Mohy and Nicholas J. Higham. A new scaling and squaring algorithm for the matrix exponential. *SIAM Journal on Matrix Analysis and Applications*, 2009. ISSN 08954798. doi: 10.1137/09074721X.

[23] Cleve Moler and Charles Van Loan. Nineteen Dubious Ways to Compute the Exponential of a Matrix. *SIAM Review*, 1978. ISSN 0036-1445. doi: 10.1137/1020098.

[24] I. Solomon. Relaxation processes in a system of two spins. *Physical Review*, 1955. ISSN 0031899X. doi: 10.1103/PhysRev.99.559.

[25] Kimberly L. Desmond and Greg J. Stanisz. Understanding quantitative pulsed CEST in the presence of MT. *Magnetic Resonance in Medicine*, 2012. ISSN 07403194. doi: 10.1002/mrm.23074.

[26] Peter C.M. van Zijl, Wilfred W. Lam, Jiadi Xu, Linda Knutsson, and Greg J. Stanisz. Magnetization Transfer Contrast and Chemical Exchange Saturation Transfer MRI. Features and analysis of the field-dependent saturation spectrum. *NeuroImage*, 2018. ISSN 10959572. doi: 10.1016/j.neuroimage.2017.04.045.

[27] H. S. Gutowsky and H. N. Cheng. Determination of kinetic parameters by the frequency dependence of the NMR coalescence temperature. *The Journal of Chemical Physics*, 1975. ISSN 00219606. doi: 10.1063/1.431673.

[28] Svante Arrhenius. Über die Dissociationswärme und den Einfluss der Temperatur auf den Dissociationsgrad der Elektrolyte. *Zeitschrift für Physikalische Chemie*, 1889. ISSN 0942-9352. doi: 10.1515/zpch-1889-0108.

[29] R. P. Bell and S. H. Bauer. The Proton in Chemistry. *Journal of The Electrochemical Society*, 1962. ISSN 00134651. doi: 10.1149/1.2425397.

[30] K. M. Ward and R. S. Balaban. Determination of pH using water protons and Chemical Exchange Dependent Saturation Transfer (CEST). *Magnetic Resonance in Medicine*, 2000. ISSN 07403194. doi: 10.1002/1522-2594(200011)44:5<799::AID-MRM18>3.0.CO;2-S.

[31] Johannes Windschuh, Moritz Zaiss, Jan Eric Meissner, Daniel Paech, Alexander Radbruch, Mark E. Ladd, and Peter Bachert. Correction of B1-inhomogeneities for relaxation-compensated CEST imaging at 7T. *NMR in Biomedicine*, 2015. ISSN 10991492. doi: 10.1002/nbm.3283.

[32] Jinyuan Zhou, Jean Francois Payen, David A. Wilson, Richard J. Traystman, and Peter C.M. Van Zijl. Using the amide proton signals of intracellular proteins and peptides to detect pH effects in MRI. *Nature Medicine*, 2003. ISSN 10788956. doi: 10.1038/nm907.

[33] O. E. Mougin, R. C. Coxon, A. Pitiot, and P. A. Gowland. Magnetization transfer phenomenon in the human brain at 7 T. *NeuroImage*, 2010. ISSN 10538119. doi: 10.1016/j.neuroimage.2009.08.022.

[34] Mina Kim, Joseph Gillen, Bennett A. Landman, Jinyuan Zhou, and Peter C.M. Van Zijl. Water saturation shift referencing (WASSR) for chemical exchange saturation transfer (CEST) experiments. *Magnetic Resonance in Medicine*, 2009. ISSN 15222594. doi: 10.1002/mrm.21873.

[35] Moritz Zaiß, Benjamin Schmitt, and Peter Bachert. Quantitative separation of CEST effect from magnetization transfer and spillover effects by Lorentzian-line-fit analysis of z-spectra. *Journal of Magnetic Resonance*, 2011. ISSN 10907807. doi: 10.1016/j.jmr.2011.05.001.

[36] Greg J. Stanisz, Ewa E. Odrobina, Joseph Pun, Michael Escaravage, Simon J. Graham, Michael J. Bronskill, and R. Mark Henkelman. T1, T2 relaxation and magnetization transfer in tissue at 3T. *Magnetic Resonance in Medicine*, 2005. ISSN 07403194. doi: 10.1002/mrm.20605.

[37] R. Mark Henkelman, Xuemei Huang, Qing-San -S Xiang, G. J. Stanisz, Scott D. Swanson, and Michael J. Bronskill. Quantitative interpretation of magnetization transfer. *Magnetic Resonance in Medicine*, 1993. ISSN 15222594. doi: 10.1002/mrm.1910290607.

[38] Jonathan G. Li, Simon J. Graham, and R. Mark Henkelman. A flexible magnetization transfer line shape derived from tissue experimental data. *Magnetic Resonance in Medicine*, 1997. ISSN 07403194. doi: 10.1002/mrm.1910370610.

[39] Elena Vinogradov, A. Dean Sherry, and Robert E. Lenkinski. CEST: From basic

principles to applications, challenges and opportunities. *Journal of Magnetic Resonance*, 2013. ISSN 10907807. doi: 10.1016/j.jmr.2012.11.024.

[40] P. Fajer, A. Watts, and D. Marsh. Saturation transfer, continuous wave saturation, and saturation recovery electron spin resonance studies of chain-spin labeled phosphatidylcholines in the low temperature phases of dipalmitoyl phosphatidylcholine bilayers. Effects of rotational dynamics a. *Biophysical Journal*, 1992. ISSN 00063495. doi: 10.1016/S0006-3495(92)81895-7.

[41] Oleg Trott and Arthur G. Palmer. R 1ρ relaxation outside of the fast-exchange limit, 2002. ISSN 10907807.

[42] Moritz Zaiss and Peter Bachert. Exchange-dependent relaxation in the rotating frame for slow and intermediate exchange - modeling off-resonant spin-lock and chemical exchange saturation transfer. *NMR in Biomedicine*, 2013. ISSN 09523480. doi: 10.1002/nbm.2887.

[43] Moritz Zaiss, Zhongliang Zu, Junzhong Xu, Patrick Schuenke, Daniel F. Gochberg, John C. Gore, Mark E. Ladd, and Peter Bachert. A combined analytical solution for chemical exchange saturation transfer and semi-solid magnetization transfer. *NMR in Biomedicine*, 2015. ISSN 10991492. doi: 10.1002/nbm.3237.

[44] Phillip Zhe Sun, Thomas Benner, Ashok Kumar, and A. Gregory Sorensen. Investigation of optimizing and translating pH-sensitive pulsed-chemical exchange saturation transfer (CEST) imaging to a 3T clinical scanner. *Magnetic Resonance in Medicine*, 2008. ISSN 07403194. doi: 10.1002/mrm.21714.

[45] Zhongliang Zu, Ke Li, Vaibhav A. Janve, Mark D. Does, and Daniel F. Gochberg. Optimizing pulsed-chemical exchange saturation transfer imaging sequences. *Magnetic Resonance in Medicine*, 2011. ISSN 07403194. doi: 10.1002/mrm.22884.

[46] Gang Xiao, Phillip Zhe Sun, and Renhua Wu. Fast simulation and optimization of pulse-train chemical exchange saturation transfer (CEST) imaging. *Physics in*

Medicine and Biology, 2015. ISSN 13616560. doi: 10.1088/0031-9155/60/12/4719.

[47] Hans Hoogduin, Vitaliy Khlebnikov, J Keupp, K S Milde, L Knutsson, Peter C M Van Zijl, and Peter Luijten. Semi continuous wave CEST with alternating sets of 4 transmit channels at 7T. *Magma*, 30(Suppl 1):S1 – S152, 2017.

[48] Jinyuan Zhou, Jaishri O. Blakeley, Jun Hua, Mina Kim, John Laterra, Martin G. Pomper, and Peter C.M. Van Zijl. Practical data acquisition method for human brain tumor amide proton transfer (APT) imaging. *Magnetic Resonance in Medicine*, 2008. ISSN 07403194. doi: 10.1002/mrm.21712.

[49] He Zhu, Craig K. Jones, Peter C.M. Van Zijl, Peter B. Barker, and Jinyuan Zhou. Fast 3D chemical exchange saturation transfer (CEST) imaging of the human brain. *Magnetic Resonance in Medicine*, 2010. ISSN 07403194. doi: 10.1002/mrm.22546.

[50] Vitaliy Khlebnikov, Nicolas Geades, Dennis W.J. Klomp, Hans Hoogduin, Penny Gowland, and Olivier Mougin. Comparison of pulsed three-dimensional CEST acquisition schemes at 7 tesla: steady state versus pseudosteady state. *Magnetic Resonance in Medicine*, 2017. ISSN 15222594. doi: 10.1002/mrm.26323.

[51] Paul Tofts. *Quantitative MRI of the Brain: Measuring Changes Caused by Disease*. 2005. ISBN 0470847212. doi: 10.1002/0470869526.

[52] Carlos J. Pérez-Torres, Cynthia A. Massaad, Susan G. Hilsenbeck, Faridis Serrano, and Robia G. Pautler. In vitro and in vivo magnetic resonance imaging (MRI) detection of GFP through magnetization transfer contrast (MTC). *NeuroImage*, 2010. ISSN 10538119. doi: 10.1016/j.neuroimage.2009.12.111.

[53] Andrew J. Carradus, Simon M. Shah, Olivier E. Mougin, Caroline L. Hoad, and Penny A. Gowland. Magnetisation transfer in human liver and kidney through acquisition of the z-spectrum. *Abstract presented at the Joint Annual Meeting ISMRM-ESMRMB 2018*, page Abstract no. 2551, 2018.

[54] James Pekar, Peter Jezzard, David A. Roberts, John S. Leigh, Joseph A. Frank, and Alan G. McLaughlin. Perfusion imaging with compensation for asymmetric magnetization transfer effects. *Magnetic Resonance in Medicine*, 1996. ISSN 07403194. doi: $10.1002/\mathrm{mrm}.1910350110$.

[55] Jun Hua, Craig K. Jones, Jaishri Blakeley, Seth A. Smith, Peter C.M. Van Zijl, and Jinyuan Zhou. Quantitative description of the asymmetry in magnetization transfer effects around the water resonance in the human brain. *Magnetic Resonance in Medicine*, 2007. ISSN 07403194. doi: $10.1002/\mathrm{mrm}.21387$.

[56] Dominik Kentrup, Philipp Bovenkamp, Annika Busch, Katharina Schuette-Nuetgen, Helga Pawelski, Hermann Pavenstädt, Eberhard Schlatter, Karl Heinz Herrmann, Jürgen R. Reichenbach, Bettina Löffler, Barbara Heitplatz, Veerle Van Marck, Nirbhay N. Yadav, Guanshu Liu, Peter C.M. van Zijl, Stefan Reuter, and Verena Hoerr. GlucoCEST magnetic resonance imaging in vivo may be diagnostic of acute renal allograft rejection. *Kidney International*, 2017. ISSN 15231755. doi: $10.1016/\mathrm{j.kint}.2017.04.015$.

[57] Samantha By, Robert L. Barry, Alex K. Smith, Bailey D. Lyttle, Bailey A. Box, Francesca R. Bagnato, Siddharama Pawate, and Seth A. Smith. Amide proton transfer CEST of the cervical spinal cord in multiple sclerosis patients at 3T. *Magnetic Resonance in Medicine*, 2018. ISSN 15222594. doi: $10.1002/\mathrm{mrm}.26736$.

[58] Dong Hoon Lee, Do Wan Lee, Jae Im Kwon, Chul Woong Woo, Sang Tae Kim, Jin Seong Lee, Choong Gon Choi, Kyung Won Kim, Jeong Kon Kim, and Dong Cheol Woo. In Vivo Mapping and Quantification of Creatine Using Chemical Exchange Saturation Transfer Imaging in Rat Models of Epileptic Seizure. *Molecular Imaging and Biology*, 2019. ISSN 18602002. doi: $10.1007/\mathrm{s}11307\text{-}018\text{-}1243\text{-}6$.

[59] Tao Jin, Ping Wang, Xiaopeng Zong, and Seong Gi Kim. MR imaging of the amide-proton transfer effect and the pH-insensitive nuclear overhauser effect at

9.4 T. *Magnetic Resonance in Medicine*, 2013. ISSN 07403194. doi: 10.1002/mrm.24315.

[60] Iris Yuwen Zhou, Enfeng Wang, Jerry S. Cheung, Xiaoan Zhang, Giulia Fulci, and Phillip Zhe Sun. Quantitative chemical exchange saturation transfer (CEST) MRI of glioma using Image Downsampling Expedited Adaptive Least-squares (IDEAL) fitting. *Scientific Reports*, 2017. ISSN 20452322. doi: 10.1038/s41598-017-00167-y.

[61] Moritz Zaiss, Johannes Windschuh, Steffen Goerke, Daniel Paech, Jan Eric Meissner, Sina Burth, Philipp Kickingereder, Wolfgang Wick, Martin Bendszus, Heinz Peter Schlemmer, Mark E. Ladd, Peter Bachert, and Alexander Radbruch. Downfield-NOE-suppressed amide-CEST-MRI at 7 Tesla provides a unique contrast in human glioblastoma. *Magnetic Resonance in Medicine*, 2017. ISSN 15222594. doi: 10.1002/mrm.26100.

[62] Steffen Goerke, Katharina S. Milde, Raul Bukowiecki, Patrick Kunz, Karel D. Klika, Thomas Wiglenda, Axel Mogk, Erich E. Wanker, Bernd Bukau, Mark E. Ladd, Peter Bachert, and Moritz Zaiss. Aggregation-induced changes in the chemical exchange saturation transfer (CEST) signals of proteins. *NMR in Biomedicine*, 2017. ISSN 10991492. doi: 10.1002/nbm.3665.

[63] Xiao Yong Zhang, Jingping Xie, Feng Wang, Eugene C. Lin, Junzhong Xu, Daniel F. Gochberg, John C. Gore, and Zhongliang Zu. Assignment of the molecular origins of CEST signals at 2 ppm in rat brain. *Magnetic Resonance in Medicine*, 2017. ISSN 15222594. doi: 10.1002/mrm.26802.

[64] Donald E. Woessner, Shanrong Zhang, Matthew E. Merritt, and A. Dean Sherry. Numerical solution of the Bloch equations provides insights into the optimum design of PARACEST agents for MRI. *Magnetic Resonance in Medicine*, 2005. ISSN 07403194. doi: 10.1002/mrm.20408.

[65] Michael T. McMahon, Assaf A. Gilad, Jinyuan Zhou, Phillip Z. Sun, Jeff W M Bulte, and Peter C M Van Zijl. Quantifying exchange rates in chemical exchange saturation transfer agents using the saturation time and saturation power

dependencies of the magnetization transfer effect on the magnetic resonance imaging signal (QUEST and QUESP): pH calibration for poly-L-lysine and a starburst dendrimer. *Magnetic Resonance in Medicine*, 2006. ISSN 07403194. doi: 10.1002/mrm.20818.

[66] Moritz Zaiss, Goran Angelovski, Eleni Demetriou, Michael T. McMahon, Xavier Golay, and Klaus Scheffler. QUESP and QUEST revisited – fast and accurate quantitative CEST experiments. *Magnetic Resonance in Medicine*, 2018. ISSN 15222594. doi: 10.1002/mrm.26813.

[67] Nicolas Geades, Benjamin A.E. E Hunt, Simon M. Shah, Andrew Peters, Olivier E. Mougin, and Penny A. Gowland. Quantitative analysis of the z-spectrum using a numerically simulated look-up table: Application to the healthy human brain at 7T. *Magnetic Resonance in Medicine*, 2017. ISSN 15222594. doi: 10.1002/mrm.26459.

[68] Michael A. Chappell, Manus J. Donahue, Yee Kai Tee, Alexandre A. Khrapitchev, Nicola R. Sibson, Peter Jezzard, and Stephen J. Payne. Quantitative Bayesian model-based analysis of amide proton transfer MRI. *Magnetic Resonance in Medicine*, 2013. ISSN 07403194. doi: 10.1002/mrm.24474.

[69] Osamu Togao, Takashi Yoshiura, Jochen Keupp, Akio Hiwatashi, Koji Yamashita, Kazufumi Kikuchi, Yuriko Suzuki, Satoshi O. Suzuki, Toru Iwaki, Nobuhiro Hata, Masahiro Mizoguchi, Koji Yoshimoto, Koji Sagiyama, Masaya Takahashi, and Hiroshi Honda. Amide proton transfer imaging of adult diffuse gliomas: Correlation with histopathological grades. *Neuro-Oncology*, 2014. ISSN 15228517. doi: 10.1093/neuonc/not158.

Chapter 3

Using MT to measure myelination evolution through adulthood

Myelin is an important substance found in the brain comprising of water, lipids, and proteins which envelops the axons of nerve cells, allowing for faster transmission of electrical signals [1]. Throughout life, several processes give rise to variation in the amount of myelin present in the human cortex. These can be categorised as myelination, which describes the process of myelin generation [2], demyelination, describing the loss of myelination which can be indicative of neurodegenerative diseases [3], and dysmyelination, which describes where the structure of the myelin sheath has become defective through damage [4]. The nature of 'healthy' demyelination in later life has been observed in T_1 weighted MR studies [5] but is not fully understood. Furthermore, it has been shown that the magnetisation transfer signal is an effective way of assessing myelination due to its macromolecule-rich structure [6, 7], and may provide advantages over T_1 weighted measures of myelin water, as the quantitative MT signal is not affected by cortical iron content [8]. This chapter aims to explore the evolution of myelination in the healthy ageing human brain using MT measured at 7T, to assess whether the demyelination observed in later life is linked to natural thinning of the cerebral cortex, and finally to assess whether the NOE signal provides any additional

information when used as a marker for myelination.

3.1 Myelination measurement using MR techniques

Ex vivo microscopy is the gold standard for assessing myelination, but MRI is currently the only viable way to image or measure myelin in the human brain *in vivo*. However, there are several MR techniques capable of generating signals sensitive to myelin. Previous studies have measured myelin via the T_1 weighted measurement of myelin water, the ratio of T_1 weighted and T_2 weighted images, and various MT metrics. Each of these has differing advantages and pitfalls.

3.1.1 Myelin structure and function

As alluded to previously, myelin is a white substance comprised of 40$\%$ water, between 36$\%$ to 45$\%$ lipids, and between 9$\%$ to 15$\%$ proteins [1]. Myelin surrounds the axon of the nerve cell in several segments, which is referred to as a myelin sheath. Each segment of the myelin sheath is around 500μm in length and is separated from the adjacent segment by a 1μm gap, which are termed nodes of Ranvier. An illustration of a nerve cell is displayed in Figure 3.1.1.

Myelin serves to increase the speed at which electrical impulses travel along an axon through saltatory conduction [9]. Here electrical signals can propagate from one node of Ranvier to the next without degradation of the signal, through formation of action potentials. As sodium ions reach a node, an electrical force pushes the ions inside the axon, which reach the next node and create another action potential, and the process repeats. This means that the electrical signal can effectively jump from one node of Ranvier to the next, without having to physically traverse the entire axon. A heavily

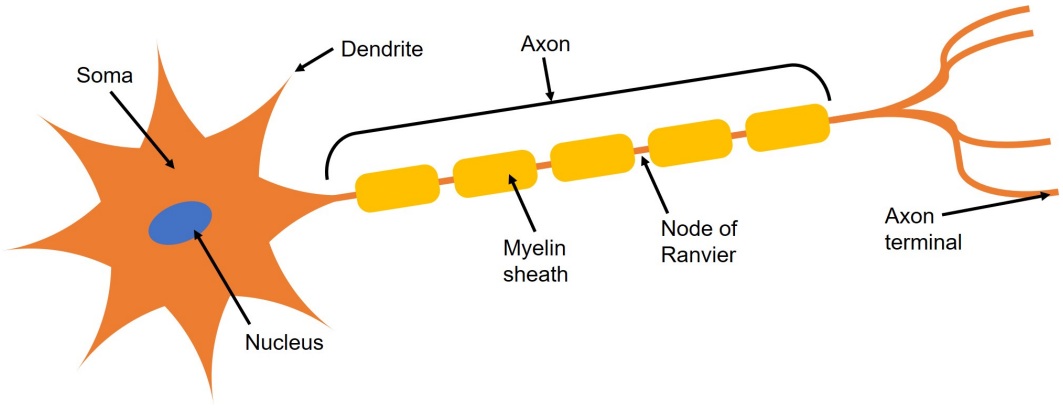

Figure 3.1.1: Illustration of a nerve cell.

myelinated axon can reach a propagation speed of 150ms^{-1}, as opposed to 0.5ms^{-1} in a completely unmyelinated axon.

3.1.2 Myelination studies employing measurements of myelin water

When considering how to image myelin water, there are three basic approaches to generate MRI contrast: proton density which is proportional to water content, and T_1 and T_2 weighted imaging which are both affected by water content, water mobility, iron content, macromolecular content and the microstructure of nearby tissues. As a large percentage of the brain is water, proton density imaging generates relatively little image contrast between myelin and other cerebral tissue.

Myelin water is restricted in its motion between myelin bilayers, which are wrapped around the axon in a 'swiss roll' configuration. These bilayers have a 3-4nm gap between them which myelin water occupies [10], and as such it has a significantly shorter T_2 (10-20ms at 1.5T) than intracellular or extracellular water (80-100ms at 1.5T) [11, 12]. By employing a multi-echo spin echo sequence, the resulting signal decay curve can be decomposed into a number of exponentials to give a histogram

of the T_2 components present [12]. The short T_2 components can be divided by the total signal in the relaxation distribution histogram to give a quantitative myelin water fraction image. This is arguably the most common method of myelin imaging [13, 14]. A similar method can be used to extract the short T_1 component from cerebral white matter, revealing a short T_1 peak of 106-225ms at 3T and 7T [15].

However, these methods do have some drawbacks. T_2 relaxation is affected by cortical iron content, [16], paramagnetic deoxyhaemoglobin [17] and tissue calcifications [18], and the multi-echo spin echo sequences required can be strongly affected by B_0 and B_1 field inhomogeneities, while T_1 is also affected by cortical iron content, as well as being sensitive to temperature [19], axonal count [20] and axon size [21].

3.1.3 Myelin measurements via T_1 / T_2 ratio

As pixel intensity is proportional to myelin content on T_1 weighted images and inversely proportional to myelin content on T_2 weighted images, the ratio of T_1 / T_2 weighted images can be considered indicative of myelin water content [22, 23] with a greater contrast than T_1 or T_2 weighted images alone.

Several recent studies, however, have questioned the reliability of using the ratio of T_1 / T_2 weighted images as a proxy for myelin content. One study [24] observed that the T_1 / T_2 weighted images had a stronger correlation with multi-echo T_2 weighted images (thought to be more representative of axon length and diameter than myelin content [25]) than their myelin water fraction images in four of their selected white matter ROIs, and speculate that a ratio image may reflect packing density of the axons rather than myelin content, based on the ROIs which had a higher signal intensity, and could also be affected by inflammation. Another study did not find any significant correlations between the ratio images and myelin water fraction maps in white matter and concluded that the contrast generated should only be taken to be a generalised measure of tissue microstructure [26].

3.1.4 MT as a marker for myelination

The proteins and lipids which compose the dry matter of myelin are macromolecules which are sensitive to the MT effect. Exchange between free water and these bound protons (and bound myelin water) produces an MT signal indicative of myelin content [27]. MTR imaging has been used frequently due to its speed and simplicity above other MT measures [28, 29, 30], and has been shown to correlate with myelin content. However, as discussed in Chapter 2, MTR is an imperfect measure of the MT signal due to its dependency on a great many other variables [31]. Of particular interest in myelin imaging is the dependency of MTR on the T_1 of the sample. As T_1 shortens with increased myelin content [32], the MTR signal which increases with myelin content is reduced due to the shorter T_1 of the sample, and furthermore this means that MTR suffers from the same drawbacks as myelin water imaging in that it is sensitive to cortical iron content and axon count.

The answer to this issue is to use a measure of the MT pool size which is not affected by the T_1 and T_2 of the surrounding free water (or indeed any underlying NOE effects) in the sample. This has been explored in several studies, in both non-human and post-mortem human subjects using a two-pool model and least-squares fitting [33, 34, 35], however is not commonly used, presumably due to the increased complexity of quantitative MT measurements *in vivo* compared to MTR imaging.

3.1.5 Myelination as measured in healthy ageing

Despite advances in imaging myelin *in vivo*, the research into age related variations in myelination levels is relatively sparse. In the early 20^{th} century, studies in post-mortem subjects revealed age related differences in cortical myelination [36], albeit on a small number of subjects. This was confirmed elsewhere in studies which also provided insights into related topology [37, 2, 38, 39]. The first human *in vivo* study in MRI which was indicative of age-related trends in myelination was the work by

Cho et al. in 1997, [5]. This study did not set out to measure myelin directly, and focused on identifying age-related changes in T_1 across the brain. The authors observed a quadratic trend with age, with the shortest T_1 values occurring around age 60, and suggested that this change may be as a result of changing myelination, but acknowledging that it could also be indicative of other factors such as membrane lipid content, cortical volume, and cortical iron content.

A more recent study advancing on this work showed that the T_1 in white matter fascicles had a parabolic trend with age, and that the T_1 measurements correlated with macromolecule tissue volume [40]. The work of Bartzokis et al. [41] has also shown age-related changes in both T_2 and diffusion in white matter, reported to follow a nonlinear "quadratic-like" trend. Other studies have reported similar findings, with one study fitting a "U-shaped smoothed spline" to the T_1 / T_2 ratio in selected cortical ROIs with age [42] and another reporting linear correlations of T_1 and T_2^* with age, but not exploring the possibility of non-linear trends [43].

Based on this, the aim of this chapter was to use the quantitative measure of MT pool size as a marker for myelination, and acquire data from subjects at a range of ages to observe trends in myelination with ageing in both grey matter and white matter ROIs. The NOE signal was also tested as a potential marker for myelination, as previous work has shown that the MT pool size and the NOE pool size are coupled in the human brain [44]. The cortical thickness of each subject was also measured in order to investigate whether the widely observed trend of cortical decline with age [45, 46, 47, 48, 49] drives the decline in myelination in later life as observed by some of the previous work in the field.

3.2 Data collection

Ethical approval for the study was granted by the University of Nottingham Medical School Research Ethics Committee. Recruitment consisted of an online screening

form to assess health and lifestyle, and subjects were excluded from the study if they had present mental illness or diagnosis of mental illness within five years, any history of neurological disorder, or family history of highly heritable mental illness (such as schizophrenia or Huntington's Chorea). The original intention was to recruit individuals with no history of mental illness, however it quickly became clear that this was not feasible due to the high proportion of individuals who have, at some point, been diagnosed with a mental illness. Participants were also excluded if they were taking any current prescription medication that crosses the blood-brain barrier, had taken any non-prescription medication within the last year (including 'legal highs'), had consumed alcohol on the scanning day or reported excessive consumption 24 hours before scanning day, and if there were any MRI or MEG contraindications. The screening form also included the Edinburgh Handedness Inventory [50] to assess left or right hand dominance. A total of 81 participants were initially recruited, and of these 58 (aged 19 to 62 years old; 27 male; 52 right-handed) were suitable for use in the study. The data used in this study forms part of a larger dataset which was initially collected for a previously published study which compares magnetoencephalography and 7T MRI [51].

3.2.1 Acquisition methods

Subjects were scanned using a Philips 7T Achieva system using a whole-head volume transmit coil and a 32-channel receive coil. A high resolution anatomical image was acquired using the Phase Sensitive Inversion Recovery sequence [52], with field of view = 240 x 216 x 160 mm^3, 0.8mm isotropic voxels, TI1/TI2 = 780ms/1600ms, which was collected in order to be able to accurately define grey matter and white matter regions.

Z-spectra were then acquired using the MT-TFE sequence [53], which employs pulsed saturation and a 3D TFE readout. The saturation train consisted of 20 Gaussian windowed sinc pulses with a bandwidth of 200Hz, each 30ms long with a shot to shot interval of 60ms to satisfy the condition of a maximum 50$\%$ duty cycle built into

the scanning software. Off-resonance saturation was applied at 17 frequency offsets in turn at 0ppm, ±1.0ppm, -2.3ppm, +2.5ppm, ±3ppm, ±3.5ppm, ±4.0ppm, +4.5ppm, -4.7ppm, ±6.7ppm, ±16.7ppm and +167ppm, with the final far off-resonance acquisition being used to normalise the z-spectra. This was repeated for three nominal $B_{1,rms}$ values of 0.33μT, 0.65μT, and 1.09μT to create three z-spectra, in order to provide additional sensitivity to effects which may be more prevalent at higher or lower saturation powers [54]. For the readout portion of the sequence, a volume acquisition was used, with a readout train of 410 gradient echoes, TE/TR/FA = 2.7 ms/5.8 ms/8°, field of view = 192 x 192 x 60 mm^3, 1.5mm isotropic image resolution, low-high k-space acquisition, and a SENSE factor (RL) of 2. Each z-spectrum was acquired in 8 minutes, resulting in a 24 minute total acquisition time for the three spectra.

A B_0 field map was also acquired for z-spectrum correction, along with a B_1 field map and a T_1 map, resulting in a total scan time of approximately 38 minutes for each participant.

3.2.2 Post-processing and MT quantification

The three sets of z-spectral images were motion corrected using FSL's [55] `mcFLIRT` function, and registered to a high contrast to noise ratio image created by averaging all the z-spectral images acquired at the highest B_1 saturation value. Each pixel in the coupled z-spectral images was then fitted simultaneously to a look-up table of z-spectra simulated using a four-pool model, by calculating the total sum-of-squares error between the three acquired spectra and the three spectra simulated for the same ratio of actual saturation powers and same actual readout pulse amplitudes, as described in Geades et al. [54]. A table of parameters used to create the look-up table is presented in Table 5.2.1. As a result of this fitting, MT and NOE pool size maps were created, which were free from contamination from each other, CEST effects, or T_1.

The PSIR images were used to create a grey matter mask and a white matter mask

Pool	Pool size, M_0 (%)	Exchange rate with free water (Hz)	T_2 (ms)	T_1s	Chemical shift (ppm)
Free water	-	-	40	Five values (1, 1.2, 1.6, 2, and 3)	0
Bound pool	Eight values (0.1, 1, 2, 5, 8, 10, 12, and 15)	50	0.009	1	-2.4
NOE pool	Eight values (0.1, 1, 2, 5, 8, 10, 12, and 15)	10	0.3	1	-3.5
Amide pool	Eight values (0.1, 1, 2, 5, 8, 10, 12, and 15)	200	10	1	+3.5

Table 3.2.1: Parameters of each pool in simulated look-up table. Saturation and imaging pulses were also scaled in the look-up table to simulate B_1 inhomogeneity, by 30%, 60%, 80%, 100%, 120%, and 150%. MT is modelled using a super-Lorentzian lineshape.

using the boundary detection tool in FreeSurfer v5.3.0 [56, 57]. If a voxel lay on the boundary between the grey and white matter, it was excluded, ensuring that there was no overlap between the two masks. These were then thresholded at a high probability value, resulting in a highly conservative grey matter mask that minimises any partial volume effects which might arise due to the lower resolution of the z-spectral images (and therefore also the MT and NOE maps).

The MT maps were registered to the PSIR images using FSL `FLIRT` and masked with the conservative GM or WM mask. The grey matter masked MT and NOE maps were then registered to the automated anatomical labelling (AAL) atlas [58], and the white matter masked maps were registered to the underlying sub-cortical regions of each ROI of the AAL atlas. A mean MT and NOE measure was calculated for each region, for each participant, creating 78 grey matter values and 78 white matter values of MT

and NOE per person for each person. 14 regions of the brain (primarily located at the base of the brain) were excluded due to limited field of view or poor B1 shimming in these areas, displayed in Figure 3.2.1.

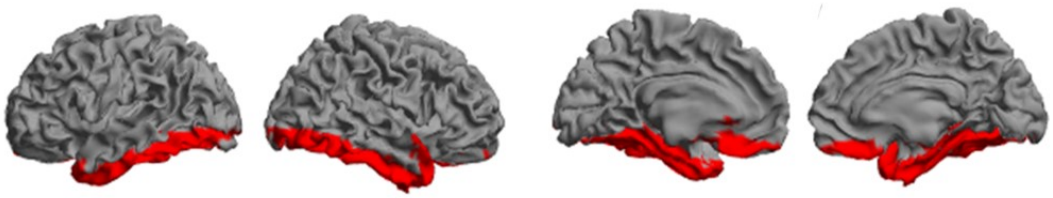

Figure 3.2.1: Regions excluded from analysis (regions 1, 2, 24, 28, 32, 34, 35, 40, 63, 67, 71, 72, 73, 74 of the cortical AAL atlas) highlighted in red.

Finally the high resolution PSIR images were registered to the AAL atlas, and the mean cortical thickness was calculated for each region within the AAL atlas for each participant using FreeSurfer.

3.3 MT variation with age

Variation of the MT signal with age was analysed across the cortex using both a linear and a quadratic model in grey and white matter separately, firstly as an average across all of the 64 used ROIs, then in four defined ROIs corresponding to the four lobes of the brain, and finally individually for each ROI of the AAL atlas. A p-value for both the linear and quadratic model was calculated, and an F-test was performed to determine whether the quadratic fit described the data significantly better than the linear fit, by comparing the R^2 of each fit considering the additional degree of freedom gained with a quadratic model to find the F statistic. We can express this using the equation

$$F = \frac{dof_Q(R_Q^2 - R_L^2)}{1 - R_Q^2} \tag{3.3.1}$$

where dof_Q is the number of degrees of freedom in the quadratic fit, and $R^2_{Q,L}$ are the R^2 values for the quadratic and linear models respectively. The F statistic is then compared to an F distribution table [59]. The relevant value is located in the table under a numerator of 2 and a denominator of dof_Q. In this chapter an $\alpha = 0.05$ cutoff was used for determining significance.

3.3.1 Variation in trends across cortex

All grey matter and all white matter ROIs were averaged to create an average value of MT in grey matter and white matter for each subject. These proved to both have a significant quadratic trend with age, as shown in Figure 3.3.1.

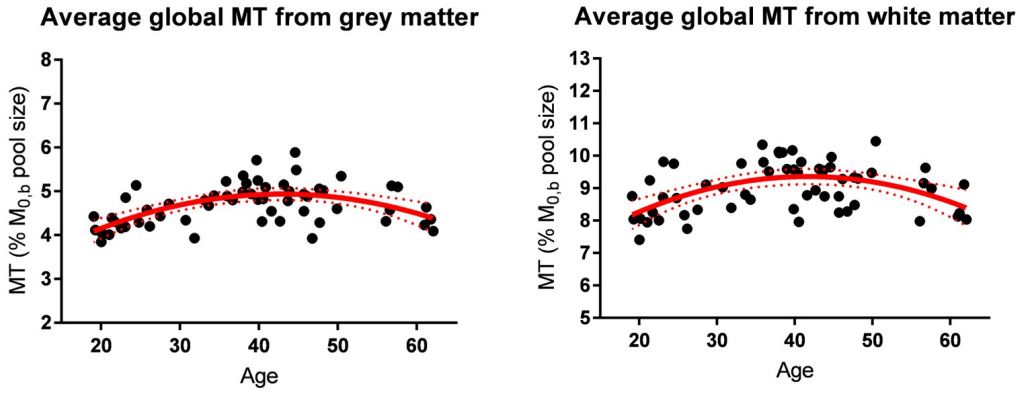

Figure 3.3.1: Quadratic variation of average grey matter and white matter MT with age, with 95% confidence intervals displayed as dotted lines.

The AAL regions lying solely in each of the frontal, parietal, occipital and temporal lobes were then averaged for each subject in both the grey and white matter. The quadratic trend with age is displayed for each of these in Figure 3.3.2. All of these trends were significant barring the white matter in the temporal lobe.

The statistics associated with these trends, including the results of the F-tests, are presented in Table 5.3.1. All significant quadratic trends were also significantly better

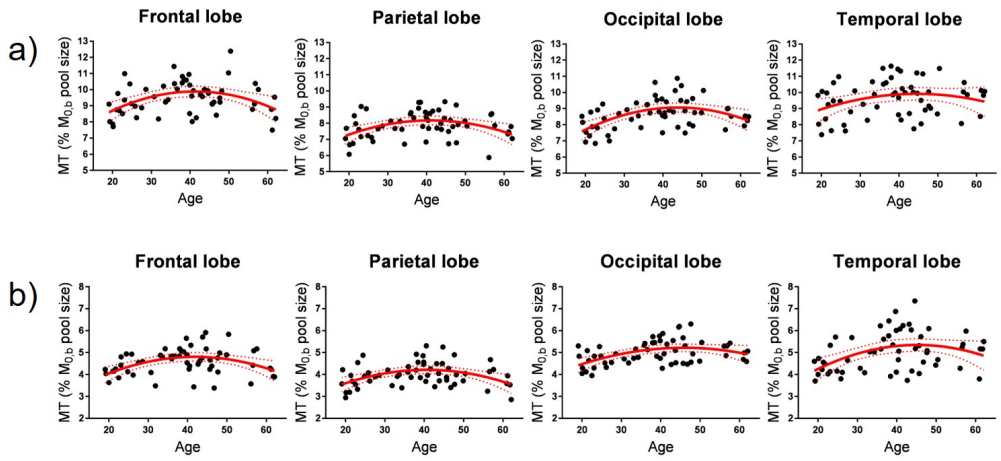

Figure 3.3.2: Quadratic variation of a) grey matter, and b) white matter MT with age in each of the four lobes of the brain, with 95% confidence intervals displayed as dotted lines.

than the linear model.

A quadratic fit was then applied to each of the 64 grey matter and 64 white matter AAL regions used in this study. Figure 3.3.3 shows the quadratic coefficient in each AAL region, which is indicative of the rate of myelination and subsequent demyelination (i.e. the 'steepness' of the quadratic curve).

The white matter and grey matter regions were then compared by pairing up each grey matter AAL region with its corresponding white matter AAL region. The MT values for each of these regions were averaged across all subjects to create an average MT value for each AAL region. A linear regression was performed between the grey matter MT values and corresponding white matter MT values to explore the regional relationship between grey and white matter myelination. The results of this analysis are displayed in Figure 3.3.4. The MT signal in each grey matter AAL region is strongly correlated with MT in each corresponding underlying white matter AAL region (R^2=0.384, p<.0001).

		Quadratic coefficient (MT%^{2} / year) $\pm$ 95% confidence intervals	Age of peak MT (years)	p-value of quadratic trend vs. null hypothesis	p-value from F-test on quadratic model compared to linear model
Grey matter	Global	-0.0014 $\pm$ 0.0003	42.9	0.00002 *	0.000005 *
	Frontal	-0.0016 $\pm$ 0.0004	41.9	0.0008 *	0.0005 *
	Parietal	-0.0014 $\pm$ 0.0004	40.6	0.0009 *	0.0007 *
	Occipital	-0.0011 $\pm$ 0.0004	45.8	0.0074 *	0.0023 *
	Temporal	-0.0017 $\pm$ 0.0007	45.2	0.0115 *	0.0044 *
White matter	Global	-0.0023 $\pm$ 0.0005	41.7	0.0001 *	0.000001 *
	Frontal	-0.0026 $\pm$ 0.0008	41.3	0.0011 *	0.0008 *
	Parietal	-0.0020 $\pm$ 0.0006	41.1	0.0025 *	0.0019 *
	Occipital	-0.0024 $\pm$ 0.0007	43.8	0.0005 *	0.0002 *
	Temporal	-0.0015 $\pm$ 0.0009	44.6	0.0847	0.0546

Table 3.3.1: Coefficients and significance of the quadratic model applied to changes in measured MT with ageing in each cerebral ROI. Significant trend (p<0.05) denoted by '*'.

3.3.2 Local variation of MT in cortical lobes

The nature of how the variation of MT across the brain changes with age was then assessed. Each AAL region is comprised of a number of voxels, each with an MT measurement associated with them, and so a standard deviation value can be calculated from the spread of measurements within each of the four defined ROIs, and across the whole of the grey or white matter. These standard deviation values were plotted against age and both a linear and a quadratic fit was applied. The results of these fits are displayed in Figure 3.3.5. The regional standard deviation of the MT increased linearly with age in grey matter, with p<0.001 in all ROIs except for the temporal lobes (p=0.006). There was no change in the standard deviation (p>0.05) of MT in the white matter ROIs with respect to age.

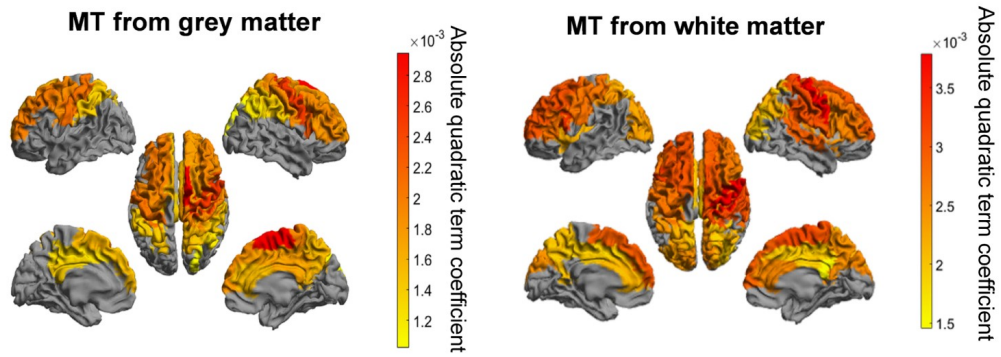

Figure 3.3.3: Quadratic coefficient of MT with age in each AAL region, showing how drastic the changes in myelination are across the brain. The white matter regions are mapped onto their corresponding overlying cortical regions for ease of viewing. Regions without a significantly non-zero quadratic trend are left grey.

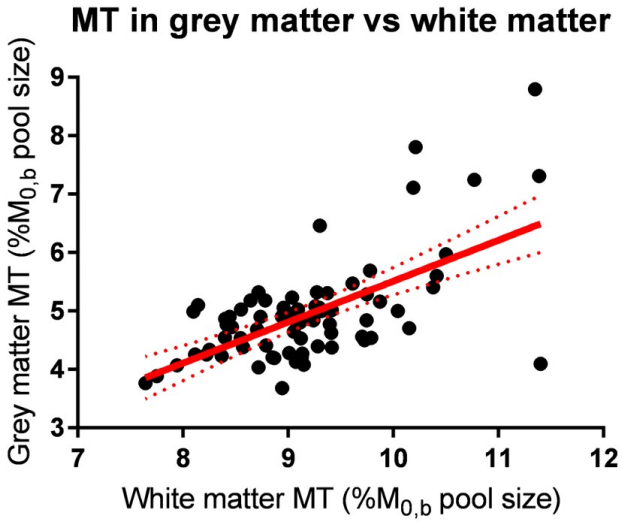

Figure 3.3.4: Correlation between grey matter and white matter MT averaged across individuals for each AAL region.

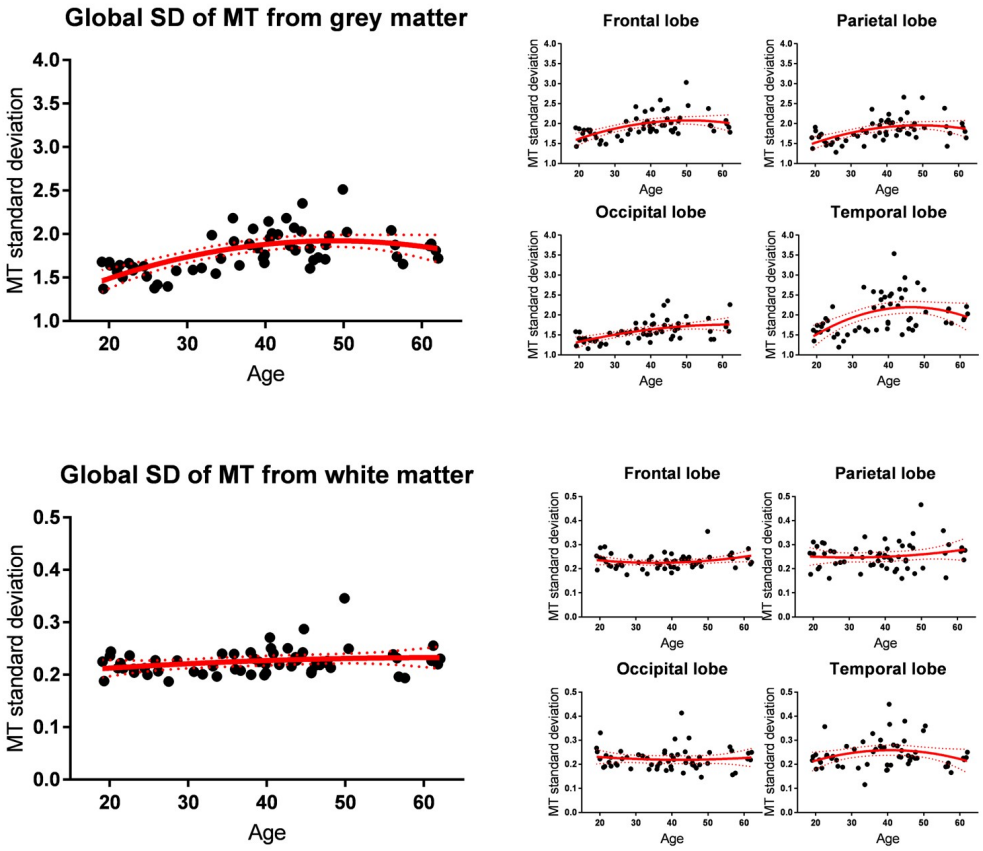

Figure 3.3.5: Age related variations in the standard deviation of MT measurements in both grey and white matter.

3.3.3 Investigating T_1 relationship with MT measurements

The age related variations in T_1 in both global grey and white matter were assessed by applying the grey and white matter masks to the acquired T_1 maps. The statistics associated with the quadratic trends fitted to the global T_1 measurements are presented in Table 5.3.2.

	Quadratic coefficient ($T_1\%^2$ / year) $\pm$ 95% confidence intervals	Age of peak T_1 (years)	p-value of quadratic trend vs. null hypothesis	p-value from F-test on quadratic model compared to linear model
Grey matter	-0.00017 $\pm$ 0.00014	48.5	0.005 *	0.0006 *
White matter	-0.000074 $\pm$ 0.000038	44.8	0.00002 *	0.000004 *

Table 3.3.2: Coefficients and significance of the quadratic model applied to changes in measured MT with ageing in each cerebral ROI. Significant trend (p<0.05) denoted by '*'.

There were significant quadratic trends with age for global grey matter and white matter T_1 measurements. These relationships are presented in Figure 3.3.6 along with the variation of T_1 with MT in each ROI averaged across participants for both grey matter and white matter. There was no correlation between T_1 and MT measurements (p>0.9) in grey matter, but a negative linear correlation was observed for white matter (p<0.001, R^2=0.23).

3.3.4 Discussion

The results presented here display a clear parabolic profile in MT with age in both grey and white matter, peaking at around 42 years of age. The trends were similar across the whole brain, but were stronger in white matter regions which are typically more heavily myelinated [60]. These results support the parabolic trend in T_1 measurements as reported previously [5, 40]. While our age of peak myelination agrees with the value of 40 years of age in white matter published by Yeatman et al., Cho et al. found the minimum T_1 value in grey matter occurred at 60, while we have a maximum MT value around the age of 42 across the whole cortex (varying between 35-48 across different brain regions). Similarly to Cho et al., we did observe T_1 in grey matter to have a minimum at a later age of 48.5 years. The discrepancy here could arise from the different age groups considered in the two studies; while here only ages between 19

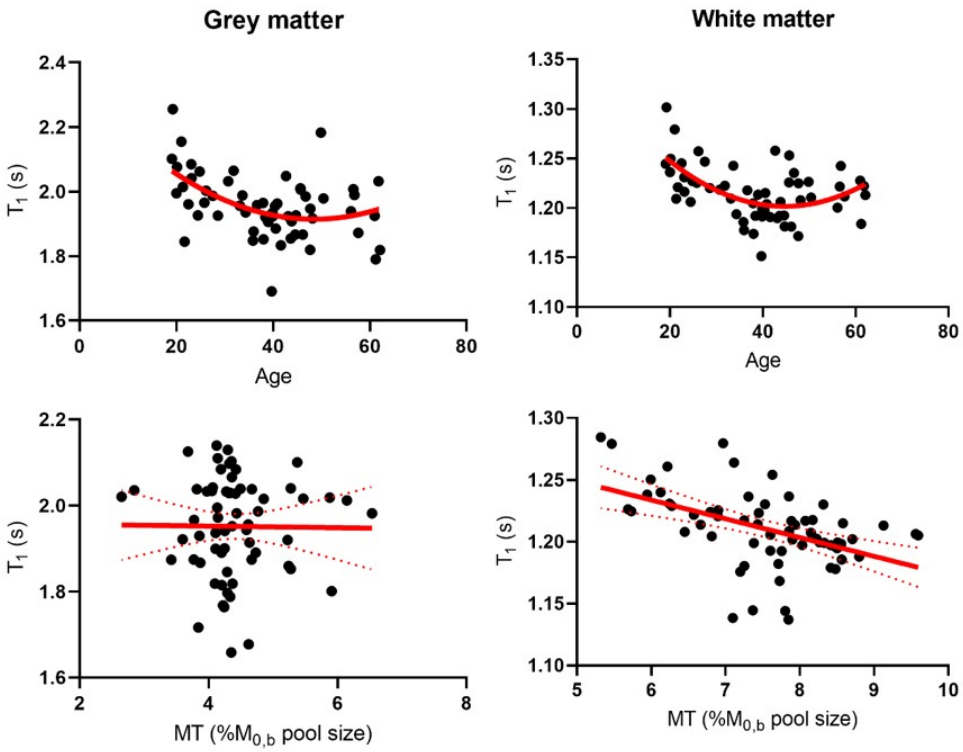

Figure 3.3.6: Age-related variations in T_1 of global grey and white matter, plotted for each participant separately. Variation of T_1 with MT is also displayed, plotted for each ROI averaged across participants for both grey and white matter.

to 62 were analysed, Cho et al. included subjects under 18 years old, as well as over 60 years old. However as previously discussed, T_1 measurements are affected by iron content which can further decrease the value of T_1. Non-haem iron is known from histology to increase with age [61] and susceptibility-weighted imaging studies have suggested that iron deposition can continue until the age of 40 or even 60 in some deep grey matter tissues [62], and is also known to increase in older age in some deep grey matter areas [61]. It is likely that both iron and myelin increase in earlier life since iron is required in myelin production in oligodendrocytes, but later in life the iron accumulation may be more pathological [63]. This is further evidenced in Figure 3.3.6 where we observed the opposing effects of decreasing myelination, which decreases the MT signal and increases T_1, and increasing iron content, which decreases T_1.

However, this was only observed in white matter, likely reflecting the effect of varying iron concentration in grey matter with age.

The standard deviation analysis reveals a linear increase in MT variation across the cortical surface, however no increase in MT variation within the white matter. The MT variation in grey matter is around an order of magnitude larger than that of white matter, most likely arising from the reduced myelination of grey matter. It is probable that the increase in variance in grey matter myelination with age arises from the reduction in the volume of the cortical surface (which will be explored further in the following section), and so there are fewer voxels to consider when finding a regional standard deviation value, as opposed to the white matter myelination where the number of voxels stays relatively constant with age.

It was also observed that the myelination was correlated with the underlying white matter myelination. This result was expected, as the grey matter neurones are primarily supported by axons in both the grey matter and underlying white matter.

3.4 Cortical thickness variation with age

Previous studies [45, 46, 47] have observed a linear decline in average global cortical thickness, with an average loss of roughly 4μm per year. The aim of this section is to confirm this finding, and perform further analysis to determine whether the cortical decline is driving the loss in myelination in later life.

3.4.1 Variations in rate of cortical thinning across cortex

The cortical thickness values in all AAL regions of each subject were averaged to create an average measure of the thickness of each subject's cortical surface. As expected

there was a significant linear trend with age, as displayed in Figure 3.4.1.

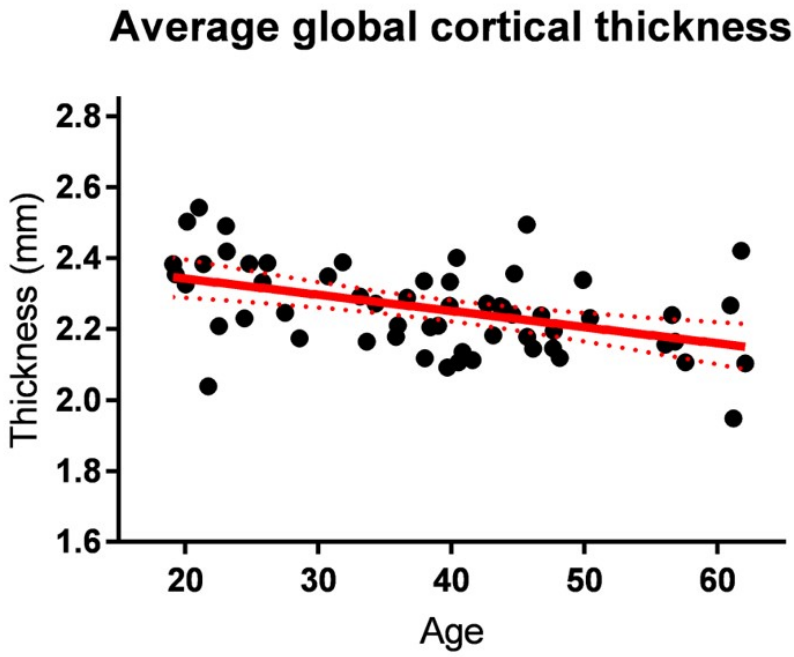

Figure 3.4.1: Linear regression of cortical thickness with age, with 95% confidence intervals displayed as dotted lines.

The same four ROIs as used in the previous section were created by averaging the cortical thicknesses in the AAL regions in each of the frontal, parietal, occipital and temporal lobes. The linear trend with age for each of these is displayed in Figure 3.4.2. All of these trends were significant barring in the temporal lobe. The statistics associated with these trends are presented in Table 5.4.1

A linear regression was then performed on each of the 64 AAL regions used in this study. Figure 3.4.3 shows the rate of cortical decline in each AAL region.

In order to explore the link between demyelination and cortical thickness, the MT and cortical thickness values were taken from each grey matter AAL region and averaged across subjects, to create an average MT measurement and an average cortical thickness measurement for each AAL region. Averaging across subjects removes age

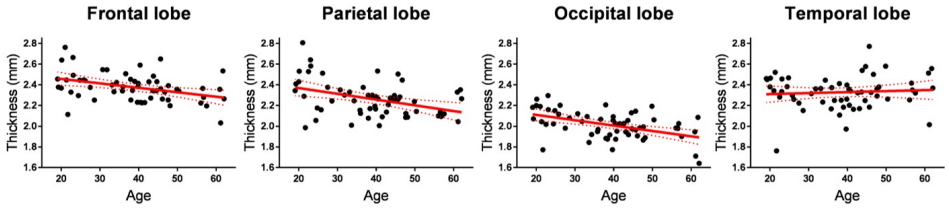

Figure 3.4.2: Linear regression of cortical thickness with age in each of the four lobes of the brain, with 95% confidence intervals displayed as dotted lines.

	Linear coefficient (μm / year) $\pm$ 95% confidence intervals	p-value of linear trend
Global	-4.56 $\pm$ 1.21	0.0004 *
Frontal	-4.31 $\pm$ 1.38	0.0028 *
Parietal	-5.57 $\pm$ 1.71	0.0019 *
Occipital	-5.19 $\pm$ 1.28	0.0002 *
Temporal	0.75 $\pm$ 1.75	0.5889

Table 3.4.1: Coefficients and significance of cortical decline in each cerebral ROI. Significant trend (p<0.05) denoted by '*'.

as a variable and allows inspection of whether increased amounts of MT are due to increased cortex thickness. No correlation was found between grey matter MT and cortical thickness, with R^2=0.004 and p=0.59 for a linear regression.

3.4.2 Local variation of thickness in cortical lobes

The way in which cortical thickness varies across the cortical surface was then analysed. A measure of the standard deviation of the cortical thickness was obtained for each of the four ROIs in the same way as detailed in section 3.3.2. These standard deviation values were plotted against age and a linear regression was performed. The results of these fits are displayed in Figure 3.4.4. Only the occipital and temporal lobes had a significantly non-zero linear trend, with the occipital lobe having a slope of +0.49μm

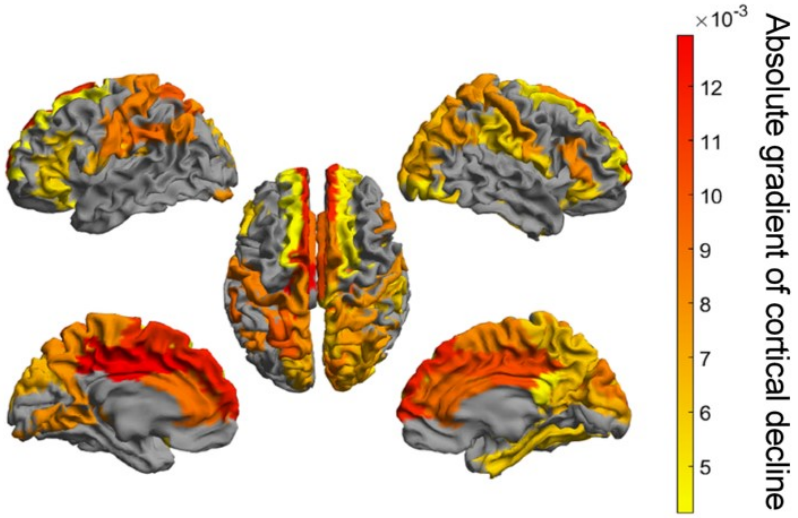

Figure 3.4.3: Absolute value of the linear coefficient of cortical thickness with age in each AAL region, showing how drastic the decline in thickness is across the cortical surface. Regions without a significantly non-zero linear trend are left grey.

per year, R^2=0.101 and p=0.015, and the temporal lobe having a slope of -0.47μm per year, R^2=0.109 and p=0.011.

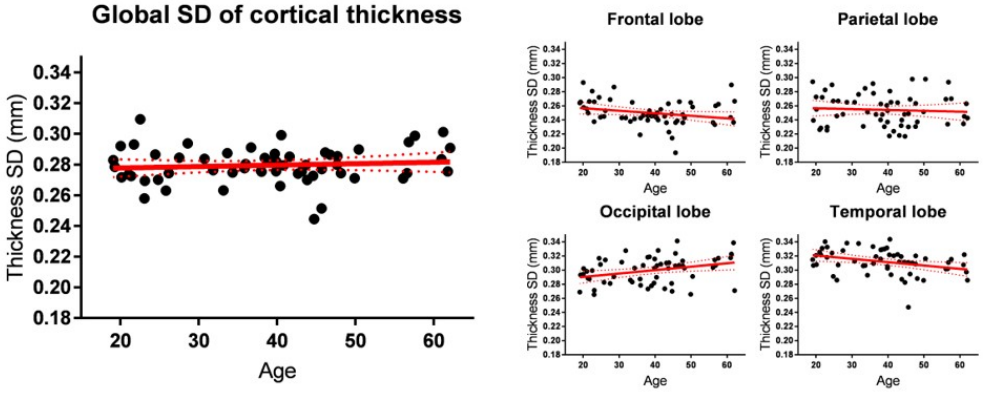

Figure 3.4.4: Age related variations in the standard deviation of cortical thickness.

3.4.3 Discussion

These results confirm the previous findings of a decrease in cortical thickness with age [45, 46, 47, 48, 49], with an average decline of -4.56 $\pm$ 1.21μm per year found here. Interestingly no significant decrease in cortical thickness was found in the temporal lobes, which is also the only ROI in which the variation of thickness across the lobe decreases with age. This has also been observed in a previous study [45], and further work into the cortical surface within the temporal lobe should be performed in order to understand the mechanisms driving this. These findings also reaffirm the possible reason for MT standard deviation increasing in grey matter but staying relatively constant in white matter.

The lack of a correlation between AAL regions with a thicker cortex and AAL regions which are more heavily myelinated warrants further discussion. As a greater volume of cortex apparently has no bearing on how heavily myelinated that particular volume is, it stands to reason that demyelination observed in later life associated with healthy ageing is not driven by the thinning of the cortex, a hypothesis which is further backed up by the fact that demyelination also appears in white matter regions, although recent work has shown that certain areas of white matter volume also decrease with age [64]. Nevertheless, the mechanism behind 'healthy demyelination' is not yet understood and requires further investigation.

3.5 NOE as a potential marker for myelination

While previous work has shown that MT and NOE pool size correlate in the human brain [65], this is not the case in all tissues [66]. This section repeats the MT analysis described in section 3.3, but instead analysing the NOE maps. Grey and white matter AAL regions were averaged globally, as well as grouped into the four ROIs, as

described previously. These data were plotted against participant age and fitted to linear and quadratic functions, and F-tests were performed to compare the significance of the quadratic model against the linear model as previously. A linear regression was then performed on the average MT and NOE values for each AAL region to explore the relationship between the MT pool size measurement and the NOE pool size measurement.

3.5.1 NOE relationships with ageing brain

Age-related trends in NOE were notably weaker than in MT, with a quadratic coefficient for grey matter being -15 $\pm$ 3 x$10^{-4}\%^2$/year, peak at 42.87 years old, p<0.0001 for MT, and -5 $\pm$ 2 x$10^{-4}\%^2$/year, peak at 44.43 years old, p=0.0027 for NOE. The strength of the quadratic curve was slightly stronger in white matter, with a quadratic coefficient of -23 $\pm$ 5 x$10^{-4}\%^2$/year, peak at 41.67 years old, p<0.0001 for MT and -8 $\pm$ 2 x$10^{-4}\%^2$/year, peak at 40.90 years old, p=0.0040 for NOE. A table of quadratic coefficients, p-values and the F-test results of each of these quadratic fits are presented in Table 5.5.1, however as several of the regional models are non-significant, only the global NOE trends are displayed in Figure 3.5.1 alongside a comparison to the MT data.

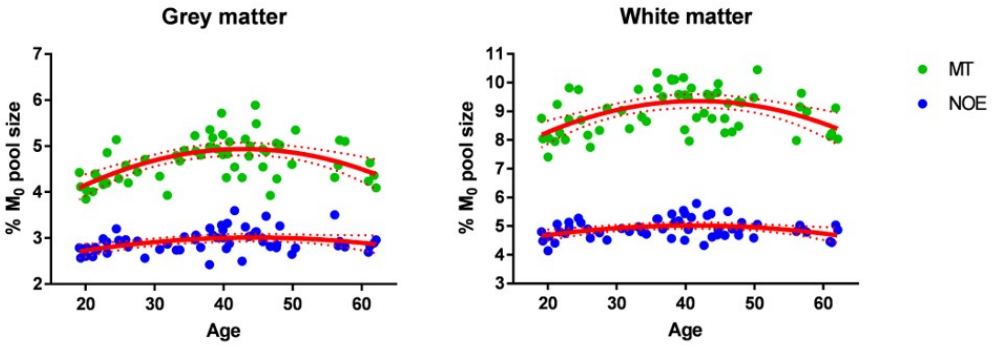

Figure 3.5.1: Quadratic trend in global NOE with age for grey matter and white matter. MT is also shown for comparison.

		Quadratic coefficient (NOE$\%^2$ / year) $\pm$ 95% confidence intervals	Age of peak NOE (years)	p-value of quadratic trend vs. null hypothesis	p-value from F-test on quadratic model compared to linear model
Grey matter	Global	-0.0005 $\pm$ 0.0004	44.4	0.0164 *	0.0078 *
	Frontal	-0.0006 $\pm$ 0.0008	47.0	0.1248	0.0711
	Parietal	-0.0006 $\pm$ 0.0004	40.6	0.0026 *	0.0022 *
	Occipital	-0.0003 $\pm$ 0.0082	45.4	0.1888	0.1352
	Temporal	-0.0005 $\pm$ 0.0036	44.0	0.0924	0.0641
White matter	Global	-0.0008 $\pm$ 0.0005	40.9	0.0050 *	0.0041 *
	Frontal	-0.0013 $\pm$ 0.0009	41.6	0.0047 *	0.0033 *
	Parietal	-0.0006 $\pm$ 0.0007	42.8	0.0665	0.0495 *
	Occipital	-0.0005 $\pm$ 0.0007	42.8	0.1658	0.1371
	Temporal	-0.0004 $\pm$ 0.0008	37.5	0.3412	0.3704

Table 3.5.1: Coefficients and significance of the quadratic model applied to changes in measured NOE with ageing in each cerebral ROI. Significant trend (p<0.05) denoted by '*'.

3.5.2 NOE correlations with MT in the brain

An average NOE value for each AAL region was calculated and a linear regression was performed with the corresponding MT measurements. There is a strong correlation between MT and NOE for each AAL region averaged across all subjects. Figure 3.5.2 displays a linear relationship with R^2=0.9478, p<0.0001 when considering the grey and white matter regions together. This relationship is retained when considering either solely the grey matter regions (R^2=0.305, p<0.0001) or solely the white matter regions (R^2=0.282, p<0.0001).

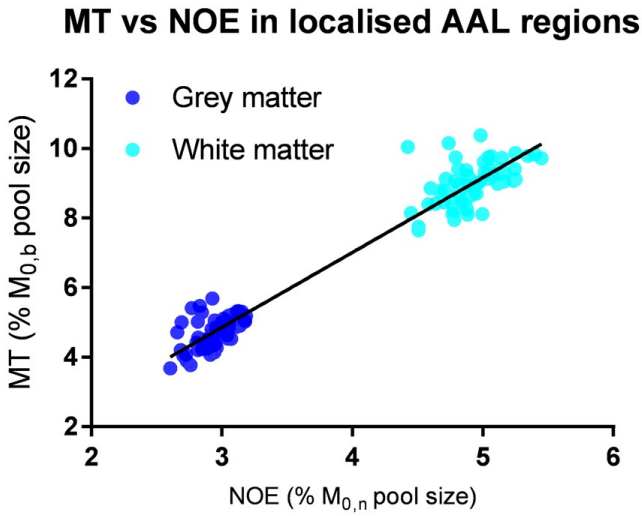

Figure 3.5.2: Correlation of MT vs. NOE averaged across individuals for each AAL region.

3.5.3 Discussion

This section shows that the relatively new measure of NOE also displays the quadratic trend with age associated with myelin concentration *in vivo*. MT and NOE were well correlated across all grey and white matter regions despite being independent measures, suggesting that similar underlying mechanisms give rise to both signals. The NOE signal in the brain is thought to originate in transfer of magnetisation from aliphatic backbones of mobile macromolecules and proteins, with the signal possibly relayed via molecular exchange [67]. As the fitting method used here models MT and NOE simultaneously and thus minimises biasing the NOE signal with underlying MT and vice versa, the results presented here suggest that NOE is correlated to myelination independently of MT, as myelin contains aliphatic groups which NOE is thought to be a measure of. However the sensitivity of the NOE signal is lower and the trends in NOE observed with age were similar to, albeit weaker than, the trends observed for MT. Nonetheless, this measure has not yet been explored fully and these results may

therefore play a role in guiding future literature.

As discussed throughout this thesis, measurement of both MT and NOE is not a trivial task. While previous studies have opted to measure MTR due to its acquisition speed, quantification of the MT pool size gives a much more reliable measure of MT. This section used a look-up table to characterise MT and NOE, as the use of pulsed saturation in the acquisition prevented further quantification. However, this measure of MT and pool size is not uncoupled from exchange rate, as only one value for MT exchange rate and one value for NOE exchange rate was used in creation of the look-up table (multiple exchange rates could not be simulated due to the unfeasible size of which the look-up table would become). Therefore the MT and NOE measures presented here would vary with temperature and pH [68], although this is not expected to be a confound in healthy subjects.

While the look-up table used in this section is capable of simultaneous fitting of overlapping peaks, consideration should be taken of the true independence of these measures. Any fit based upon the Bloch-McConnell equations has the same problems in that the mathematical model may not be correct, which may lead to errors such as misrepresentation of the MT spectrum, which is modelled here as a super-Lorentzian however there is uncertainty surrounding its true shape [69]. In addition, even if the model does perfectly represent the physical system, it may not provide the required sensitivity to separate parameters, such as MT and NOE pool size. This will depend on the chosen sampling parameters and inherent noise levels.

3.6 Summary

This chapter has used MT pool size as a marker for myelination due to its reduced sensitivity to aspects of brain structure other than myelin, and has shown that it has a strong parabolic trend with age in both grey and white matter, peaking on average at age 42. The analysis into cortical decline has revealed that the demyelination seen in

healthy subjects in later life is not driven by the loss in cortical volume, and therefore must instead be as a result of another mechanism. The NOE effect has also been introduced as a possible marker for myelination, however further work into the true origin of this signal is necessary to explore where this measure may best be an asset.

References

[1] W. T. Norton and Wendy Cammer. Isolation and Characterization of Myelin. In *Myelin*. 1984. doi: 10.1007/978-1-4757-1830-0{_}5.

[2] Paul Emil Flechsig. *Anatomie des menschlichen Gehirns und Rückenmarks auf myelogenetischer Grundlage*, volume 1. G. Thieme, 1920.

[3] O. Fernández, V. E. Fernández, and M. Guerrero. Enfermedades desmielinizantes del sistema nervioso central. *Medicine (Spain)*, 2015. ISSN 15788822. doi: 10.1016/j.med.2015.04.001.

[4] Charles M. Poser. Leukodystrophy and the Concept of Dysmyelination. *Archives of Neurology*, 1961. ISSN 15383687. doi: 10.1001/archneur.1961.00450090089013.

[5] Seong Cho, Dana Jones, Wilburn E. Reddick, Robert J. Ogg, and R. Grant Steen. Establishing norms for age-related changes in proton T1 of human brain tissue in vivo. *Magnetic Resonance Imaging*, 1997. ISSN 0730725X. doi: 10.1016/S0730-725X(97)00202-6.

[6] Terri S Armstrong, Marlene Z Cohen, Jeffrey Weinberg, and Mark R Gilbert. Imaging techniques in neuro-oncology. In *Seminars in oncology nursing*, volume 20, pages 231–239. Elsevier, 2004. ISBN 0749-2081.

[7] Martina F. Callaghan, Patrick Freund, Bogdan Draganski, Elaine Anderson, Marinella Cappelletti, Rumana Chowdhury, Joern Diedrichsen, Thomas H.B. FitzGerald, Peter Smittenaar, Gunther Helms, Antoine Lutti, and Nikolaus

Weiskopf. Widespread age-related differences in the human brain microstructure revealed by quantitative magnetic resonance imaging. *Neurobiology of Aging*, 2014. ISSN 15581497. doi: 10.1016/j.neurobiolaging.2014.02.008.

[8] S. Lorio, A. Lutti, F. Kherif, A. Ruef, J. Dukart, R. Chowdhury, R. S. Frackowiak, J. Ashburner, G. Helms, N. Weiskopf, and B. Draganski. Disentangling in vivo the effects of iron content and atrophy on the ageing human brain. *NeuroImage*, 2014. ISSN 10959572. doi: 10.1016/j.neuroimage.2014.09.044.

[9] D Purves, GJ Augustine, and D Fitzpatrick. Increased Conduction Velocity as a Result of Myelination. *Neuroscience*, 2001.

[10] H. Inouye and D. A. Kirschner. Membrane interactions in nerve myelin. I. Determination of surface charge from effects of pH and ionic strength on period. *Biophysical Journal*, 1988. ISSN 00063495. doi: 10.1016/S0006-3495(88)83085-6.

[11] V. Vasilescu, Eva Katona, V. Simplâceanu, and D. Demco. Water compartments in the myelinated nerve. III. Pulsed NMR result. *Experientia*, 1978. ISSN 14209071. doi: 10.1007/BF01932339.

[12] Alex Mackay, Kenneth Whittall, Julian Adler, David Li, Donald Paty, and Douglas Graeb. In vivo visualization of myelin water in brain by magnetic resonance. *Magnetic Resonance in Medicine*, 1994. ISSN 15222594. doi: 10.1002/mrm.1910310614.

[13] Thomas Prasloski, Alexander Rauscher, Alex L. MacKay, Madeleine Hodgson, Irene M. Vavasour, Corree Laule, and Burkhard Mädler. Rapid whole cerebrum myelin water imaging using a 3D GRASE sequence. *NeuroImage*, 2012. ISSN 10538119. doi: 10.1016/j.neuroimage.2012.06.064.

[14] Evan P. Minty, Thorarin A. Bjarnason, Cornelia Laule, and Alex L. Mackay. Myelin water measurement in the spinal cord. *Magnetic Resonance in Medicine*, 2009. ISSN 07403194. doi: 10.1002/mrm.21936.

[15] Christian Labadie, Jing Huei Lee, William D. Rooney, Silvia Jarchow, Monique Aubert-Frécon, Charles S. Springer, and Harald E. Möller. Myelin water mapping

by spatially regularized longitudinal relaxographic imaging at high magnetic fields. *Magnetic Resonance in Medicine*, 2014. ISSN 07403194. doi: 10.1002/mrm.24670.

[16] Carsten Stüber, Markus Morawski, Andreas Schäfer, Christian Labadie, Miriam Wähnert, Christoph Leuze, Markus Streicher, Nirav Barapatre, Katja Reimann, Stefan Geyer, Daniel Spemann, and Robert Turner. Myelin and iron concentration in the human brain: A quantitative study of MRI contrast. *NeuroImage*, 2014. ISSN 10959572. doi: 10.1016/j.neuroimage.2014.02.026.

[17] Jan Sedlacik, Christian Kutschbach, Alexander Rauscher, Andreas Deistung, and Jürgen R. Reichenbach. Investigation of the influence of carbon dioxide concentrations on cerebral physiology by susceptibility-weighted magnetic resonance imaging (SWI). *NeuroImage*, 2008. ISSN 10538119. doi: 10.1016/j.neuroimage.2008.07.008.

[18] Zhen Wu, Sandeep Mittal, Karl Kish, Yingjian Yu, J. Hu, and E. Mark Haacke. Identification of calcification with MRI using susceptibility-weighted imaging: A case study. *Journal of Magnetic Resonance Imaging*, 2009. ISSN 10531807. doi: 10.1002/jmri.21617.

[19] Neil Gelman, James R. Ewing, Jay M. Gorell, Eric M. Spickler, and Enez G. Solomon. Interregional variation of longitudinal relaxation rates in human brain at 3.0 T: Relation to estimated iron and water contents. *Magnetic Resonance in Medicine*, 2001. ISSN 07403194. doi: 10.1002/1522-2594(200101)45:1<71::AID-MRM1011>3.0.CO;2-2.

[20] Klaus Schmierer, Claudia A.M. Wheeler-Kingshott, Daniel J. Tozer, Phil A. Boulby, Harold G. Parkes, Tarek A. Yousry, Francesco Scaravilli, Gareth J. Barker, Paul S. Tofts, and David H. Miller. Quantitative magnetic resonance of post-mortem multiple sclerosis brain before and after fixation. *Magnetic Resonance in Medicine*, 2008. ISSN 07403194. doi: 10.1002/mrm.21487.

[21] Kevin D. Harkins, Junzhong Xu, Adrienne N. Dula, Ke Li, William M. Valentine, Daniel F. Gochberg, John C. Gore, and Mark D. Does. The microstructural

correlates of T1 in white matter. *Magnetic Resonance in Medicine*, 2016. ISSN 15222594. doi: 10.1002/mrm.25709.

[22] Matthew F Glasser and David C Van Essen. Mapping human cortical areas in vivo based on myelin content as revealed by T1- and T2-weighted MRI. *The Journal of neuroscience : the official journal of the Society for Neuroscience*, 2011. ISSN 1529-2401. doi: 10.1523/JNEUROSCI.2180-11.2011.

[23] Rebecca Shafee, Randy L. Buckner, and Bruce Fischl. Gray matter myelination of 1555 human brains using partial volume corrected MRI images. *NeuroImage*, 2015. ISSN 10959572. doi: 10.1016/j.neuroimage.2014.10.054.

[24] Muzamil Arshad, Jeffrey A. Stanley, and Naftali Raz. Test–retest reliability and concurrent validity of in vivo myelin content indices: Myelin water fraction and calibrated T1w/T2w image ratio. *Human Brain Mapping*, 2017. ISSN 10970193. doi: 10.1002/hbm.23481.

[25] Adrienne N. Dula, Daniel F. Gochberg, Holly L. Valentine, William M. Valentine, and Mark D. Does. Multiexponential T2, magnetization transfer, and Quantitative histology in white matter tracts of rat spinal cord. *Magnetic Resonance in Medicine*, 2010. ISSN 07403194. doi: 10.1002/mrm.22267.

[26] Md Nasir Uddin, Teresa D. Figley, Ruth Ann Marrie, and Chase R. Figley. Can T1w/T2w ratio be used as a myelin-specific measure in subcortical structures? Comparisons between FSE-based T1w/T2w ratios, GRASE-based T1w/T2w ratios and multi-echo GRASE-based myelin water fractions. *NMR in Biomedicine*, 2018. ISSN 10991492. doi: 10.1002/nbm.3868.

[27] Tanguy Duval, Nikola Stikov, and Julien Cohen-Adad. Modeling white matter microstructure. *Functional Neurology*, 2016. ISSN 19713274. doi: 10.11138/FNeur/2016.31.4.217.

[28] Klaus Schmierer, Francesco Scaravilli, Daniel R. Altmann, Gareth J. Barker, and David H. Miller. Magnetization transfer ratio and myelin in postmortem multiple

sclerosis brain. *Annals of Neurology*, 2004. ISSN 03645134. doi: 10.1002/ana.20202.

[29] M. Filippi, A. Campi, V. Dousset, C. Baratti, V. Martinelli, N. Canal, G. Scotti, and G. Comi. A magnetization transfer imaging study of normal-appearing white matter in multiple sclerosis. *Neurology*, 1995. ISSN 1526632X. doi: 10.1212/WNL.45.3.478.

[30] Irene M. Vavasour, Cornelia Laule, David K B Li, Anthony L. Traboulsee, and Alex L. MacKay. Is the magnetization transfer ratio a marker for myelin in multiple sclerosis? *Journal of Magnetic Resonance Imaging*, 2011. ISSN 10531807. doi: 10.1002/jmri.22441.

[31] Andrew J. Carradus, Simon M. Shah, Olivier E. Mougin, Caroline L. Hoad, and Penny A. Gowland. Magnetisation transfer in human liver and kidney through acquisition of the z-spectrum. *Abstract presented at the Joint Annual Meeting ISMRM-ESMRMB 2018*, page Abstract no. 2551, 2018.

[32] J. P. Mottershead, K. Schmierer, M. Clemence, J. S. Thornton, F. Scaravilli, G. J. Barker, P. S. Tofts, J. Newcombe, M. L. Cuzner, R. J. Ordidge, W. I. McDonald, and D. H. Miller. High field MRI correlates of myelin content and axonal density in multiple sclerosis: A post-mortem study of the spinal cord. *Journal of Neurology*, 2003. ISSN 03405354. doi: 10.1007/s00415-003-0192-3.

[33] Daniel J. Tozer, G. R. Davies, D. R. Altmann, D. H. Miller, and P. S. Tofts. Correlation of apparent myelin measures obtained in multiple sclerosis patients and controls from magnetization transfer and multicompartmental T 2 analysis. *Magnetic Resonance in Medicine*, 2005. ISSN 07403194. doi: 10.1002/mrm.20479.

[34] C. Laule, E. Leung, D. K.B. Li, A. L. Traboulsee, D. W. Paty, A. L. MacKay, and G. R.W. Moore. Myelin water imaging in multiple sclerosis: Quantitative correlations with histopathology. *Multiple Sclerosis*, 2006. ISSN 13524585. doi: 10.1177/1352458506070928.

[35] Klaus Schmierer, Daniel J. Tozer, Francesco Scaravilli, Daniel R. Altmann, Gareth J. Barker, Paul S. Tofts, and David H. Miller. Quantitative magnetization transfer imaging in postmortem multiple sclerosis brain. *Journal of Magnetic Resonance Imaging*, 2007. ISSN 10531807. doi: 10.1002/jmri.20984.

[36] T Kaes. *Die Grosshirnrinde des Menschen in ihren Maßen und ihrem Fasergehalt. Ein gehirnanatomischer Atlas mit erläuterndem Text*. 1907.

[37] HARRY CAMPBELL. PRINCIPLES OF HEREDITY: A REVIEW*. *British Journal of Inebriety*, 3(1):31–35, 1905. ISSN 0366-0796. doi: doi:10.1111/j.1360-0443.1905.tb04399.x. URL https://doi.org/10.1111/j.1360-0443.1905.tb04399.x.

[38] Adolf Hopf. Über die Verteilung myeloarchitektonischer Merkmale in der isokortikalen Schläfenlappenrinde beim Menschen. *J Hirnforsch*, 2(1):36–54, 1955.

[39] Oskar Vogt. Über strukturelle Hirnzentra. *mit besonderer Berücksichtigung der strukturellen Felder des Cortex pallii [On the structural centers of the brain, with particular emphasis on the structural regions of the cortex]. Anatomischer Anzeiger*, 20:74–114, 1906.

[40] Jason D. Yeatman, Brian A. Wandell, and Aviv A. Mezer. Lifespan maturation and degeneration of human brain white matter. *Nature Communications*, 2014. ISSN 20411723. doi: 10.1038/ncomms5932.

[41] George Bartzokis, Po H. Lu, Panthea Heydari, Alexander Couvrette, Grace J. Lee, Greta Kalashyan, Frank Freeman, John W. Grinstead, Pablo Villablanca, J. Paul Finn, Jim Mintz, Jeffry R. Alger, and Lori L. Altshuler. Multimodal magnetic resonance imaging assessment of white matter aging trajectories over the lifespan of healthy individuals. *Biological Psychiatry*, 2012. ISSN 00063223. doi: 10.1016/j.biopsych.2012.07.010.

[42] Håkon Grydeland, Kristine B. Walhovd, Christian K. Tamnes, Lars T. Westlye, and Anders M. Fjell. Intracortical myelin links with performance variability across the human lifespan: Results from T1- and T2- weighted MRI myelin mapping

and diffusion tensor imaging. *Journal of Neuroscience*, 2013. ISSN 02706474. doi: 10.1523/JNEUROSCI.2811-13.2013.

[43] B. Draganski, J. Ashburner, C. Hutton, F. Kherif, R. S.J. Frackowiak, G. Helms, and N. Weiskopf. Regional specificity of MRI contrast parameter changes in normal ageing revealed by voxel-based quantification (VBQ). *NeuroImage*, 2011. ISSN 10538119. doi: 10.1016/j.neuroimage.2011.01.052.

[44] Craig K. Jones, Alan Huang, Jiadi Xu, Richard A.E. Edden, Michael Schär, Jun Hua, Nikita Oskolkov, Domenico Zacà, Jinyuan Zhou, Michael T. McMahon, Jay J. Pillai, and Peter C.M. van Zijl. Nuclear Overhauser enhancement (NOE) imaging in the human brain at 7T. *NeuroImage*, 2013. ISSN 10538119. doi: 10.1016/j.neuroimage.2013.03.047.

[45] David H. Salat, Randy L. Buckner, Abraham Z. Snyder, Douglas N. Greve, Rahul S R Desikan, Evelina Busa, John C. Morris, Anders M. Dale, and Bruce Fischl. Thinning of the cerebral cortex in aging. *Cerebral Cortex*, 2004. ISSN 10473211. doi: 10.1093/cercor/bhh032.

[46] Anders M. Fjell, Kristine B. Walhovd, Christine Fennema-Notestine, Linda K. McEvoy, Donald J. Hagler, Dominic Holland, James B. Brewer, and Anders M. Dale. One-year brain atrophy evident in healthy aging. *Journal of Neuroscience*, 2009. ISSN 02706474. doi: 10.1523/JNEUROSCI.3252-09.2009.

[47] Larson J. Hogstrom, Lars T. Westlye, Kristine B. Walhovd, and Anders M. Fjell. The structure of the cerebral cortex across adult life: Age-related patterns of surface area, thickness, and gyrification. *Cerebral Cortex*, 2013. ISSN 10473211. doi: 10.1093/cercor/bhs231.

[48] Christopher R. Madan and Elizabeth A. Kensinger. Cortical complexity as a measure of age-related brain atrophy. *NeuroImage*, 2016. ISSN 10959572. doi: 10.1016/j.neuroimage.2016.04.029.

[49] Christopher R. Madan and Elizabeth A. Kensinger. Predicting age from cortical

structure across the lifespan. *European Journal of Neuroscience*, 2018. ISSN 14609568. doi: 10.1111/ejn.13835.

[50] R. C. Oldfield. The assessment and analysis of handedness: The Edinburgh inventory. *Neuropsychologia*, 1971. ISSN 00283932. doi: 10.1016/0028-3932(71)90067-4.

[51] Benjamin A.E. E Hunt, Prejaas K. Tewarie, Olivier E. Mougin, Nicolas Geades, Derek K. Jones, Krish D. Singh, Peter G. Morris, Penny A. Gowland, and Matthew J. Brookes. Relationships between cortical myeloarchitecture and electrophysiological networks. *Proceedings of the National Academy of Sciences of the United States of America*, 2016. ISSN 10916490. doi: 10.1073/pnas.1608587113.

[52] Olivier Mougin, Rasha Abdel-Fahim, Robert Dineen, Alain Pitiot, Nikos Evangelou, and Penny Gowland. Imaging gray matter with concomitant null point imaging from the phase sensitive inversion recovery sequence. *Magnetic Resonance in Medicine*, 2016. ISSN 15222594. doi: 10.1002/mrm.26061.

[53] Olivier Mougin, Matthew Clemence, Andrew Peters, Alain Pitiot, and Penny Gowland. High-resolution imaging of magnetisation transfer and nuclear Overhauser effect in the human visual cortex at 7 T. *NMR in Biomedicine*, 2013. ISSN 09523480. doi: 10.1002/nbm.2984.

[54] Nicolas Geades, Benjamin A.E. E Hunt, Simon M. Shah, Andrew Peters, Olivier E. Mougin, and Penny A. Gowland. Quantitative analysis of the z-spectrum using a numerically simulated look-up table: Application to the healthy human brain at 7T. *Magnetic Resonance in Medicine*, 2017. ISSN 15222594. doi: 10.1002/mrm.26459.

[55] Mark W. Woolrich, Saad Jbabdi, Brian Patenaude, Michael Chappell, Salima Makni, Timothy Behrens, Christian Beckmann, Mark Jenkinson, and Stephen M. Smith. Bayesian analysis of neuroimaging data in FSL. *NeuroImage*, 2009. ISSN 10959572. doi: 10.1016/j.neuroimage.2008.10.055.

[56] Anders M. Dale, Bruce Fischl, and Martin I. Sereno. Cortical surface-based analysis: I. Segmentation and surface reconstruction. *NeuroImage*, 1999. ISSN 10538119. doi: 10.1006/nimg.1998.0395.

[57] Bruce Fischl. FreeSurfer, 2012. ISSN 10538119.

[58] N. Tzourio-Mazoyer, B. Landeau, D. Papathanassiou, F. Crivello, O. Etard, N. Delcroix, B. Mazoyer, and M. Joliot. Automated anatomical labeling of activations in SPM using a macroscopic anatomical parcellation of the MNI MRI single-subject brain. *NeuroImage*, 2002. ISSN 10538119. doi: 10.1006/nimg.2001.0978.

[59] R. A. Fisher. Moments and product moments of sampling distributions. *Proceedings of the London Mathematical Society*, 1930. ISSN 1460244X. doi: 10.1112/plms/s2-30.1.199.

[60] Rud Virchow. Ueber das ausgebreitete Vorkommen einer dem Nervenmark analogen Substanz in den thierischen Geweben. *Archiv für Pathologische Anatomie und Physiologie und für Klinische Medicin*, 1854. ISSN 09456317. doi: 10.1007/BF02116709.

[61] B. Hallgren and P. Sourander. THE EFFECT OF AGE ON THE NON-HAEMIN IRON IN THE HUMAN BRAIN. *Journal of Neurochemistry*, 1958. ISSN 14714159. doi: 10.1111/j.1471-4159.1958.tb12607.x.

[62] Dan Wang, Wen Bin Li, Xiao Er Wei, Yue Hua Li, and Yong Ming Dai. An Investigation of Age-Related Iron Deposition Using Susceptibility Weighted Imaging. *PLoS ONE*, 2012. ISSN 19326203. doi: 10.1371/journal.pone.0050706.

[63] James R. Connor and Sharon L. Menzies. Relationship of iron to oligodendrocytes and myelination. *GLIA*, 1996. ISSN 08941491. doi: 10.1002/(SICI)1098-1136(199606)17:2<83::AID-GLIA1>3.0.CO;2-7.

[64] Farnaz Farokhian, Chunlan Yang, Iman Beheshti, Hiroshi Matsuda, and Shuicai Wu. Age-related gray and white matter changes in normal adult brains. *Aging and Disease*, 2017. ISSN 21525250. doi: 10.14336/AD.2017.0502.

[65] Nicolas Geades, Olivier E. Mougin, Simon Shah, and Penny A. Gowland. Are MT and NOE (at -3.5 ppm) in z-spectroscopy coupled in the brain? In *Ismrm*, 2017.

[66] Simon M. Shah, Olivier E. O.E. Olivier E. Mougin, A.J. Andrew J. Carradus, Nicolas Geades, Richard Dury, William Morley, and Penny A. P.A. Gowland. The z-spectrum from human blood at 7T. *NeuroImage*, 167, 2018. ISSN 10959572. doi: 10.1016/j.neuroimage.2017.10.053.

[67] Peter C.M. van Zijl, Wilfred W. Lam, Jiadi Xu, Linda Knutsson, and Greg J. Stanisz. Magnetization Transfer Contrast and Chemical Exchange Saturation Transfer MRI. Features and analysis of the field-dependent saturation spectrum. *NeuroImage*, 2018. ISSN 10959572. doi: 10.1016/j.neuroimage.2017.04.045.

[68] K. M. Ward, A. H. Aletras, and R. S. Balaban. A New Class of Contrast Agents for MRI Based on Proton Chemical Exchange Dependent Saturation Transfer (CEST). *Journal of Magnetic Resonance*, 2000. ISSN 10907807. doi: 10.1006/jmre.1999.1956.

[69] Greg J. Stanisz, Ewa E. Odrobina, Joseph Pun, Michael Escaravage, Simon J. Graham, Michael J. Bronskill, and R. Mark Henkelman. T1, T2 relaxation and magnetization transfer in tissue at 3T. *Magnetic Resonance in Medicine*, 2005. ISSN 07403194. doi: 10.1002/mrm.20605.

Chapter 4

Measuring exchange rates via a Particle Swarm Optimisation algorithm

As discussed in Chapter 2, it is analytically impossible to solve the Bloch McConnell equations for the variables representing properties of present exchanging pools given only the z-spectrum, without prior knowledge or assumption of one of either pool size or exchange rate. While methods discussed in section 2.5 seek for ways to overcome this, all make prior assumptions about the system, and some rely on initial guesses which can bias the results if incorrect, and in addition the look-up table approach used in the previous chapter does not allow for continuous values of variables to be fitted. This chapter presents a novel method of fitting the z-spectrum to find key physical variables with fewer assumptions than any other currently published method, and tests its feasibility in both creatine phantoms and in cerebral grey and white matter *in vivo*.

4.1 PSO design and implementation

The particle swarm optimisation (PSO) algorithm is a stochastic search method created by Eberhart in 1995 [1], and modified in 1998 [2] to the version used in this chapter. PSO is effective in solving highly nonlinear problems [3], where standard search techniques may find local minima in the variable space, as opposed to the true global solution. PSO has some similarities to the genetic algorithm, in that both are based on a 'population' of possible solutions, and both evolve over time towards the true solution [4]. Eberhart states in his original 1995 paper that PSO has some influences from the genetic algorithm, but is primarily influenced by the social behaviour of animals, for example a flock of birds mimicking the collective intelligence of the flock to find food rather than the individual intelligence of any given member of the flock.

4.1.1 PSO mechanics

The PSO algorithm is used to solve highly nonlinear multi-dimensional problems based on iterative methods in which a set of initial randomised guesses evolve towards the global solution. Given an appropriate set of bounds for each variable, the PSO algorithm initialises a number of these guesses for all variables, termed as particles. The value of each variable serves as coordinates for the position of each particle in variable space. Each particle is also randomly assigned a velocity, which is used to calculate its position in the next iteration of the algorithm. A minimisation function is used to calculate how close these particles are to the optimal solution, and in the next iteration the calculation of the new particle velocity is influenced both by the memory of the particle itself and the memory of the swarm, as well as its own prior velocity. In simple terms, the velocity of any given particle is dependent on where it is currently going, the best place it has been, and the best place any particle has been [5].

The PSO algorithm is expressed mathematically as

$$\mathbf{v}_{k+1}^{i} = w\mathbf{v}_{k}^{i} + c_1 rand\frac{\mathbf{p}^{i} - \mathbf{x}_{k}^{i}}{\Delta t} + c_2 rand\frac{\mathbf{p}_{k}^{g} - \mathbf{x}_{k}^{i}}{\Delta t} \tag{4.1.1}$$

where $\mathbf{x}_k^i$ is the position of particle i at iteration k, $\mathbf{v}_{k,k+1}^i$ is the velocity of particle i at its current/next iteration, $\mathbf{p}^i$ is the best position of particle i from all iterations, and $\mathbf{p}_k^g$ is the best position of any particle during the current iteration. There are three coefficients which determine how much influence each of these components has on the new particle velocity. The inertia factor, w is a coefficient which controls the influence of current motion, and is usually set between 0.4-1.4. The self confidence range, c_1, controls the influence of individual particle memory, and is usually set between 1.5-2. Finally the swarm confidence range, c_2, controls the influence of the swarm, and is usually set between 2-2.5 [4].

The simplest way to visualise the mechanics of PSO is by considering a 1-dimensional problem with several local minima, as displayed in Figure 4.1.1. Here PSO is deemed necessary, as typical minimisation functions such as MATLAB's `lsqcurvefit` [6] are likely to present one of the local minima as the solution. The user has initialised 7 particles here to solve the problem. Note that this is an exaggerated illustration.

In Figure 4.1.1 the global solution is found after 20 iterations. There are a number of possible stopping criteria for PSO algorithms which can be implemented. The simplest of these is that the algorithm is forced to run for a fixed number of iterations, which means that the algorithm may not find the solution in time, or conversely that it may waste time after the solution has been found. The PSO can also stop after a solution has been found that is close to the optimal solution, so that the minimisation function becomes below a predefined tolerance level. This can be useful as in some cases PSO may continue to search for a solution with a degree of accuracy that is unnecessary for a given problem. Finally the algorithm can be set to stop after the global solution has not been improved upon for a given number of iterations, as a way of ensuring that no further solution would be found with continued searching.

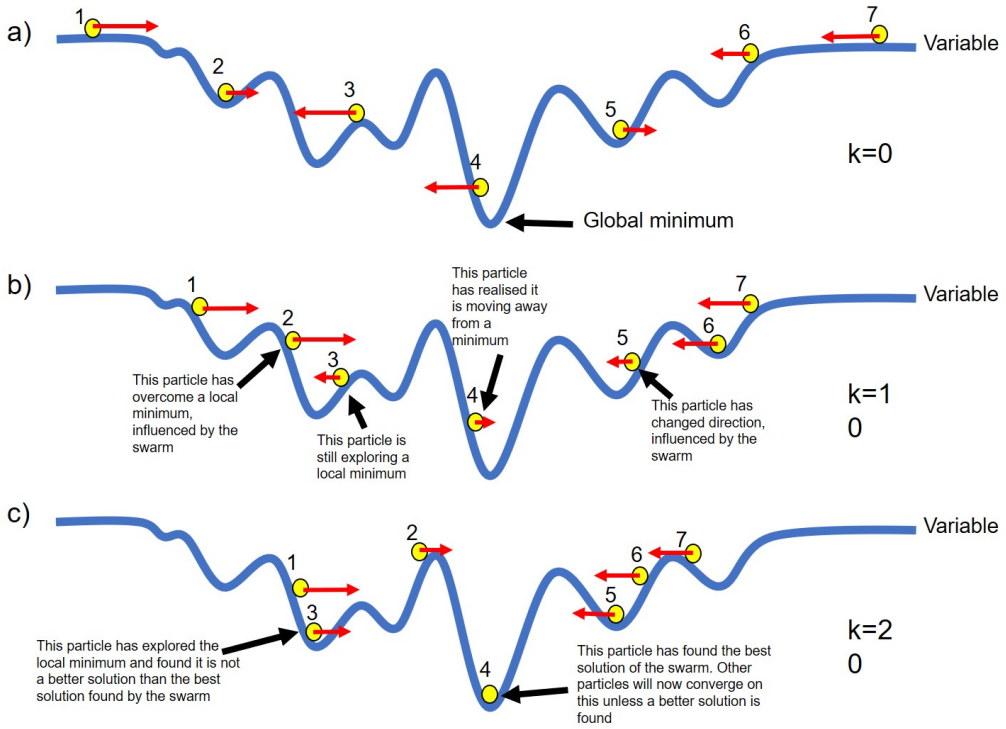

Figure 4.1.1: Evolution of the swarm in a 1-dimensional problem, with the function and its local minima represented by the blue line, particles by yellow circles, and their velocities by red arrows. a) Initialisation of the algorithm, with randomly positioned particles and randomly assigned velocities. b) Positions and velocities of the particles after 10 iterations, where influence of the swarm has started to work out where the global minimum might be. c) Positions and velocities of the particles after 20 iterations, where the global minimum has been found. If so defined by the user, the algorithm can end here.

4.1.2 Application to the z-spectrum

The key problem in quantifying the z-spectrum to find the values of the parameters describing the exchanging pools is that a) the pool size, exchange rate, and apparent T_2 of any given pool can create similar changes on the shape of the z-spectrum, and b) overlapping exchanging pools can further confuse measurement of this effect. Because of this there are often a number of possible solutions which can give z-spectra closely

resembling that of an acquired dataset, meaning that determining the values of the physical parameters that actually give rise to the z-spectrum can be difficult. It is for this reason that the PSO algorithm is appropriate for quantification of the z-spectrum, as it is ideal in finding the global solution amongst many local minima.

For this thesis, the PSO algorithm modified to quantify the z-spectrum (hereafter referred to as the z-PSO) was written in C, as initial testing showed this to have increased evaluation speed compared to MATLAB's inbuilt `particleswarm` function [6], and also allows for parallelisation of the z-PSO, as will be explored in section 4.1.3.

The main Bloch-McConnell simulation in the z-PSO is performed using a spectrum calculated according to equation 2.3.6, restated here for clarity.

$$Z(\Delta\omega, t) = (\cos^2(\theta) - Z(\Delta\omega)_{ss})e^{\frac{-t_{sat}}{T_{1,\rho}}} + Z_{ss} \tag{4.1.2}$$

where $Z_{ss}(\Delta\omega)$ is the system in the steady-state condition for saturation applied at $\Delta\omega$ (as previously defined in equation 2.3.1), $T_{1,\rho}$ refers to the overall longitudinal relaxation time of the system in the rotating frame, t_{sat} is the time that saturation is applied for, and θ is the angle between the applied resonance frequency and the frequency of the pool of interest in the rotating frame, such that $\theta = \arctan(\frac{\omega_1}{\Delta\omega})$, in which $\omega_1 = \gamma.B_1$, where γ is the gyromagnetic ratio of protons. This equation is modelled through the simulation of each pool as a Lorentzian lineshape. As stated in Chapter 2, the $T_{1,\rho}$ term can be expressed as a sum of the present exchanging pools, such that $\frac{1}{T_{1,\rho}(\Delta\omega)} = R_{eff}(\Delta\omega) + R_{ex,b}(\Delta\omega) + R_{ex,c}(\Delta\omega) + R_{ex,n}(\Delta\omega)$ in a four pool model. The R_{eff} term has been previously defined in equation 2.3.3. Each R_{ex} term can be expressed in the form of a Lorentzian lineshape [7], such that

$$R_{ex,c}(\Delta\omega) = M_{0,c}.k_c\frac{A_c(\Delta\omega)}{\frac{\Gamma_c}{2}^2 + (\Delta\omega - \delta\omega_c)^2} \tag{4.1.3}$$

for the $R_{ex,c}$ pool as an example, where

$$\Gamma_c = 2\sqrt{w_1^2 \frac{k_c + \frac{1}{T_{2,c}}}{k_c} + (k_c + \frac{1}{T_{2,c}})^2} \tag{4.1.4}$$

and

$$A_c(\Delta\omega) = \frac{\omega_1^2}{(\Delta\omega^2 + \omega_1^2)}.(\delta\omega_c^2 + \frac{\Delta\omega^2 + \omega_1^2}{T_{2,c}.k_c} + \frac{k_c + \frac{1}{T_{2,c}}}{T_{2,c}}) \tag{4.1.5}$$

where $M_{0,c}$, k_c, $T_{2,c}$ and $\delta\omega_c$ are the variables that are fitted by the z-PSO for pool c. $M_{0,c}$ is the pool size of the exchanging pool c expressed as a fraction, k_c is the exchange rate of pool c with water expressed in Hz, $T_{2,c}$ is the apparent T_2 of exchanging pool c expressed in seconds, and $\delta\omega_c$ is the frequency offset of the peak of pool c. Through summation of all R_{ex} terms along with the R_{eff} term we can simulate the z-spectrum as described by equation 3.1.2.

This method assumes that our data has been acquired using CW saturation with a saturation time of at least $T_{1,f}/4$ [7]. The only prior information we give the z-PSO is the number of exchanging pools present and their frequency offsets, which are allowed to vary by 0.1ppm around their expected value when the algorithm is run. The z-PSO is given the acquired z-spectra (which should be at multiple acquisition powers for the same sample), the frequency offsets at which they were acquired, the nominal B_1 values of each saturation block, the saturation time, the observed T_1 of the sample, and the actual B_1 (as a fraction of the nominal B_1) of the sample. Z-spectra must be normalised so that the units are S_{sat}/S_0, and are assumed to be B_0 corrected via one of the methods described in section 2.2.2.

Exchanging pools are then fitted sequentially depending on their frequency offset, before being refitted while considering the whole spectrum (section 4.1.3 shows why this is a much more effective fitting method than fitting all exchanging pools at once). Let us consider a 4 pool model, containing free water, MT, APT, and NOE. The z-PSO reads in the acquired data and firstly fits a 2 pool model of free water and MT

to the data, excluding points in the range of -5ppm to -1ppm, and +1ppm to +5ppm. In this stage there are 6 variables to be fitted: the T_1 and T_2 of free water, and the MT pool size, exchange rate, apparent T_2, and peak position. Particles are allowed to explore possible values of each of these variables between predetermined bounds. Z-spectra are simulated and compared to the real data through a sum of least squares difference, so that no difference is a perfect fit. This is the value that the z-PSO aims to minimise, and so through this finds the optimal solution for each parameter.

After finding the MT parameters, the z-PSO then fits a 3 pool model of free water, MT, and APT to the data, now only excluding points between 1ppm to -5ppm. However in this fit, the previously determined values for free water and MT are used as fixed parameters, and the z-PSO only fits 4 variables: the APT pool size, exchange rate, apparent T_2, and peak position. Once solved, the z-PSO then fits the 4 pool model to the data considering all data points, but still only the four variables of the newly added NOE pool are fitted, while the other parameters are taken from the previous fits. Finally each exchanging pool is refitted once more, but this time including all data points and using the latest fitted values for the variables of each exchanging pool. This stage removes any errors arising from overlapping exchanging pools, which may have affected the initial fits when other pools were not considered. A flowchart of the z-PSO is displayed in Figure 4.1.2.

It is important to note that for computational speed it is necessary to model the MT pool as a Lorentzian lineshape. As stated in chapter 2, this model holds true around the water resonance [8], and so does not affect the fitted values of underlying CEST or NOE pools, however the fitted values of the MT pool (particularly exchange rate and apparent T_2) can only be considered indicators of their true values or of the underlying physics, since the shape is not representative of the entire pool shape. When fitting the z-PSO throughout this thesis, the University of Nottingham High Performance Computer is used, implementing 100 1GB cores with classical x86 hardware.

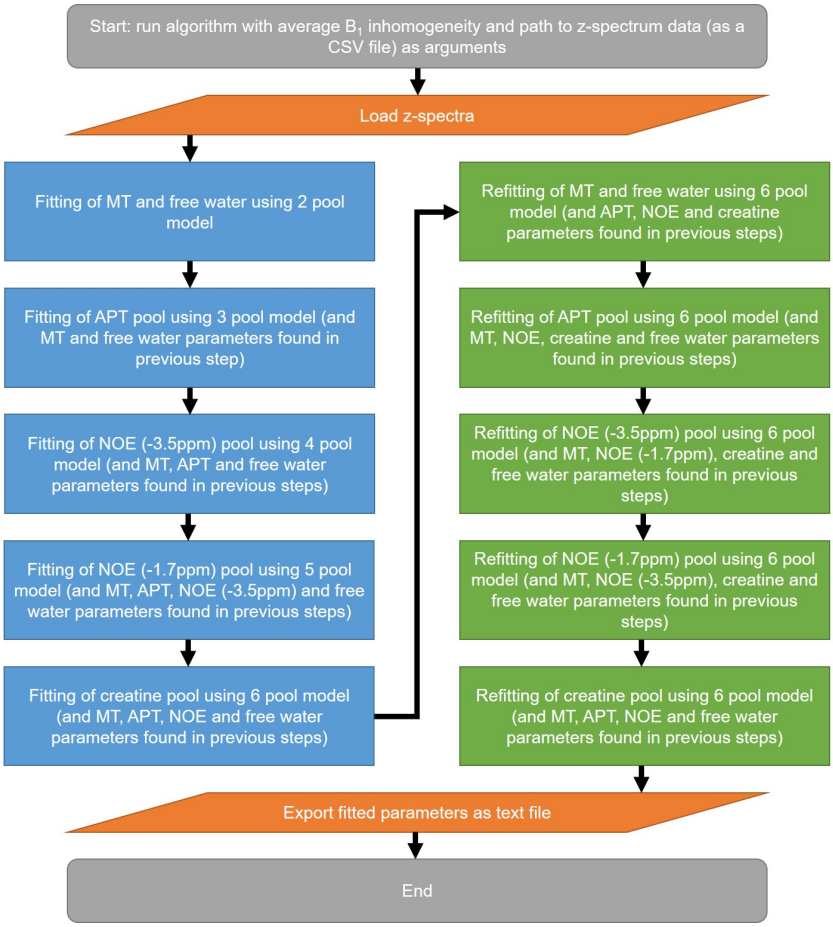

Figure 4.1.2: Flowchart showing the stages of the z-PSO.

4.1.3 Optimisation of PSO parameters for z-spectrum fitting

There are two important questions to ask ourselves when using the PSO: how many iterations do we need, and how many particles do we need? The first of these questions is answered by simple observation. After repeated fitting of sample z-spectrum data it was observed that the solution usually did not improve after around 150-190 iterations, and so for confidence the number of iterations was fixed at 250, and no sample tested has needed more than this to converge on a solution.

The second question is more complex. Surprisingly there is apparently no literature advising users of PSO how many particles to use, so investigations were performed to determine this. We can intuitively discern that the number of particles needed to adequately search a variable space must be proportional to the number of particles searching across one variable to the power of the number of variables. For clarity on this, we can visualise a 3-dimensional variable space as shown in Figure 4.1.3, housing one particle per segment.

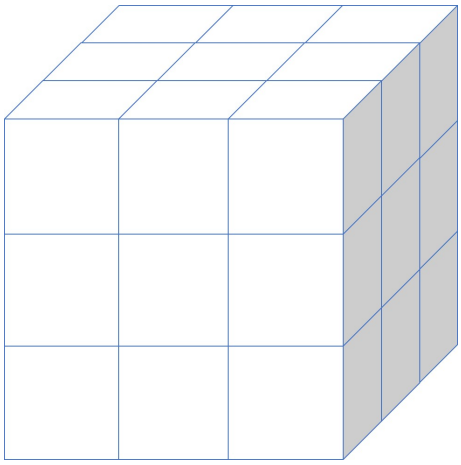

Figure 4.1.3: 3D variable space divided so that 3 particles are searching each dimension, making 27 particles total.

Here we can imagine a line across a cube face as 1 dimension, we would need 3 particles to search each section of this one-dimensional space. If we then extend to the cube face, we need $3^2 = 9$ particles to search 2 dimensions to an equal degree, and for the whole cube $3^3 = 27$ particles are required to maintain the same degree of swarm coverage. This makes it clear as to why fitting each pool in the z-spectrum individually is much more effective than fitting all pools simultaneously; for a 6 pool model we have 22 parameters that need to be fit, and $N^6 + 4N^4 << N^{22}$ where N is an integer greater than 1, representing the number of particles in the swarm.

To test for the optimal number of particles, sample z-spectra acquired from cerebral grey matter were fitted to a 6 pool model (free water, MT, amides, NOE(-3.5ppm), NOE(-1.7ppm), and amines). The dataset comprised of 312 data points: 63 off-

resonance frequencies acquired at 5 saturation powers. Fits were run with varying number of particles and the sum of squares difference between the real data and simulated spectra created from the fitted results was used as a metric to determine goodness of fit. Computation time was also considered as a factor. The results of this test are displayed in Figure 4.1.4.

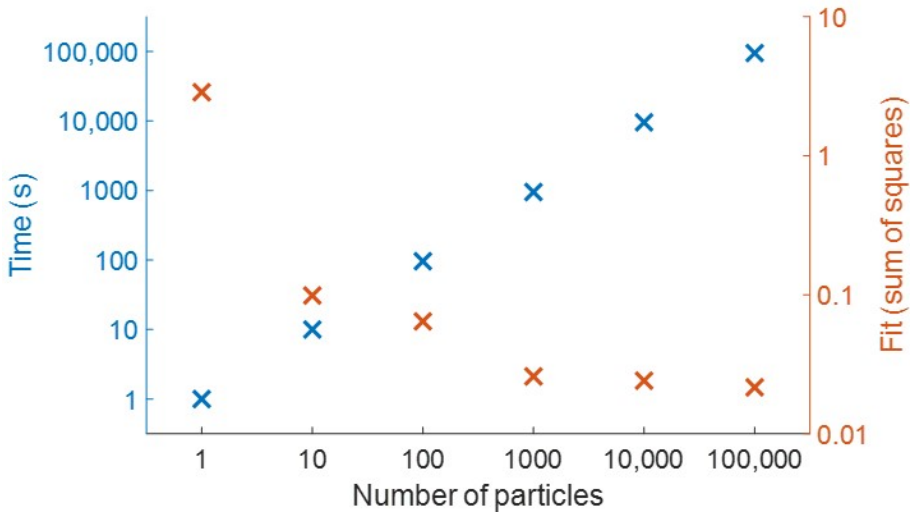

Figure 4.1.4: Results of fit dependency on number of particles.

The test reveals a linear relationship between time taken for the fit to complete and number of particles used as expected (coincidentally roughly one particle per second). The sum of squares difference declined exponentially with increasing number of particles, showing drastic initial improvements in the fit and then diminishing returns beyond 1000 particles. Interestingly the fit using one particle is analogous to using simple least-squares fitting techniques.

The next test was to determine whether repeated sets of smaller swarms could be used to find solutions as accurately as one large swarm. The advantage of this would be that smaller swarms could be run simultaneously to drastically reduce total fitting time. Fits containing smaller numbers of particles were repeated so that the number of particles multiplied by the number of repeats was equal to 100,000 (for example the 1000 particle fit was repeated 100 times). The best fit from all of the repeated

measurements was then taken for each swarm size. Results of this test are displayed in Figure 4.1.5.

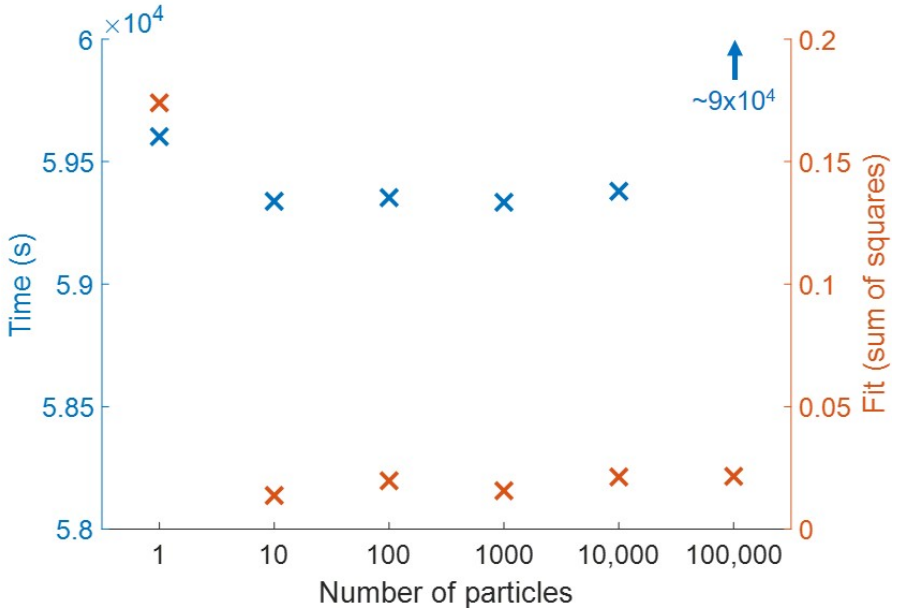

Figure 4.1.5: Results of fit dependency on number of particles, with smaller swarms repeated proportionally to the inverse of their population size.

We can see that increasing the swarm size has little effect on the computation time, and for more than one particle the goodness of fit does not change, showing that even the smallest of swarms are better at finding the solution than a series of individual particles. Interestingly here, one particle repeated 100,000 times is analogous to simple least-squares fitting methods with multiple starting points, showing just how powerful the collective intelligence of even small swarms is. It is unclear as to why the 100,000 particle fit took 9000s as opposed to around 6000s like the other trials, however this fit was performed on a different day to the others, so it is possible that system updates may have increased computation speed.

Further investigation into one of these results reveals that this number of repeats appears appropriate for this problem. Figure 4.1.6 shows the 100 individual repeat results for the 1000 particle fits. The z-PSO improves on the first attempt twice: once after 5 fits, and once after 63 fits. No fits after this are close to improving

on this particular fit. The University of Nottingham High Performance Computing system allows for a maximum of 400 parallel computations per user, and therefore by utilising the 100 repeats of 1000 particle swarms, we can fit 4 z-spectra datasets at once, taking the time required to perform one 1000 particle fit, which is roughly 16 minutes.

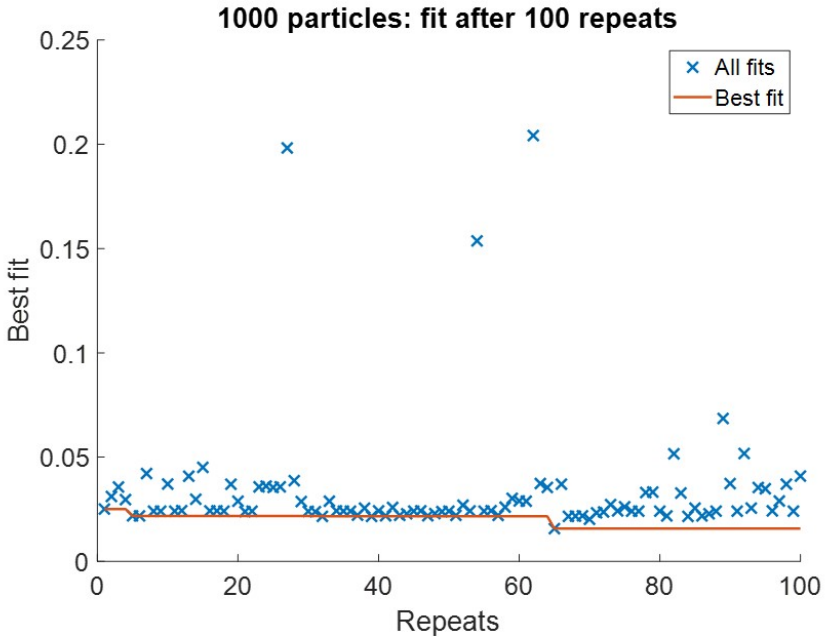

Figure 4.1.6: Results of the 1000 particle swarm fits, repeated 100 times. The orange line displays the best overall fit updated after every repeat. We can see that during the course of the 100 repeats, there were two repeats which yielded improvements over the best previous fit.

4.2 Testing sensitivity of the z-PSO

Once the z-PSO fitting approach had been optimised, analysis was performed to determine how accurate and precise the solutions were. To do this, z-spectra were simulated using the Bloch-McConnell equations for a range of pool sizes, exchange rates, and apparent T_2s for firstly a CEST pool, and secondly an underlying MT pool.

Noise was added to these simulated spectra which were then fitted. This was repeated ten times and the resulting parameters were compared to the simulated values, to identify regions where the z-PSO was incapable of performing well.

4.2.1 CEST fitting

In order to test the feasibility of fitting CEST pools, z-spectra were simulated with one exchanging pool located at +3.5ppm, sampled at 63 off-resonance frequencies and 5 saturation powers. 27 datasets were simulated, with combinations of small, medium and large pool size (0.1%, 0.5%, and 1.0%), slow, medium and fast exchange rate (10Hz, 100Hz, and 1000Hz), and short, medium and long T_2 (1ms, 10ms, and 100ms). Simulated datasets are shown in Figure 4.2.1.

For each of the ten trials, 0.5% Gaussian noise was added to each of the data points in the simulated spectra, representative of noise seen during experimental z-spectrum acquisition. Figure 4.2.2 shows the fitted pool size for each of the datasets. The colour used for the error bars indicates the percentage error on the mean compared to the expected value (shown by the red dotted line). We can see that the z-PSO can struggle at very low exchange rates, particularly when the pool size in question is also small.

Figure 4.2.3 shows the results of fitted exchange rate for each of the datasets. We can see again that for very slow exchange rates the z-PSO can struggle to find the correct answer, especially at longer apparent T_2s. However, when considering that an error of 100% on an exchange rate of 10Hz tells us that the exchange rate is between 0-20Hz, the information provided is still useful.

Figure 4.2.4 shows the results of fitted $T_{2,c}$ for each of the datasets. We can see that longer T_2s are difficult to fit. This is consistent with section 2.2.2 which showed that there is little noticeable difference in the shape of the z-spectrum beyond a T_2 of around 20ms for an exchanging pool. A similar lack of sensitivity to $T_{2,c}$ was found for

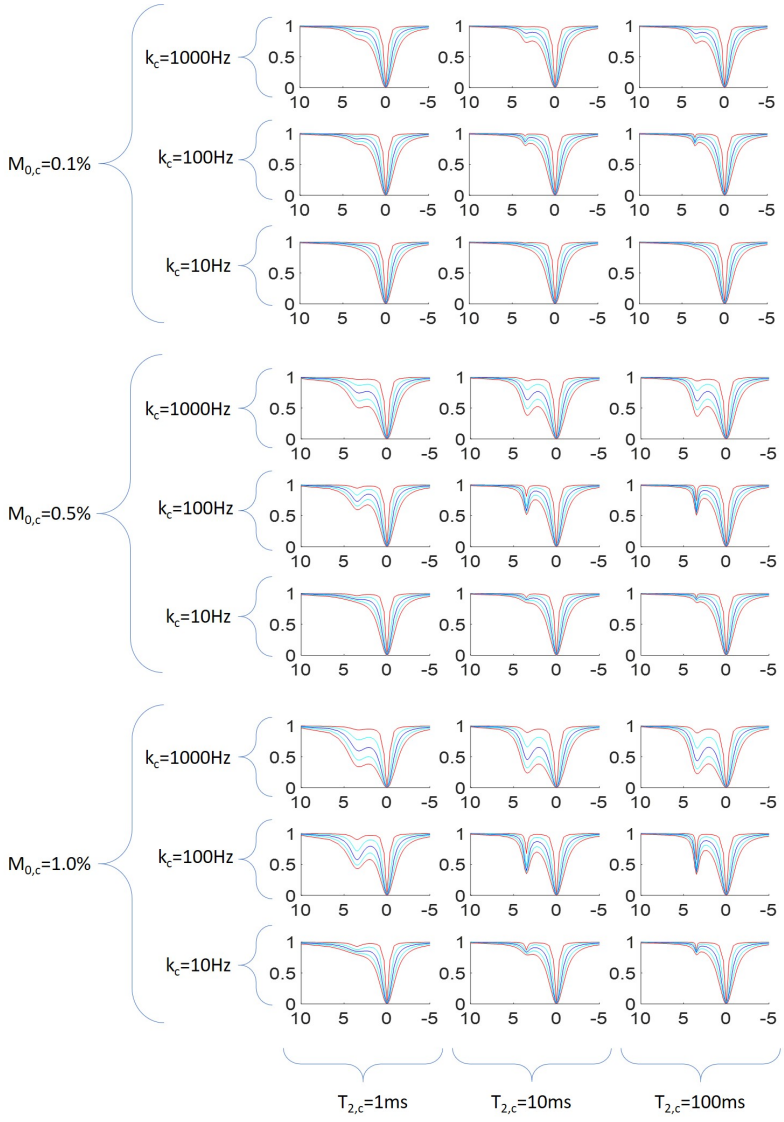

Figure 4.2.1: Simulated z-spectra with a range of CEST pool sizes, exchange rates, and apparent T_2s.

all areas the z-PSO fails to fit accurately, as can be seen in Figure 4.2.5, which shows the overlaid spectra simulated from the results of the trial fits as solid lines, with the original noiseless datasets as red 'x's.

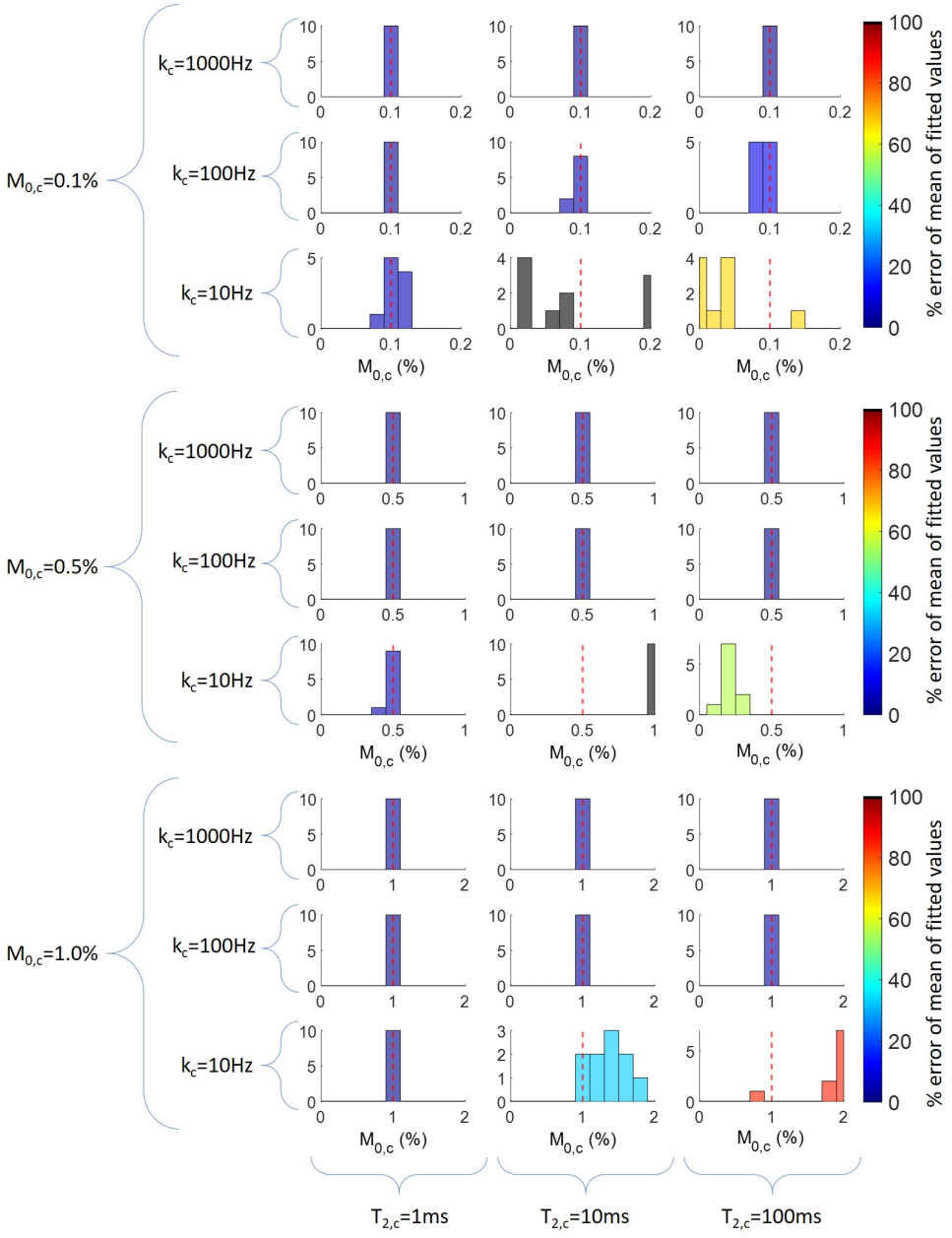

Figure 4.2.2: Variation in fitted value of the CEST pool size for varying pool sizes, exchange rates, and T_2s. The red dotted line shows the actual value used when simulating the spectra, and bar colour shows the percentage error of the mean fitted data compared to the target value.

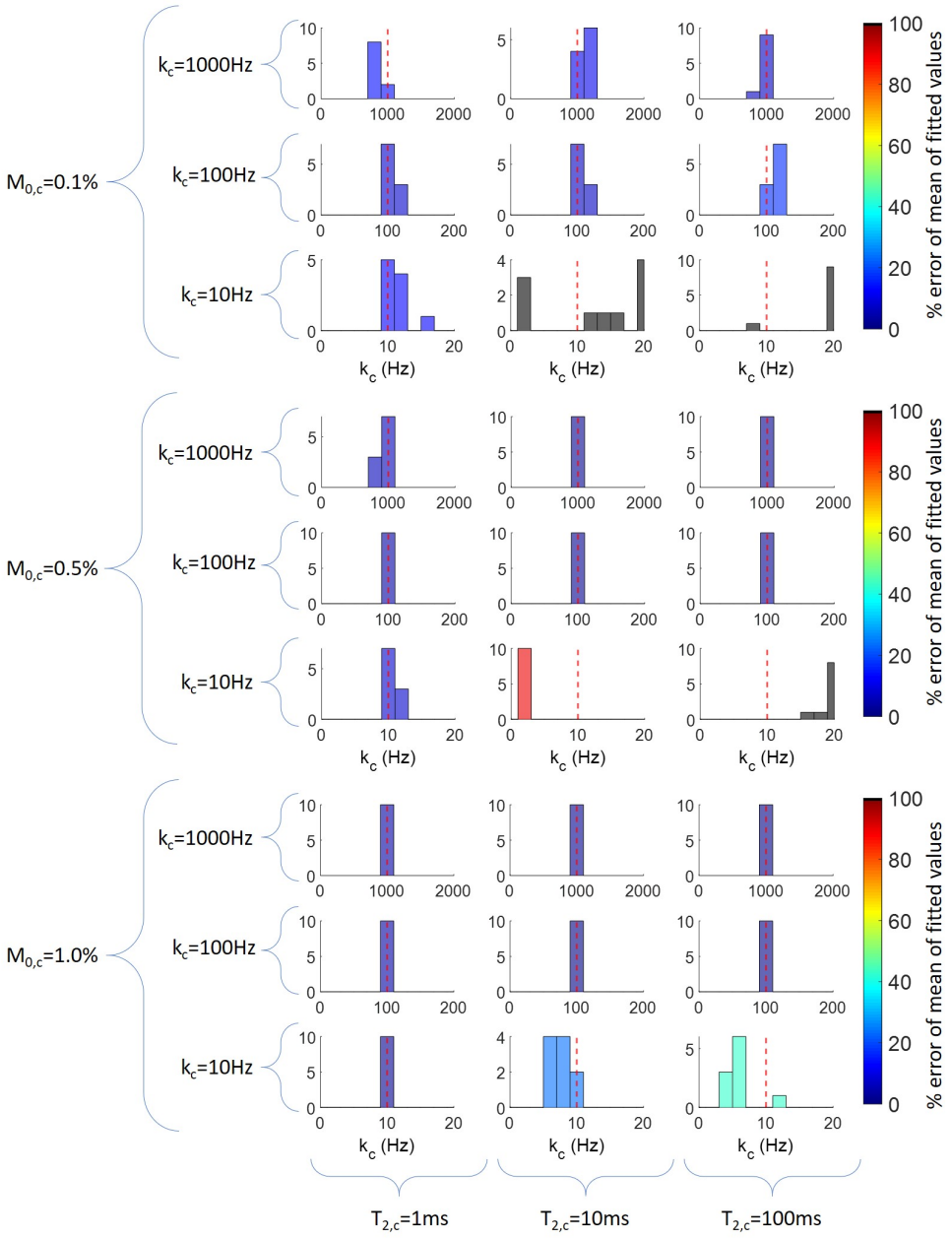

Figure 4.2.3: Variation in fitting CEST exchange rate for varying pool sizes, exchange rates, and T_2s. The red dotted line shows the actual value used when simulating the spectra, and bar colour shows the percentage error of the mean fitted data compared to the target value.

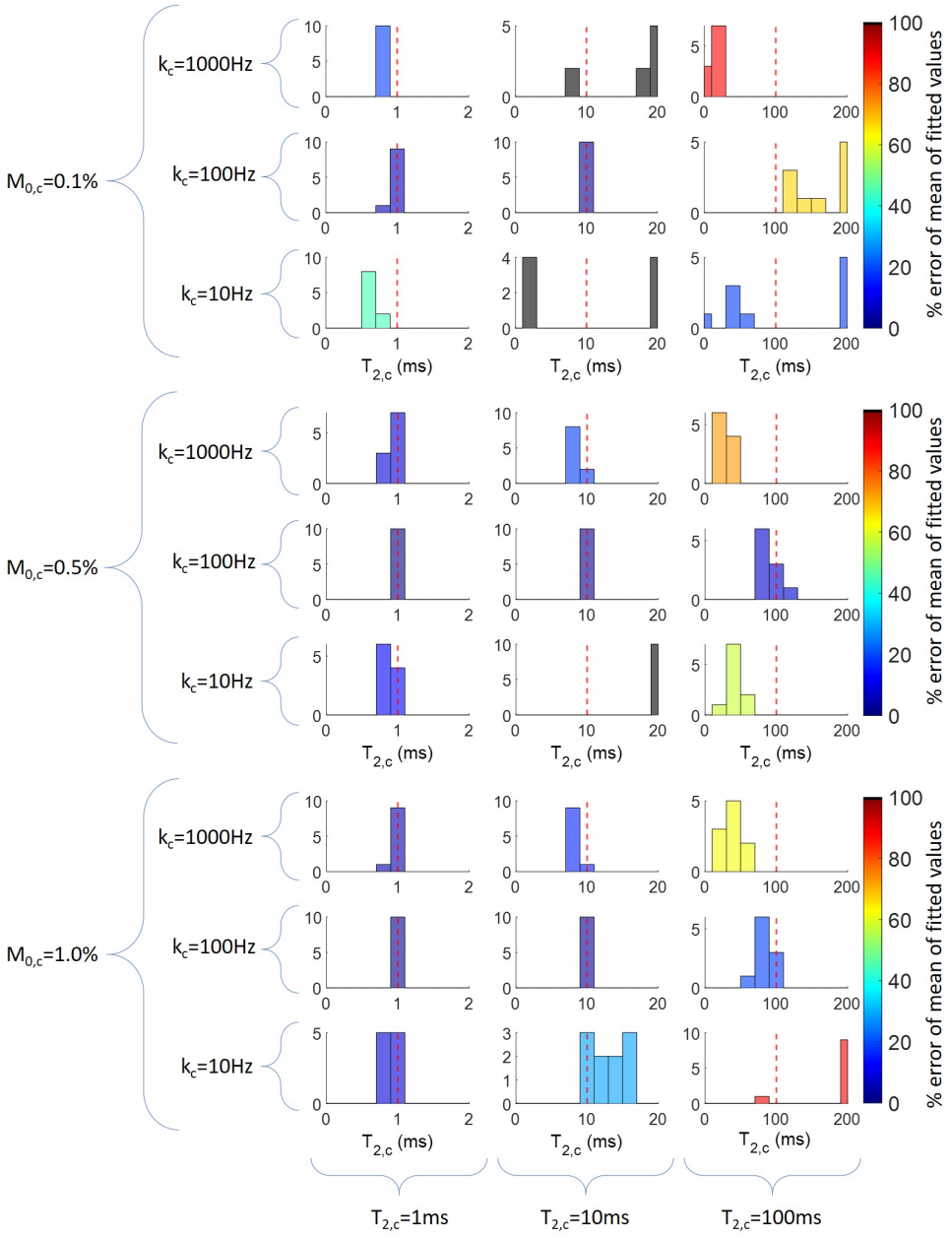

Figure 4.2.4: Variation in fitting CEST apparent T_2 for varying pool sizes, exchange rates, and T_2s. The red dotted line shows the actual value used when simulating the spectra, and bar colour shows the percentage error of the mean fitted data compared to the target value.

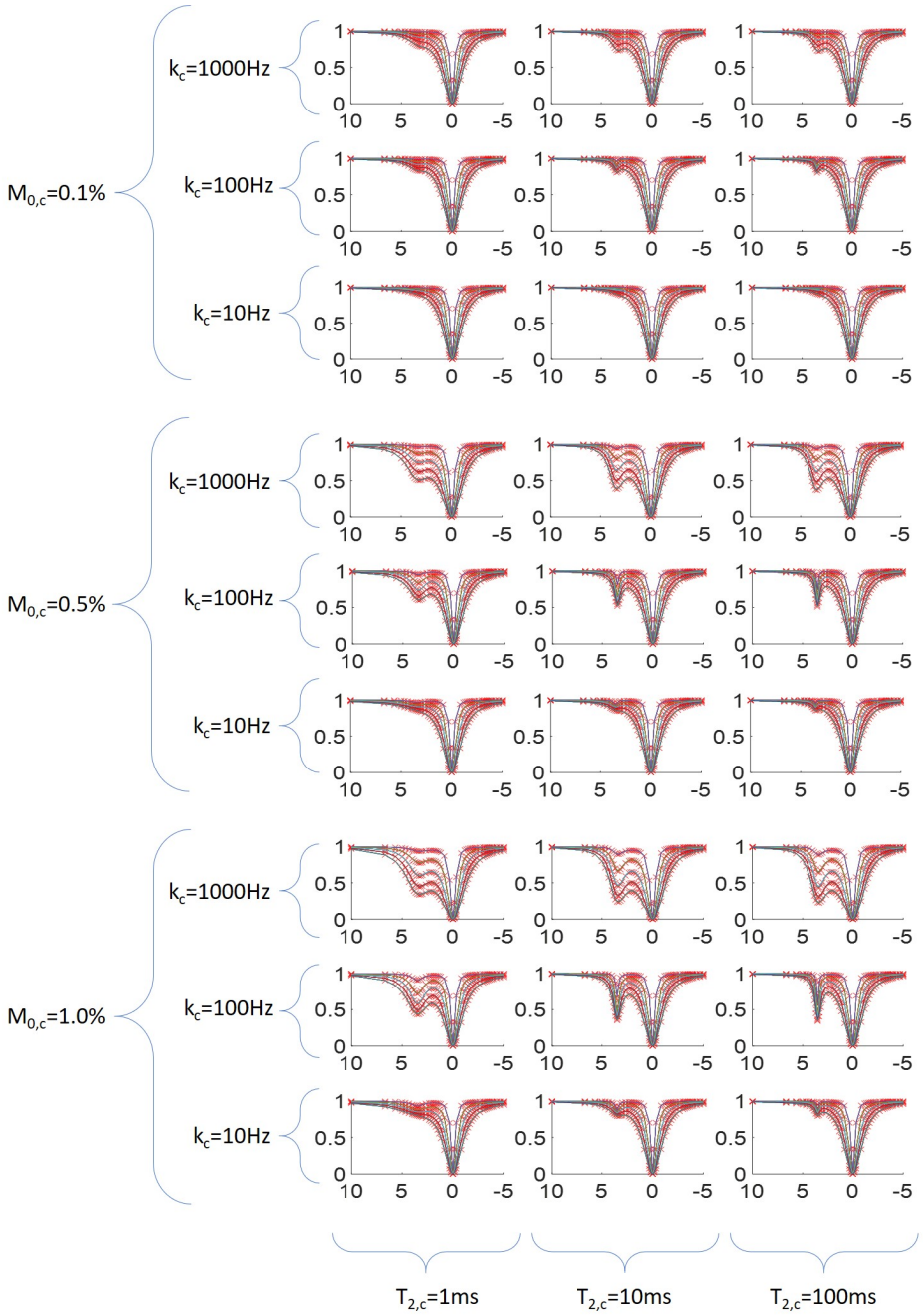

Figure 4.2.5: Overlaid fits created from the simulated results (solid lines) compared to the original simulations (red 'x's).

4.2.2 MT fitting capabilities

A similar test was then performed to ensure that a) MT could be fitted accurately, and b) the fitting of exchanging pools was not affected by other underlying pools. Z-spectra were fitted using the same basic parameters, but this time using a 3 pool model (free water, MT, and one CEST pool located at +3.5ppm). The values of the CEST pool were fixed at $M_{0,c} = 1\%$, $k_c = 100Hz$, and $T_{2,c} = 10ms$, while the values of the MT pool were varied between small, medium and large pool size (1%, 5%, and 10%), slow, medium and fast exchange rate (1Hz, 10Hz, and 100Hz), and short, medium and long T_2 ($50\mu s$, $100\mu s$, and $200\mu s$).

Results of fitting the MT pool size are displayed in Figure 4.2.6. The z-PSO fits the data with very little error apart from at very slow exchange rates with small pool sizes.

Figure 4.2.7 shows the results of fitted MT exchange rate. The z-PSO struggles to fit the exchange rate correctly when there is very little MT present.

Figure 4.2.8 shows the results of fitted $T_{2,b}$ for each of the datasets. Again the z-PSO only struggles when there is little MT present, and even then only at slow exchange rates.

Figure 4.2.9 shows the overlaid spectra simulated from the results of the trial fits as solid lines, with the original noiseless datasets as red 'x's, showing again that the z-PSO fits the spectra very well, and only struggles when changing the parameters would not affect the shape of the z-spectrum, meaning the pools are impossible to fit further without additional data.

To check that the presence of the MT pool is not biasing the CEST results, Figure 4.2.10 shows the results of the fitted CEST pool for each of the datasets, showing variation in $M_{0,c}$, k_c, and $T_{2,c}$.

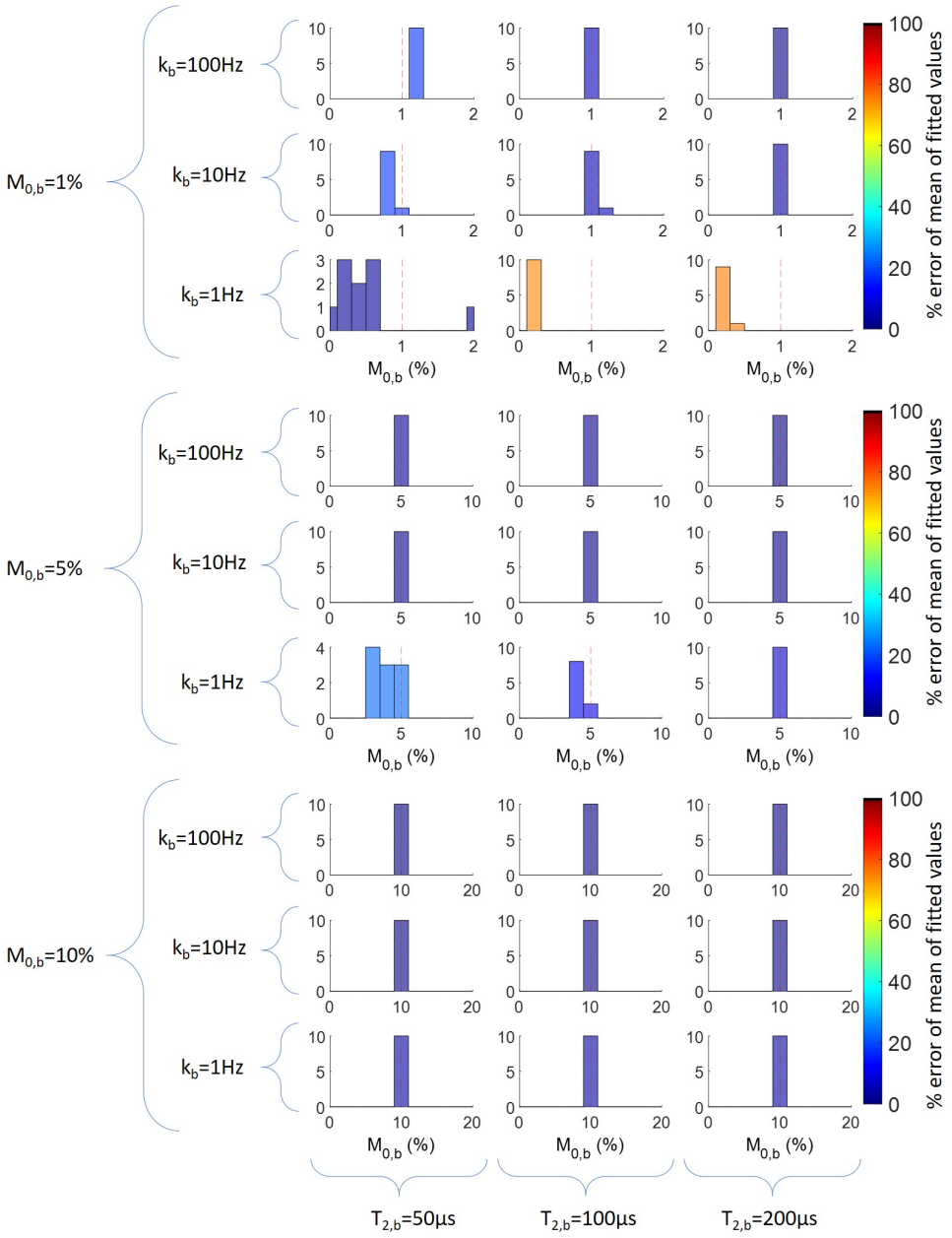

Figure 4.2.6: Variation in fitting MT pool size for varying pool sizes, exchange rates, and T_2s. The red dotted line shows the actual value used when simulating the spectra, and bar colour shows the percentage error of the mean fitted data compared to the target value.

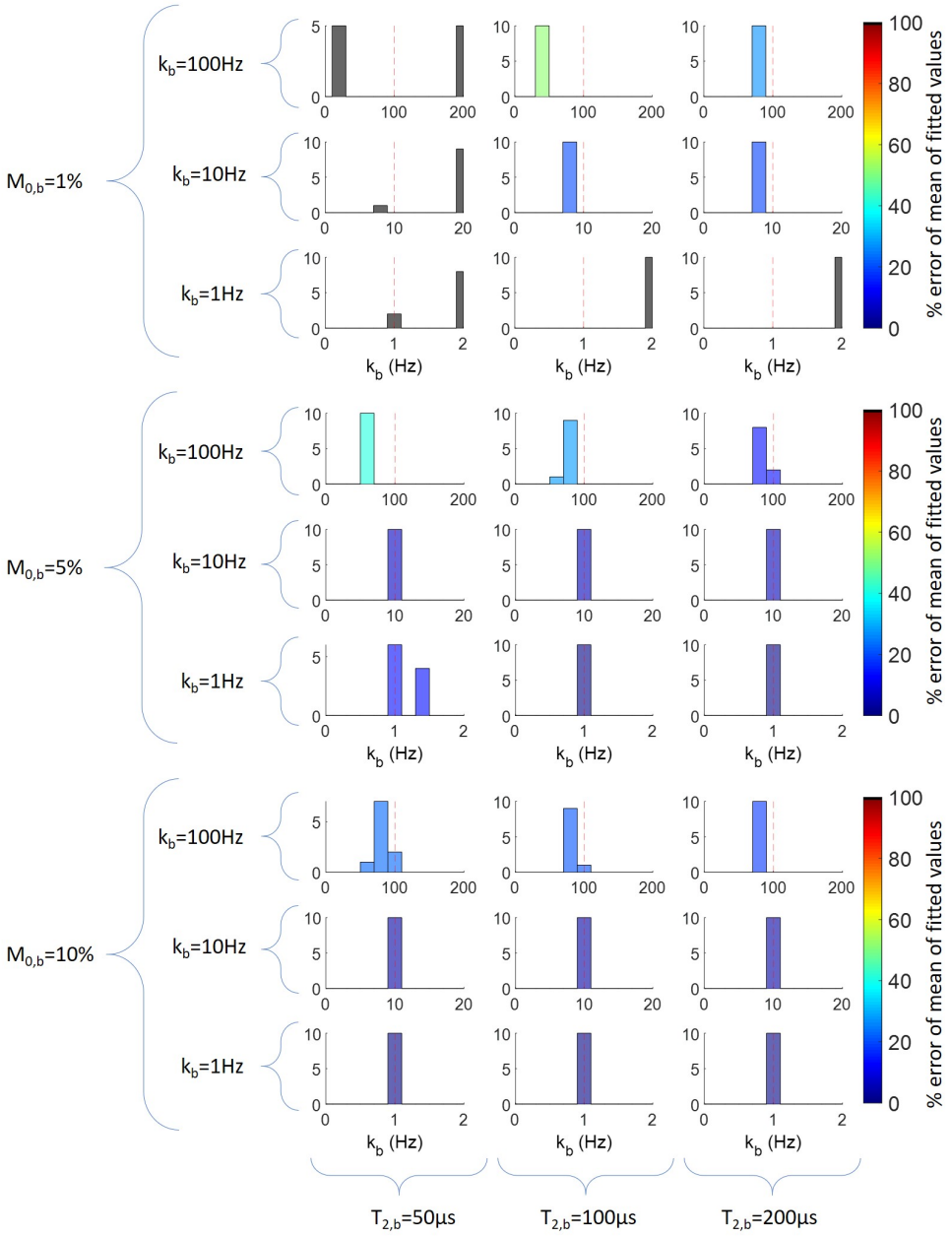

Figure 4.2.7: Variation in fitting MT exchange rate for varying pool sizes, exchange rates, and T_2s. The red dotted line shows the actual value used when simulating the spectra, and bar colour shows the percentage error of the mean fitted data compared to the target value.

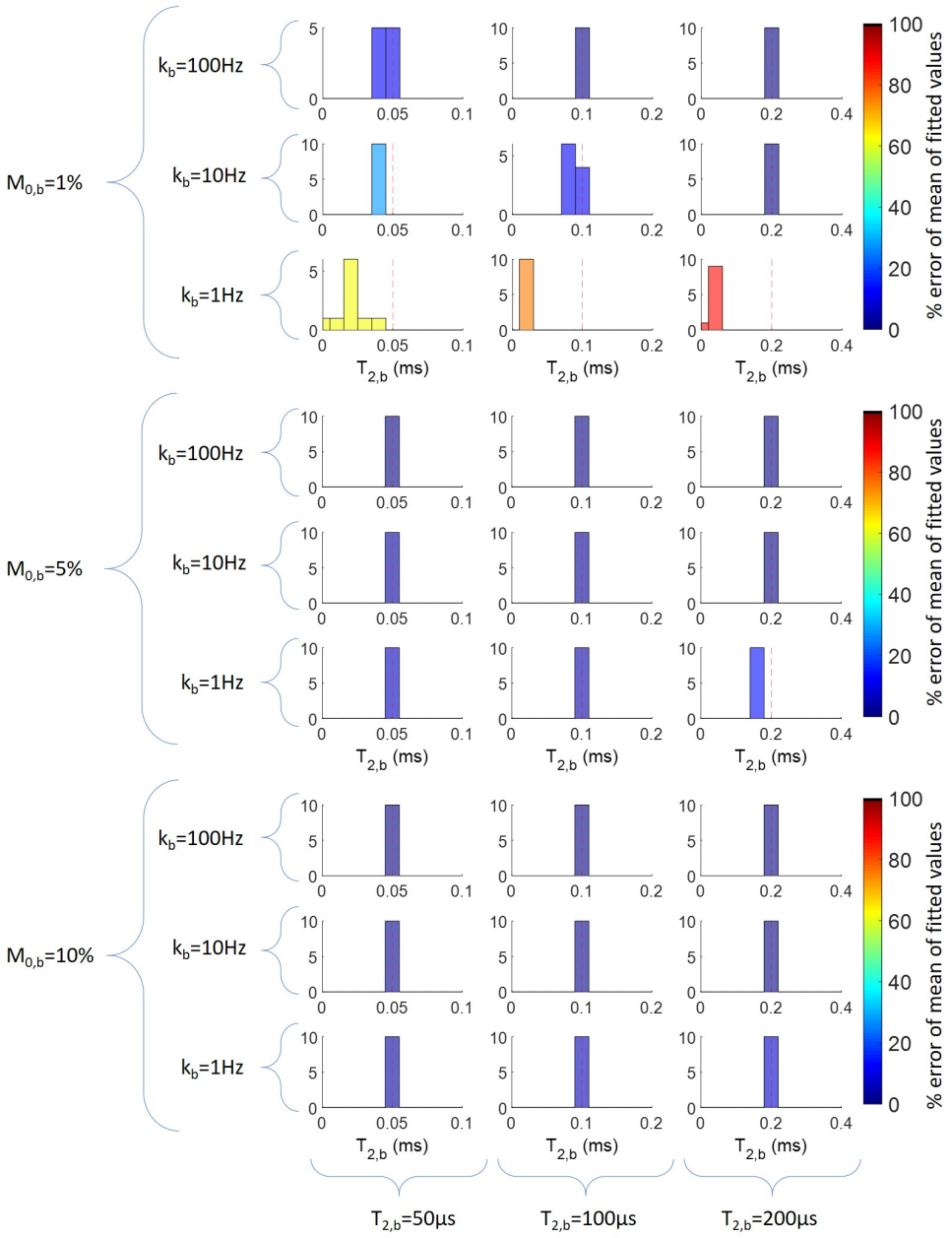

Figure 4.2.8: Variation in fitting MT apparent T_2 for varying pool sizes, exchange rates, and T_2s. The red dotted line shows the actual value used when simulating the spectra, and bar colour shows the percentage error of the mean fitted data compared to the target value.

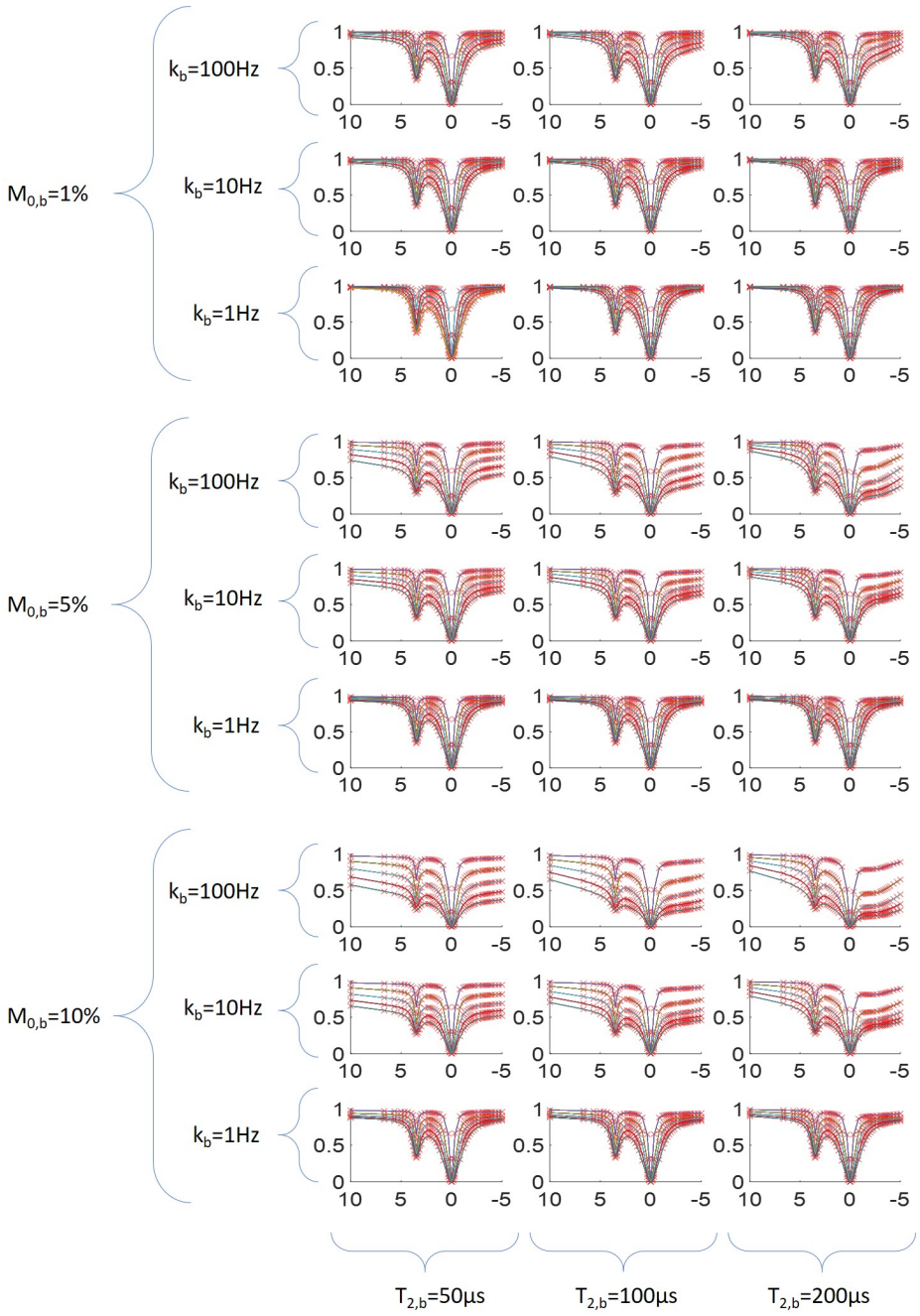

Figure 4.2.9: Overlaid fits created from the simulated results (solid lines) compared to the original simulations (red 'x's).

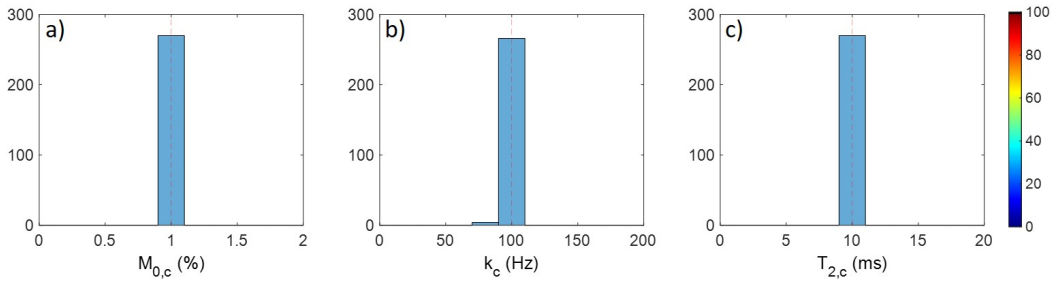

Figure 4.2.10: Variation in fitting the a) pool size, b) exchange rate, and c) T_2 of the CEST pool when underlying MT is present, showing that including an underlying MT pool in the fit does not cause systematic or random errors in the fitting of CEST pools.

4.3 Quantification of the z-spectrum of creatine phantoms

To validate the z-PSO using real data, creatine phantoms were used, as creatine has been shown to have a strong CEST signal resonating at +2.0ppm [9]. Three creatine phantoms were created by dissolving 1g of creatine in 100ml of water. This solution was then split into three and buffered to pH 5.5, 7.0, and 8.5 respectively using phosphate buffer solution. Solutions were tested using pH strips (Simplex Health) to ensure they closely matched the targeted pH. 6ml of each solution was then extracted and placed in a sealed test tube to create the three phantoms. By varying both the pH and temperature of creatine in solution, we should be able to observe a change in exchange rate.

4.3.1 Z-spectrum acquisition at 7T

The three phantoms were placed in a water bath connected to an external heat pump, and the water bath was placed inside a NOVA 8ch pTx head coil inside a 7T Achieva system. The heat pump remained outside of the scanner room due to its metallic

components, and plastic tubes were passed through a hole in the wall connecting it to the water bath. The water bath was heated to $40°$C before scanning.

As we were unable to perform CW saturation, instead we used semi-CW saturation, as described in section 2.3.1. In order for this to be an acceptable replacement, we must first ensure that the RF output from the odd and even channels are matched. Following a survey scan of the sample, two B_1 maps were acquired, one using only the odd channels and one using only the even channels. The RF power in a central region of interest in the sample was compared between the two maps, and individual channels could be tuned so that the RF power matched. If necessary, a set of two repeat maps was acquired until the RF power from the odd channels was equal to the RF power from the even channels, within a 5% margin.

Once the coils had been appropriately tuned, B_0 and B_1 maps of the sample were acquired. The water bath was then switched off and allowed to settle for 2 minutes, as it was found that flow around the samples affected the signal in the z-spectrum. Z-spectra were acquired at 64 off-resonance frequencies between $\pm 100,000$Hz with a 3 second saturation train comprised of 60 alternating odd / even blocks of 50ms, and a voxel size of 1x1x3mm (with the longest dimension aligned with the test tube). 3 z-spectra were acquired, at a $B_{1,max}$ of 0.5μT, 1.0μT, and 1.5μT, with the acquisition of each spectrum taking under 10 minutes (3s saturation, 1.7s readout, 4.3s recovery for each acquired point on the z-spectrum). Between each z-spectrum acquisition, the water pump was temporarily switched back on to heat the water bath back to $40°$C, as the bath usually cooled by $1-2°$C during each acquisition, before switching it off and allowing the water to settle again. After acquiring these three z-spectra, the water bath was cooled to $30°$C and the three z-spectra were re-acquired in the same way. This was repeated at $20°$C and finally at $10°$C.

After acquisition, each of the 12 spectral images were processed using in-house functions written in MATLAB [6]. Each of the three phantoms were masked to produce 12 datasets of varying pH and temperature, each comprising of three z-spectra at different saturation powers. The first acquired point in each z-spectrum was discarded,

as we found in practice this point always had a lower signal than the next acquired point at the same offset frequency, potentially due to the system still approaching the steady-state. These datasets were then B_0 corrected by shifting the z-spectrum in each pixel by the value of the field offset in the corresponding pixel in the acquired B_0 map. Finally, z-spectra were normalised by dividing each point in the z-spectrum by the point acquired at +333ppm. It was assumed that this signal is equivalent to the sample after no saturation (S_0), as there are no exchanging pools to be saturated this far off resonance. Figure 4.3.1 shows the processed spectra acquired from the three creatine phantoms at varying temperature.

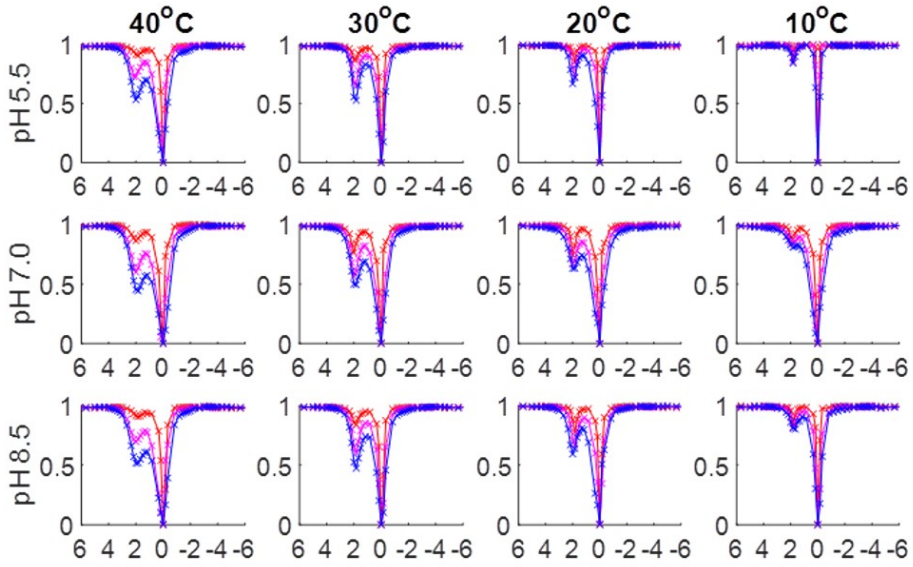

Figure 4.3.1: Z-spectra from three creatine phantoms at varying pH, acquired at a range of temperatures, with a saturation power of 0.5μT (red), 1.0μT (magenta), and 1.5μT (blue).

4.3.2 Quantification results

These z-spectra were then fitted using the z-PSO adapted to a 2 pool model, with the creatine peak position allowed to vary between +1.9ppm and +2.1ppm. The pool

size, exchange rate, and apparent T_2 of creatine were all given wide bounds. $M_{0,c}$ was allowed to vary between $0-5\%$, k_c was allowed to vary between 1-5000Hz, and $T_{2,c}$ was allowed to vary between 0.5-100ms. Results of this fit are presented in Table 3.3.1.

	40°C			30°C			20°C			10°C		
	M_0 (%)	k (Hz)	T_2 (ms)	M_0 (%)	k (Hz)	T_2 (ms)	M_0 (%)	k (Hz)	T_2 (ms)	M_0 (%)	k (Hz)	T_2 (ms)
pH 5.5	0.57	797	>100	0.44	270	39.1	0.26	226	24.3	0.19	61	76.6
pH 7.0	0.18	729	>100	0.19	345	>100	0.19	192	93.0	0.10	117	14.7
pH 8.5	0.19	905	>100	0.20	360	>100	0.18	255	17.2	0.17	79	96.6

Table 4.3.1: Results of fitting z-spectra from creatine phantoms

All of the $T_{2,c}$ fits hit the upper bounds, since as we have shown previously in this "long $T_{2,c}$" regime, variations in $T_{2,c}$ do not affect the shape of the z-spectrum and so are undetectable. The $M_{0,c}$ values are all expected to be roughly the same, however there are certain areas where the fit differs from the most commonly measured 0.2% (it is difficult to calculate what the 'true' value should be due to packing of molecules and availability of proton exchange sites). For example in the pH 5.5 phantom at 40°C the $M_{0,c}$ is clearly too high, however we have shown that there is not enough information for a reliable fit at such short exchange rates.

Figure 4.3.2 shows exchange rate variation with temperature in each of the pH phantoms. We can see clear differences in exchange rate with temperature here, however we cannot separate pH values using this particular dataset. This could potentially be achieved by scanning phantoms with a higher creatine content.

Recent work has demonstrated that the presence of phosphates catalyses CEST agents [10]. This results in the altering of the visible CEST contrast, as in this case the exchangeable amine protons present in creatine may be preferring to exchange with the PBS, therefore obscuring some of the CEST contrast which would be visible

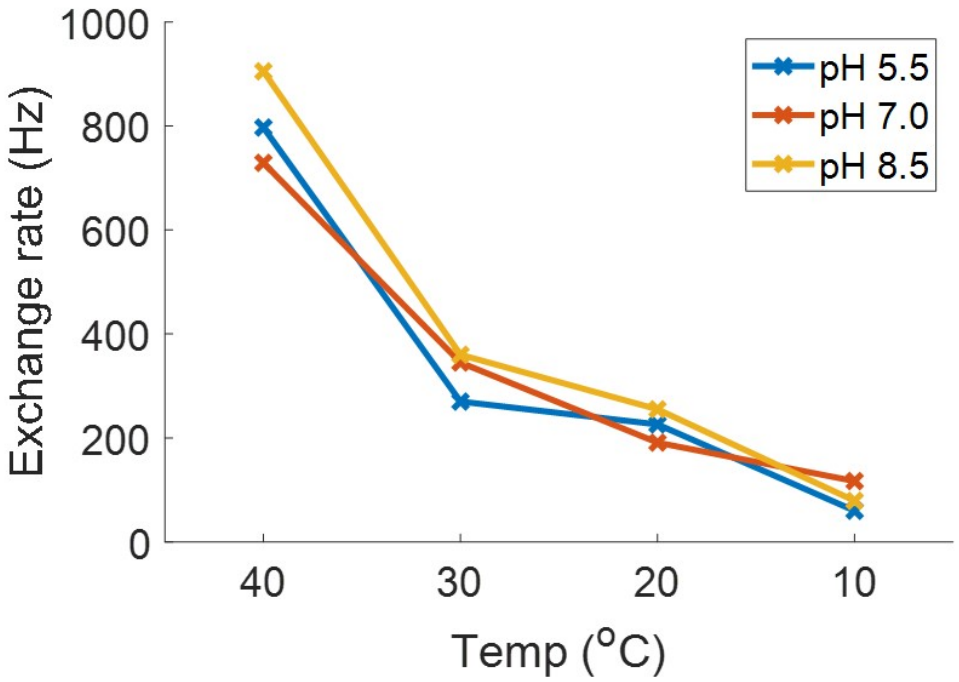

Figure 4.3.2: Exchange rate variation with temperature, following a roughly exponential decline. Different pHs do not display a discernible difference in exchange rate.

through exchange with free water. This may be the reason why there is no discernible difference between the CEST contrast at different pH levels.

This section has applied the z-PSO fitting method to real data, with successful results. While pH was unable to be determined through exchange rate fitting, the creatine exchange rate follows a roughly exponential decline with temperature, which is as expected as defined by the Arrhenius equation stated previously in section 2.2.2.

4.4 Quantification of *in vivo* cerebral grey and white matter

The human brain is an area of great interest when it comes to z-spectroscopy, due to the fact that it contains a range of CEST sensitive metabolites, and also pH sensitive changes are often indicative of serious physiological conditions such as ischaemic stroke [11]. Attempts to quantify the z-spectrum in the human brain have been made previously using some of the quantification methods described in section 2.5. For example, using the look-up table described in section 2.5.2 and used in chapter 3, the MT, amide, and NOE(+3.5ppm) pool size has been quantified for both grey and white matter [12]. Another study using a trust-region-reflective algorithm to quantify all three parameters for MT, amide, and NOE pools finds somewhat similar results [13]. However the authors concede that by using a trust-region-reflective algorithm their solutions are biased by their initial guesses. Table 3.4.1 shows a summary of the results published in these two studies.

4.4.1 Acquisition and post-processing of spectra

Following local ethical approval, 6 healthy volunteers (4 female, age 24$\pm$1 years) were recruited for the study. Subjects were scanned in a 7T Achieva system using a NOVA 8ch pTx head coil, and the same tuning steps used to match the RF output on the odd and even channels was followed. B_0 and B_1 maps were acquired as before. Z-spectra were acquired using the same settings as for the creatine phantoms, except with different B_1 values used for the saturation train. Here 5 spectra were acquired with a B_1 of 0.33, 0.67, 1.00, 1.33, and 1.67μT respectively. Subjects were encouraged to watch television during the scan, partly to alleviate boredom over the 60 minute scan time, but also because there have anecdotally been reports that watching television reduces head motion (this has been proven in children under the age of ten [14]). This was achieved by the subject wearing periscopic glasses allowing them to see out of

			MT	Amides	NOE
M_0 (%)	GM	Geades	4.4 ± 0.4	0.20 ± 0.02	3.0 ± 0.1
		Liu	3.462 ± 0.42	0.25 ± 0.05	1.18 ± 0.16
	WM	Geades	8.9 ± 0.3	0.21 ± 0.03	5.0 ± 0.1
		Liu	6.18 ± 0.43	0.22 ± 0.04	2.39 ± 0.22
k (Hz)	GM	Geades	Fixed at 50	Fixed at 200	Fixed at 10
		Liu	63.48 ± 4.5	281.93 ± 0.87	24.5 ± 1.65
	WM	Geades	Fixed at 50	Fixed at 200	Fixed at 10
		Liu	67.5 ± 6.98	281.21 ± 0.6	27.45 ± 2.18
T_2 (ms)	GM	Geades	Fixed at 0.009	Fixed at 10	Fixed at 0.3
		Liu	0.10428 ± 0.00380	28.54 ± 7.14	402.7 ± 25.48
	WM	Geades	Fixed at 0.009	Fixed at 10	Fixed at 0.3
		Liu	0.0838 ± 0.0015	22.7 ± 5.8	0.3180 ± 0.0073

Table 4.4.1: Literature results of fitted z-spectra parameters [12, 13].

the bore and look at a projection screen. Figure 4.4.1 shows sample spectral images acquired from one of the subjects at 1.67μT. A high resolution T_1 weighted anatomical image was also acquired for motion correction purposes.

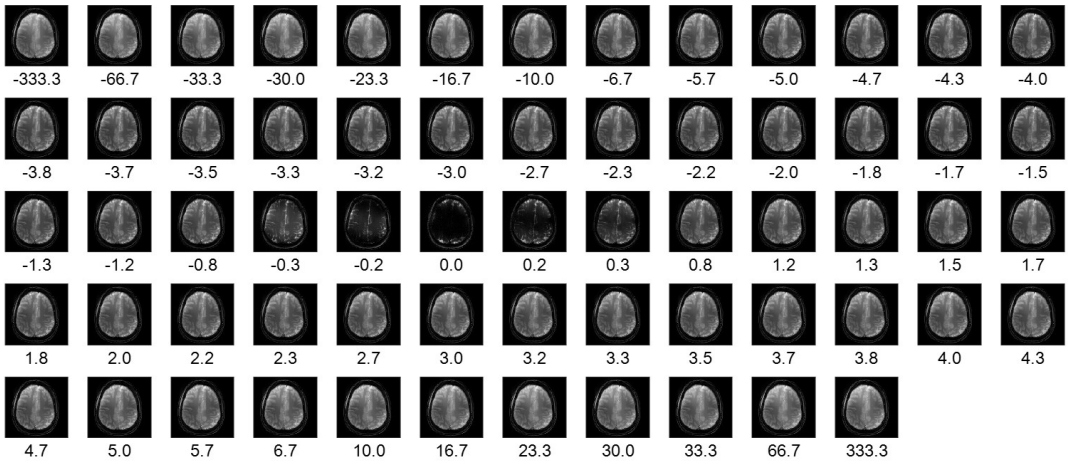

Figure 4.4.1: A central slice of the spectral images acquired from one subject at 1.67μT, with corresponding frequency offset in ppm displayed underneath.

After acquisition, spectral images were motion corrected using the `MCFLIRT` tool in FSL [15, 16, 17], which transforms the spectral images so that they are mapped onto the first acquired spectral image, meaning that motion between z-spectral images acquired is minimised. Spectral images were then motion corrected using `FLIRT` (FMRIB's Linear Image Registration Tool), which transformed the spectral images so that they were in the same image space as the high resolution anatomical image. This anatomical image was then masked using `FAST` (FMRIB's Automated Segmentation Tool) [18], to create high resolution grey matter and white matter masks. If a pixel lay on the boundary between grey and white matter, it was excluded. These masks were then applied to the spectral images, which were B_0 corrected and averaged using in-house MATLAB code, to create an average grey matter and an average white matter set of spectra for each subject. These spectra are displayed in Figure 4.4.2.

The grey matter and white matter masks were then applied to the B_1 map and averaged to give an average value of B_1 inhomogeneity in the grey matter and white matter of each subject. This is later multiplied by the targeted RF powers to give the true B_1 values of each spectrum.

4.4.2 Quantification results

The grey matter and white matter spectra for each subject were fitted using the z-PSO adapted to a six pool model comprising of free water (0ppm), MT (-2.34ppm), amides (+3.5ppm), amines (+2.0ppm), NOE (-3.5ppm), and a second NOE (-1.7ppm). This was decided based on the observable peaks in the acquired spectra.

Table 4.4.2 shows the results of fitting these spectra. The values in this table are averaged across subjects, and the error stated is the standard deviation of the fitted values across subjects.

Figure 4.4.3 shows the results of fitting the MT pool in grey matter and white matter for each subject, and the results of the two tailed t-test between the two. There is a

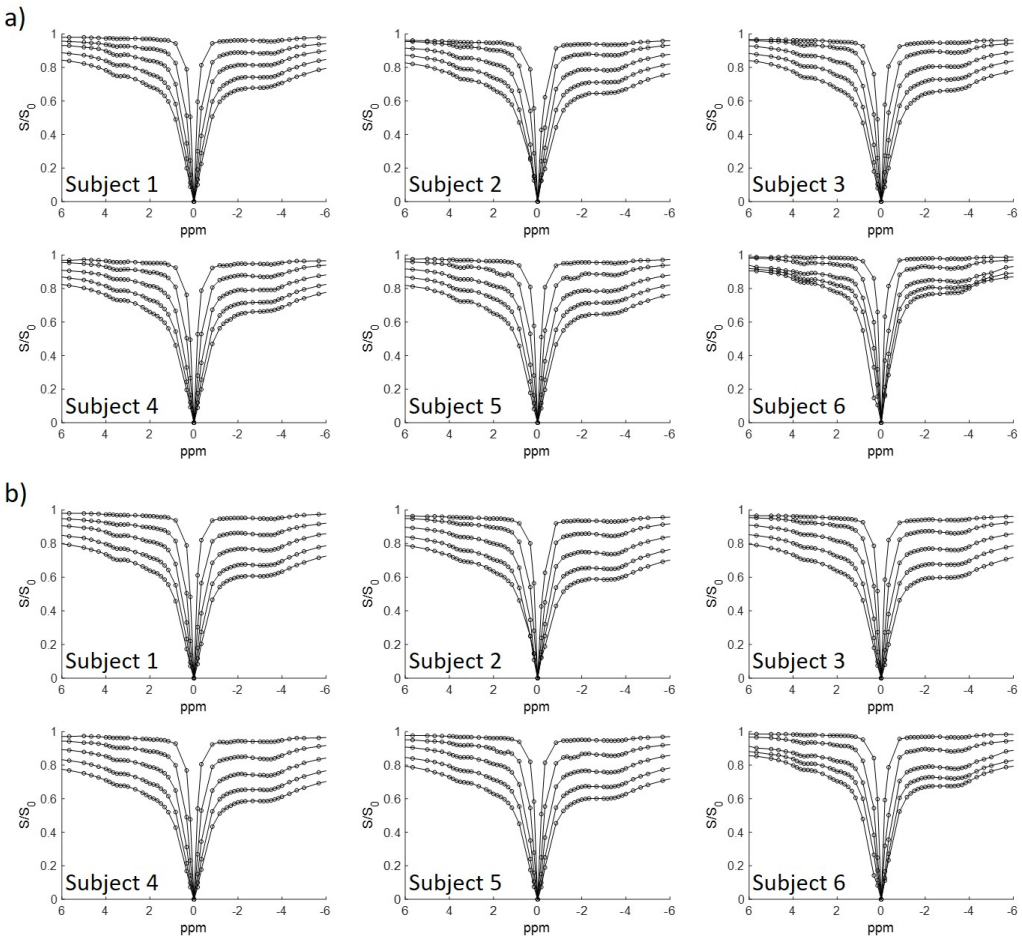

Figure 4.4.2: Averaged spectra from a) GM, and b) WM voxels in each subject

significant difference between MT pool size in grey matter and white matter.

Figure 4.4.4 shows the results of fitting the amide pool in grey matter and white matter for each subject, and the results of the two tailed t-test between the two. There are no significant differences here between grey matter and white matter. One $T_{2,c}$ value in subject 4's white matter appears to have fit poorly, which skews the mean result in table 4.4.1.

Figure 4.4.5 shows the results of fitting the amine pool in grey matter and white matter for each subject, and the results of the two tailed t-test between the two.

4.4. QUANTIFICATION OF *IN VIVO* CEREBRAL GREY AND WHITE MATTER

There are no significant differences here between grey matter and white matter.

Figure 4.4.6 shows the results of fitting the NOE pool located at -3.5ppm in grey matter and white matter for each subject, and the results of the two tailed t-test between the two. There are no significant differences here between grey matter and white matter. Again one $T_{2,n}$ value in subject 6's grey matter appears to have fit poorly.

Figure 4.4.7 shows the results of fitting the second NOE pool located at -1.7ppm in grey matter and white matter for each subject, and the results of the two tailed t-test between the two. There is a significant difference between the NOE(-1.7ppm) pool size in grey matter and white matter. One k_c value in subject 5's grey matter appears to have fit poorly.

Figure 4.4.8 shows the fitted spectra in a) grey matter, and b) white matter, showing that the z-PSO has accurately fitted the acquired spectra, and values which appear to have fit poorly are likely down to noise in the acquired data rather than poor performance of the z-PSO.

		MT	Amides	Amines	NOE (-3.5ppm)	NOE (-1.7ppm)
M_0 (%)	GM	5.32 ± 0.30	0.18 ± 0.07	0.30 ± 0.50	0.26 ± 0.05	0.04 ± 0.01
	WM	7.25 ± 0.49	0.10 ± 0.06	0.85 ± 0.89	0.42 ± 0.05	0.03 ± 0.01
k (Hz)	GM	6.96 ± 2.85	136 ± 97	74 ± 106	65 ± 59	317 ± 265
	WM	7.37 ± 2.43	354 ± 342	46 ± 75	38 ± 10	200 ± 54
T_2 (ms)	GM	0.0091 ± 0.0015	0.51 ± 0.03	4 ± 6	0.90 ± 0.16	13 ± 23
	WM	0.080 ± 0.008	17 ± 41	12 ± 12	0.81 ± 0.05	3.7 ± 1.4

Table 4.4.2: Fitted values averaged across subjects ± one standard deviation.

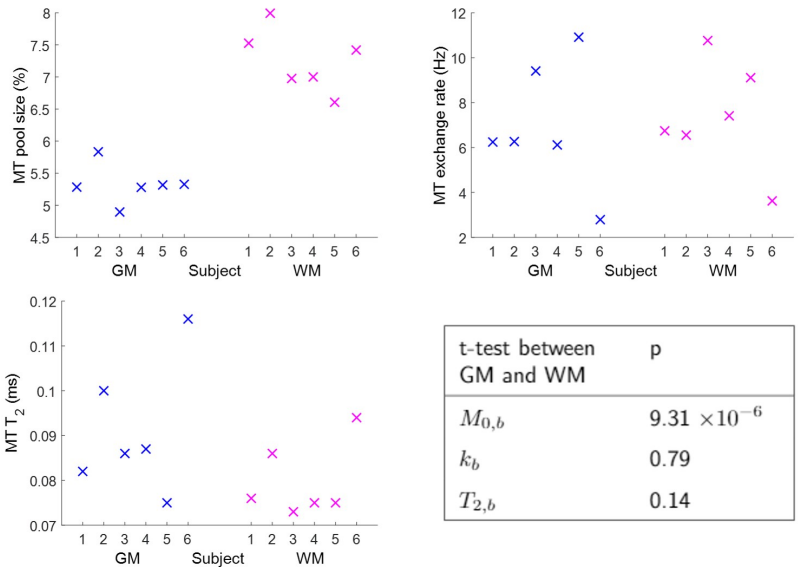

t-test between GM and WM	p
$M_{0,b}$	9.31×10^{-6}
k_b	0.79
$T_{2,b}$	0.14

Figure 4.4.3: Results of fitting the MT pool in each subject for grey matter and white matter.

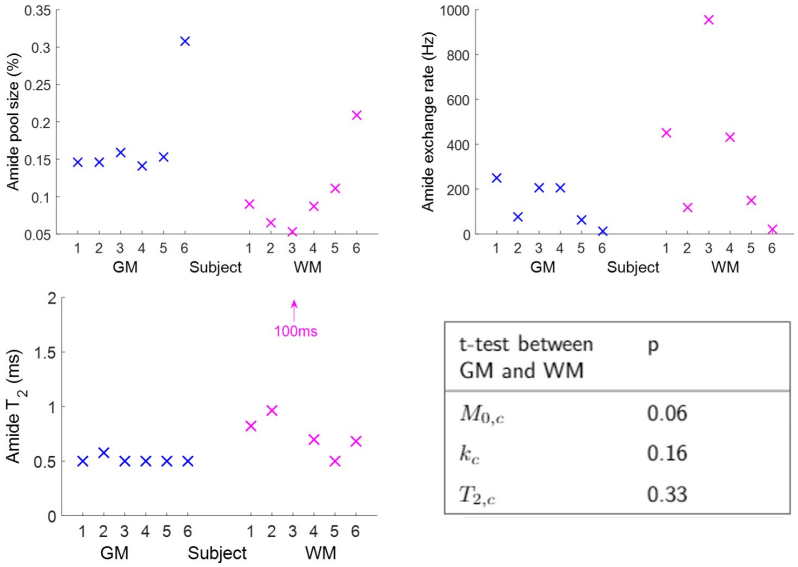

t-test between GM and WM	p
$M_{0,c}$	0.06
k_c	0.16
$T_{2,c}$	0.33

Figure 4.4.4: Results of fitting the amide pool in each subject for grey matter and white matter

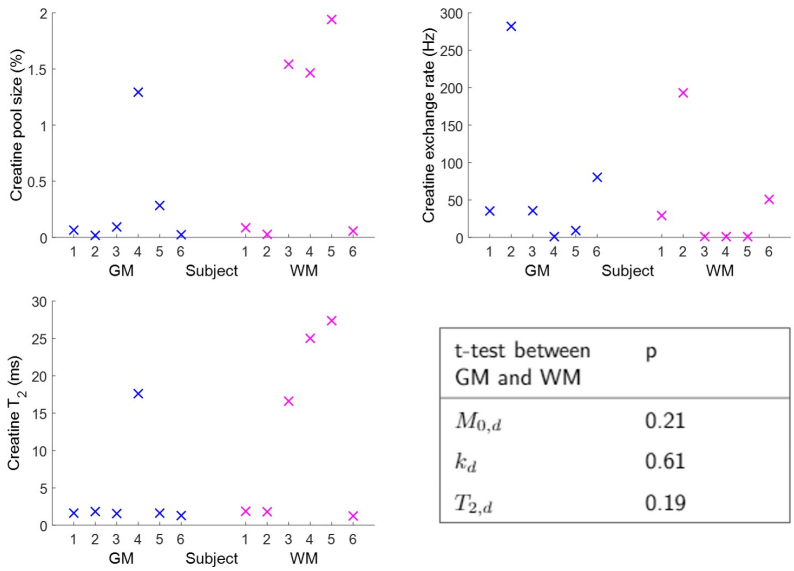

t-test between GM and WM	p
$M_{0,d}$	0.21
k_d	0.61
$T_{2,d}$	0.19

Figure 4.4.5: Results of fitting the amine pool in each subject for grey matter and white matter

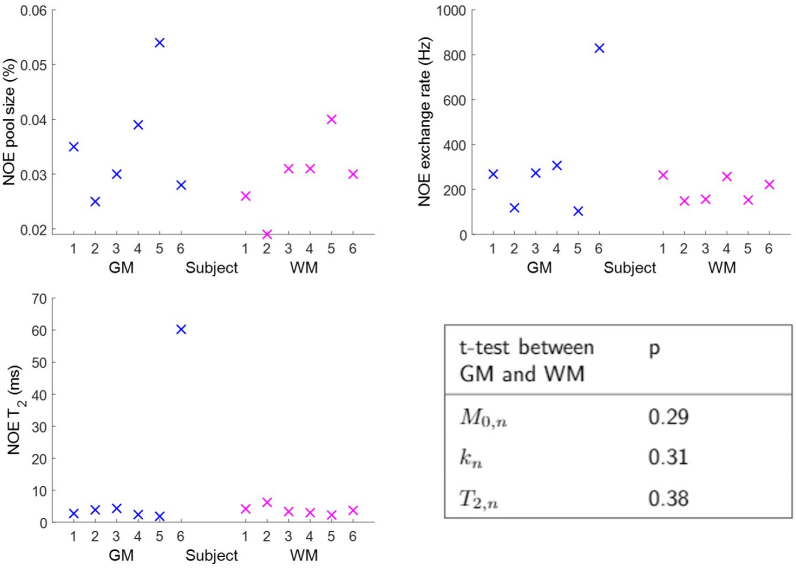

t-test between GM and WM	p
$M_{0,n}$	0.29
k_n	0.31
$T_{2,n}$	0.38

Figure 4.4.6: Results of fitting the NOE pool located at -3.5ppm in each subject for grey matter and white matter

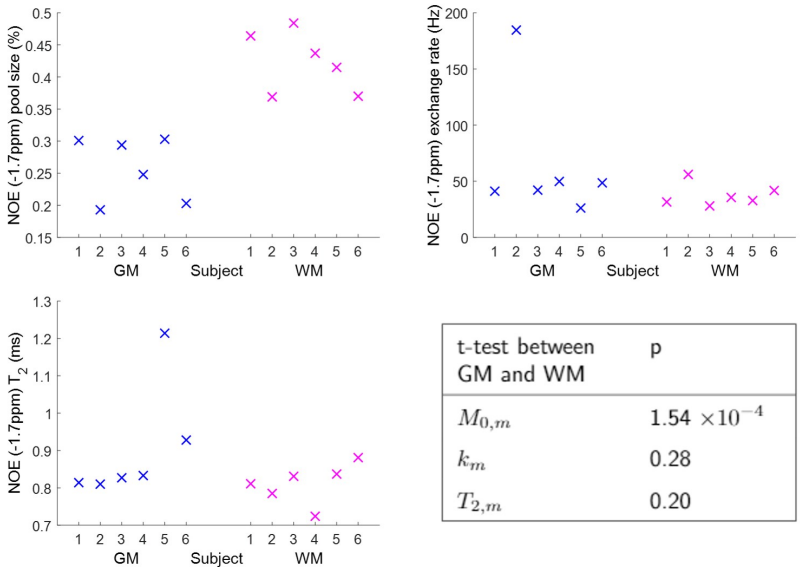

t-test between GM and WM	p
$M_{0,m}$	1.54×10^{-4}
k_m	0.28
$T_{2,m}$	0.20

Figure 4.4.7: Results of fitting the second NOE pool located at -1.7ppm in each subject for grey matter and white matter

4.4.3 Discussion

The results of this fit agree with previous results in some areas and disagree in others. The MT pool size is slightly above that reported by Geades [12] or Liu [13] as mentioned previously, but there are reports of MT pool size being measured as 10% [19, 20] or higher [21, 22]. These latter two studies use two pool models, and therefore are inclined to overestimate the MT pool size by also measuring the NOE pool in their MT measurement. We confirm previous findings that MT pool size is higher in white matter than in grey matter [12, 13], which is primarily due to white matter being more heavily myelinated than grey matter.

Our amide results agree with Liu [13], although admittedly with a higher variance in the exchange rate between subjects. This may however reflect that their results are influenced by their starting points using the trust-region-reflective algorithm. Elsewhere the exchange rate of the amide pool has been quoted as 616 ± 29Hz in grey matter and 575 ± 20Hz in white matter [23], and in a separate study as 365 ± 23Hz

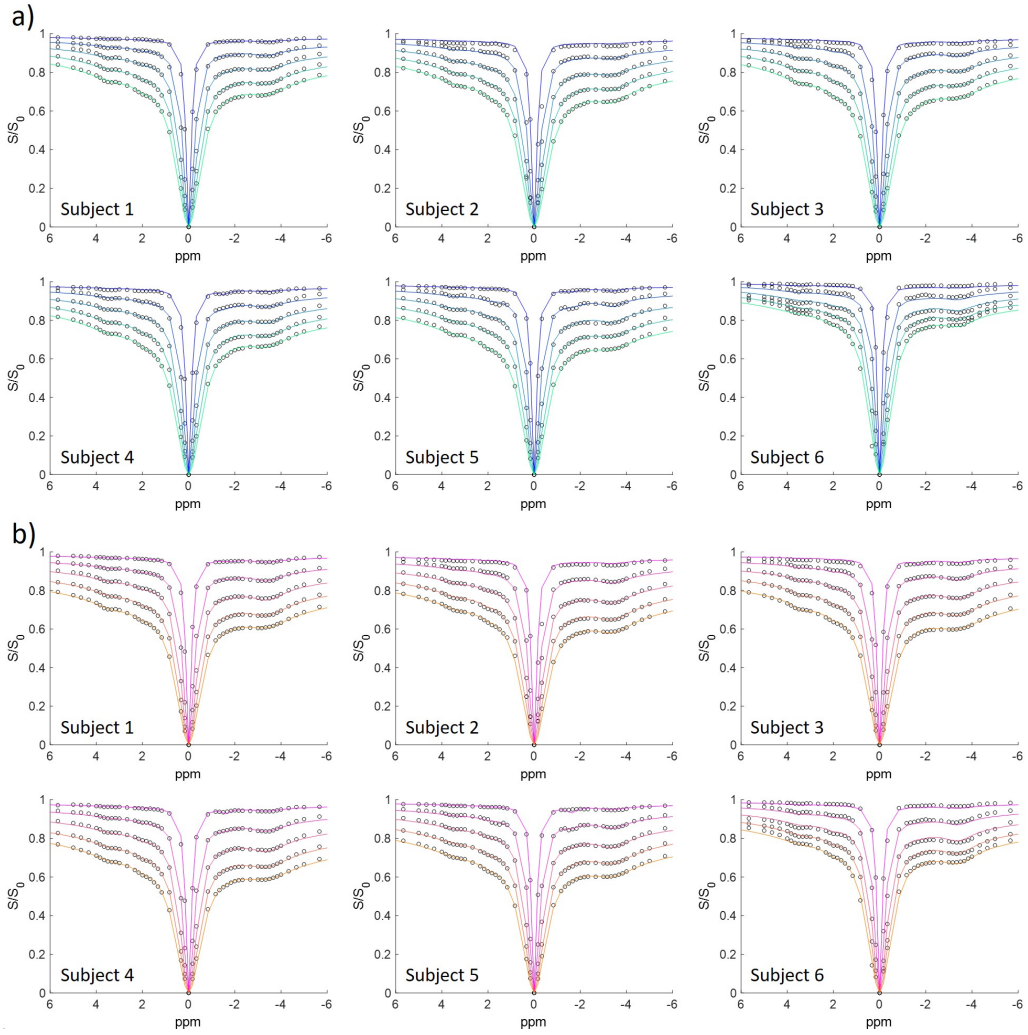

Figure 4.4.8: Fitted spectra for each subject in a) grey matter, and b) white matter.

in grey matter and 162 ± 20Hz in white matter [24]. There has been less work on quantification of the NOE(-3.5ppm) pool, however our pool size fraction is around ten times smaller than that reported by Geades [12] or Liu [13], although our exchange rate and $T_{2,n}$ measurements are comparable.

The second NOE pool located at -1.7ppm is of particular interest. It has not previously been fully quantified in the human brain. Here we show that the pool size is

significantly higher in white matter than grey matter. It has been speculated that this may be indicative of mobile membrane proteins [25], but further work is needed to work out exactly where this signal arises from in the human brain.

4.5 Limitations of the z-PSO

Particle Swarm Optimisation is advantageous over other fitting methods, as it reduces the number of prior assumptions that need to be made about the system. There are however some limits in how we can use the z-PSO, and some assumptions that we are forced to make which may bias the results.

4.5.1 Practical limitations

The main issue with the z-PSO is the same as any other fitting method, in that we need to know the peaks we are fitting for. This becomes more complex in living tissue where there are many CEST sensitive metabolites present. If we simply include more and more pools, we risk overfitting to the point where the results become meaningless. Conversely if we use too few pools, the z-PSO will try to stretch out the fitted Lorentzians to cover as many of the missed pools as possible, artificially shortening the T_2 of the measured exchanging pool. The most appropriate way we have found is simply to fit for the peaks we deem visible with the human eye in the acquired spectra, although with this method we must be aware that we may actually be measuring a superposition of underlying CEST pools, regardless of the fitting method used. In addition to this, depending on the size of the ROI fitted over, it should be noted that exchange rate may vary both spatially and temporally due to physiological changes in both pH and temperature.

The other practical limitation of the z-PSO using this minimisation function is that we must acquire our z-spectra using a saturation train resembling CW saturation. This is

necessary as in the fitting algorithm the z-spectra must be simulated for every particle per every iteration. If we were to extend the z-PSO to fit spectra acquired through pulsed irradiation, this would extend computation time to an unfeasible degree, as we would have to simulate spectra using equation 2.2.7, which, as detailed in section 2.2, is an arduous calculation due to the matrix exponential which must be solved. However, one study has shown that pulsed irradiation may be a suitable alternative to CW saturation when measuring samples containing only slow exchanging pools [26].

4.5.2 The MT lineshape problem

We know that the MT lineshape is Lorentzian around the centre [8], however this does not hold true beyond $\pm$10ppm. We tested various lineshapes to try to find a better fit to the MT lineshape, however we found that a Lorentzian, super-Lorentzian, Gaussian, and a superposition of two Lorentzians all had equally poor fits away from resonance.

To test this further, the results of one of the grey matter fits were simulated, but with the MT pools size set to zero, to create an MT-free spectrum. This was subtracted from the actual data to leave only the MT lineshape. As Figure 4.5.1 shows, this was then fitted with an increasing number of summed Gaussians to see what it would take to fit this shape.

A superposition of five Gaussians was found to fit the MT lineshape, however fitting this number of shapes is essentially meaningless as too many new parameters have been introduced in order to force the shape to fit.

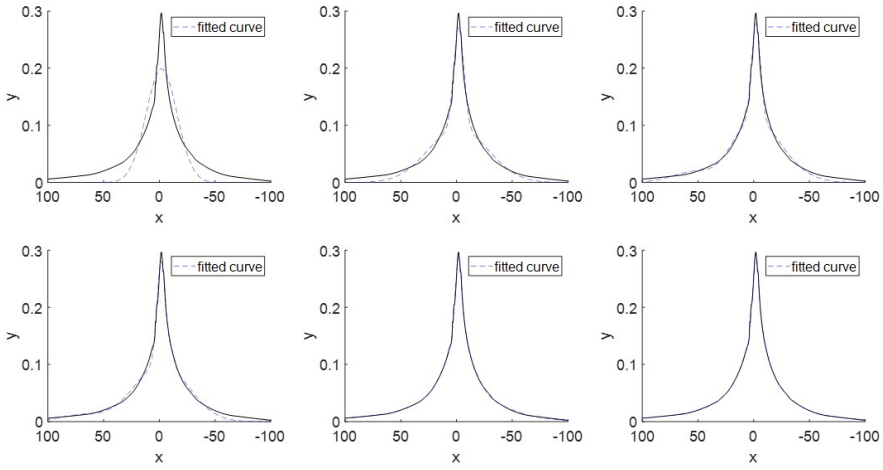

Figure 4.5.1: The MT lineshape in grey matter, with one to six summed Gaussians fitted to the data.

4.6 Summary

This chapter has introduced the z-PSO: a novel method of quantifying the z-spectrum by adapting the direct solutions to the Bloch-McConnell solutions under continuous wave saturation to a Particle Swarm Optimisation algorithm. This has been optimised for z-spectrum fitting, and tested on creatine phantoms and *in vivo* cerebral grey and white matter. Results from the grey matter and white matter fitting largely agree with previous results, while reporting new findings of interest, particularly information about the NOE peak located at -1.7ppm in the human brain. The z-PSO is especially useful for rigorous analysis of z-spectra, however for large sample sizes simpler fitting methods with shorter computation time may still be preferred.

References

[1] Russell Eberhart and James Kennedy. New optimizer using particle swarm theory. In *Proceedings of the International Symposium on Micro Machine and Human Science*, 1995. doi: 10.1109/mhs.1995.494215.

[2] Yuhui Shi and Russell Eberhart. Modified particle swarm optimizer. In *Proceedings of the IEEE Conference on Evolutionary Computation, ICEC*, 1998. doi: 10.1109/icec.1998.699146.

[3] Riccardo Poli. Analysis of the Publications on the Applications of Particle Swarm Optimisation. *Journal of Artificial Evolution and Applications*, 2008. ISSN 1687-6229. doi: 10.1155/2008/685175.

[4] Rania Hassan, Babak Cohanim, Olivier De Weck, Gerhard Venter, Postdoctoral Associate, Engineering Systems, The Jet, and Engineering Systems. a Copmarison of Particle Swarm. *American Institute of Aeronautics and Astronautics*, 2004.

[5] Gerhard Venter and Jaroslaw Sobieszczanski-Sobieski. Particle swarm optimization. In *Collection of Technical Papers - AIAA/ASME/ASCE/AHS/ASC Structures, Structural Dynamics and Materials Conference*, 2002. doi: 10.4018/ijmfmp.2015010104.

[6] Version 9.6 2019 The Mathworks, Inc. MATLAB. MATLAB - MathWorks - MATLAB, 2019.

[7] Moritz Zaiss, Zhongliang Zu, Junzhong Xu, Patrick Schuenke, Daniel F. Gochberg, John C. Gore, Mark E. Ladd, and Peter Bachert. A combined analytical solution for chemical exchange saturation transfer and semi-solid magnetization transfer. *NMR in Biomedicine*, 2015. ISSN 10991492. doi: 10.1002/nbm.3237.

[8] Greg J. Stanisz, Ewa E. Odrobina, Joseph Pun, Michael Escaravage, Simon J. Graham, Michael J. Bronskill, and R. Mark Henkelman. T1, T2 relaxation and

magnetization transfer in tissue at 3T. *Magnetic Resonance in Medicine*, 2005. ISSN 07403194. doi: 10.1002/mrm.20605.

[9] Mohammad Haris, Anup Singh, Kejia Cai, Feliks Kogan, Jeremy McGarvey, Catherine Debrosse, Gerald A. Zsido, Walter R.T. Witschey, Kevin Koomalsingh, James J. Pilla, Julio A. Chirinos, Victor A. Ferrari, Joseph H. Gorman, Hari Hariharan, Robert C. Gorman, and Ravinder Reddy. A technique for in vivo mapping of myocardial creatine kinase metabolism. *Nature Medicine*, 2014. ISSN 10788956. doi: 10.1038/nm.3436.

[10] Jingwen Yao, Chencai Wang, and Benjamin M. Ellingson. Influence of phosphate concentration on amine, amide, and hydroxyl CEST contrast. *Magnetic Resonance in Medicine*, 2021. ISSN 15222594. doi: 10.1002/mrm.28481.

[11] Piotr Orlowski, Michael Chappell, Chang Sub Park, Vicente Grau, and Stephen Payne. Modelling of pH dynamics in brain cells after stroke. *Interface Focus*, 2011. ISSN 20428901. doi: 10.1098/rsfs.2010.0025.

[12] Nicolas Geades, Benjamin A.E. E Hunt, Simon M. Shah, Andrew Peters, Olivier E. Mougin, and Penny A. Gowland. Quantitative analysis of the z-spectrum using a numerically simulated look-up table: Application to the healthy human brain at 7T. *Magnetic Resonance in Medicine*, 2017. ISSN 15222594. doi: 10.1002/mrm.26459.

[13] Dapeng Liu, Jinyuan Zhou, Rong Xue, Zhentao Zuo, Jing An, and Danny J.J. Wang. Quantitative characterization of nuclear overhauser enhancement and amide proton transfer effects in the human brain at 7 Tesla. *Magnetic Resonance in Medicine*, 2013. ISSN 07403194. doi: 10.1002/mrm.24560.

[14] Deanna J. Greene, Jonathan M. Koller, Jacqueline M. Hampton, Victoria Wesevich, Andrew N. Van, Annie L. Nguyen, Catherine R. Hoyt, Lindsey McIntyre, Eric A. Earl, Rachel L. Klein, Joshua S. Shimony, Steven E. Petersen, Bradley L. Schlaggar, Damien A. Fair, and Nico U.F. Dosenbach. Behavioral interventions for reducing head motion during MRI scans in children. *NeuroImage*, 2018. ISSN 10959572. doi: 10.1016/j.neuroimage.2018.01.023.

[15] Fsl. FMRIB Software Library, 2006.

[16] Mark W. Woolrich, Saad Jbabdi, Brian Patenaude, Michael Chappell, Salima Makni, Timothy Behrens, Christian Beckmann, Mark Jenkinson, and Stephen M. Smith. Bayesian analysis of neuroimaging data in FSL. *NeuroImage*, 2009. ISSN 10959572. doi: 10.1016/j.neuroimage.2008.10.055.

[17] Stephen M. Smith, Mark Jenkinson, Mark W. Woolrich, Christian F. Beckmann, Timothy E.J. Behrens, Heidi Johansen-Berg, Peter R. Bannister, Marilena De Luca, Ivana Drobnjak, David E. Flitney, Rami K. Niazy, James Saunders, John Vickers, Yongyue Zhang, Nicola De Stefano, J. Michael Brady, and Paul M. Matthews. Advances in functional and structural MR image analysis and implementation as FSL. In *NeuroImage*, 2004. doi: 10.1016/j.neuroimage.2004.07.051.

[18] Yongyue Zhang, Michael Brady, and Stephen Smith. Segmentation of brain MR images through a hidden Markov random field model and the expectation-maximization algorithm. *IEEE Transactions on Medical Imaging*, 2001. ISSN 02780062. doi: 10.1109/42.906424.

[19] Thomas E. Yankeelov, Richard G. Abramson, and C. Chad Quarles. Quantitative multimodality imaging in cancer research and therapy, 2014. ISSN 17594782.

[20] O. E. Mougin, R. C. Coxon, A. Pitiot, and P. A. Gowland. Magnetization transfer phenomenon in the human brain at 7 T. *NeuroImage*, 2010. ISSN 10538119. doi: 10.1016/j.neuroimage.2009.08.022.

[21] Stefan Ropele, Thomas Seifert, Christian Enzinger, and Franz Fazekas. Method for quantitative imaging of the macromolecular 1H fraction in tissues. *Magnetic Resonance in Medicine*, 2003. ISSN 07403194. doi: 10.1002/mrm.10427.

[22] Richard D. Dortch, Jay Moore, Ke Li, Marcin Jankiewicz, Daniel F. Gochberg, Jane A. Hirtle, John C. Gore, and Seth A. Smith. Quantitative magnetization transfer imaging of human brain at 7T. *NeuroImage*, 2013. ISSN 10538119. doi: 10.1016/j.neuroimage.2012.08.047.

[23] Mehran Shaghaghi, Weiwei Chen, Alessandro Scotti, Haiqi Ye, Yan Zhang, Wenzhen Zhu, and Kejia Cai. In vivo quantification of proton exchange rate in healthy human brains with omega plot. *Quant Imaging Med Surg*, 9(10):1686–1696, 2019.

[24] Hye Young Heo, Zheng Han, Shanshan Jiang, Michael Schär, Peter C.M. van Zijl, and Jinyuan Zhou. Quantifying amide proton exchange rate and concentration in chemical exchange saturation transfer imaging of the human brain. *NeuroImage*, 2019. ISSN 10959572. doi: 10.1016/j.neuroimage.2019.01.034.

[25] Kimberly L. Desmond, Firas Moosvi, and Greg J. Stanisz. Mapping of amide, amine, and aliphatic peaks in the CEST spectra of murine xenografts at 7 T. *Magnetic Resonance in Medicine*, 2014. ISSN 15222594. doi: 10.1002/mrm.24822.

[26] Y. K. Tee, A. A. Khrapitchev, N. R. Sibson, S. J. Payne, and M. A. Chappell. Evaluating the use of a continuous approximation for model-based quantification of pulsed chemical exchange saturation transfer (CEST). *Journal of Magnetic Resonance*, 2012. ISSN 10907807. doi: 10.1016/j.jmr.2012.07.003.

Chapter 5

Measuring physiological changes in human blood via the z-spectrum

As blood is present in almost every organ of the body, understanding the z-spectrum which arises from blood is of great importance when performing *in vivo* z-spectrum imaging, as some component of this spectrum will be present in most biological tissues. This chapter aims to explore and characterise the signals which arise from human blood, by using the z-PSO to fit z-spectra obtained from *ex vivo* human blood. This is taken further by exploring the feasibility of measuring endogenous and exogenous compounds in blood using CEST contrast, first by investigating the possibility of measuring blood glucose levels, and then by expanding on previous work measuring pH using the CEST contrast of Iopamidol solution by adding this compound to human blood and attempting to measure its pH *ex vivo*.

5.1 CEST and NOE signals in human blood

In order to better understand the z-spectrum of human blood, we must first determine which CEST and NOE signals occur in the spectrum. This is tricky, as all current fitting methods require the pools present to be known beforehand, and also because the effect of coalescence means that different pools can combine to produce z-spectra of very similar shapes. This section aims to determine the most likely composition of the human blood z-spectrum by fitting a variety of pools to z-spectra acquired at various saturation powers in an attempt to separate components with different exchange rates using the z-PSO. The assumption here is that the best fit is most likely to be the correct one, using the sum of squares difference between the fitted spectrum and the acquired spectrum as a means of assessing goodness of fit.

5.1.1 Z-spectrum acquisition

Following ethical approval from the University of Nottingham Ethics Committee, a 6ml blood sample was taken from a healthy 24 year old male volunteer and deposited in a vacutainer containing heparin, which is an anticoagulant. A drop of this blood sample was removed and deposited into an i-STAT CHEM8+ test cartridge (Abbot Point of Care Inc.) to measure the haematocrit level of the sample along with relevant molecules.

The tube was fixed into a perspex holder, which could be placed in a purpose-built rotary water bath. The water bath was made to be a cylindrical shape with a diameter of 140mm, in order to fit inside the 7T head coil. One end of the cylinder had a notch in which a pole could be placed, so that the user could rotate the water bath using the pole while the sample was in the magnet bore, to avoid the blood settling and the plasma separating from the concentrated red blood cells. This end of the water bath

also had a water inlet and outlet through which rubber pipes could be affixed. These were connected to a water pump outside of the magnet hall, which meant that water could circulate through the water bath. This enabled us to keep the samples at $37°$C throughout the scanning procedure, while frequently rotating the sample to prevent the plasma and concentrated red blood cells from separating. The experimental setup is shown in Figure 5.1.1.

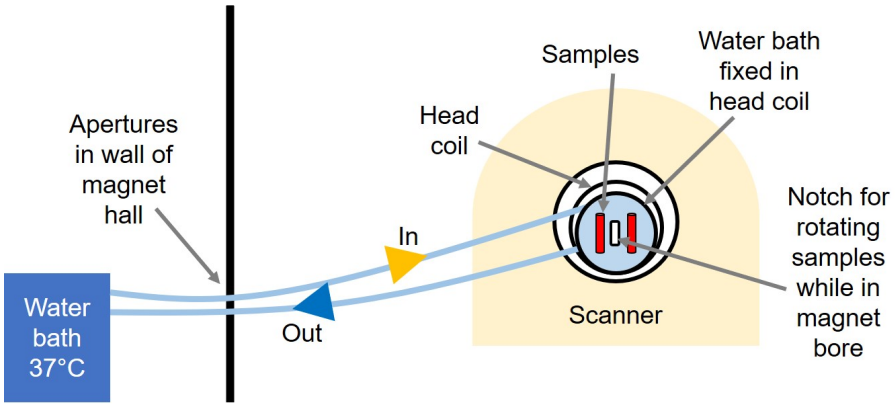

Figure 5.1.1: Diagram of experimental setup to maintain sample temperature at 37°C.

The blood sample was scanned using a 7T Achieva system with a NOVA 8ch pTx head coil. Prior to scanning, the heat pump was set to $37°$C in order to mimic physiological conditions. Once this temperature was reached, tuning of the odd and even channels was performed as described in section 4.3.1, and B_0 and B_1 maps were acquired.

Initial testing showed that leaving the pump on during z-spectrum acquisition produced flow artefacts in the images. To combat this, the heat pump was switched off and the system was left to settle for 120 seconds. A z-spectrum was then acquired using semi-CW saturation, with a 3 second saturation block comprised of sixty 50ms pulses alternating on the odd and even channels, followed by a TFEPI readout scheme [1, 2] with a duration of 1.7s, which was chosen to balance image quality with acquisition speed.

The TFEPI sequence modifies the standard TFE sequence described in section 1.4.6 by adding in a portion of EPI-like gradient switching to speed up acquisition. As

shown in the pulse sequence diagram in Figure 5.1.2, an RF pulse is applied before strong negative gradients are applied in the phase and frequency encoding directions. A positive gradient is applied in the frequency encoding direction, but then instead of returning to the centre of k-space after one line is acquired, the phase encoding gradient is 'blipped' on in the positive direction, and a negative gradient is applied in the frequency encoding direction, acquiring another line of k-space. The number of lines of k-space acquired per shot is termed the EPI factor. For example, if the EPI factor was 5, then five lines of k-space would be acquired after a single RF pulse, before the process was repeated acquiring a different portion of k-space. Increasing the EPI factor reduces scan time but increases EPI artefacts such as image distortion.

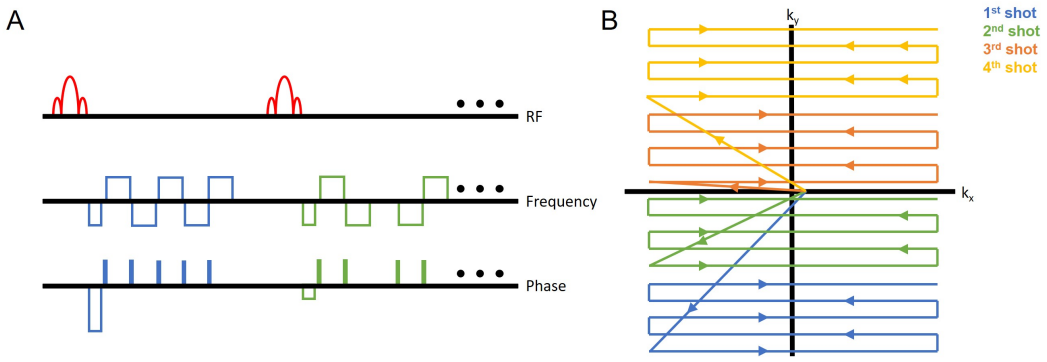

Figure 5.1.2: a) TFEPI scan sequence, and b) TFEPI traversal of k-space.

For this experiment an EPI factor of 11 was chosen after initial testing to determine the maximum possible EPI factor which did not severely affect image quality. A 'half-scan' factor of 0.8 was also employed, meaning that only 80% of k-space was acquired due to its inherent conjugate symmetry [3]. The total saturation and readout time was 4.7s, however a TR of 9 seconds was chosen to reduce the degree of saturation from the previous acquisition being carried over to the subsequent one. It is likely there was some residual saturation at the end of each TR, but this was mitigated by acquiring the two start up scans at the beginning of each spectrum which were discarded from further analysis. After these start up scans, it is likely the amount of saturation at the end of the long FFE readout train was dominated by the readout pulses (rather than prior off-resonance saturation of the water signal), and so the

longitudinal magnetisation prior to saturation reached a steady state regardless of the position in the z-spectrum. The order of off-resonance frequencies that were acquired was such that the outermost frequencies were acquired first, alternating between positive and negative, before progressing further towards the centre and ending on the water resonance, which allowed the power output of the system to stabilise. 64 off-resonance frequencies were acquired in total, and acquisition of the full z-spectrum took just under ten minutes.

Once the first z-spectrum had been acquired, the blood sample was rotated in the water bath to prevent the red blood cells from separating from the plasma, and the heat pump was switched back on until the system returned to $37°$C. The heat pump was then switched back off and left to settle for a further 120 seconds, before another z-spectrum was acquired. This process was repeated until 5 z-spectra had been acquired, with saturation pre-pulses of 0.33μT, 0.67μT, 1.00μT, 1.33μT, and 2.00μT respectively.

After scanning had been completed, the blood sample was once again analysed using an i-STAT CHEM8+ test cartridge to explore if the sample had been affected by being held *ex vivo* for the duration of the scan time. The haematocrit level remained constant at 45$\%$, which is in line with the literature values of between 42.5$\%$ and 47.4$\%$ reported for healthy males [4, 5, 6, 7, 8, 9], and the blood-glucose level dropped from 2.7mMol/L to <1.1mMol/L (less than the lowest permitted value measurable by the i-STAT cartridges) over the course of the scan. The starting blood-glucose level was less than the average of 5.5mMol/L [10], however the subject had unintentionally fasted for 12 hours prior to blood collection. As a point of interest, this value is on the threshold of being considered as hypoglycemia (low blood sugar) [11], however this value is not a cause for concern under these circumstances in non-diabetic subjects, and also the i-STAT test does not have a stated margin of error (its degree of precision is 0.1mMol/L, however of course the device may be less accurate than this in practice).

5.1.2 Correcting the z-spectrum due to systematic errors

The z-spectrum acquired from the *ex vivo* human blood sample was corrected for B_0 inhomogeneities using the acquired field map, as described in section 4.3.1. Upon further analysis, it was evident that a systematic acquisition error had altered the results, where the signal from some of the higher saturation powers was greater than the signal from some of the lower saturation powers in the wings of the spectrum, which is physically impossible. This is illustrated in Figure 5.1.3.

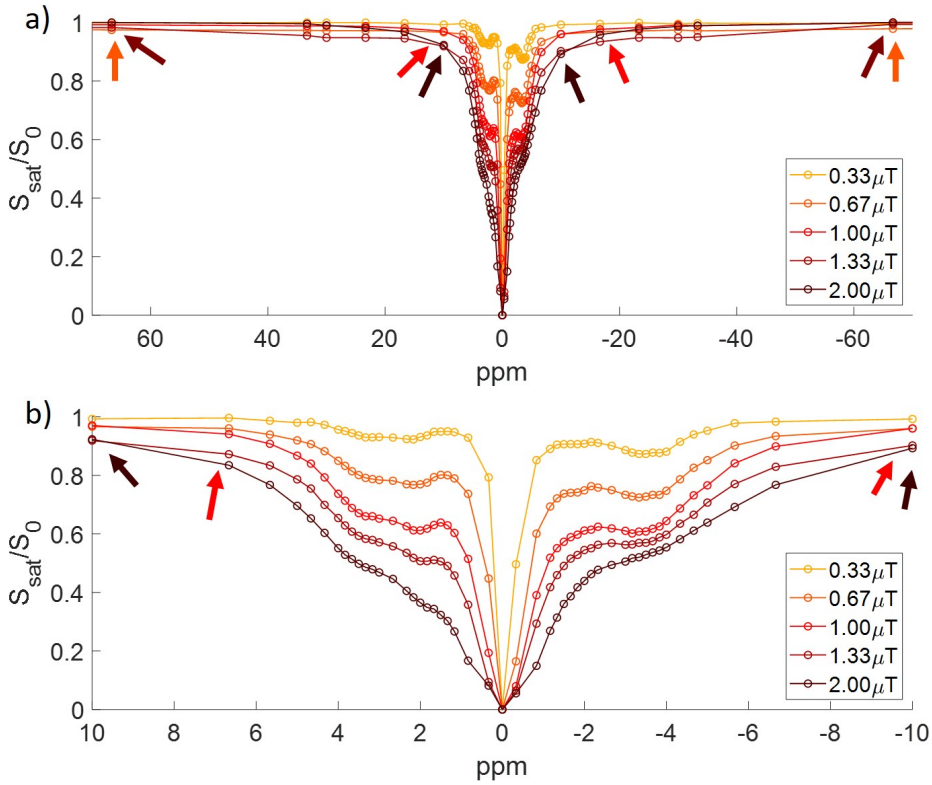

Figure 5.1.3: The z-spectrum acquired from *ex vivo* human blood at 37°C, viewed a) between ±70ppm, and b) between ±10ppm, showing clear errors between ±(10-70)ppm. Spectra acquired with saturation power of 0.33μT, 0.67μT, 1.00μT, 1.33μT, and 2.00μT. Arrows indicate obvious errors in the acquired spectrum.

As we can see from Figure 5.1.3, only points between $\pm$10 to $\pm$60ppm were affected by this systematic error. The off-resonance frequencies were acquired furthest off-resonance first and on-resonance last, alternating positive and negative frequencies, and the spectra were acquired starting with the highest saturation power and finishing with the lowest. There was also an extended period of time between acquisition of the 1.33μT spectrum and the 1.00μT spectrum where field maps were acquired. This suggests that the system (probably the RF amplifier) takes time to stabilise and acquire the correct signal, causing inconsistent signals to be acquired initially, and hence suggesting an explanation for why the most strongly affected frequencies are those outside of $\pm$10ppm in the 0.67μT spectrum and the 1.00μT spectrum. A similar problem to this had previously been observed on the system, which is why the acquisition of the far off-resonance frequency was acquired twice at the start of each scan with the first of the two being discarded, however it appears in this case the system took many more acquisitions before the data was acquired correctly. It is evident that the signal arising from the central points between +7ppm to -7ppm appears to have been acquired as would be expected, the spacing of the spectra appears appropriate in this region.

In order to minimise the effects of this error, four options were considered. The first of these was to simply discard points outside of $\pm$7ppm, with the exception of those acquired at $\pm$100kHz ($\pm$333ppm) which were used for normalisation. This left a spectrum with 49 points in each of the five z-spectra as opposed to the original 64. The second option was to normalise the spectrum using the point acquired at -10kHz ($\pm$33.3ppm), as from observation of the data it was assumed that no significant MT pool was present and therefore no off-resonance pools would be located here. This left a spectrum with 56 points in each of the five z-spectra. The third and fourth options were to repeat these ideas but discarding the middle and highest saturation power. The thought process behind this was that the z-spectra were acquired in order of highest saturation power to lowest, but with around thirty minutes between the acquisition of the second and third highest. This meant that if the system needed to acquire a certain amount of off-resonance frequencies to allow the power output to stabilise, these powers would be the most strongly affected by this systematic error.

The resulting z-spectra from these options are displayed in Figure 5.1.4.

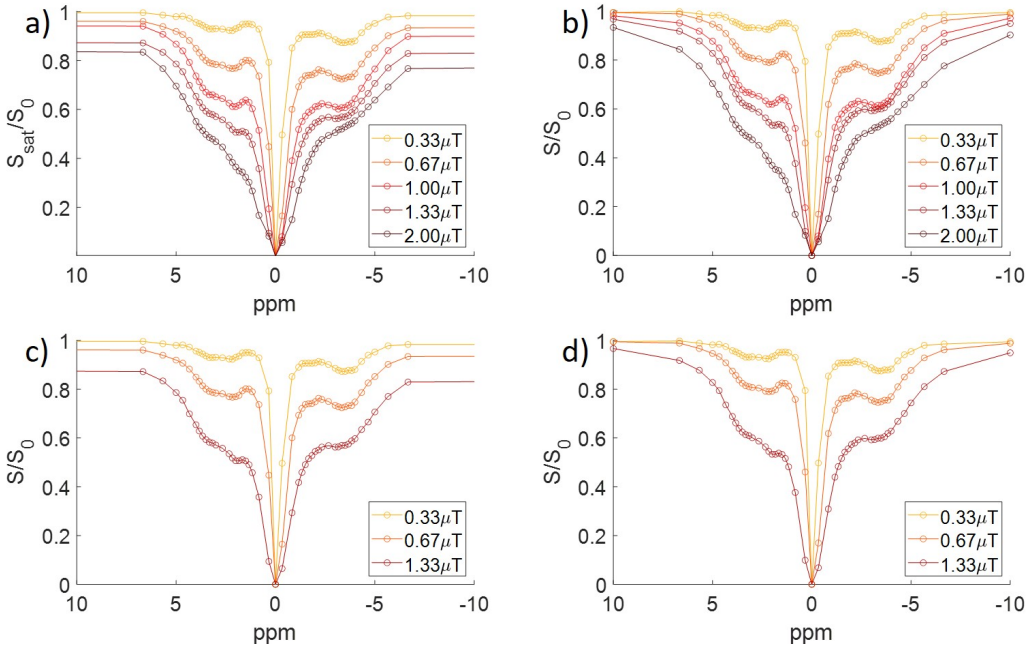

Figure 5.1.4: The amended z-spectra, a) discarding points between -70ppm to -10ppm and +10ppm to +70ppm, b) normalising the z-spectra at -33.3ppm instead of +333ppm, c) replicating (a) but with saturation powers of 1.00μT and 2.00μT discarded, and b) replicating (d) but with saturation powers of 1.00μT and 2.00μT discarded.

From these options it was decided that the dataset with five saturation powers normalised at +333ppm with points outside of $\pm$7ppm discarded would be used for analysis. While the systematic error in normalisation remains, this was deemed closest to a z-spectrum shape that might be expected. The reasoning for this was that firstly the central points seemed to be accurate and unaffected by the error introduced by pausing the acquisition, so fitting to five saturation powers yields much stronger results than fitting to three, and secondly the central datapoints seemed closer to what we would expect when normalising to +333ppm. This is especially evident around -3.5ppm where we would expect the largest NOE signal, as the signal at this frequency from the z-spectrum acquired with a saturation power of 1.00μT appears to be very low compared to where we would expect the spectrum, almost touching the 1.33μT

spectrum. However the signal at -10ppm seems relatively high, suggesting reasonable normalisation. Future work should involve acquiring more data to allow the amplifiers to stabilise before acquiring the spectrum, and further work should be performed to understand the variability in this systematic error.

5.1.3 Fitting the z-spectrum

The question of evaluating which exchanging pools are present is not a trivial one. The task was split into two parts: identifying NOE pools and identifying CEST pools. The MT contribution to the z-spectrum was assumed to be negligible, as previous work has fitted a low AREX value of 0.05 for an MT pool offset at -2.4ppm acquired at 0.9μT [12], and this may have been inflated by the presence of nearby NOE pools.

For the part of the experiment exploring the signals present upfield from the water resonance, four potential NOE signals were considered based on previous reports. These were the most commonly reported NOE signal located at -3.5ppm [13] attributed to tertiary aliphatic protons, the newly reported NOE signal located at -1.7ppm [14, 12] attributed to mobile membrane protons, and NOE signals theorised to be located at -2.25ppm and -2.75ppm [15], corresponding to primary and secondary aliphatic protons respectively.

The spectrum was fitted using the z-PSO for all possible combinations of these pools, leading to fifteen total fits. For every fitted pool, ten thousand particles were used, and this was repeated 100 times, producing the equivalent of a 1 million particle fit. Initially only the frequencies around the water resonance (-0.8ppm to +0.8ppm) and the point far off resonance were used to fit values for the T_1 and T_2 of free water. Each NOE pool was then fitted twice, once with an initial fit considering only the points around the pool of interest, and the second fit considering all points in the relevant half of the spectrum. Discarding the irrelevant CEST data points resulted in five z-spectra each with 29 data points.

A similar method was used for the CEST signals. Four possible CEST sources were identified using literature and visual analysis of the z-spectrum. The first two of these were the amide pool located at +3.5ppm, which is the most commonly reported CEST signal [16], and glutamate, which produces an amine signal at +3.0ppm [17]. As these pools have only a singular resonance, they can be fitted as normal using a single Lorentzian.

The other two CEST pools which were fitted here were more complex. The first of these were the signals arising from glycosaminoglycans (GAGs) which have a dual resonance located at +3.2 ppm and between +0.9ppm and +1.9ppm, the latter of which is commonly assumed to have a maximum signal at +1.0ppm [18]. For this pool two Lorentzians were required, with independent exchange rates and T_2s, but coupled pool sizes. Each GAG molecule contains three -OH groups and one -NH group, therefore the pool size of the Lorentzian located at +1.0ppm must be three times the pool size of the Lorentzian located at +3.2ppm. Human blood is known to contain a variety of proteoglycans, which are molecules comprised of one or two types of GaG chains bound to a protein molecule [19]. The final pool we fitted for was glucose. We already knew that there was some glucose present in blood from the i-STAT tests performed before and after the initial experiment. This pool is even more complex as there are seven labile protons leading to four sources of CEST signal. For clarity the structure of glucose is displayed in Figure 5.1.5. The first proton resonates at +0.66ppm arising from the -OH group attached to the carbon atom not in the pyranose ring. There are three at +1.28ppm arising from the three -OH groups attached to the carbon atoms in the pyranose ring. There is one remaining proton in a glucose molecule, but depending on the anomeric conformation of the molecule, it can have a resonance of +2.08ppm if the molecule is in the form of α-glucose, and +2.88ppm if the molecule is in the form of β-glucose [20]. This leads to four Lorentzians located at the aforementioned off-resonance frequencies, with the pool size ratios of each being 1 : 3 : AR : (1-AR) for +0.66ppm : +1.28ppm : +2.08ppm : +2.88ppm, where AR is the anomeric ratio of α-glucose to β-glucose, usually taking the value of approximately 0.36 at equilibrium [20].

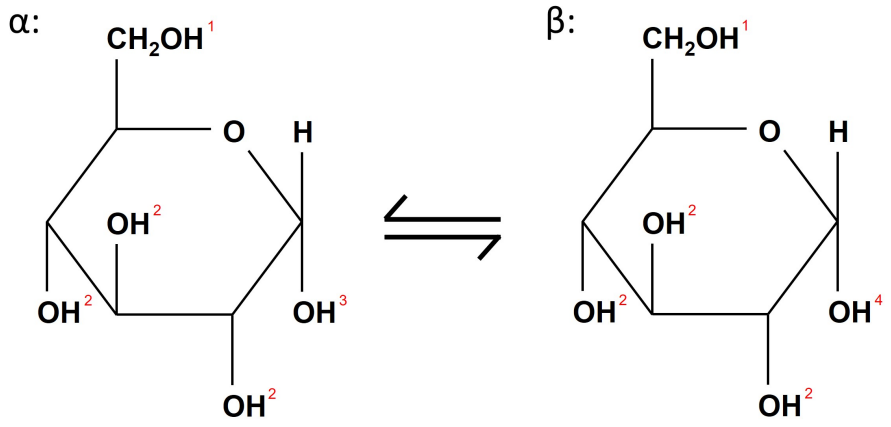

Figure 5.1.5: Chemical structure of α and β glucose. Protons labelled with superscript 1 resonate at +0.66ppm, protons labelled 2 resonate at +1.28ppm, protons labelled 3 resonate at +2.08ppm, and protons labelled 4 resonate at +2.88ppm.

CEST signals arising from pools such as creatine or glycogen were not considered as they are known not to be present in blood. Creatine is located and broken down in the muscles, into a waste product called creatinine, which is removed in the blood [21].

5.1.4 F-tests on NOE pools

The results of fitting the blood spectrum with only one NOE pool are displayed in Figure 5.1.6, with the best fit displayed in green. Placing a pool at -2.75ppm fits the best here, although it is evident from the spectrum that this is only the best fit because it is better at satisfying the least sum of squares difference condition on average across the whole spectrum. The fit of a pool located at -3.5ppm clearly appears to fit the spectral features of interest best, but misses some points between 0ppm and -2ppm.

Figure 5.1.7 shows the results of fitting two NOE pools to the z-spectrum. We can see that placing a pool at -3.5ppm and another at -1.7ppm fits the data well, both when considering the sum of squares difference and the fit to known spectral features.

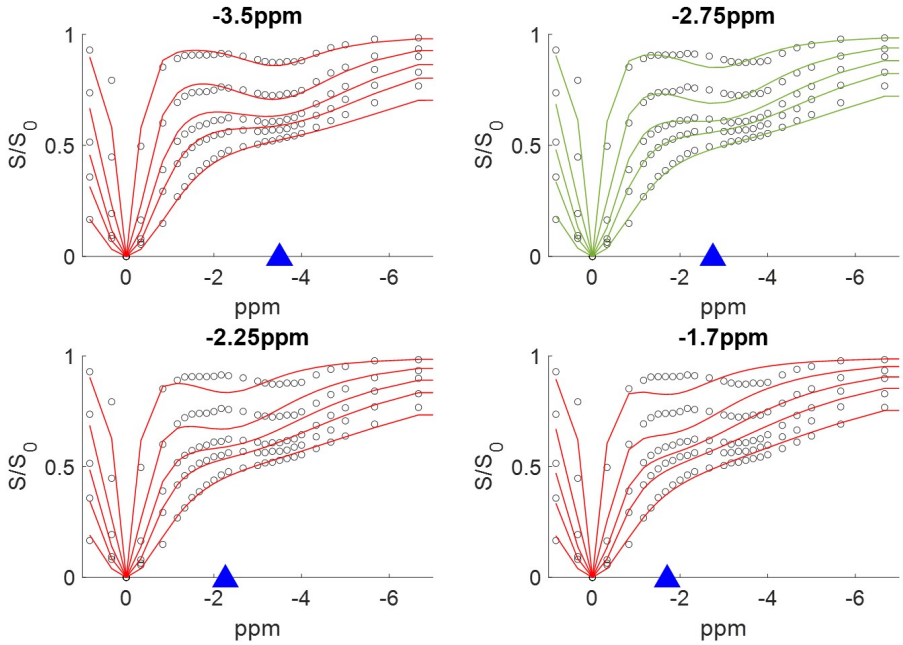

Figure 5.1.6: The z-spectrum acquired from *ex vivo* human blood fitted with a single NOE pool. Pool positions indicated with blue marker on x-axis. The fit with the least sum of squares difference with the acquired data is displayed in green. Points between +0.8ppm and +7ppm were ignored for this fit.

Figure 5.1.8 shows the results of fitting three NOE pools to the z-spectrum. Adding in a pool at -2.75ppm produced the best fit.

Finally, Figure 5.1.9 shows the results of fitting all four of the NOE pools to the z-spectrum. We can see overfitting in some areas, particularly on the -1.7ppm pool for the lowest power.

In order to determine whether the inclusion of additional pools resulted in a statistically significant increase in goodness of fit, the F-test for nested models was used. Here the residual sum of squares difference between the data and the fitted models are compared to calculate the F statistic. We can express this using the equation

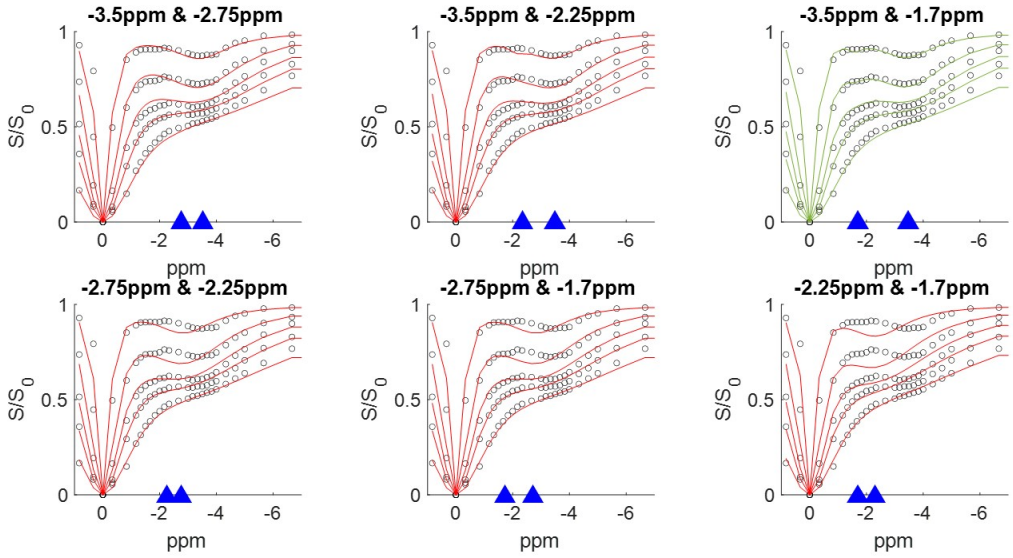

Figure 5.1.7: The z-spectrum acquired from *ex vivo* human blood fitted with two NOE pools.

$$F = (\frac{SSq_1 - SSq_2}{p_2 - p_1})/(\frac{SSq_2}{n - p_2}) \tag{5.1.1}$$

where $SSq_{1,2}$ is the residual sum of squares difference of model 1 and 2 respectively, $p_{1,2}$ are the number of parameters in model one and two respectively, and n is the number of data points. In this particular case, the number of parameters is the number of fitted pools, and the number of data points is 145, 29 for each of the 5 acquired spectra.

This F statistic is then compared to an F distribution table [22]. The relevant value is located in the table under a numerator of p_2-p_1, and a denominator of $n-p2$. Because most F distribution tables only give results for denominators in set increments, a value of 200 was used for the denominator. This is only a marginally less accurate test than using the correct denominator, as the value of the F statistic follows an exponential decline with increasing denominator.

Table 5.1.1 shows the results of the F-tests for the best fitting spectra for each

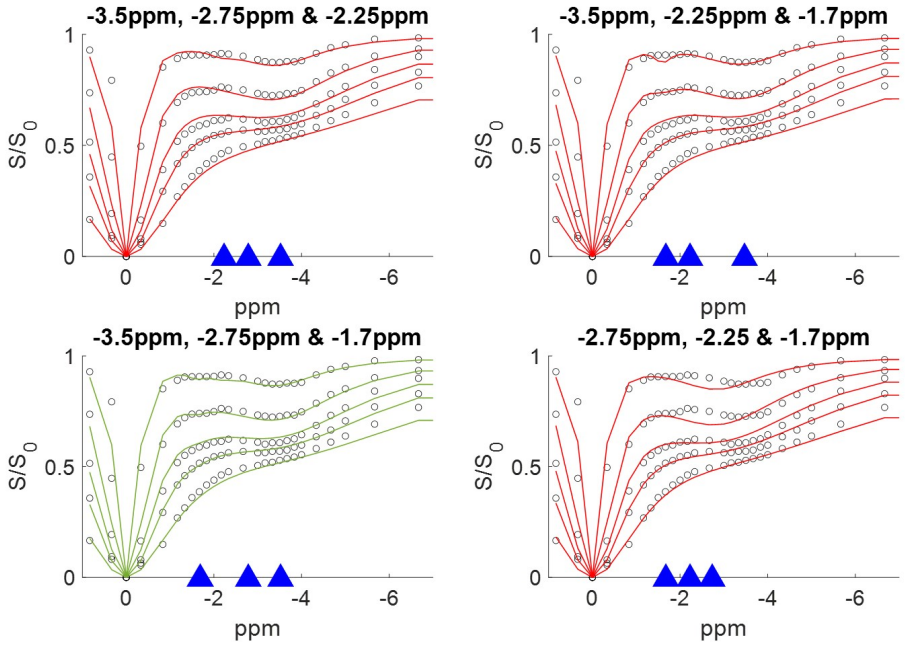

Figure 5.1.8: The z-spectrum acquired from *ex vivo* human blood fitted with three NOE pools.

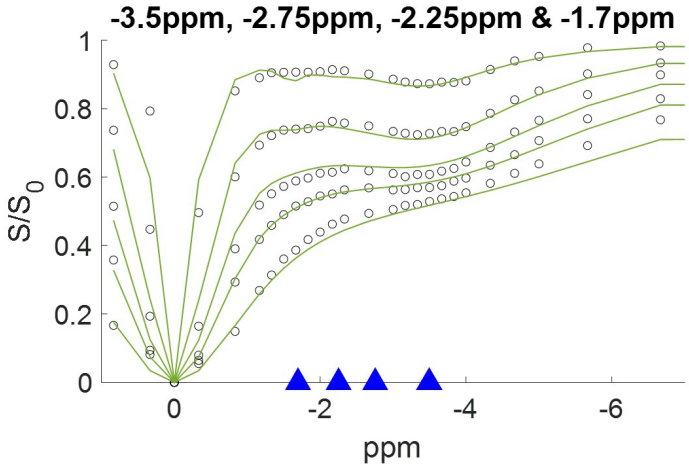

Figure 5.1.9: The z-spectrum acquired from *ex vivo* human blood fitted with all four considered NOE pools.

number of pools fitted to the data. For this test, an F statistic greater than 3.89 passes the F-test with p<0.05, and an F statistic greater than 6.76 passes the F-test with p<0.01. A positive F-test result indicates that the specified number of pools yields a significantly better fit than the previous model, so for example if fitting with four pools gave a positive result, this indicates that it is more appropriate to fit the data with four pools than three pools, and so forth.

Number of NOE pools	Sum of squares difference	F-test result
1	0.16675	N/A
2	0.15825	7.6773*
3	0.16067	-2.1366
4	0.16178	-0.9677

Table 5.1.1: F-test results of fitting NOE pools. Values marked * pass the F-test with a threshold of p<0.01.

The F-test confirms the previous finding of two NOE peaks in blood located at -3.5ppm and -1.7ppm [12] with p<0.01, suggesting that additional NOE peaks sometimes identified in other tissues [23, 24] do not originate from the blood. Interestingly the addition of further peaks leads to overfitting of certain pools which causes errors in the fits of existing pools. Table 5.1.1 is encouraging for the validity of the z-PSO as a fitting method, as it suggests that the sum of squares difference between the fit and the data might also be indicative of whether the pools which are being fitted for are the correct number of pools, as well as simply how accurate the fitted parameters are.

5.1.5 F-tests on CEST pools

The results of fitting CEST pools to the z-spectrum from human blood are displayed in Figures 5.1.10 and 5.1.11. The GaGCEST signal produces two CEST peaks, and the glucoCEST signal produces four CEST peaks, which has been accounted for when

considering the number of degrees of freedom each CEST pool gives rise to in the F-tests.

Figure 5.1.10 shows the fits for 1-4 CEST pools. The best fit in each case is highlighted in green, and the sources of signal which are fitted for are indicated above each fitted spectrum. It is visually apparent from these fitted spectra that the inclusion of glucose is essential for a good fit, as all other fitted spectra clearly fail to fit a pool located at around +2.0ppm.

Figure 5.1.11 shows the fits for 5-8 CEST pools. These appear to fit the z-spectrum reasonably well, although there is some visual evidence of overfitting on the spectrum with 8 fitted pools around the +2.0ppm glucose peak on the lower three of the five saturation powers.

An F-test was conducted comparing the best fitting spectra for each number of fitted pools. Table 5.1.2 shows the results of these F-tests. As previously, an F statistic greater than 3.89 passes the F-test with $p<0.05$, an F statistic greater than 5.10 passes the F-test with $p<0.025$, and an F statistic greater than 6.76 passes the F-test with $p<0.01$.

The F-test here yields interesting results. Going from 5 to 6 peaks reduced the probability from the F-test from under 0.025 to under 0.05. However we have prior knowledge of the sources of CEST signal which should be present. From the i-STAT tests we know that glucose is present. It is also known that human blood contains GaGs which aid in the regulation of blood coagulation [25]. This points us to our model with six CEST pools, which fits GaGs and glucose to the z-spectrum with $p<0.05$. The addition of further pools to this model does not yield a fit which passes the F-test, so we can reasonably conclude that these are the CEST signals giving rise to the shape of this z-spectrum.

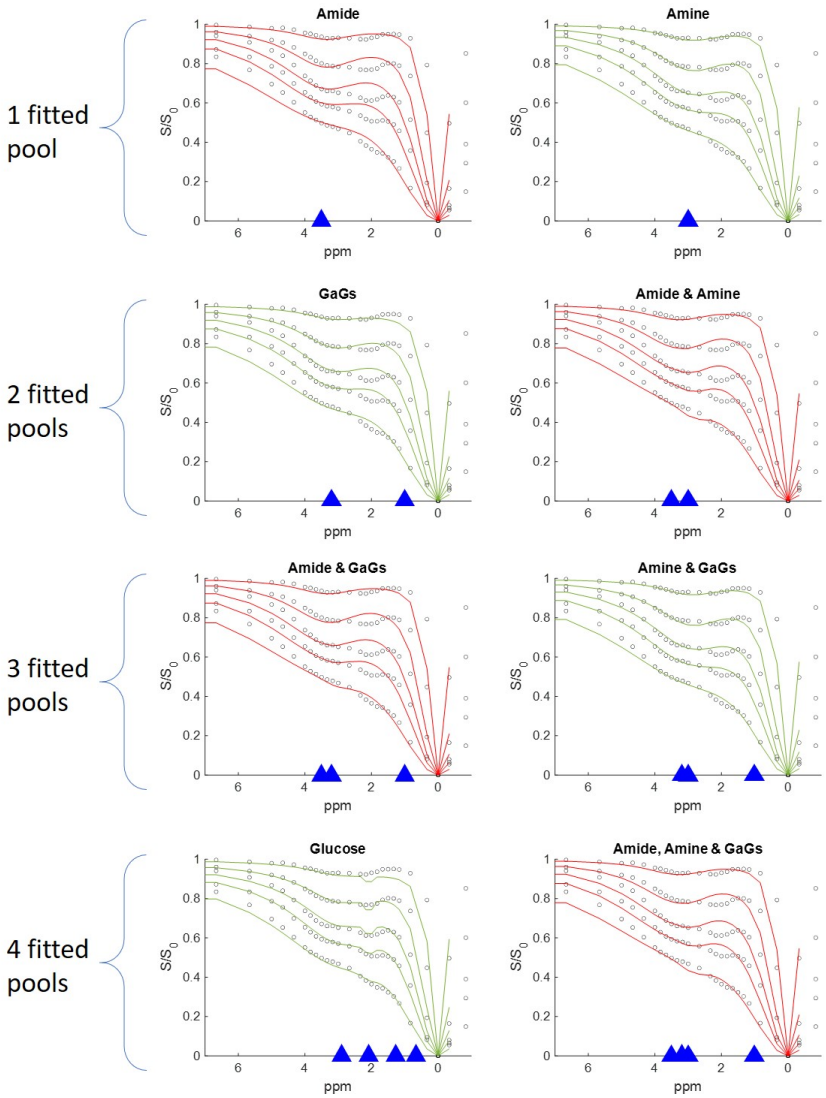

Figure 5.1.10: The z-spectrum acquired from *ex vivo* human blood fitted with 1-4 CEST pools. Pool positions indicated with blue marker on x-axis. The fit with the least sum of squares difference with the acquired data is displayed in green. Points between -0.8ppm and -7ppm were ignored for this fit.

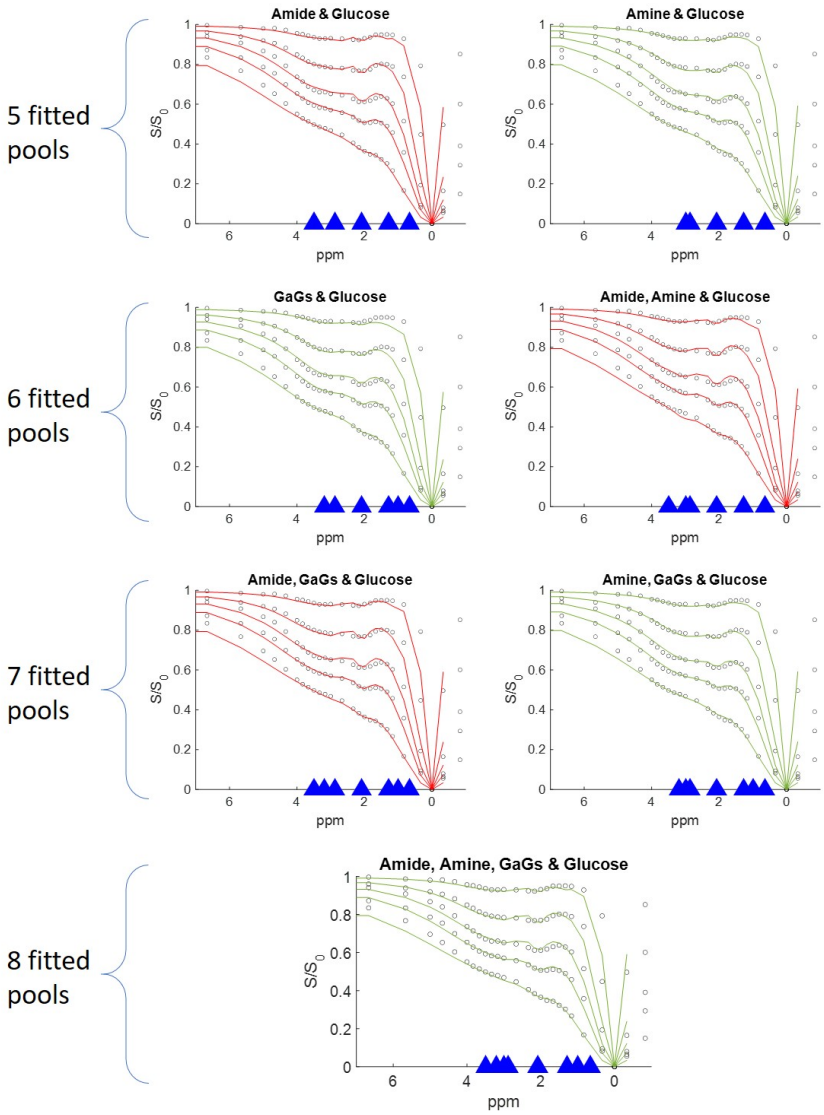

Figure 5.1.11: The z-spectrum acquired from *ex vivo* human blood fitted with 5-8 CEST pools.

5.1.6 The full human blood z-spectrum

After concluding that the signals present in the z-spectrum from human blood arise from glucose, GaGs, and two NOE pools located at -3.5ppm and -1.7ppm, these could

Number of CEST pools	Sum of squares difference	F-test result
1	0.23424	N/A
2	0.25185	-12.2533
3	0.23272	-12.7875
4	0.22098	7.3258***
5	0.21223	5.9600**
6	0.20547	4.4221*
7	0.21236	-4.2056
8	0.22607	-8.3080

Table 5.1.2: F-test results on the best fits of fitting CEST peaks. Values marked *** pass the F-test with a threshold of p<0.01, values marked ** pass the F-test with a threshold of p<0.025, and values marked * pass the F-test with a threshold of p<0.05.

be fitted together to determine the parameters of these exchanging pools, taking overlapping peaks into account. The z-PSO was run with 10,000 particles for each exchanging pool, and repeated 100 times to produce the equivalent of a 1 million particle fit. The resulting fitted spectrum is displayed in Figure 5.1.12, and the fitted parameters for these peaks are displayed in Table 5.1.3.

Exchanging pool	Pool size (%)	Exchange rate (Hz)	T_2 (ms)
NOE (-3.5ppm)	3.78	10	0.54
NOE (-1.7ppm)	0.47	13	1.9
GaG (+3.2ppm)	1.28	31	0.70
GaG (+1.0ppm)	3.85	<1	69
Glucose (0.66ppm)	0.50	>10,000	>100
Glucose (1.28ppm)	1.50	<1	>100
Glucose (2.08ppm)	0.18	119	4.6
Glucose (2.88ppm)	0.33	9	100

Table 5.1.3: Fitted values from the z-spectrum of human blood

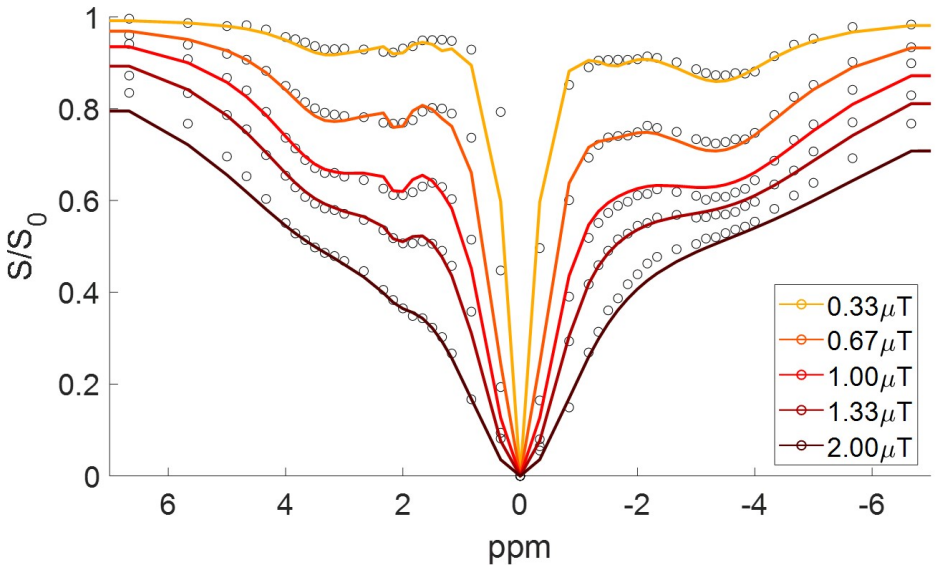

Figure 5.1.12: The z-spectrum acquired from *ex vivo* human blood fitted with GaG and glucose CEST pools,and two NOE pools.

As we can see from Figure 5.1.12, while this model was a good approximation of the z-spectrum in human blood, there were several remaining issues. For the CEST (positive) side of the spectrum, there were some areas in which the model fitted the data particularly well, for example the spectrum acquired at 1.33μT, however there were areas in which the peaks in the fitted spectrum became particularly sharp, such as for the spectrum acquired at 0.67μT. This was reflected in the fitted values where the glucose and GaG pools had peaks which fit to exchange rates of over 10kHz or under 1Hz, which are unreasonably high and low respectively. The algorithm struggled to calculate the exchange rates for the pools close to water, both for GaGs and glucose. This is one of the most difficult areas to fit as the water saturation obscures much of the data, and it is likely that there are also other fast exchanging pools arising from -OH groups present in this region. On the NOE (negative) side of the spectrum the algorithm achieved results comparable to those achieved from fitting the NOE pools alone, as seen in Figure 5.1.7. There were still some discrepancies between the fitted values and the data, particularly at higher saturation powers, which most likely arise from issues with inconsistent B_1 output during the scan. Finally we can see at higher

powers the algorithm overfitted the data far away from water, which may suggest that further CEST and NOE pools are present in human blood, rather than the fewer wider pools which were fitted here to encompass the apparent signals.

This section has systematically probed the z-spectrum from human blood and found that two NOE pools along with GaG and glucose CEST pools are present. However, some of the fitted exchange rates indicate that there may in fact be other CEST pools present. This experiment should be repeated on a z-spectrum free of artefacts arising from poor RF power stabilisation, potentially also at more RF powers and varying pH levels or temperatures, in order to better probe exchanging pools. Performing high resolution MRS on the blood sample may also be helpful, as this may reveal other molecules (or molecular groups) present in human blood which could influence the z-spectrum fitting.

5.2 Estimating blood-glucose levels via glucoCEST

Developing a sequence which has the potential to measure *in vivo* blood-glucose levels is of great interest. Non-invasive assessment of glucose uptake and delivery has huge potential applications in cancer diagnostics [26]. The ability to map blood-glucose levels through measurement of the glucose-sensitive CEST signal, termed glucoCEST, has the potential to provide insights into the nature of glucose delivery and metabolism in various organs in the body. The glucoCEST signal has been shown to be dependent on 2-Deoxy-D-glucose concentration in phantom work [27]. It has also been shown to increase between a control sample of human concentrated red blood cells, and a similar sample with an added 50mMol/L of glucose [27]. However, this concentration is far greater than what we would expect to see *in vivo* under normal conditions, and previous work has shown that measurement of the glucoCEST signal *in vivo* is difficult at clinical field strengths [28]. The blood sugar range of a healthy individual

typically resides between 3.9mMol/L and 7.1mMol/L [10], while hyperglycemia is generally accepted to occur above 11mMol/L [29, 30], and hypoglycemia is generally accepted to occur below 2.8mMol/L [11]. The purpose of this section is therefore to test whether we are able to measure changes in blood-glucose in this physiologically relevant range using glucoCEST, and calibrate the resulting CEST signals so that we can quantify glucose concentration in modified *ex vivo* blood samples.

5.2.1 Phantom investigations

In order to verify that the CEST signal from glucose could be seen at all at these lower concentrations, a glucose phantom was scanned. A 50ml test tube was filled with deionised water and 4mMol/L (36mg) of 2-Deoxy-D-glucose was added and dissolved. The test tube had a screw-on cap, and so was tightly sealed and placed in a 37°C water bath directly before scanning. The system did not have to be connected to a heat pump as the scanning protocol was short enough that cooling of the water bath towards room temperature was not a significant issue.

The glucose phantom was scanned using a 7T Achieva system with a NOVA 8ch pTx head coil. Tuning of the odd and even channels was performed as described previously, and a B_0 map was acquired. A z-spectrum was then acquired using semi-CW saturation, with a 3 second saturation block comprised of sixty 50ms pulses alternating on the odd and even channels, followed by the TFEPI readout scheme described in section 5.1.1. The z-spectrum was acquired with a $B_{1,max}$ of 1μT at 42 off-resonance frequencies, 41 of which were evenly spaced between +3.3ppm and -3.3ppm, with the remaining off-resonance frequency acquired at +333ppm for normalisation.

The z-spectral images were post-processed using an in-house MATLAB [31] script. The images were first normalised using the far off-resonance (333ppm) point, and then corrected for B_0 inhomogeneities using the acquired field map, as described in section 4.3.1. The glucoCEST signal was then characterised using the asymmetry method detailed in section 2.4.2. Figure 5.2.1 shows the z-spectrum acquired from

the glucose phantom.

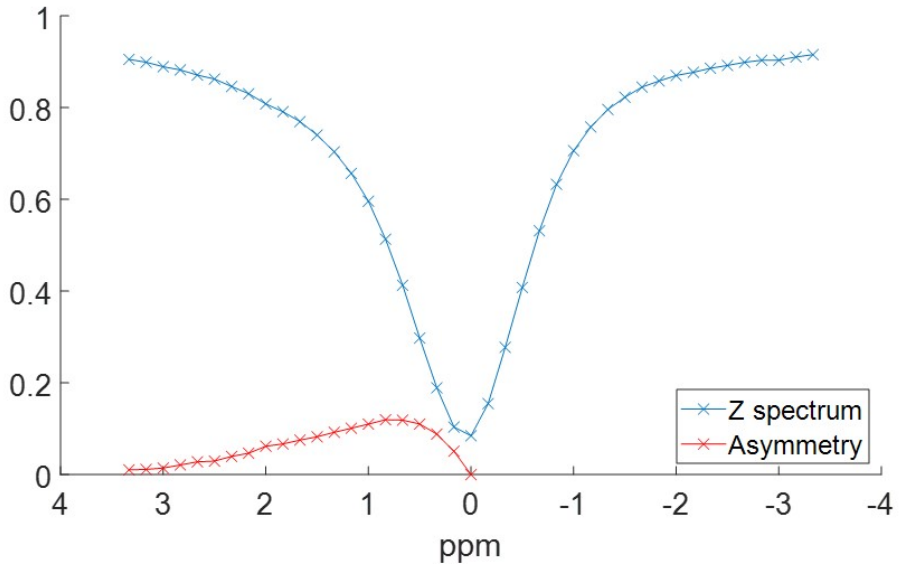

Figure 5.2.1: The z-spectrum acquired from a 2DG phantom, with the asymmetry of the spectrum revealing the glucoCEST signal.

While the presence of 2DG is not immediately evident at first glance at the z-spectrum, the asymmetry analysis reveals that effect of 2DG can be resolved at this comparatively low concentration, the shapes of which closely match previous work [27]. We can see the main peak at around 0.66ppm, with possible evidence of one of the other peaks located at +2.08ppm, while the other two peaks appear to have coalesced and were not observable under the conditions if this experiment. It is also not impossible that 2DG may produce an NOE signal which would reduce sensitivity in asymmetry analysis, especially with recent reports of glycogen producing its own 'glycoNOE' signal [32], however no such signal has been reported previously from glucose.

5.2.2 Z-spectra from blood with varying blood-glucose levels

The next step was to prepare a range of blood samples with differing amounts of blood glucose. One healthy volunteer donated 14 6ml samples of blood after a night of fasting to ensure starting blood-glucose level was relatively low. These samples were centrifuged for 15 minutes at 800rpm to separate concentrated red blood cells (cRBCs) from the plasma, and the plasma was removed.

These samples were then split into pairs and washed in solutions containing 7 different concentrations of glucose. Each sample was centrifuged after washing, and the glucose solution was removed. This was repeated two further times to maximise glucose absorption. Identical pairs of samples were then combined to create 7 samples with volumes of between 5-6ml. A drop of each sample was removed and deposited into an i-STAT CHEM8+ test cartridge (Abbot Point of Care Inc.) to measure the resulting blood-glucose level of each sample. The i-STAT CHEM8+ test was also performed directly after the experiment. Table 5.2.1 shows the blood-glucose levels of the samples before and after scanning, along with the mean value to reflect the properties which the samples were most likely to have during the scanning protocol.

The samples were fixed into the rotary water bath described in section 5.1.1, which was heated to 37°C prior to the experiment, and the setup was scanned using a 7T Achieva system with a NOVA 8ch pTx head coil as previously. Tuning of the odd and even channels was performed as described previously, and B_0 and B_1 maps were acquired. The heat pump was then switched off and the system was left to settle for 120 seconds to minimise flow artefacts. A z-spectrum was then acquired using semi-CW saturation identical to the sequence performed for the glucose phantom validation experiment, aside from the fact that 63 off-resonance frequencies were acquired between +333ppm and -333ppm. The B_1 max was also altered to 0.33μT for the first z-spectrum acquisition, which took 9 minutes 30 seconds. The heat pump was then switched back on until the system returned to 37°C, at which point it was

Glucose solution	Solution composition	Mean blood-glucose level (mMol/L)	Mean haematocrit level (%)
0mM	100ml saline + 0mg glucose	1.55 (1.6 to 1.5)	44.0 (44 to 44)
2mM	100ml saline + 36mg glucose	2.80 (2.9 to 2.7)	69.0 (71 to 67)
4mM	100ml saline + 72mg glucose	3.65 (3.8 to 3.5)	68.5 (72 to 69)
6mM	100ml saline + 108mg glucose	4.50 (4.6 to 4.4)	70.0 (71 to 69)
8mM	100ml saline + 144mg glucose	6.90 (7.1 to 6.7)	49.5 (50 to 49)
12mM	100ml saline + 216mg glucose	7.90 (8.0 to 7.8)	50.0 (50 to 50)
16mM	100ml saline + 288mg glucose	10.20 (10.4 to 10.0)	68.0 (69 to 67)

Table 5.2.1: Glucose solutions used in phantom preparation and i-STAT results. Change in blood-glucose level and haematocrit from before to after scanning indicated in parentheses. 71mg of salt was also added to each solution.

once again switched off and the system was left to settle for 120 seconds. Four further z-spectra were acquired using this protocol, with $B_{1,max}$ values of 0.67μT, 1.00μT, 1.33μT, and 1.67μT respectively.

The resulting z-spectra were post-processed using in-house MATLAB [31] scripts. Each blood sample was masked and the spectra within each sample were normalised using the far off-resonance +333ppm point. The z-spectra were then corrected for B_0 inhomogeneities using the acquired field map, as described in section 4.3.1, and the resulting z-spectra in each sample were averaged. In order for direct comparison between the samples, the z-spectra also had to be B_1 corrected. The blood sample masks were applied to the acquired B_1 map to find the actual B_1 in each sample. Each point in the five z-spectra of varying saturation power could then be interpolated from the actual B_1 to the target B_1, utilising the multiple saturation powers to model how each point in the z-spectrum changes with increasing B_1 in each sample.

5.2. ESTIMATING BLOOD-GLUCOSE LEVELS VIA GLUCOCEST

Quantifying the glucoCEST signal using the asymmetry method is clearly not appropriate here, as there are multiple sources of signal in the acquired spectrum. However, aside from the glucose signal, the underlying signal should be completely identical in each sample, as the initial blood sample was taken from the same subject at the same time. It should therefore be possible to compare the averaged signals at the points where the four glucose pools resonate, namely +0.66ppm, +1.28ppm, +2.08ppm, and +2.88ppm [20]. Z-spectral images were not acquired at these exact frequencies, so the four closest off-resonance frequencies to these were taken and averaged, which were +0.83ppm, +1.17ppm, +2.0ppm, and +3.0ppm. These were then plotted against the average blood-glucose level of each sample during acquisition to give a qualitative view of how the glucoCEST signal changes in human blood within a range we would expect to see *in vivo*.

Figure 5.2.2 shows the B_0 and B_1 corrected z-spectra acquired from each of the seven samples. A change in glucoCEST signal is not obvious in the z-spectra.

Figure 5.2.3 shows the change in the glucoCEST metric between samples of varying blood-glucose level for each saturation power. No change in the glucoCEST signal is discernible.

As we can see from Figure 5.2.3, changes in blood-glucose level across the expected physiological range appear to have no effect on the magnitude of the glucoCEST signal from blood. This is not completely unexpected, as the previously reported change of the glucoCEST signal at 50mMol/L was relatively small [27]. The aforementioned study was also conducted at 9.4T, leading to greater resolution of any CEST peaks present. It is possible that higher saturation powers may see some blood-glucose level dependent changes, as glucose has a fast exchange rate with the free water pool and so is more prevalent at higher powers, however this seems unlikely given that no signal change at all could be seen between blood-glucose levels of 2mMol/L and 10mMol/L here.

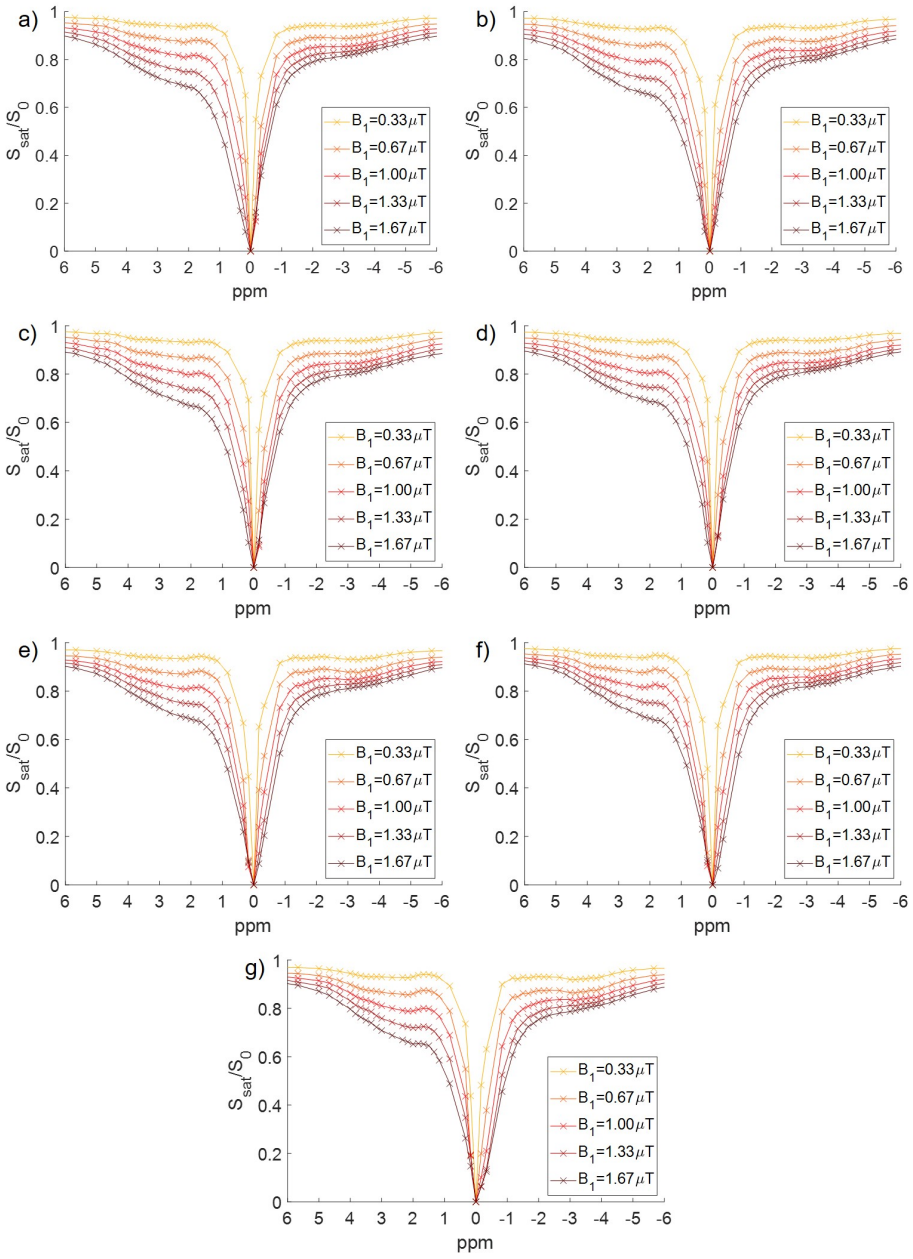

Figure 5.2.2: The z-spectra acquired from blood samples with a blood glucose level of a) 1.55mMol/L, b) 2.80mMol/L, c) 3.65mMol/L, d) 4.50mMol/L, e) 6.90mMol/L, f) 7.90mMol/L, and g) 10.20mMol/L.

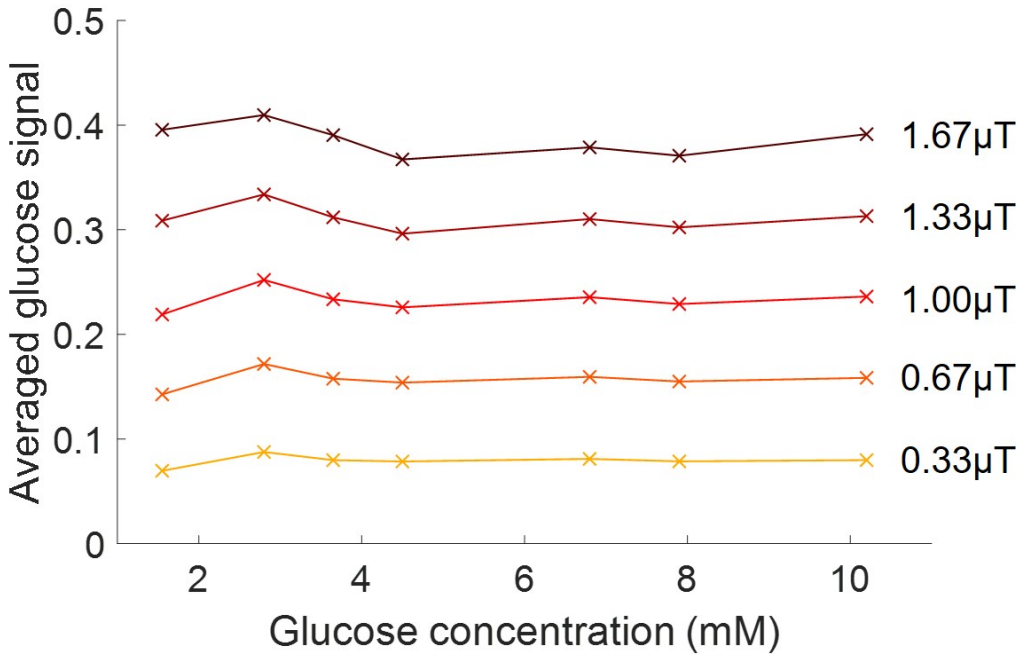

Figure 5.2.3: Evolution of the glucoCEST signal with increasing blood-glucose levels.

5.3 Measuring blood pH via CEST contrast

Previous work has shown that there may be a small amount of pH dependency on the CEST signal located at the amide frequency, and the NOE signal located at -3.5ppm in human blood samples [12]. However, this dependency was not found to be significant, as the apparent change in signal was small and non-linear, and the error bars were too large to draw any direct conclusions from the relationships between pH and CEST or NOE signals originating from endogenous CEST compounds. This section aims to determine a method of measuring the pH of human blood through the measurement of the CEST signals of an exogenous CEST contrast agent, namely Iopamidol, over a physiological range. Iopamidol has two CEST peaks located at +4.2ppm and +5.5ppm with different exchange rates, which therefore evolve differently with changing pH

[33]. These two peaks correspond to the amide and 2-hydrooxypropanamido groups respectively. It is therefore possible to utilise a ratiometric approach, dividing the magnitude of one peak by the other, to calibrate for pH.

Significant pH contrast has been demonstrated in Iopamidol phantoms between pH 6.0 and pH 7.5 [33], and this method has also been employed in mouse kidneys to provide accurate pH measurements in the pH 5.5 to pH 7.4 range [34]. It is important also to note that the sensitivity of this approach will be strongly dependent on saturation power, as the 2-hydrooxypropanamido group has an exchange rate estimated to be four times faster than the exchange rate of the amide group [33]. The normal pH level of blood is 7.4 [35], however certain diseases can cause either acidosis or alkalosis, causing blood pH to either drop down to pH 6.8 or lower in extreme cases [36], or rise above pH 7.8 [37], both of which can be fatal. Iopamidol is already used as a contrast agent in CT imaging [38], and therefore the safety of administering this compound intravenously has been thoroughly tested. This section therefore aims to utilise the ratiometric approach used elsewhere [33] to determine the pH of a variety of phosphate buffered *ex vivo* human blood samples, in order to calibrate the results with pH over a physiological range.

5.3.1 Calibrating the CEST signals of Iopamidol with pH

Following local ethical approval, five 6ml blood samples were taken from one healthy volunteer and stored in heparin tubes. The samples were centrifuged for 15 minutes at 800rpm to separate concentrated red blood cells (cRBCs) from the plasma, and the plasma was removed. The samples were then washed 3 times with phosphate-buffered saline solutions at pH 6.8, pH 7.2, pH 7.6, pH 8.0, and pH 8.4, before being re-centrifuged and the phosphate-buffered saline removed. 1ml of Iopamidol (300mg/1ml) was added to each of the samples as a pH dependent contrast agent.

The samples were fixed into the rotary water bath described in section 5.1.1, which was heated to 37°C prior to the experiment, and the setup was scanned using a 7T Achieva system with a NOVA 8ch pTx head coil using the exact same protocol as described in section 5.2.2. The odd and even channels were matched and B_0 and B_1 maps were acquired. Z-spectra were once again acquired using semi-CW saturation at 5 $B_{1,max}$ values of 0.33μT, 0.67μT, 1.00μT, 1.33μT, and 1.67μT at 64 off-resonance frequencies between $\pm$333ppm, with a TFEPI readout.

The z-spectra from each sample were post-processed using in-house MATLAB [31] scripts. Each sample was masked and the spectra within each sample were normalised using the far off-resonance +333ppm point. The z-spectra were then corrected for B_0 inhomogeneities using the acquired field map, as described previously, and the resulting z-spectra in each sample were averaged. The z-spectra were B_1 corrected as described in section 5.2.2, by masking the acquired B_1 map with the blood sample masks, and then interpolating each point in the five z-spectra of varying saturation power to model the z-spectra which would have been acquired at the target B_1, so that the samples could have been measured directly. As the B_1 inhomogeneity was relatively high in this case (ranging between 140$\%$-280$\%$), spectra were B_1 corrected to 200$\%$ of the target B_1 values in order to stay within the sampled range.

The z-spectra were then fitted to a twelfth order polynomial between +3ppm to +6ppm. As data had not been acquired directly at +4.2ppm or +5.5ppm, this was necessary to estimate the value of the z-spectrum at these points, and also reduced the error of simply acquiring two images at these off-resonance frequencies, as the estimated values of these frequencies were dependent on the several images acquired at the off-resonance frequencies neighbouring these. A ratiometric value was then obtained by dividing the value of the peak at +5.5ppm by the peak at +4.2ppm, and plotted against pH for each saturation power.

Figure 5.3.1 shows the B_0 and B_1 corrected z-spectra acquired from each of the five samples. We can see the evolution of the Iopamidol signals located at +4.2ppm and +5.5ppm.

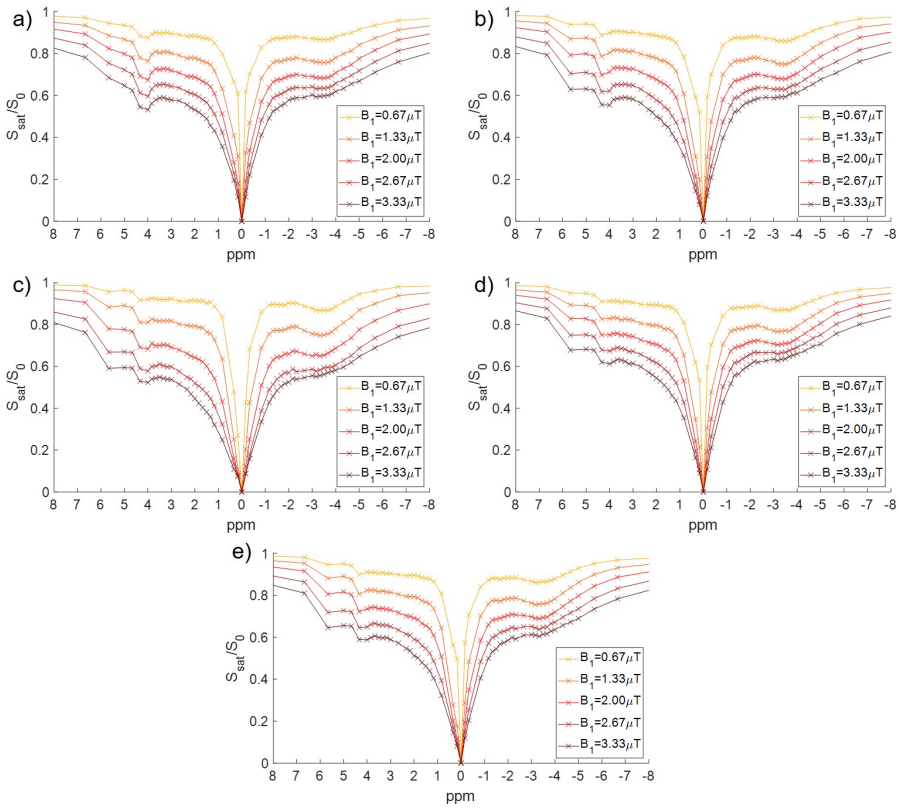

Figure 5.3.1: The z-spectra acquired from blood samples with added Iopamidol, with pH levels of a) 6.8, b) 7.2, c) 7.6, d) 8.0, and e) 8.4.

Figure 5.3.2 shows the results of spline fitting of the z-spectra between +3ppm and +6ppm. The nature of the dependency of the Iopamidol signals on pH is more apparent here.

Figure 5.3.3 shows the relationship between the ratio of the Iopamidol peaks with blood pH. Error bars have been created through error propagation of the uncertainty associated with each point on the acquired z-spectra, estimated through observing the variance of repeated acquisitions of the same z-spectrum point in the water between the blood samples. We can see that in the physiological range, acquiring a spectrum at relatively low saturation power can provide us with the information we need to determine pH.

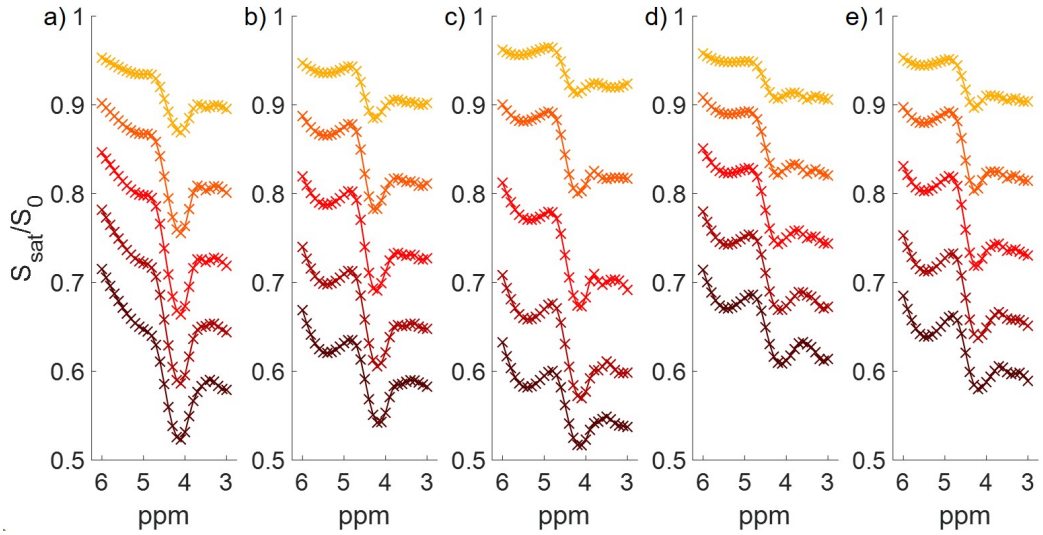

Figure 5.3.2: Spline fitting of the z-spectra presented in Figure 5.3.1 between +3ppm and +6ppm, with pH levels of a) 6.8, b) 7.2, c) 7.6, d) 8.0, and e) 8.4.

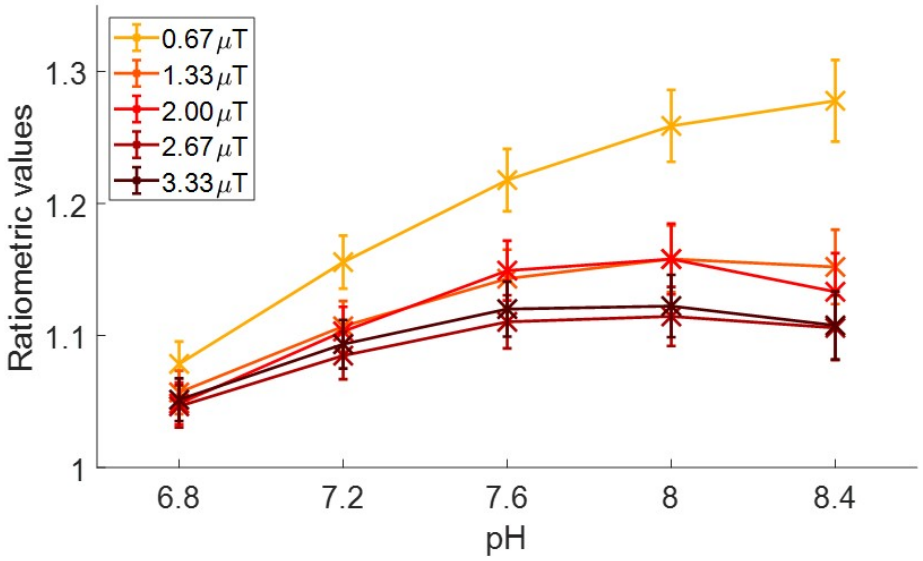

Figure 5.3.3: Ratiometric analysis of the CEST peaks displayed in Figure 5.2.2, obtained by dividing the value of the peak at +5.5ppm by the peak at +4.2ppm, plotted against sample pH for each saturation power.

We can see clearly that higher saturation powers are far less suitable for determining the pH of blood in the physiological range. Acquiring the z-spectrum with a saturation power of 0.67μT however, gives excellent sensitivity over the physiological range, especially between pH 7.2 and pH 7.6, where the pH level of healthy blood is. Further work could more accurately determine the optimum saturation power for pH measurement within this range.

As mentioned in section 4.3, recent work has shown that the presence of PBS may significantly alter the CEST signal [39]. However this work suggests that amide protons are unaffected by the presence of phosphate. PBS should however be considered as a confounding factor where CEST experiments are performed involving any systems involving any exchangeable protons other than amide protons.

5.3.2 Potential applications and future work

The applications for a safe pH dependent CEST contrast agent are not limited to blood. Iopamidol is a readily available CT contrast agent which can be administered in humans orally and intravenously. This method of pH determination could also have uses in the stomach or the bowel, where acidity regulation is key, however further work would have to be performed to investigate the capabilities of Iopamidol as a CEST agent under such harshly acidic conditions. The pH value of muscle also changes after exercise, and accurate *in vivo* measurements of this during exercise may be of great importance when understanding the mechanisms of fatigue [40].

5.4 Summary

The z-spectrum from human blood is complex in its makeup, and the nature of the signals we see are difficult to interpret. In the first part of the chapter, an attempt at deconstructing the z-spectrum into its constituent parts was performed using the

PSO fitting method introduced in the previous chapter. A reasonable model for the z-spectrum of human blood was found, however certain discrepancies in the fitting suggest that the true model is more complex than the one used here. Practical applications of the human blood z-spectrum were then explored, firstly using GlucoCEST as a marker of blood-glucose levels. Unfortunately no correlation could be defined between glucose and the GlucoCEST signal within a physiological range, most likely due to the signal being so small. Finally the feasibility of measuring blood pH using Iopamidol as a CEST agent was explored, and it was found that it is possible to measure blood pH over a physiological range, given that an appropriately low saturation power is used for acquisition. This is an important result as it may have applications beyond the blood, such as in gastrointestinal or muscle imaging.

References

[1] Piotr A. Wielopolski, Mary Adamis, Pottumarthi Prasad, Jochen Gaa, and Robert Edelman. Breath-Hold 3D STAR MR Angiography of the Renal Arteries Using Segmented Echo Planar Imaging. *Magnetic Resonance in Medicine*, 1995. ISSN 15222594. doi: 10.1002/mrm.1910330319.

[2] Neville D. Gai, S. Lalith Talagala, and John A. Butman. Whole-brain cerebral blood flow mapping using 3D echo planar imaging and pulsed arterial tagging. *Journal of Magnetic Resonance Imaging*, 2011. ISSN 10531807. doi: 10.1002/jmri.22437.

[3] D. A. Feinberg, J. D. Hale, J. C. Watts, L. Kaufman, and A. Mark. Halving MR imaging time by conjugation: Demonstration at 3.5 kG. *Radiology*, 1986. ISSN 00338419. doi: 10.1148/radiology.161.2.3763926.

[4] A. Richardson Jones, Dean Twedt, William Swaim, and Eugene Gottfried. Diurnal change of blood count analytes in normal subjects. *American Journal of Clinical Pathology*, 1996. ISSN 00029173. doi: 10.1093/ajcp/106.6.723.

[5] M. Maes, S. Scharpé, W. Cooreman, A. Wauters, H. Neels, R. Verkerd, F. De Meyer, P. D'Hondt, D. Peeters, and P. Cosyns. Components of biological, including seasonal, variation in hematological measurements and plasma fibrinogen concentrations in normal humans. *Experientia*, 1995. ISSN 00144754. doi: 10.1007/BF01929358.

[6] D. Dot, J. Miro, and X. Fuentes-Arderiu. Within-subject biological variation of hematological quantities and analytical goals. *Archives of Pathology and Laboratory Medicine*, 1992. ISSN 00039985.

[7] Myfanwy J. Borel, Scott M. Smith, Janice Derr, and John L. Beard. Day-to-day variation in iron-status indices in healthy men and women. *American Journal of Clinical Nutrition*, 1991. ISSN 00029165. doi: 10.1093/ajcn/54.4.729.

[8] A. C. Looker, C. T. Sempos, K. Liu, C. L. Johnson, and E. W. Gunter. Within-person variance in biochemical indicators of iron status: Effects on prevalence estimates. *American Journal of Clinical Nutrition*, 1990. ISSN 00029165. doi: 10.1093/ajcn/52.3.541.

[9] C. G. Fraser, S. P. Wilkinson, R. G. Neville, J. D.E. Knox, J. F. King, and R. S. MacWalter. Biologic variation of common hematologic laboratory quantities in the elderly. *American Journal of Clinical Pathology*, 1989. ISSN 00029173. doi: 10.1093/ajcp/92.4.465.

[10] Goodarz Danaei, Mariel M. Finucane, Yuan Lu, Gitanjali M. Singh, Melanie J. Cowan, Christopher J. Paciorek, John K. Lin, Farshad Farzadfar, Young Ho Khang, Gretchen A. Stevens, Mayuree Rao, Mohammed K. Ali, Leanne M. Riley, Carolyn A. Robinson, and Majid Ezzati. National, regional, and global trends in fasting plasma glucose and diabetes prevalence since 1980: Systematic analysis of health examination surveys and epidemiological studies with 370 country-years and 2·7 million participants. *The Lancet*, 2011. ISSN 01406736. doi: 10.1016/S0140-6736(11)60679-X.

[11] Mary F. Carroll, Mark R. Burge, and David S. Schade. Severe hypoglycemia in adults, 2003. ISSN 13899155.

[12] Simon M. Shah, Olivier E. O.E. Olivier E. Mougin, A.J. Andrew J. Carradus, Nicolas Geades, Richard Dury, William Morley, and Penny A. P.A. Gowland. The z-spectrum from human blood at 7T. *NeuroImage*, 167, 2018. ISSN 10959572. doi: 10.1016/j.neuroimage.2017.10.053.

[13] Kimberly L. Desmond, Firas Moosvi, and Greg J. Stanisz. Mapping of amide, amine, and aliphatic peaks in the CEST spectra of murine xenografts at 7 T. *Magnetic Resonance in Medicine*, 2014. ISSN 15222594. doi: 10.1002/mrm.24822.

[14] Xiao Yong Zhang, Feng Wang, Aqeela Afzal, Junzhong Xu, John C. Gore, Daniel F. Gochberg, and Zhongliang Zu. A new NOE-mediated MT signal at around -1.6 ppm for detecting ischemic stroke in rat brain. *Magnetic Resonance Imaging*, 2016. ISSN 18735894. doi: 10.1016/j.mri.2016.05.002.

[15] Peter C.M. van Zijl, Wilfred W. Lam, Jiadi Xu, Linda Knutsson, and Greg J. Stanisz. Magnetization Transfer Contrast and Chemical Exchange Saturation Transfer MRI. Features and analysis of the field-dependent saturation spectrum. *NeuroImage*, 2018. ISSN 10959572. doi: 10.1016/j.neuroimage.2017.04.045.

[16] Jinyuan Zhou, Bachchu Lal, David A. Wilson, John Laterra, and Peter C.M. Van Zijl. Amide Proton Transfer (APT) Contrast for Imaging of Brain Tumors. *Magnetic Resonance in Medicine*, 2003. ISSN 07403194. doi: 10.1002/mrm.10651.

[17] Kejia Cai, Mohammad Haris, Anup Singh, Feliks Kogan, Joel H. Greenberg, Hari Hariharan, John A. Detre, and Ravinder Reddy. Magnetic resonance imaging of glutamate. *Nature Medicine*, 2012. ISSN 10788956. doi: 10.1038/nm.2615.

[18] Wen Ling, Ravinder R. Regatte, Gil Navon, and Alexej Jerschow. Assessment of glycosaminoglycan concentration in vivo by chemical exchange-dependent saturation transfer (gagCEST). *Proceedings of the National Academy of Sciences of the United States of America*, 2008. ISSN 00278424. doi: 10.1073/pnas.0707666105.

[19] Merton Bernfield, Martin Götte, Pyong Woo Park, Ofer Reizes, Marilyn L. Fitzgerald, John Lincecum, and Masahiro Zako. Functions of cell surface heparan sulfate proteoglycans, 1999. ISSN 00664154.

[20] Moritz Zaiss, Annasofia Anemone, Steffen Goerke, Dario Livio Longo, Kai Herz, Rolf Pohmann, Silvio Aime, Michal Rivlin, Gil Navon, Xavier Golay, and Klaus Scheffler. Quantification of hydroxyl exchange of D-Glucose at physiological conditions for optimization of glucoCEST MRI at 3, 7 and 9.4 Tesla. *NMR in Biomedicine*, 2019. ISSN 10991492. doi: 10.1002/nbm.4113.

[21] Lewis Heitkemper and Dirksen O' Brien Bucher. *Medical-Surgical Nursing Assessment and Management of Clinical Problems*. 2007. ISBN 9780323091473.

[22] R. A. Fisher. Moments and product moments of sampling distributions. *Proceedings of the London Mathematical Society*, 1930. ISSN 1460244X. doi: 10.1112/plms/s2-30.1.199.

[23] Peter C.M. van Zijl, Wilfred W. Lam, Jiadi Xu, Linda Knutsson, and Greg J. Stanisz. Magnetization Transfer Contrast and Chemical Exchange Saturation Transfer MRI. Features and analysis of the field-dependent saturation spectrum. *NeuroImage*, 2018. ISSN 10959572. doi: 10.1016/j.neuroimage.2017.04.045.

[24] Craig K. Jones, Alan Huang, Jiadi Xu, Richard A.E. Edden, Michael Schär, Jun Hua, Nikita Oskolkov, Domenico Zacà, Jinyuan Zhou, Michael T. McMahon, Jay J. Pillai, and Peter C.M. van Zijl. Nuclear Overhauser enhancement (NOE) imaging in the human brain at 7T. *NeuroImage*, 2013. ISSN 10538119. doi: 10.1016/j.neuroimage.2013.03.047.

[25] Ulf Lindahl, John Couchman, Koji Kimata, and Jeffrey D. Esko. *Proteoglycans and Sulfated Glycosaminoglycans*. 2015. ISBN 9780879697709.

[26] Simon Walker-Samuel, Rajiv Ramasawmy, Francisco Torrealdea, Marilena Rega, Vineeth Rajkumar, S. Peter Johnson, Simon Richardson, Miguel Gonçalves, Harold G. Parkes, Erik Årstad, David L. Thomas, R. Barbara Pedley, Mark F.

Lythgoe, and Xavier Golay. In vivo imaging of glucose uptake and metabolism in tumors. *Nature Medicine*, 2013. ISSN 10788956. doi: 10.1038/nm.3252.

[27] F A Nasrallah, G Pages, P W Kuchel, X Golay, and K H Chuang. Imaging brain deoxyglucose uptake and metabolism by glucoCEST MRI. *J Cereb Blood Flow Metab*, 2013. ISSN 1559-7016. doi: 10.1038/jcbfm.2013.79.

[28] Mina Kim, Francisco Torrealdea, Sola Adeleke, Marilena Rega, Vincent Evans, Teresita Beeston, Katerina Soteriou, Stefanie Thust, Aaron Kujawa, Sachi Okuchi, Elizabeth Isaac, Wivijin Piga, Jonathan R. Lambert, Asim Afaq, Eleni Demetriou, Pratik Choudhary, King Kenneth Cheung, Sarita Naik, David Atkinson, Shonit Punwani, and Xavier Golay. Challenges in glucoCEST MR body imaging at 3 Tesla. *Quantitative Imaging in Medicine and Surgery*, 2019. ISSN 22234306. doi: 10.21037/qims.2019.10.05.

[29] H. Yki-Jarvinen, E. Helve, and V. A. Koivisto. Hyperglycemia decreases glucose uptake in type I diabetes. *Diabetes*, 1987. ISSN 00121797. doi: 10.2337/diab.36.8.892.

[30] A. M. Lam, H. R. Winn, B. F. Cullen, and N. Sundling. Hyperglycemia and neurological outcome in patients with head injury. *Journal of Neurosurgery*, 1991. ISSN 00223085. doi: 10.3171/jns.1991.75.4.0545.

[31] Version 9.6 2019 The Mathworks, Inc. MATLAB. MATLAB - MathWorks - MATLAB, 2019.

[32] Yang Zhou, Peter C.M. van Zijl, Xiang Xu, Jiadi Xu, Yuguo Li, Lin Chen, and Nirbhay N. Yadav. Magnetic resonance imaging of glycogen using its magnetic coupling with water. *Proceedings of the National Academy of Sciences of the United States of America*, 2020. ISSN 10916490. doi: 10.1073/pnas.1909921117.

[33] Phillip Zhe Sun, Dario Livio Longo, Wei Hu, Gang Xiao, and Renhua Wu. Quantification of iopamidol multi-site chemical exchange properties for ratiometric chemical exchange saturation transfer (CEST) imaging of pH. *Physics in*

Medicine and Biology, 2014. ISSN 13616560. doi: 10.1088/0031-9155/59/16/4493.

[34] Dario Livio Longo, Walter Dastrù, Giuseppe Digilio, Jochen Keupp, Sander Langereis, Stefania Lanzardo, Simone Prestigio, Oliver Steinbach, Enzo Terreno, Fulvio Uggeri, and Silvio Aime. Iopamidol as a responsive MRI-chemical exchange saturation transfer contrast agent for pH mapping of kidneys: In vivo studies in mice at 7 T. *Magnetic Resonance in Medicine*, 2011. ISSN 1522-2594. doi: 10.1002/mrm.22608.

[35] Michael D. Gooch. Identifying acid-base and electroylyte imbalances. *Nurse Practitioner*, 2015. ISSN 15388662. doi: 10.1097/01.NPR.0000469255.98119.82.

[36] T. Neuenfeldt and H. B. Hopf. Successful treatment of extreme metabolic acidosis and profound hypothermia. *Anaesthesist*, 2009. ISSN 0003-2417. doi: 10.1007/s00101-009-1615-z.

[37] Swagata Tripathy. Extreme metabolic alkalosis in intensive care. *Indian Journal of Critical Care Medicine*, 2009. ISSN 09725229. doi: 10.4103/0972-5229.60175.

[38] Dushyant V. Sahani, Gilles Soulez, Ke Min Chen, Luigi Lepanto, Jian Rong Xu, Rendon C. Nelson, Luigi Grazioli, Angelo Vanzulli, and Jay P. Heiken. A comparison of the efficacy and safety of iopamidol-370 and iodixanol-320 in patients undergoing multidetector-row computed tomography. *Investigative Radiology*, 2007. ISSN 00209996. doi: 10.1097/RLI.0b013e3181514413.

[39] Jingwen Yao, Chencai Wang, and Benjamin M. Ellingson. Influence of phosphate concentration on amine, amide, and hydroxyl CEST contrast. *Magnetic Resonance in Medicine*, 2021. ISSN 15222594. doi: 10.1002/mrm.28481.

[40] L. Hermansen and J. B. Osnes. Blood and muscle pH after maximal exercise in man. *Journal of applied physiology*, 1972. ISSN 00218987. doi: 10.1152/jappl.1972.32.3.304.

Chapter 6

Abdominal z-spectroscopy

Quantification of z-spectrum imaging in the abdomen presents unique challenges, as motion artefacts and localised changes in B_0 due to respiration are much greater than in the brain due to close proximity to the lungs. Furthermore blood pulsatility in organs such as the liver or kidney may further affect the z-spectrum as unsaturated blood flows into these organs at a high velocity between saturation and acquisition. However quantification of z-spectrum effects in abdominal organs would prove to be very useful, as MT has the potential to be a marker for fibrosis due to its high content of collagen, immobilised phospholipid cell membranes, and other macromolecules [1], which has been proven using MTR in both animal [2, 3] and human [4] subjects. In addition to this, quantification of glycogen in the liver is of particular interest, as blood sugar can only currently be measured *ex vivo*, whereas imaging provides an opportunity for localisation, and furthermore understanding how liver and muscle tissue metabolises glucose into glycogen may lead to further discoveries in understanding diseases such as diabetes where hypoglycemia is an issue. This chapter describes work which explores how to quantify these effects, first by investigating the MT signal from liver, gut wall and other abdominal tissues at 3T, before moving to 7T where CEST effects are more prominent. The manner in which the MT signal changes between 3T and 7T was then analysed, before performing an experiment which attempted to measure liver glycogen

synthesis over time after a high glucose content meal, using the GlycoCEST signal.

6.1 Quantification of MT in liver and gastrointestinal tract tissue

There are several conditions in which the normal functional tissue of abdominal organs can be replaced by scar tissue. The general term for this process is known as fibrosis. For example, cirrhosis is the buildup of fibrotic scar tissue in the liver, and can be a symptom of hepatitis B, hepatitis C, non-alcoholic fatty liver disease, or as a result of excessive alcohol consumption, among other potential causes [5]. Currently the most common and most reliable method of confirming cirrhosis is through a liver biopsy [6], although there are some imaging methods which correlate with cirrhosis such as magnetic resonance elastography [7], as a more heavily scarred liver will become stiffer than the comparatively soft healthy liver tissue. However, magnetic resonance elastography is also sensitive to several biological confounding effects such as liver steatosis (abnormally high fat retention), venous congestion and right heart failure [8].

Crohn's disease is a chronic condition in which the wall of the gastrointestinal tract becomes heavily inflamed [9]. It is usually diagnosed visually through endoscopy, and confirmed with a blood test, as anaemia may also be indicative of inflammation in the ileum due to impaired vitamin B12 absorption [10]. More recently it has been shown that diffusion-weighted MRI may have the potential to identify inflammation of the gastrointestinal tract [11], although this is sensitive to iron content and can suffer from artefacts such as poor fat saturation due to the EPI readout [12].

Measurement of the MT signal can be regarded as advantageous over magnetic resonance elastography and diffusion-weighted imaging for assessing fibrosis, in that it is relatively insensitive to iron deposition and steatosis [13, 14], and more directly dependent on fibrosis. As discussed, the major disadvantage of MT imaging in the

abdomen is its high sensitivity to localised B_0 and B_1 shifts. Therefore the aim of this section is to develop a reliable method of measuring MT in the liver, the wall of the gastrointestinal tract, and other abdominal organs or tissues. This is tested in healthy subjects, with the intention of developing a protocol suitable for imaging Crohn's patients or other individuals who may have some degree of abdominal fibrotic scarring.

6.1.1 Respiratory effects in MTR measures

A key constraint in abdominal imaging is the need for short imaging times, in order to overcome respiratory motion. MTR is widely used as a clinical marker of MT effects as it is a fast measure to perform [15, 16]. However, given that the MTR signal is affected by respiration, it is vital that we know to what degree the localised changes in the B_0 field arising from this alters MTR before conclusions are drawn from MTR data. To investigate this, one healthy subject was scanned using a 3T Philips Ingenia wide-bore system. Three MTR images were collected in succession, by firstly acquiring a far off-resonance image with a saturation train acquired at +100,000Hz, analogous to a no-saturation image, followed by three off-resonance images with a saturation train acquired at +1000Hz to saturate the MT pool. The subject was instructed to hold their breath during each of the four image acquisitions. The acquisition of each image took 2.3s with a 2.7s gap between each.

Figure 6.1.1 shows the MTR images acquired 5 seconds apart from each other. Even when the MTR images are acquired with a perfect breath-hold, there are respiratory driven artefacts which arise from how much air is held in the lungs, leading to local variations in the B_0 field. The effects of blood pulsatility are also apparent, but it appears that this is mainly an issue in the vessels themselves.

It is therefore clear that MTR alone is likely to be an unstable measure here, as the effects of respiration cannot be controlled or accounted for by acquiring only one point on the z-spectrum. Acquiring a full z-spectrum will inherently give a more reliable

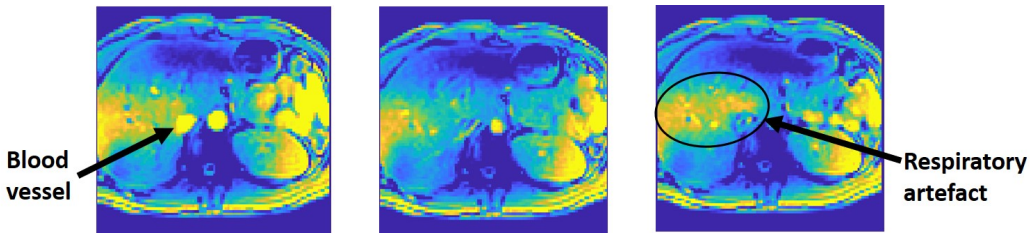

Figure 6.1.1: MTR images acquired on the same subject in quick succession, showing clear lack of repeatability when used in the abdomen.

measure of MT as more points are acquired, and the smoothness of the spectrum gives a qualitative measure for the noise in the data.

6.1.2 Respiratory and cardiac gating

Two healthy subjects were recruited to test z-spectrum acquisition with respiratory gating and cardiac triggering applied to the sequence. Z-spectra were acquired from a single slice with transverse orientation, using an MT-TFE sequence [17] comprising of a saturation train of 30 Gaussian windowed sinc pulses with pulse duration/spacing 30/80ms and a $B_{1,rms}$ of 2.19μT, and a single shot TFE readout scheme. 47 frequencies were acquired between $\pm$50,000Hz ($\pm$391ppm) in order to sample the full width of the MT peak [18], with acquisition of all 47 frequencies taking 2 minutes and 30 seconds. The z-spectrum initially appeared to be noisy from a visual on-scanner assessment, so four further repeats of the z-spectrum acquisition were performed.

The liver, kidney medulla, and back muscles were masked using in-house MATLAB [19] scripts to exclude blood vessels, and the five spectral images were normalised using the image acquired with +391ppm saturation and concatenated. These spectra were B_0 corrected by shifting each z-spectrum so that the minimum point on each aligned with 0ppm, and then interpolating using a twelfth order polynomial to calculate the z-spectrum values at the acquired frequencies. The highest and lowest signals recorded at each off-resonance frequency were discarded to remove outliers and reduce scatter, and the remaining points were averaged. This reduced noise to a degree in which the

resulting z-spectra looked as expected, as can be seen in Figure 6.1.2.

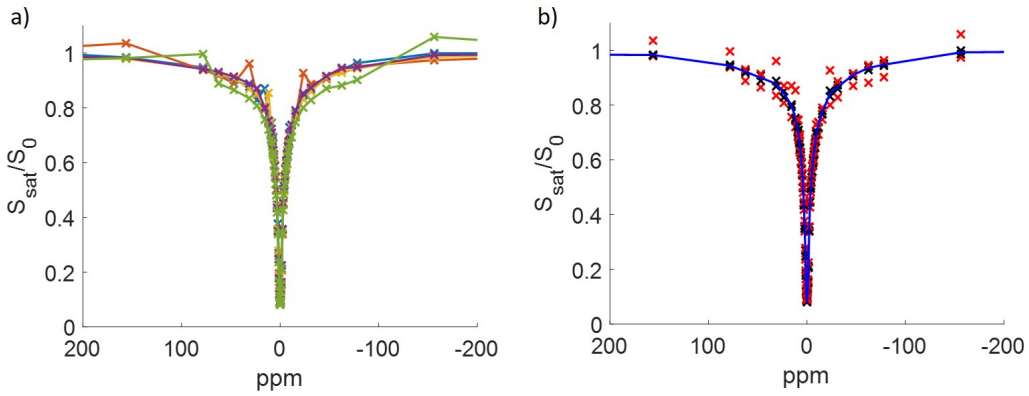

Figure 6.1.2: a) 5 z-spectra taken from an ROI covering the liver, showing clear artefacts. b) The 5 z-spectra displayed as 'x's, with the highest and lowest (red) signals discarded, and the remaining (black) points averaged to create an average z-spectrum (blue), which is much smoother.

Once averaged z-spectra had been obtained from each of the three ROIs from each subject, Lorentzian fitting was performed to quantify the amount of MT present. No CEST or NOE effects were visible in the spectrum, due in part to their low concentrations compared to MT. A two pool model was therefore used to fit the data, with a Lorentzian lineshape used for free water, and a super-Lorentzian lineshape used for the MT pool, the centre of which was allowed to vary. Figure 6.1.3 shows the Lorentzian fitting results in the liver ROI of one subject.

The amplitude of the MT super-Lorentzian was then taken to be a measure of the MT present. This measure assumes that the exchange rate between the bound pool and the free pool is constant across tissues and subjects. Temperature and pH variations are not expected to be a confound in healthy subjects but further work should be performed to investigate the nature of proton exchange in scar tissue and healthy tissue to confirm that this measure is suitable. The results of the MT fitting are displayed in Figure 6.1.4.

The MT measurements are consistent across the two subjects, suggesting that taking the average of 5 z-spectra is a suitable indicator of MT, and is far less hampered

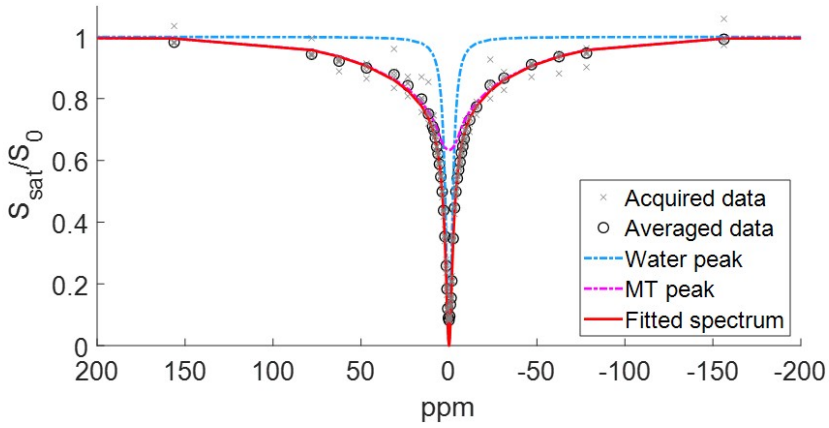

Figure 6.1.3: a) Lorentzian fitting performed with a 2 pool model to the z-spectrum from the liver of one subject (black circles), with both individual pools displayed as well as the final fit.

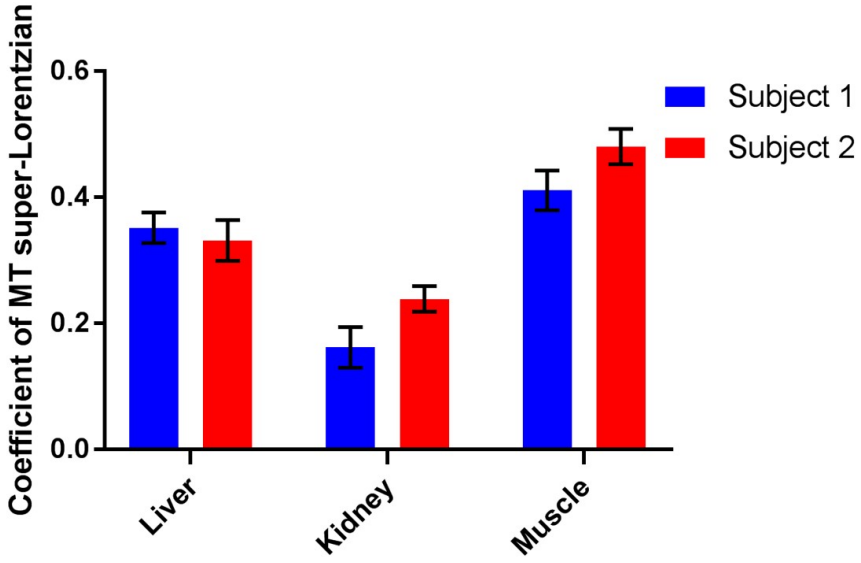

Figure 6.1.4: MT as measured from the coefficient of the fitted super-Lorentzian using a two pool model. Error bars are calculated from performing Lorentzian fitting to adjacent data points above and below the mean spectrum.

by artefacts caused by respiration or blood flow pulsatility, which will be present but

undetectable in studies simply measuring MTR. However, acquisition of five separate z-spectra is time consuming, taking 12.5 minutes. The following section details how to acquire a high fidelity z-spectrum without the need to collect multiple repeats, by helping the subject to regulate their breathing.

It was hypothesised that the large signal artefacts seen in the previous section were partly as a result from localised B_0 shifts arising from subjects holding different amounts of air in their lungs each time they were being asked to hold their breath during an acquisition, and partly from subjects breathing at a rate which was not consistent throughout the z-spectrum acquisition, resulting in varying TR between each acquired off-resonance image. To combat this, a method of encouraging subjects to breathe regularly was implemented. Subjects were shown a projector screen during a scan with automated cues appearing, with "Breathe in" shown for 1.5s, "Breathe out" shown for 1.5s, and "Hold" shown for 2.5s, a rate that all subjects stated they were comfortable with in testing. This eliminated the artefacts seen in Figure 6.1.2 during normal respiratory gating, as displayed in Figure 6.1.5, which shows three z-spectra acquired once each at three different values of $B_{1,rms}$ from the liver when acquired and masked using the same sequence and procedure as described above. Lorentzian fitting was performed to assess how the MT metric changes with increasing saturation power.

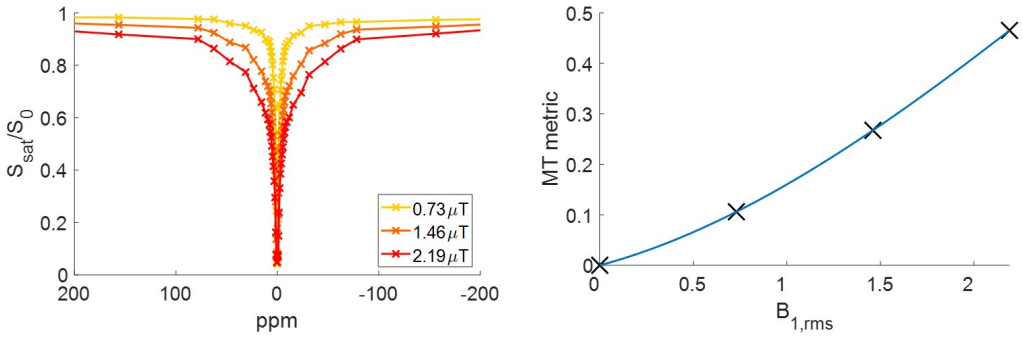

Figure 6.1.5: a) Z-spectra acquired from the liver when the subject was asked to regulate their breathing, showing vast reductions in noise when compared to standard respiratory gating. b) Plot of the MT super-Lorentzian amplitude with increasing saturation power, with a point at (0,0) included to aid the fit.

These results indicate that this is a reliable method of acquiring z-spectra in abdominal tissues. Future work should include acquiring more datasets to confirm the validity of this method, which was unfortunately not possible for this study. This respiratory gating technique could also be used to improve MTR imaging, but acquisition of the entire z-spectrum allows for accurate B_0 correction through identification of the location of the central water peak, and acquisition of several saturation powers allows for correction of local B_1 inhomogeneities.

6.1.3 Gastrointestinal z-spectroscopy

Once this initial testing had been completed an experimental protocol was devised to measure MT in the wall of the gastrointestinal tract. Two healthy volunteers (aged 24, 1F), were recruited for the study. Subjects ingested a solution containing 2.5% Mannitol and 0.2% locust bean gum 30 minutes prior to the scan, and a further 500ml immediately before the scan, as recommended when performing MRI of the bowel wall [20]. Mannitol increases MRI contrast between the lumen and the bowel wall [21], and the addition of locust bean gum serves to counteract some of the recognised side effects associated with Mannitol ingestion, which can include flatulence and alteration of gastrointestinal microbiota leading to bowel spasms and diarrhoea [22, 23, 24]. Subjects were also cannulated prior to the scan, and once in the scanner a 20mg dose of Buscopan® was administered intravenously. Buscopan® is an antispasmodic drug, and therefore halts normal peristaltic motion allowing for images of the bowel to be acquired without motion artefacts [25]. There is a small but serious risk of cardiac arrest when administering Buscopan® intravenously [26], and as such the heart rate of each subject was monitored throughout the scan.

Once the Buscopan® had been administered, the z-spectrum were acquired. Subjects lay prone in the scanner to minimise the effects of respiratory motion on the bowel wall, and visual triggers were shown as described previously. The MT-TFE sequence [17] was employed to acquire single-slice images in the coronal plane using the same parameters as detailed in section 6.1.2, however this time 48 off-resonance frequencies

between ±100,000Hz were acquired in a pseudo-random non-linear order. This was done so that the whole of the z-spectrum would be sampled to some degree if the effects of the Buscopan® began to wear off before the four minutes it took to acquire the entire z-spectrum were up.

The images were assessed visually to determine if motion had occurred before the completion of z-spectrum acquisition, which was the case for one of the subjects. The z-spectral images acquired after this point were discarded. The bowel wall was then masked manually by drawing around the ROI, as can be seen in Figure 6.1.6, and for further comparison two further ROIs were created in the liver and the abdominal muscle. For illustrative purposes the MTR for each of these regions from one subject is displayed in Figure 6.1.7, although as previously the coefficient of the fitted super-Lorentzian will be the metric used for MT.

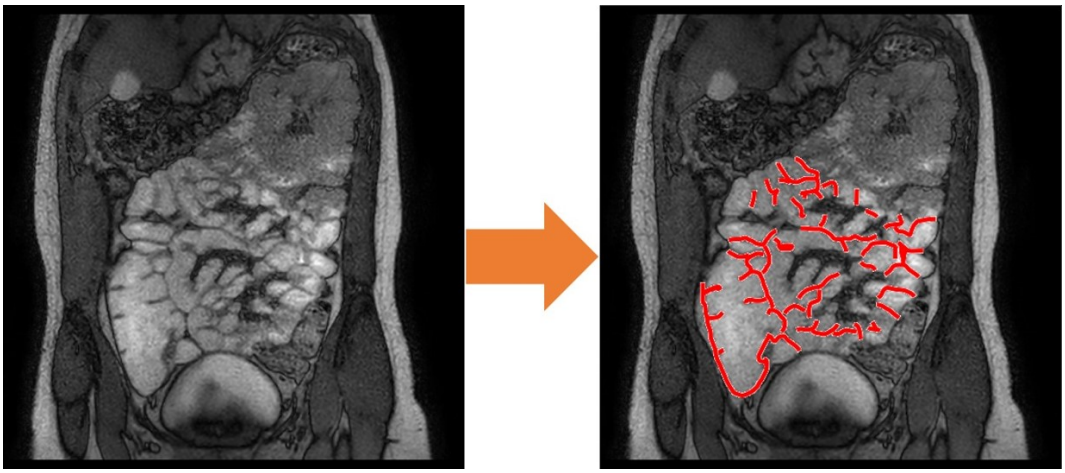

Figure 6.1.6: Example of an acquired z-spectral image and the applied bowel wall mask.

The z-spectra from each of these ROIs were averaged and subsequently B_0 corrected pixel-by-pixel using in house MATLAB scripts, by identifying the minimum point on each z-spectrum and shifting the entire spectrum so that this minimum aligned with the water resonance at 0ppm. A two pool Lorentzian fit was then performed in order to quantify the MT and water pools. Initial testing showed that a Lorentzian line-shape fitted the data better than a super-Lorentzian in all cases, so here a Lorentzian

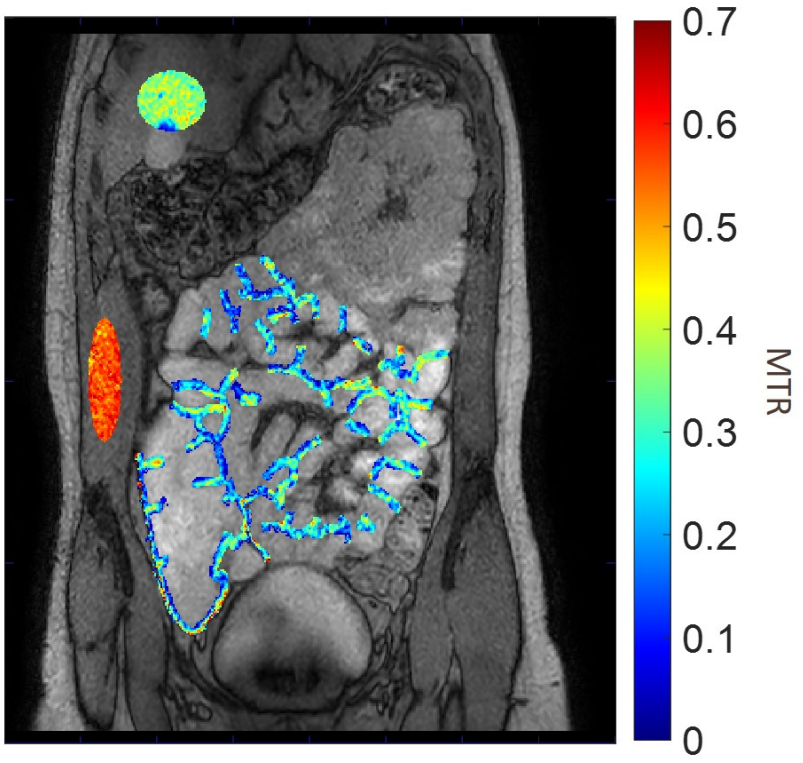

Figure 6.1.7: MTR map from one subject, to illustrate the ROIs used.

lineshape is used for the MT pool. Figure 6.1.8 shows the z-spectra from the three ROIs in both subjects, including the Lorentzian fitting.

Table 6.1.1 shows the amplitude of the MT peak in each ROI. The width of the peak is also included for interest, as this is indicative of the T_2 of the bound pool. The MT peak appears consistent in different tissues across the two subjects.

	Amplitude		Width (ppm)	
	Subject 1	Subject 2	Subject 1	Subject 2
Bowel wall	0.22	0.27	108.6	122.7
Liver	0.36	0.38	56.1	58.1
Muscle	0.52	0.60	143.0	163.1

Table 6.1.1: Resulting parameters of the Lorentzian fit to the bound pool.

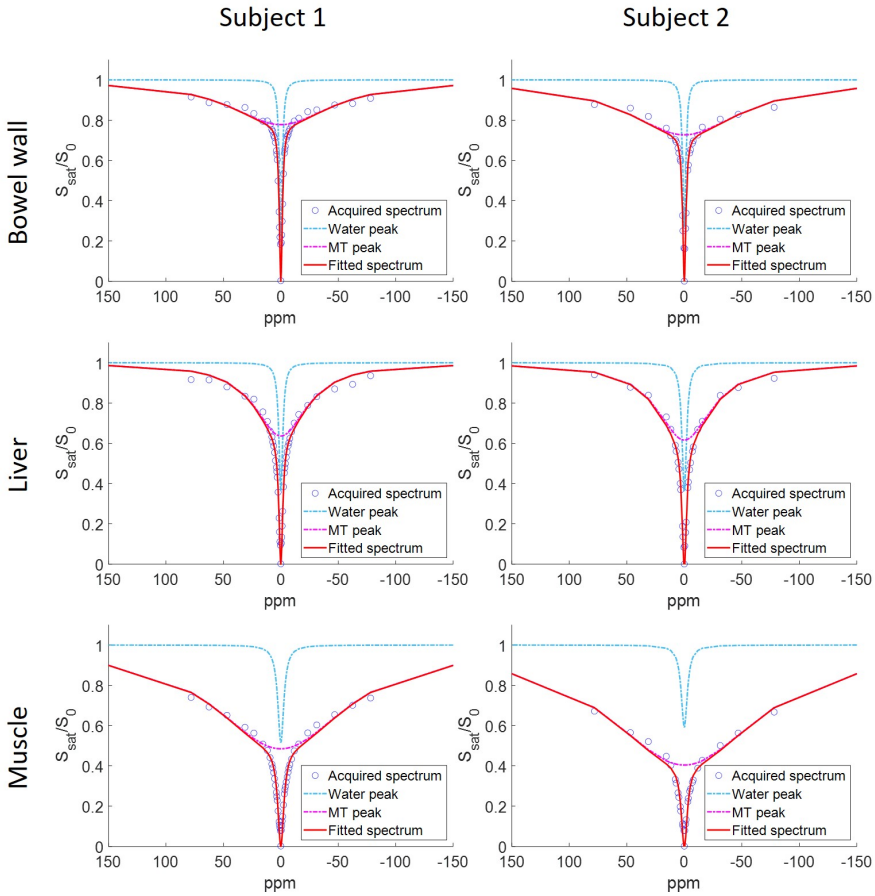

Figure 6.1.8: Lorentzian fitting of the z-spectra from the bowel wall (first row), liver (second row) and abdominal muscle (third row) in subject 1 (first column) and subject 2 (second column).

6.1.4 Discussion

It is clear from the results presented here that MTR is not an appropriate method of measuring abdominal MT, even when the MTR images are acquired both respiratory gated and cardiac gated. The protocol described in section 6.1.3 offers robust and pragmatic z-spectrum imaging in the abdomen which can be used for MT quantification. The first ever z-spectrum of the bowel wall is presented here, and the results of the Lorentzian fits indicate that we can reliably quantify MT in the bowel wall using

this regulated breathing method of acquiring a z-spectrum. The measured Lorentzian amplitudes from the liver and abdominal muscle are relatively consistent across both subjects, and the amplitudes measured in the liver match up to the amplitudes of the super-Lorentzians acquired from the liver when using the protocol acquiring and averaging five repeated z-spectra. There is a 15% difference in the muscle MT between experiments, although it is important to note that the super-Lorentzian fitting was performed on back muscle and the Lorentzian fitting was performed on abdominal muscle (as displayed in the ROI on Figure 6.1.7), as these lineshapes were found to be the best fit to the acquired data.

The change in the width of the MT pool between tissues warrants further discussion. These widths are consistent between the two subjects suggesting that we are observing a real biological effect rather than a fitting or acquisition anomaly. A wider MT peak is either indicative of a slower exchange rate with free water due to local temperature or pH differences, a shorter T_2 due to structural tissue differences, or a combination of these. The pH of healthy liver is 6.99 $\pm$ 0.03 [27] and the pH of healthy muscle is 7.08 at rest [28], however this drops to pH 6 in the wall of the small intestine [29] which may reduce exchange rate and widen the MT pool. However the difference in width between liver and abdominal muscle is likely to be due to changes in the T_2 of the bound pool, as abdominal temperature is expected to be reasonably consistent in healthy subjects.

The MT pool cannot be fully quantified without acquisition of further saturation powers. If several z-spectra were acquired, a fitting method such as a look-up table could be used to quantify the MT pool size, exchange rate, and T_2, in order to further understand the biological effects at play. This would have use beyond measuring the amount of MT present, since a measure of exchange rate could be used as a marker for pH. However, the total duration of z-spectra acquisition is limited by the properties of Buscopan®, which in this study could only effectively halt bowel motion for around 8 minutes. Therefore if we wanted to acquire additional z-spectra with varying saturation powers, it would be necessary to decrease the spectral resolution, which may be reasonable for measuring MT.

To get an indication of which off-resonance frequencies are required to maintain reasonable precision in Lorentzian fitting, the fitting was performed on an existing dataset with selected frequencies omitted to observe the influence each point has on the fit. The bowel wall z-spectrum from subject 1 was taken and symmetrical datapoints were removed one by one, starting with ±391ppm, so that the far off-resonance frequency remained as this is vital for normalisation. Lorentzian fitting was performed on the dataset with each of these frequencies removed and the degree to which the height of the MT Lorentzian varied from the fit performed with all frequencies was recorded. Figure 6.1.9 shows this variation plotted against off-resonance frequency to yield a measure of influence that each point had on the Lorentzian fitting for this dataset.

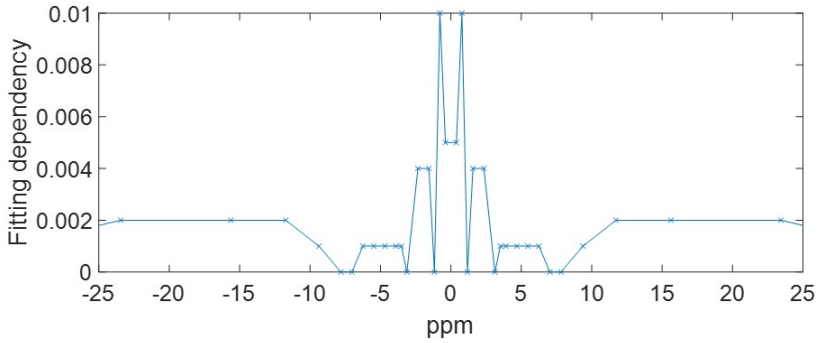

Figure 6.1.9: Variation of Lorentzian fitting of the z-spectra from the bowel wall of subject 1, where a result of zero suggests that the off-resonance frequency in question has no influence on the fit.

From this test we can see that the datapoints acquired at ±7.8ppm, ±7.0ppm, ±3.1ppm, and ±1.2ppm had no influence on the Lorentzian fitting. As a final test all eight of these points were removed simultaneously and the fit was performed again, and it was confirmed that removing all of these points together had no effect on the Lorentzian fit. Removing these eight off-resonance frequencies would reduce total acquisition time from 4 minutes to 3 minutes 20 seconds. However it could be that this result depends on the noise in this particular dataset, and this work should be extended further.

Future work should employ this protocol to validate that MT data acquired from the

z-spectrum can be used as a marker for fibrosis, by recruiting subjects with Crohn's disease as well as a healthy control group, and comparing the amount of MT measured in both. This is the basis of the MERIT study which was planned to start in spring 2020 and will now start in late 2020. This protocol could also be used in subjects afflicted with liver or kidney fibrosis. Finally it is interesting to note that no CEST or NOE signals were visible. Assuming that validation in subjects with fibrotic scarring is successful, it may be of interest to repeat the study at 7T in order to better visualise any CEST or NOE signals present and further characterise the z-spectrum of fibrosis.

6.2 Magnetisation transfer imaging at 7T

Imaging at 7T provides some significant advantages over the clinically used field strengths of 3T and 1.5T [30, 31]. Most importantly for CEST imaging, the chemical shift increases from 128Hz to 298Hz per ppm, and so while CEST and NOE peaks are less visible at clinical field strengths, they are better resolved at ultra-high fields. This is also aided by sharpening of the water peak, meaning that a lesser degree of coalescence occurs between free water and exchanging pools. SNR is also higher at 7T which means that higher resolution imaging is available. Increasing the B_0 also lengthens T_1 which improves sensitivity to MT effects. However, imaging at higher field strengths also comes with some drawbacks. An increase in SAR can mean that only lower flip angles are possible, and poorer uniformity of the transmitted B_1 field in the body can lead to position dependent flip angles and unexpected contrast.

6.2.1 Acquisition methods

The 7T body imaging described in the remainder of this chapter was performed using an 8 channel transmit, 32 channel receive body array (MRCoils, Zaltbommel, Netherlands), with the eight transmit elements placed round the subject so that four are on the posterior side and four are on the anterior side. Power limits for each of the trans-

mit elements can be altered at the scanner. A comprehensive and extensive review of this system can be found within Doran 2020 [32]. A single healthy subject (age 24, male) was recruited for initial testing.

As the RF output for each transmit array can be determined separately, it is possible to perform semi-CW saturation using the body coil. The assumption with this technique is that RF coverage originating from each of the eight transmit elements is fairly evenly distributed across the abdomen. Figure 6.2.1 shows a far off-resonance spectral image signal, which is dependent on transmit and receive elements.

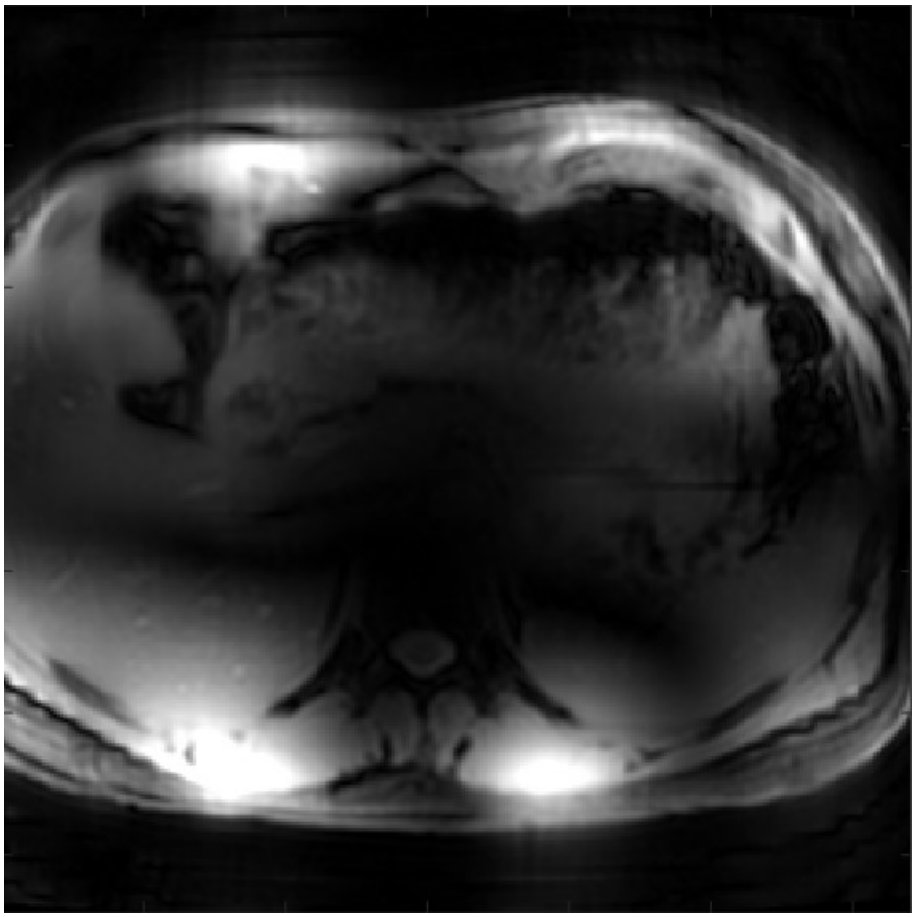

Figure 6.2.1: Z-spectral image acquired at +333ppm, acquired using semi-CW saturation and a TFEPI readout scheme.

While there is evidence of significant signal loss in the centre of the body, a reasonable amount of SNR is present in more distal regions. As evidenced in section 2.3.1, we need the average signal in a given ROI to be constructed fairly evenly from the odd and even channels to perform semi-CW saturation. By selecting a large enough ROI, for example in the liver, we can ensure this is the case, as will be evidenced later in this section.

Unfortunately, due to a combination of SAR and hardware limits, the maximum saturation power we can achieve from the body coil is somewhat limited. A $B_{1,max}$ of approximately 1μT could be achieved, half that which was possible in the multi-transmit head coil used in chapters 3 and 4. This was even less in practice, as B_1 mapping showed relatively poor RF coverage. An example B_1 map acquired with the AFI technique is displayed in Figure 6.2.2.

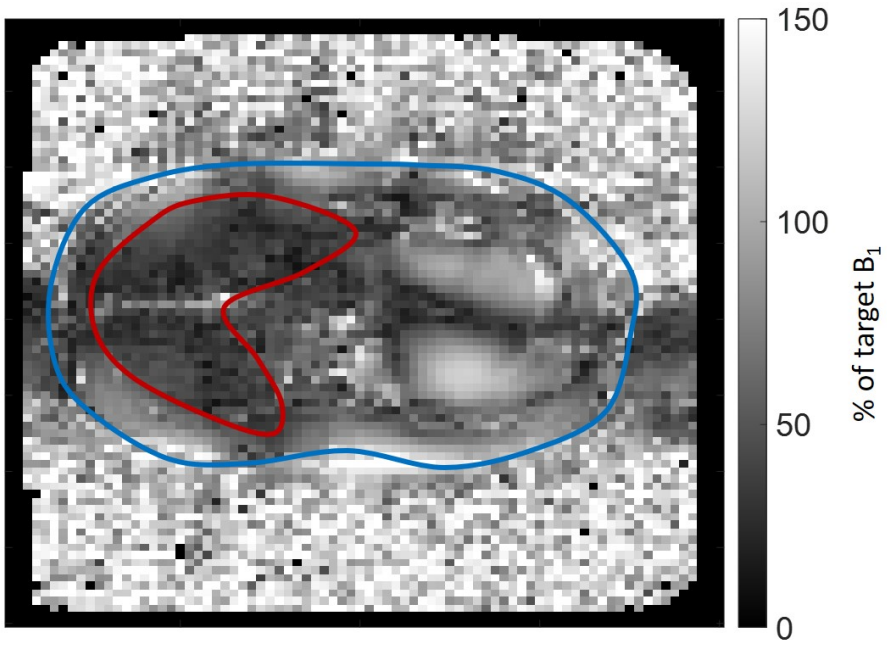

Figure 6.2.2: B_1 map acquired showing the poor B_1 transmit field in the liver. For clarity the liver is roughly outlined in red and the body is roughly outlined in blue.

Despite this it was still possible to collect a z-spectrum from a single slice which had adequate SNR, by selecting an ROI at the base of the liver, which is displayed in Figure

6.2.3. Volume B_0 shimming was performed over the liver and RF shimming (phase-nulling) was performed on a small target ROI using in-house software to maximise the homogeneity of the B_1 field in the chosen ROI.

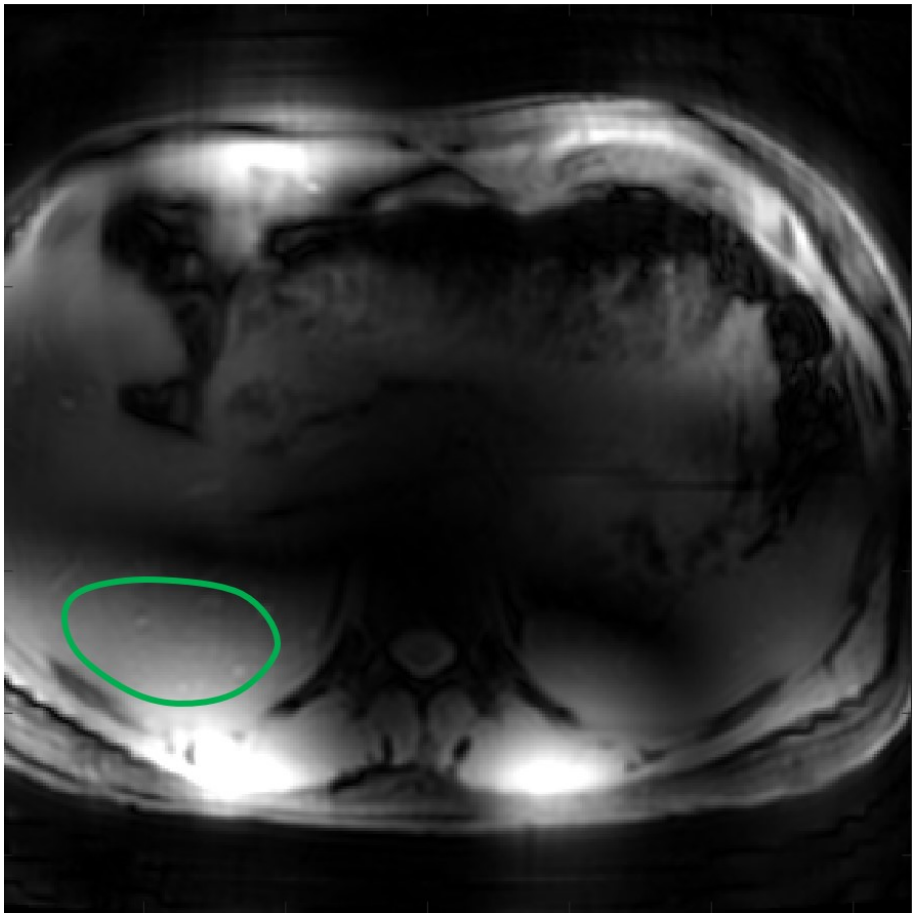

Figure 6.2.3: An example of a chosen liver ROI (green line), which was selected using a polygon shape tool.

Sixty-four off-resonance frequencies were then acquired using semi-CW saturation, with 50 alternating odd/even pulses, each 60ms long and with a $B_{1,max}$ of 1μT, resulting in a 3s saturation train. A TFEPI readout scheme was used, lasting 1.7s, and so the acquisition of each z-spectral image lasted 4.7s. The subject held their breath in this time, and was given 4.3s after the acquisition of every z-spectral image to breathe, resulting in a total of 9s per off-resonance image and a total z-spectrum acquisition

time of 10 minutes. Figure 6.2.4 shows the resulting z-spectrum following post-processing, which was performed using in-house MATLAB [19] scripts to B_0 correct the spectra by locating the minimum point in the z-spectrum and subsequently shifting the entire spectrum so that the minimum was aligned with 0ppm. The z-spectra in the target ROI were then masked, averaged, and normalised using the +333ppm point. As far as we are aware this is the first *in vivo* human liver z-spectrum to be presented at 7T. More features can be seen here than in the 3T liver spectrum displayed in Figure 6.1.5(a).

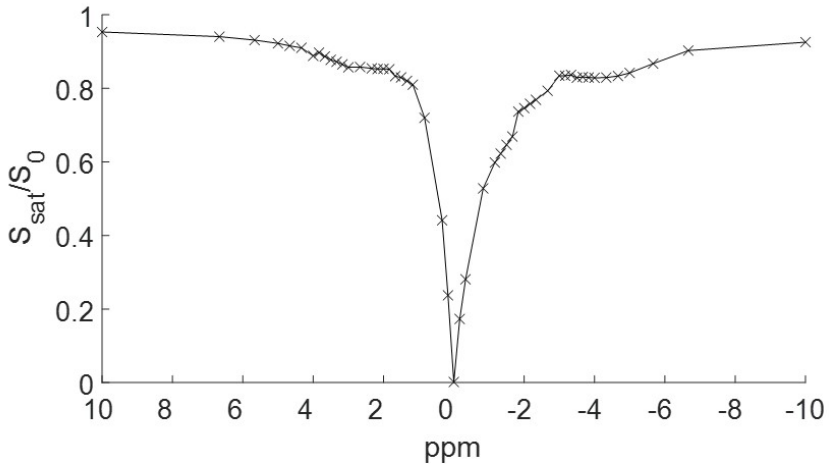

Figure 6.2.4: Z-spectrum acquired from *in vivo* human liver at 7T.

6.2.2 Abdominal MT: 3T vs. 7T comparison

There are several notable differences in the human liver z-spectrum when acquired at 7T as opposed to 3T. Note that the two spectra cannot be directly and quantifiably compared, as each were acquired with a different saturation power. The two z-spectra, which were acquired from the same subject, are presented for comparison in Figure 6.2.5.

The first thing that is evident when comparing these two z-spectra is that we are clearly achieving a much higher saturation power when performing z-spectrum imaging at 3T.

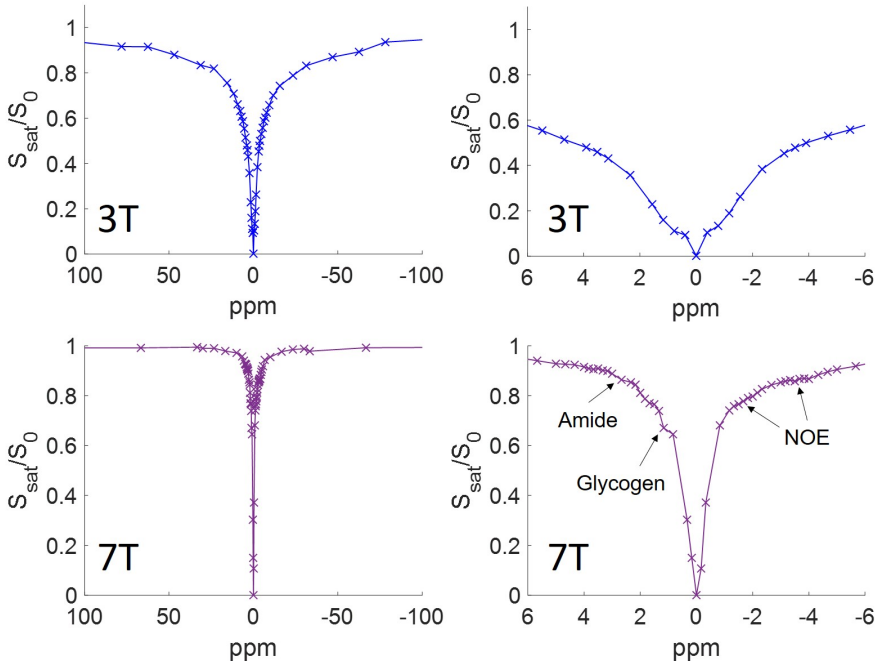

Figure 6.2.5: Z-spectra acquired from *in vivo* human liver ROIs at 3T (blue, top) and 7T (purple, bottom), presented covering a wide range of frequencies (left), and zoomed in around the water resonance (right).

This is evidenced by the much wider peak around the water resonance, along with the wider MT peak, proving that we are saturating it further. The T_2 of free water also decreases at higher field strengths, which narrows the water peak. As we have seen in Figure 6.2.2, we achieve relatively low B_1 in the liver compared to our target B_1 at 7T. However, this is an issue regarding the 7T body coil rather than the fact that we are performing z-spectrum imaging at a higher field strength, and further development is required to attempt to resolve this within safe operating limits.

Another feature of note when comparing the two spectra is the increased spectral resolution at 7T, which allowed us to resolve CEST and NOE effects which cannot be observed at 3T. Two particularly notable features here were the amide peak around +3.5ppm and the NOE peak at around -3.5ppm, which are commonly detected signals in biological tissues. We could also see an additional signal in the liver at 7T located

at around 1.5ppm, which is the resonance frequency of glycogen. This is of great interest in the liver and will form the basis of section 6.3. The NOE peaks are also of interest; a peak resonating at -1.7ppm could be observed, which may correspond to blood as detailed in Chapter 4.

6.2.3 Quantifying liver MT at 7T

As multiple z-spectra with varying saturation powers have not been acquired, the most appropriate method of MT quantification was to use a Lorentzian lineshape fitting method. Two additional healthy subjects (2 female, ages 24-26) were recruited and z-spectrum acquisition was performed as above, and B_0 correction was performed as described previously. The three z-spectra are displayed in Figure 6.2.6.

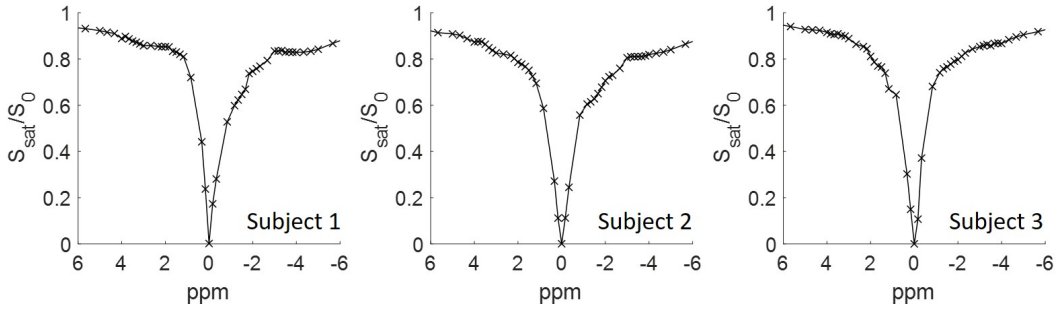

Figure 6.2.6: 7T liver z-spectra acquired from three different subjects.

Lorentzian lineshape fitting was then performed as described in section 6.1.2. However, in this instance, the fit was biased by modifying the minimisation function so that the MT pool never overfitted the data, ensuring that the MT Lorentzian always remained above any data points. This ensured that any CEST and NOE peaks were ignored by the two pool fit, leaving only the MT to be fit to the outer points. CEST and NOE quantification in the 7T liver z-spectrum is explored further in Section 6.3. Figure 6.2.7 shows the results of the two pool Lorentzian fits.

We have developed a method of acquiring *in vivo* z-spectra in the human liver at 7T which is capable of reliably measuring MT between subjects. Note that the MT

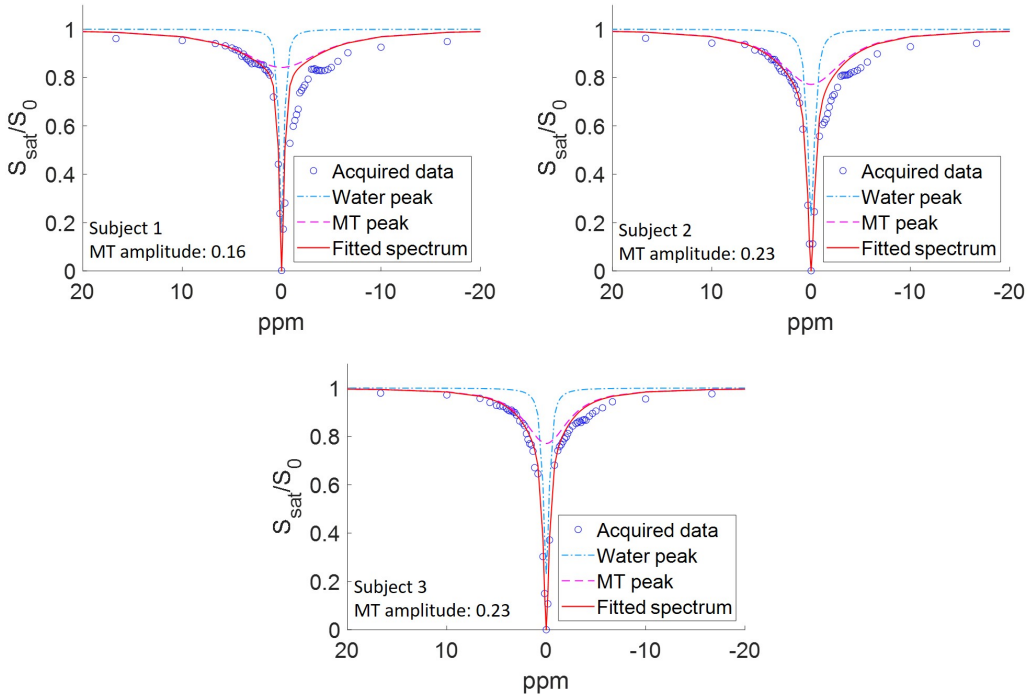

Figure 6.2.7: Lorentzian fits to the z-spectra from three subjects, with the height of the MT Lorentzian indicated on each.

Lorentzian amplitudes presented above are not directly comparable to Figure 6.1.4 or the data presented in Table 6.1.1, as a different saturation power has been applied here, and the MT lineshape would be different at 7T as compared to 3T. Similarly the discrepancy in lineshapes between subjects most likely arise from variations in the local B_1 field due to patient size and coil positioning. While MT imaging at 7T comes with challenges such as increased inhomogeneity of the B_1 transmit field, the higher resolution and signal-to-noise ratio associated with 7T MRI has the potential to improve the precision and sensitivity of the measurement of the MT signal.

6.3 Measuring glycogen in the liver through GlycoCEST

Glycogen is the primary short-term energy storage unit in humans, and plays a key role in glucose metabolism and homeostasis. Glycogen content is typically reasonably consistent across healthy individuals, ranging from 200-300mM in the liver when fasting [33], and from 318mM [34] to 470mM [35] after a meal. However this concentration can become depleted in individuals suffering from diabetes [36] or obesity [37]. These values have all been obtained by using ^{13}C MRS, which is the most common way to measure hepatic glycogen *in vivo* [38, 39]. However, these ^{13}C MRS experiments are time consuming (even more so if a labelled exogenous tracer is used) and can be particularly difficult in patients with significant adipose tissue.

CEST imaging offers an alternative approach to mapping glycogen [40]. The approach of measuring glycogen by analysing the CEST signal it produces is termed GlycoCEST, which has the potential to provide improved signal strength and reduced scan time compared to ^{13}C MRS, without the need for additional multi-nuclear equipment. Previous studies have shown that GlycoCEST is sensitive to *in vivo* changes in glycogen stores in humans at 3T [41]. Deng et al. acquired a full z-spectrum of 41 off-resonance frequencies between -5ppm to +5ppm at 0.25ppm intervals. However, the analysis involved a simple MTR asymmetry calculation, which may be particularly problematic given recent reports of an NOE signal which may arise from glycogen (termed GlycoNOE) [42], located directly opposite the GlycoCEST peak.

The aim of this section was to develop a method of monitoring liver glycogen by acquiring the whole z-spectrum at 7T, which provides considerably enhanced sensitivity and specificity to CEST and NOE effects, and to analyse this in a way which has minimal confounds with other signals present in the z-spectrum. This was performed *in vivo* in the human liver, and the response to fasting and feeding was observed.

6.3.1 Phantom validation

Given the issues of achieving a high saturation power using the body coil outlined in section 6.2, the first step was to acquire a z-spectrum from a glycogen-rich phantom in order to observe the GlycoCEST signal. A cylindrical phantom comprised of a suitable quantity of glycogen dissolved in distilled water was prepared. Two z-spectra were acquired, one using a NOVA 8ch pTx head coil, and the other using the MRCoils 8TX/32RX fractionated dipole body array, using the same sequence for both. Z-spectra were acquired at 64 off-resonance frequencies between $\pm$333ppm using semi-CW acquisition as described in section 6.2. A B_1 map was also acquired to quantify the difference in RF distribution and coverage between the two coils. Figure 6.3.1 shows the z-spectrum acquired from the phantom in both coils. The average B_1 was measured at 180% of the target B_1 (1μT) in the head coil, but only 30% of the target B_1 in the body coil.

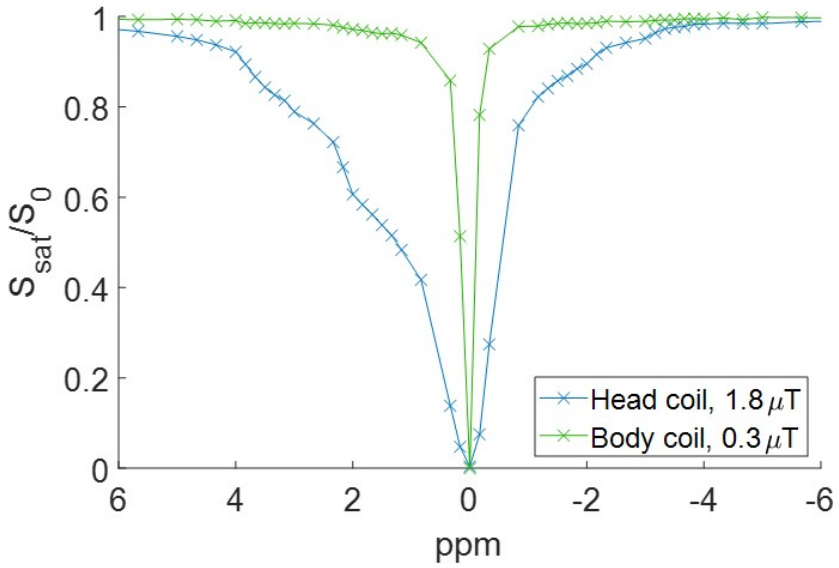

Figure 6.3.1: Z-spectra acquired from the glycogen phantom, highlighting the difference in the B_1 transmit filed between the two coils.

We can see from the nature of the peak in the z-spectrum acquired from the head

coil that the most prominent GlycoCEST signal is located between +0.8ppm and +1.8ppm. However, even with reduced saturation power from the body coil, this peak is still visible, albeit vastly reduced in amplitude. It is inconclusive from this data whether this GlycoCEST peak will be visible *in vivo* when acquired using the body coil due to competing effects in the z-spectrum such as MT, however it is at least reassuring that it can be seen with an effective saturation power of only 0.3μT. As glycogen has a relatively high exchange rate, the shape of the peak has a high temperature dependency, and so may be more pronounced *in vivo*. It is also worth noting that there appears to be a second exchanging pool at +3.2ppm, which is not visible at lower powers. This may be indicative of the presence of glycosaminoglycans (GAGs) in the phantom, which are long polysaccharides consisting of repeating sugar units. As mentioned in chapter 4, these compounds have a dual resonance located at +3.2 ppm and between +0.9ppm and +1.9ppm [43].

6.3.2 *In vivo* study protocol

4 subjects (2 male and 2 female) aged 24, 26, 36, and 55 years were recruited for the study. Subjects were asked to fast overnight, starting from 8pm, with the study beginning at 12 noon the next day, meaning a minimum of 16 hours of fasting. Subjects were all scanned on the same day. The scanning protocol lasted 30 minutes, and so subjects were interleaved. Figure 6.3.2 shows a timeline for the scanning protocol.

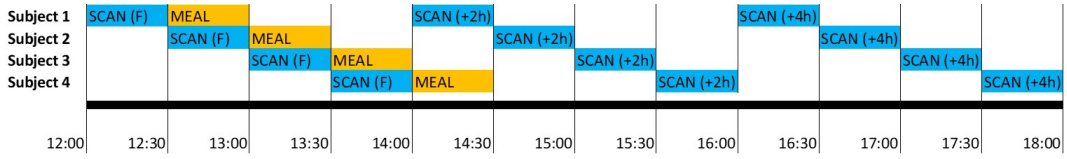

Figure 6.3.2: Timeline of study protocol. Scanning sessions highlighted blue, meal time highlighted in yellow. Total study duration was 6 hours.

The scanning protocol was similar to that described in section 6.2.1. A survey scan was performed to locate the liver, and single slice B_0 and B_1 maps were acquired

in the transverse plane. A small ROI was selected towards the posterior of the subject, and B_0 and B_1 shimming was performed across the selected ROI. A z-spectrum with a reduced number of acquisition frequencies was first acquired around the water frequency to assure that the B_0 shimming had been successful, with 7 off-resonance frequencies acquired from +1.5ppm to -1.5ppm at 0.5ppm intervals. If the lowest signal was 0.5ppm away from the scanner resonance, this was deemed acceptable as small B_0 variations could be corrected in post processing. The full z-spectrum was then acquired as detailed in section 6.2.1. 64 off-resonance frequencies were acquired between $\pm$333ppm using Semi-CW acquisition.

The meal offered to subjects was high in both carbohydrates and glucose, and consisted of an assortment of foods including takeaway pizza and chocolate cake. Subjects were encouraged to eat as much as they were comfortable with during their allocated thirty minutes of meal time. At the end of the scan subjects were asked how well they were able to follow these instructions.

Once the study had been completed, one subject was scanned a final three times in succession. This was done to assess the repeatability of acquiring the z-spectrum.

6.3.3 Analysis of spectra

The spectral images were post-processed using in-house MATLAB [19] scripts. The target ROI in the liver was masked and voxels in the ROI were averaged to create one z-spectrum for each set of z-spectral images. These were then normalised to the +333ppm point in the z-spectrum, and B_0 corrected by locating the minimum of the z-spectrum, and shifting the entire spectrum so that the minimum was aligned with 0ppm.

Figure 6.3.3 shows the z-spectra acquired to assess repeatability. It is clear that repeatability is very good between subsequent acquisitions, except for the peak occurring at the glycogen location which appears to grow over the course of 30 minutes. Other

possible peaks of interest are highlighted, along with a point in the z-spectrum where the subject admitted to missing a breath hold.

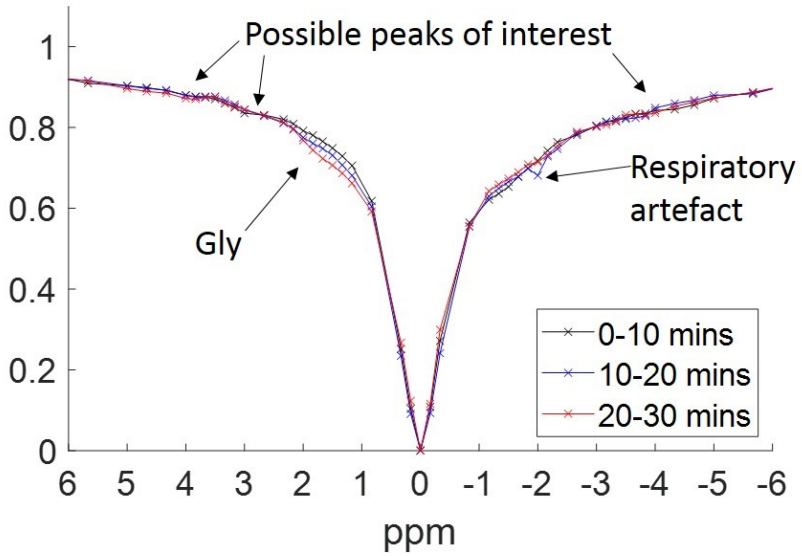

Figure 6.3.3: Z-spectra acquired repeatedly from one subject in quick succession. Possible peaks of interest are highlighted, along with a good example of the detrimental effects of missing a breath hold during acquisition of a point in the z-spectrum.

The z-spectra acquired from the rest of the study were then analysed in the same way. Figure 6.3.4 shows the series of z-spectra acquired from each subject. The data here is clearly extremely noisy. Subjects 2, 3, and 4 admitted that they may have fallen asleep during the scans, as the high amount of carbohydrate-rich food combined with the repetitive noise of the scanner during z-spectrum acquisition and the requirement to focus in breathing creates an environment where it can become difficult to remain awake and alert. This may have resulted in the subjects not holding their breath at the correct times and for the correct duration, leading to the breathing artefacts seen in section 6.1. Subject 1, however, was confident that they remained awake throughout the scanning procedure, and indeed this is reflected in the relatively noiseless z-spectra displayed in Figure 6.3.4(a).

After initial analysis, two peaks were quantified in the z-spectra by measuring the area

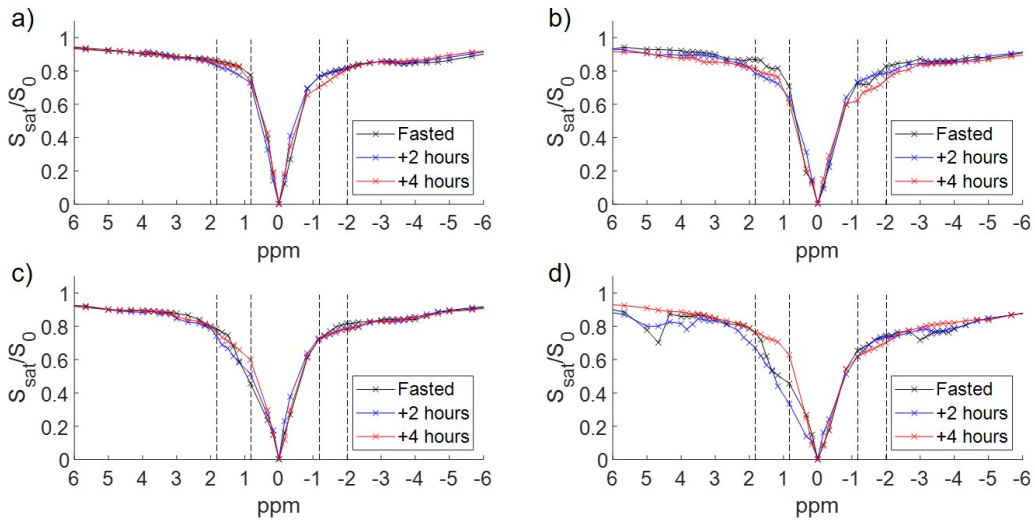

Figure 6.3.4: Z-spectra acquired from each subject, labelled (a-d). Of the four, only subject 1 managed to remain conscious throughout the scanning protocol, as shown in (a). Fasted spectra are displayed in black, and the spectra acquired 2 and 4 hours after the meal are displayed in blue and red respectively. Dotted lines show the location of the CEST and NOE peaks used for analysis.

under the z-spectrum at two hours and four hours post-meal relative to the fasted spectrum. These were the glycogen peak, located between +0.8ppm and +1.8ppm, and an NOE peak located between -2ppm and -1.17ppm. This method of quantification was chosen to overcome systematic errors which would arise from an asymmetry analysis, and in the absence of z-spectra acquired at further saturation powers, full quantification could not be performed.

Figure 6.3.5 shows the results of quantifying the two peaks. Error bars have been created by estimating the expected amount of variation in the fasted spectrum. For each subject, the standard deviation of the area under the spectrum between +6.7ppm and +5.7ppm, +5.7ppm and +4.7ppm, and +4.7ppm and +3.7ppm was calculated to give an indication of how each subject's breathing rate was altering the spectrum shape close to the glycoCEST peak. An identical symmetrical analysis was performed on the negative side of the spectrum to estimate error on the NOE peak. It should be noted that this is an imperfect measure as a missed breath hold alters the shape of

the z-spectrum quite dramatically, as can be seen particularly well in Figure 6.3.4(d).

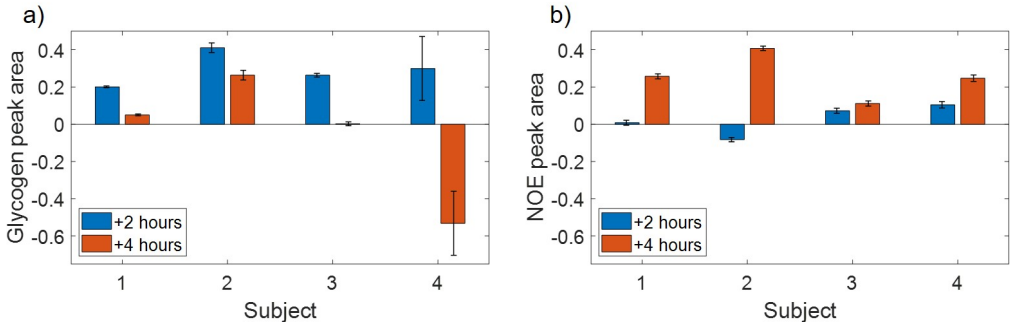

Figure 6.3.5: Change in the peak area between +0.8ppm and +1.8ppm corresponding to glycogen, and between -2ppm and -1.17ppm corresponding to the NOE peak, from the fasted spectrum. Error bars indicate standard deviation in adjacent CEST and NOE signals where the signal was not expected to change, to estimate spectrum variation.

These results indicate that the glycoCEST signal seems to reach a maximum two hours after feeding, whereas the NOE peak appeared to reach a maximum after 4 hours. However the results clearly varied hugely between subjects due to the induced effects of drowsiness during the scanning protocol, and realistically only the results from subject 1 should be considered. The origin of the NOE signal observed here is still in question. Previous work has attributed this as 'glycoNOE' [42] which would be directly correlated with the glycoCEST signal, but here we observe the signals behaving independently of each other. This is further evidenced in the repeatability study shown in Figure 6.3.3, in which the glycoCEST signal marginally increases over the course of 30 minutes but the observed NOE signal marginally decreases over the same period. It is possible that this NOE signal is due to changes in blood volume in the liver [44].

6.3.4 Future work

While this study demonstrates a promising initial investigation into measuring liver glycogen levels *in vivo*, there are clearly several issues that need to be resolved. Several

further variations of the study have since been attempted, and after these investigations a more robust study protocol has been designed.

The first and most obvious issue was to prevent subjects from falling asleep during z-spectrum acquisition. It was found that this could be achieved if the scanner operator spoke to the patient frequently during the scan. We found that if the patient was informed how far through the z-spectrum they were every five dynamics, they were able to retain a sufficient level of concentration to stay awake throughout the ten minute acquisition time.

Subjects should also be given a meal better optimised to detect glycogen uptake in the liver. As glycogen is a glucose storage unit, a high-glucose energy drink should be used (8.9g glucose / 100ml) in place of the unmeasured quantity of high-carbohydrate and high-sugar foods given previously. We suggest that subjects would drink a litre of this drink, however this was estimated based on body weight, gastric emptying rates, and the requirement to stay in the scanner long enough without the need to urinate. This may be revised in the future following further investigations.

This revised version of the experiment was performed alternating two subjects every 30 minutes, in order to further increase the temporal resolution of the study. However, it was found that the B_1 saturation power changed considerably between each z-spectrum acquisition, due to repositioning of the body coil. While a B_1 map is acquired as part of the scanning protocol, it is impossible to correct for changes in B_1 without the acquisition of multiple saturation powers, and even then B_1 correction using the required non-linear interpolation of the z-spectra would not be particularly robust. However, based on this finding we can now outline a study which should be able to accurately quantify the evolution of the glycoCEST peak and any other peaks in the liver following a meal.

6.3.5 Proposed protocol

As previously, a subject should fast overnight to ensure glycogen depletion in the liver. The subject should also be asked not to drink for 1.5 hours before the start of the scan and encouraged to urinate before scanning commences. The scanning protocol for the fasted scan should be performed as described throughout this section, with the scanner operator speaking to the subject after every five z-spectrum dynamics acquired to assist the subject in staying awake. When the fasted set of scans is complete, the patient should then remain in the scanner and ingest the glucose drink through a gastric catheter, given the narrow bore of the Philips 7T Achieva system. The glucose drink should be altered so that a set quantity of glucose per kilogram of the subject's body weight is dissolved in 500ml of water, to help avoid the need to urinate. Z-spectra should then be acquired at a minimum rate of one every thirty minutes after the subject has consumed the glucose drink. This results in a very long time that the subject has to remain in the scanner (ideally over two hours, if not more), which is why it is suggested that subjects are not continually subjected to z-spectrum acquisition, and are allowed breaks between. We can see evidence that this approach works in Figure 6.3.3 and Figure 6.3.4(a), where a z-spectrum was acquired from a subject three times without them leaving the scanner, and the saturation power was near identical each time.

Alternatively, multiple z-spectra acquired with different saturation powers could be collected for each timepoint, for example at 0.67μT, 1.33μT, and 2.00μT, along with a B_1 field map. If three z-spectra were collected while the subject is fasted, and then three were collected at hourly intervals after drinking a high-glucose drink, this would allow for B_1 correction of the acquired z-spectra while giving the subject more freedom, as the z-spectra could be interpolated back to the target B_1 as described in section 4.2. Using this protocol, the patient would be in the scanner for around 40 minutes per acquisition, leaving a 20 minute break between subsequent scans if we wanted to acquire once per hour. This would also allow us to acquire more timepoints, and we could potentially map the evolution of glycogen for the desired period of 4

hours after ingestion.

6.4 Summary

Z-spectrum imaging in the abdomen is still in its early stages, however it can enable unique applications such as fibrosis imaging and glycogen mapping. This chapter began by reviewing current methods of MT measurement in the abdomen before proposing and trialling a new protocol for z-spectrum imaging in the abdomen at clinical field strengths, which proved to be robust and repeatable, and free from respiratory effects. However, constraints were applied to acquisition of data on human subjects and therefore further data should be acquired to validate this protocol. Some of the challenges when moving to ultra-high field strengths were then explored, before conducting initial studies into how GlycoCEST imaging could be used to track glycogen changes after a meal. The chapter finishes by detailing what should be the ideal protocol to properly conduct this study, which hopefully can be used in the near future.

References

[1] Jeremy Adler, Scott D. Swanson, Phyllissa Schmiedlin-Ren, Peter D.R. Higgins, Christopher P. Golembeski, Alexandros D. Polydorides, Barbara J. McKenna, Hero K. Hussain, Trevor M. Verrot, and Ellen M. Zimmermann. Magnetization transfer helps detect intestinal fibrosis in an animal model of Crohn disease. *Radiology*, 2011. ISSN 00338419. doi: $10.1148/\mathrm{radiol.10091648}$.

[2] Kai Jiang, Christopher M. Ferguson, John R. Woollard, Xiangyang Zhu, and Lilach O. Lerman. Magnetization Transfer Magnetic Resonance Imaging Noninvasively Detects Renal Fibrosis in Swine Atherosclerotic Renal Artery Stenosis

at 3.0 T. *Investigative Radiology*, 2017. ISSN 15360210. doi: 10.1097/RLI.0000000000000390.

[3] Kai Jiang, Christopher M. Ferguson, Behzad Ebrahimi, Hui Tang, Timothy L. Kline, Tyson A. Burningham, Prassana K. Mishra, Joseph P. Grande, Slobodan I. Macura, and Lilach O. Lerman. Noninvasive assessment of renal fibrosis with magnetization transfer MR imaging: Validation and evaluation in murine renal artery stenosis. *Radiology*, 2017. ISSN 15271315. doi: 10.1148/radiol.2016160566.

[4] Shila Pazahr, Iris Blume, Pascal Frei, Natalie Chuck, Daniel Nanz, Gerhard Rogler, Michael Patak, and Andreas Boss. Magnetization transfer for the assessment of bowel fibrosis in patients with Crohn's disease: Initial experience. *Magnetic Resonance Materials in Physics, Biology and Medicine*, 2013. ISSN 09685243. doi: 10.1007/s10334-012-0355-2.

[5] Johannes Wiegand and Thomas Berg. The etiology, diagnosis and prevention of liver cirrhosis: Part 1 of a series on liver cirrhosis. *Deutsches Arzteblatt international*, 2013. ISSN 1866-0452. doi: 10.3238/arztebl.2013.0085.

[6] A. Grant and J. Neuberger. Guidelines on the use of liver biopsy in clinical practice, 1999. ISSN 00175749.

[7] J. Foucher, E. Chanteloup, J. Vergniol, L. Castéra, B. Le Bail, X. Adhoute, J. Bertet, P. Couzigou, and V. De Lédinghen. Diagnosis of cirrhosis by transient elastography (FibroScan): A prospective study. *Gut*, 2006. ISSN 00175749. doi: 10.1136/gut.2005.069153.

[8] An Tang, Guy Cloutier, Nikolaus M. Szeverenyi, and Claude B. Sirlin. Ultrasound elastography and MR elastography for assessing liver fibrosis: Part 2, diagnostic performance, confounders, and future directions. *American Journal of Roentgenology*, 2015. ISSN 15463141. doi: 10.2214/AJR.15.14553.

[9] Daniel J.B. Marks, Farooq Z. Rahman, Gavin W. Sewell, and Anthony W. Segal. Crohn's disease: An immune deficiency state, 2010. ISSN 10800549.

[10] Amy K. Hara, Jonathan A. Leighton, Russell I. Heigh, Virender K. Sharma, Alvin C. Silva, Giovanni De Petris, Joseph G. Hentz, and David E. Fleischer. Crohn disease of the small bowel: Preliminary comparison among CT enterography, capsule endoscopy, small-bowel follow-through, and ileoscopy. *Radiology*, 2006. ISSN 00338419. doi: 10.1148/radiol.2381050296.

[11] Rakesh Sinha, Prabhakar Rajiah, Iswaran Ramachandran, Scott Sanders, and Paul D. Murphy. Diffusion-weighted MR imaging of the gastrointestinal tract: Technique, indications, and imaging findings. *Radiographics*, 2013. ISSN 02715333. doi: 10.1148/rg.333125042.

[12] Robin Bülow, Birger Mensel, Peter Meffert, Diego Hernando, Matthias Evert, and Jens Peter Kühn. Diffusion-weighted magnetic resonance imaging for staging liver fibrosis is less reliable in the presence of fat and iron. *European Radiology*, 2013. ISSN 09387994. doi: 10.1007/s00330-012-2700-2.

[13] Thomas Allkemper, Florian Sagmeister, Vito Cicinnati, Susanne Beckebaum, Hendrik Kooijman, Christian Kanthak, Christoph Stehling, and Walter Heindel. Evaluation of fibrotic liver disease with whole-liver t1r MR imaging: A feasibility study at 1.5 T. *Radiology*, 2014. ISSN 15271315. doi: 10.1148/radiol.13130342.

[14] Feng Zhao, Min Deng, Jing Yuan, Gao Jun Teng, Anil T. Ahuja, and Yi Xiang J. Wang. Experimental evaluation of accelerated T1rho relaxation quantification in human liver using limited spin-lock times. *Korean Journal of Radiology*, 2012. ISSN 12296929. doi: 10.3348/kjr.2012.13.6.736.

[15] A. Alanen, Markku Komu, R. Leino, and S. Toikkanen. MR and magnetisation transfer imaging in cirrhotic and fatty livers. *Acta Radiologica*, 1998. ISSN 02841851. doi: 10.3109/02841859809172459.

[16] Katsuyoshi Ito, Minoru Hayashida, Shogo Izumitani, Tomoko Fujimine, Takeo Onishi, and Katsuhiro Genba. Magnetisation transfer MR imaging of the kidney: Evaluation at 3.0 T in association with renal function. *European Radiology*, 2013. ISSN 09387994. doi: 10.1007/s00330-013-2841-y.

[17] Olivier Mougin, Matthew Clemence, Andrew Peters, Alain Pitiot, and Penny Gowland. High-resolution imaging of magnetisation transfer and nuclear Overhauser effect in the human visual cortex at 7 T. *NMR in Biomedicine*, 2013. ISSN 09523480. doi: 10.1002/nbm.2984.

[18] Steven D. Wolff and Robert S. Balaban. Magnetization transfer contrast (MTC) and tissue water proton relaxation in vivo. *Magnetic Resonance in Medicine*, 1989. ISSN 15222594. doi: 10.1002/mrm.1910100113.

[19] Version 9.6 2019 The Mathworks, Inc. MATLAB. MATLAB - MathWorks - MATLAB, 2019.

[20] Waleed Ajaj, Susanne C. Goehde, Hubert Schneemann, Stefan G. Ruehm, Jörg F. Debatin, and Thomas C. Lauenstein. Dose optimization of mannitol solution for small bowel distension in MRI. *Journal of Magnetic Resonance Imaging*, 2004. ISSN 10531807. doi: 10.1002/jmri.20166.

[21] Thomas C. Lauenstein, Herbert Schneemann, Florian M. Vogt, Christoph U. Herborn, Stefan G. Rühm, and Jörg F. Debatin. Optimization of oral contrast agents for MR imaging of the small bowel. *Radiology*, 2003. ISSN 00338419. doi: 10.1148/radiol.2281020161.

[22] Carlo E. Zanoni, Celeste Bergamini, Maurizio Bertoncini, Lucio Bertoncini, and Alberto Garbini. Whole-gut lavage for surgery - A case of intraoperative colonic explosion after administration of mannitol. *Diseases of the Colon & Rectum*, 1982. ISSN 00123706. doi: 10.1007/BF02564173.

[23] Marc Andre Bigard, Pierre Gaucher, and Claude Lassalle. Fatal colonic explosion during colonoscopic polypectomy. *Gastroenterology*, 1979. ISSN 00165085. doi: 10.1016/0016-5085(79)90172-0.

[24] Susan J. La Brooy, C. L. Fendick, A. Avgerinos, C. B. Williams, and J. J. Misiewicz. POTENTIALLY EXPLOSIVE COLONIC CONCENTRATIONS OF HYDROGEN AFTER BOWEL PREPARATION WITH MANNITOL. *The Lancet*, 1981. ISSN 01406736. doi: 10.1016/S0140-6736(81)91553-1.

[25] Johannes M. Froehlich, Michael A. Patak, Constantin Von Weymarn, Christoph F. Juli, Christoph L. Zollikofer, and Klaus Ulrich Wentz. Small bowel motility assessment with magnetic resonance imaging. *Journal of Magnetic Resonance Imaging*, 2005. ISSN 10531807. doi: 10.1002/jmri.20284.

[26] Risk of serious adverse effects with hyoscine butylbromide. *Reactions Weekly*, 2017. ISSN 0114-9954. doi: 10.1007/s40278-017-26917-5.

[27] R. Park, W. J. Leach, and A. I. Arieff. Determination of liver intracellular pH in vivo and its homeostasis in acute acidosis and alkalosis. *American Journal of Physiology - Renal Fluid and Electrolyte Physiology*, 1979. ISSN 1931-857X. doi: 10.1152/ajprenal.1979.236.3.f240.

[28] K. Sahlin, R. C. Harris, B. Nylind, and E. Hultman. Lactate content and pH in muscle samples obtained after dynamic exercise. *Pflügers Archiv European Journal of Physiology*, 1976. ISSN 00316768. doi: 10.1007/BF00585150.

[29] Jan Fallingborg. Intraluminal pH of the human gastrointestinal tract. *Danish Medical Bulletin*, 1999. ISSN 09078916.

[30] Mark E. Ladd, Peter Bachert, Martin Meyerspeer, Ewald Moser, Armin M. Nagel, David G. Norris, Sebastian Schmitter, Oliver Speck, Sina Straub, and Moritz Zaiss. Pros and cons of ultra-high-field MRI/MRS for human application, 2018. ISSN 00796565.

[31] Ewald Moser, Freddy Stahlberg, Mark E. Ladd, and Siegfried Trattnig. 7-T MR-from research to clinical applications?, 2012. ISSN 09523480.

[32] Emma Doran. *Development of Abdominal MRI at 7 Tesla*. PhD thesis, University of Nottingham, 2020.

[33] Kitt F. Petersen, Gary W. Cline, David P. Gerard, Inger Magnusson, Douglas L. Rothman, and Gerald I. Shulman. Contribution of net hepatic glycogen synthesis to disposal of an oral glucose load in humans. *Metabolism: Clinical and Experimental*, 2001. ISSN 00260495. doi: 10.1053/meta.2001.22561.

[34] Roy Taylor, Inger Magnusson, Douglas L. Rothman, Gary W. Cline, Andrea Caumo, Claudio Cobelli, and Gerald I. Shulman. Direct assessment of liver glycogen storage by 13C nuclear magnetic resonance spectroscopy and regulation of glucose homeostasis after a mixed meal in normal subjects. *Journal of Clinical Investigation*, 1996. ISSN 00219738. doi: 10.1172/JCI118379.

[35] Kitt F. Petersen, Thomas Price, Gary W. Cline, Douglas L. Rothman, and Gerald I. Shulman. Contribution of net hepatic glycogenolysis to glucose production during the early postprandial period. *American Journal of Physiology - Endocrinology and Metabolism*, 1996. ISSN 01931849. doi: 10.1152/ajpendo.1996.270.1.e186.

[36] Alan D. Proia. Glycogen storage diseases. In *Garner and Klintworth's Pathobiology of Ocular Disease Part B, Third Edition*. 2007. ISBN 9781420093919. doi: 10.5005/jp/books/11585{_}30.

[37] G. I. Shulman, D. L. Rothman, D. Smith, C. M. Johnson, J. B. Blair, and R. A. DeFronzo. Mechanism of liver glycogen repletion in vivo by nuclear magnetic resonance spectroscopy. *Journal of Clinical Investigation*, 1985. ISSN 00219738. doi: 10.1172/JCI112078.

[38] Laurel O. Sillerud and Robert G. Shulman. Structure and Metabolism of Mammalian Liver Glycogen Monitored by Carbon-13 Nuclear Magnetic Resonance. *Biochemistry*, 1983. ISSN 15204995. doi: 10.1021/bi00274a015.

[39] Inger Magnusson, Douglas L. Rothman, Lee D. Katz, Robert G. Shulman, and Gerald I. Shulman. Increased rate of gluconeogenesis in type II diabetes mellitus a 13C nuclear magnetic resonance study. *Journal of Clinical Investigation*, 1992. ISSN 00219738. doi: 10.1172/JCI115997.

[40] Peter C.M. Van Zijl, Craig K. Jones, Jimin Ren, Craig R. Malloy, and A. Dean Sherry. MRI detection of glycogen in vivo by using chemical exchange saturation transfer imaging (glycoCEST). *Proceedings of the National Academy of Sciences of the United States of America*, 2007. ISSN 00278424. doi: 10.1073/pnas.0700281104.

[41] Min Deng, Shu Zhong Chen, Jing Yuan, Queenie Chan, Jinyuan Zhou, and Yì Xiáng J. Wáng. Chemical Exchange Saturation Transfer (CEST) MR Technique for Liver Imaging at 3.0 Tesla: an Evaluation of Different Offset Number and an After-Meal and Over-Night-Fast Comparison. *Molecular Imaging and Biology*, 2016. ISSN 18602002. doi: 10.1007/s11307-015-0887-8.

[42] Yang Zhou, Peter C.M. van Zijl, Xiang Xu, Jiadi Xu, Yuguo Li, Lin Chen, and Nirbhay N. Yadav. Magnetic resonance imaging of glycogen using its magnetic coupling with water. *Proceedings of the National Academy of Sciences of the United States of America*, 2020. ISSN 10916490. doi: 10.1073/pnas.1909921117.

[43] Wen Ling, Ravinder R. Regatte, Gil Navon, and Alexej Jerschow. Assessment of glycosaminoglycan concentration in vivo by chemical exchange-dependent saturation transfer (gagCEST). *Proceedings of the National Academy of Sciences of the United States of America*, 2008. ISSN 00278424. doi: 10.1073/pnas.0707666105.

[44] Simon M. Shah, Olivier E. O.E. Olivier E. Mougin, A.J. Andrew J. Carradus, Nicolas Geades, Richard Dury, William Morley, and Penny A. P.A. Gowland. The z-spectrum from human blood at 7T. *NeuroImage*, 167, 2018. ISSN 10959572. doi: 10.1016/j.neuroimage.2017.10.053.

Conclusions

This thesis presents a new method of quantifying the underlying physical parameters which give rise to the shape of the z-spectrum. In particular it has demonstrated the use of a Particle Swarm Optimisation (PSO) algorithm in addressing this problem. Unlike similar existing methods, the z-PSO is not dependent on any initial guesses, and accurate quantification relies only on selecting the correct exchanging pools for fitting. This method and other quantification methods are used throughout this thesis for a wide range of *in vivo* and *ex vivo* applications in blood, brain and body.

Chapter 3 used the MT pool size as a marker for myelination to assess variation in myelination levels across the adult lifespan. The look-up table was chosen as an analysis method here as it is more suitable than the z-PSO for a quick analysis of large datasets, especially when we are primarily interested in the pool sizes of exchanging pools. Global and lobewise analyses are performed, and it is shown that the myelination varies with age across the cortex, peaking at around age 42. This is compared with the T_1 measurements which have a peak later in life, most likely due to the buildup of cortical iron which can decrease T_1 measurements. The widely known decline in cortical thickness is also observed, which is compared to the grey matter MT measurements. No correlation was found between grey matter MT and cortical thickness, suggesting that cortical thinning is not driven by demyelination in later life. Finally the NOE pool size was also explored as a marker for myelination and it was found to follow a similar (albeit weaker) parabolic trend with age, which may be of use in understanding the origin of the signal in the human brain.

The z-PSO was presented and evaluated in chapter 4. This revealed that the algorithm was capable of accurately quantifying the underlying z-spectrum parameters, up to the limit of the information provided in the z-spectrum. The algorithm was tested on a creatine phantom at a range of temperatures, and successfully managed to fit exchange rates which exhibited an approximate expected exponential decline with decreasing temperature, which is the relationship we would expect considering the Arrhenius equation. The z-PSO was then used to fit a six pool model to cerebral grey and white matter, and the results were found to largely agree with similar analyses using other quantification methods where available. Of particular interest, the only significant differences between the cerebral grey and white matter were in the MT pool size, which has been reported previously, and the NOE signal located at -1.7ppm, which is currently of great interest. The z-PSO has many potential future applications in measuring the exchange rates of a variety of CEST and NOE sources, both *in vivo* and in phantom work.

Chapter 5 applied the z-PSO to a human blood z-spectrum in order to attempt to determine the origin of the signals seen in the spectrum. F-tests on the fitted data demonstrated that the most likely sources of signal were from glucose, glycosaminoglycans (GaGs), and two NOE signals at -3.5ppm and -1.7ppm. The ability to measure glucose using the CEST signal was then probed further, but it was found that we were unable to measure changes in the glucoCEST signal in a physiological range of between 1.55mMol/L to 10.20mMol/L. The potential for *in vivo* pH measurement using Iopamidol as an endogenous CEST contrast agent was then explored. It was found that by using a low saturation power it was possible to distinguish between pH levels in a physiologically relevant range. This could be utilised in future studies, for example measuring muscle pH *in vivo* before and after exercise.

Finally the potential applications of abdominal z-spectroscopy were explored in chapter 6. The issues with current methods of measuring abdominal MT are outlined and illustrated, and a respiratory and cardiac gated protocol is described to measure liver and kidney MT. This was then developed further with a protocol in which the subject was prompted to hold their breath at regular intervals, which appeared to remove any

artefacts. This was used to measure MT in the intestinal wall, and was found to give reliable results. This protocol will be used in a future study. The possibility of performing z-spectroscopy at 7T was then explored, with an experiment to measure the evolution of glycogen through measurement of the glycoCEST signal. This experiment was performed with promising indications, however suffered from a fatal systematic error, along with other parts of the experiment which could be optimised. The chapter therefore concluded by providing a protocol for repeating this experiment in the future, which should hopefully prove to be a robust way of measuring the evolution of the glycoCEST signal in the liver following a meal.

In conclusion, this thesis presents a new robust and reliable method of quantifying signals seen in z-spectroscopy, with the aim of developing the measurement of MT, CEST and NOE effects for clinical use. These signals have been measured in a number of *in vivo* situations, with potential future applications such as *in vivo* pH measurement of muscle using Iopamidol in exercise studies, diagnosis of Crohn's disease through measurement of bowel fibrosis, and further understanding of glycogen metabolism disorders, among many more.